uOttawa

L'Université canadienne
Canada's university

FACULTÉ DES ÉTUDES SUPÉRIEURES ET POSTOCTORALES

uOttawa

L'Université canadienne
Canada's university

FACULTY OF GRADUATE AND POSDOCTORAL STUDIES

Jonathat Ethier

AUTEUR DE LA THÈSE / AUTHOR OF THESIS

M.A.Sc. (Electrical Engineering)

GRADE / DEGREE

School of Information Technology and Engineering

FACULTÉ, ÉCOLE, DÉPARTEMENT / FACULTY, SCHOOL, DEPARTMENT

MIMO Antenna Design Using Characteristic Mode Concepts

TITRE DE LA THÈSE / TITLE OF THESIS

Prof. McNamara

DIRECTEUR (DIRECTRICE) DE LA THÈSE / THESIS SUPERVISOR

CO-DIRECTEUR (CO-DIRECTRICE) DE LA THÈSE / THESIS CO-SUPERVISOR

EXAMINATEURS (EXAMINATRICES) DE LA THÈSE / THESIS EXAMINERS

Prof. E. Gad

Prof. A. Petosa

Gary W. Slater

Le Doyen de la Faculté des études supérieures et postdoctorales / Dean of the Faculty of Graduate and Postdoctoral Studies

MIMO Antenna Design Using Characteristic Mode Concepts

by

Jonathan Ethier, B. A. Sc.

A thesis submitted to the
Faculty of Graduate and Postdoctoral Studies
in partial fulfillment of the requirements for the degree of

Master of Applied Science
in Electrical Engineering

Ottawa-Carleton Institute for Electrical and Computer Engineering
School of Information Technology and Engineering
Faculty of Engineering
University of Ottawa

June 6th, 2008

Your file Votre référence
ISBN: 978-0-494-48453-1
Our file Notre référence
ISBN: 978-0-494-48453-1

Abstract

In this thesis we show how characteristic mode (CM) theory can be used to in the design of the antennas with the low envelope correlation coefficients preferred for MIMO antennas. This is due to the fact that the radiated fields of CMs are orthogonal over the radiation sphere. We show how a handheld device structure can be excited at various points (which form the multi-antenna ports) to ensure that each port excites a set of CMs such that the mode indices in each set are different for each antenna. It is this important result which causes the natural orthogonality properties of the CMs to be transferred to the overall radiation patterns of the multiple antennas. The CM analysis we have performed includes the effects of structure losses; it appears to be the first time that the computation of such modes have been reported. A logical and satisfying methodology for MIMO antenna design is the result. The methodology is extended to include arbitrary MIMO scattering environments using polarization sensitive generalized characteristic modes, which is the first of its kind from both the theory and methodology perspective. This design approach for MIMO antennas is not restricted to handheld devices, and can be used in a variety of applications. Lastly we discuss the various port mode theories that yield far-field orthogonality for perfect scattering environments, the application of which has already been discussed in the literature. We show succinctly that physical port symmetry yields frequency insensitive modes, but very minor symmetry breaking yields very narrow low envelope correlation bandwidth, something that is not discussed in the literature, but discussed in detail in this thesis.

Publications

Jonathan Ethier, Eric Lanoue and Derek McNamara, "MIMO Handheld Antenna Design Approach Using Characteristic Mode Concepts", *Microwave and Optical Technology Letters*, Volume 50, No. 7, July 2008, pp.1724 – 1727.

Jonathan Ethier and Derek McNamara, "The Use of Generalized Modes in the Design of MIMO Antennas", *13th Biennial IEEE Conference on Electromagnetic Field Computation (CEFC 2008) Digest*, Athens, Greece, May 11 – 15.

Jonathan Ethier and Derek McNamara, "An Interpretation of Mode-Decoupled MIMO Antennas in Terms of Characteristic Port Modes", *13th Biennial IEEE Conference on Electromagnetic Field Computation (CEFC 2008) Digest*, Athens, Greece, May 11 – 15.

Acknowledgements

I would like to express my thanks to my supervisor throughout my Master's research, Dr. Derek A. McNamara. His comments, patience and helpful criticism have been critical in the development of this thesis. The financial support of the National Science and Engineering Research Council (NSERC) is gratefully acknowledged.

The many discussions with, and helpful suggestions from my research colleagues Eric Lanoue and Igor Acimovic are duly acknowledged, be they engineering topics or discussions on life, liberty and the pursuit of happiness. The support of the technical and support staff at the University of Ottawa is also greatly appreciated, namely Alain LeHenaff, for his help with lab related duties.

My thanks to the professors who taught the graduate courses in electromagnetics, namely Dr. Derek A. McNamara, Dr. Aldo Petosa and Dr. Pierre Berini, who are all committed teachers, not just lecturers.

Many thanks go to my family, especially my parents Don and Anne, who have always encouraged me to never settle or pass on once in a lifetime opportunities. Thanks also go to my nephew, Steven, who reminds me that answers are not always found at the end of an equation, but rather in the guise of a multiple choice question.

Finally, and most importantly, I would like to thank my wife, Dawn. Aside from the usual thanks for the support and understanding as all loved ones tend to give, she has also been a terrific sounding board, listening to me drone on about modes, waves and eigenvalues. I really believe she deserves an honorary degree in engineering. Thanks also go to the little one inside her who has been an enormous source of motivation in the last months of preparation for this thesis.

Contents

Chapter 1

INTRODUCTION

1.1 Introductory Remarks

The need for more capacity in wireless communications has resulted in increasing interest in multiple-input multiple-output (MIMO) systems to exploit the properties of multipath channels. The amplified need for capacity is the result of an exponential increase in the number of wireless users and the demand for the multimedia capabilities of handhelds.

MIMO systems employ multiple antennas in a scattering rich environment and take advantage of the multipath fading to yield increased capacity. By modeling the scattering environment in what is known as the channel matrix, along with the multiple signals transmitted and received, a MIMO system can utilize a myriad of algorithms to increase capacity far beyond the theoretical limit of ideal line-of-sight communications found in single input, single output (SISO) systems.

The principal requirement for MIMO antennas is that the envelope correlation between the antennas be low. Envelope correlation can be interpreted as a measure of similarity between the far-field patterns of the individual antennas, with the measurement taken over the entire sphere, or perhaps over constrained regions of the far-field or relative to a pre-defined weighting function. In common with any other communications system we also require the maximum effective gain (MEG) to be high. Together these two figures of merit lead to increased capacity.

The groundwork has been laid for the mathematical framework in which MIMO resides, but there has been no structured design methodology for high performance MIMO antennas.

In many handheld communications devices there is little room for the placement of antennas. This problem is exacerbated when more than one antenna is needed, as is the case for MIMO systems. It has been stated by many that, especially for handheld devices where such electrically-small multi-functional antennas will be needed, the packaging and circuitry will become integral parts of the antennas. It is then useful to be able to utilize as much of the existing handheld device structure to form the required antennas.

The theory of characteristic modes is ideally suited for analyzing handheld devices, as it naturally determines resonances for entire structures, not just single radiating element antennas. In this way, characteristic modes (CM) can be used to develop multiple antennas on single contiguous structures without having to rely on optimization routines. For the cases of handheld devices, the chassis, ground plane and various electronic components all contribute to the overall functionality of handheld radiating structure. Furthermore, the modes determined using CM analysis have tantalizing properties in the far-field, namely, the modal fields are orthogonal over the far-field sphere, much the same as the ubiquitous spherical wave expansion functions. The advantage of these characteristic modal fields over spherical wave expansion functions is that their physical source resides on the surface of the conductor being analyzed and often represents an achievable current distribution via feed mechanisms.

The ability to design multiple antennas on single contiguous structures, the orthogonality properties of the far-field patterns and the physical realization of the sources makes characteristic mode analysis ideally suited for high-performance MIMO antenna design.

1.2 Overview of Thesis

Since we intend to show that characteristic modes have direct application to MIMO antenna design, we require a software tool in which to compute and analyze the modes of handheld devices. To date, no commercial software tools are immediately capable of computing characteristic modes, hence we are required to develop our own code or at least take advantage of and alter an existing formulation. Fortunately, antenna analysis can be performed in software development environments such as MATLAB. The software tool we shall develop consists of a moment method formulation, which is currently the only numerical method capable of solving explicitly for characteristic modes. Since the formulation is entirely MATLAB based, we are able to consider every detail of the code. The general moment method engine was tuned for faster computation, as well as increased accuracy. The requirements of the characteristic mode software includes an eigenvalue solver, normalization routines, feeding schemes, and various computational tools such as measuring envelope correlation (via surface integration) and S-parameters extraction (to name a few).

It is necessary to understand the theoretical concepts that describe MIMO communications theory, Characteristic Mode Analysis, and the Method of Moments; all three of which are discussed in Chapter 2. In chapter 2.2, we discuss MIMO antenna design requirements, namely envelope correlation and mean effective gain. In chapter 2.3 we consider the various Characteristic modal formulations, their properties and the methods one can use to compute and analyze these modes. Finally, in chapter 2.4 we discuss the moment method formulation and how we will use it to compute the characteristic mode quantities.

The implementation of our Characteristic Mode Analysis software design is outlined in Chapter 3, as well as an extensive software validation in section 3.3. We will consider the impedance operator symmetry, and ensure that our discrete matrix representations are symmetric as required by the modal theories. Additionally, we will compare computed results to known closed-form values. Lastly, we will validate a finite conductivity

formulation by showing the expected asymptotic behaviour of the modes as conductivity becomes arbitrarily large.

Throughout Chapter 4, we will consider fundamental studies of characteristic modes. We derive new figures of merit that allow a more satisfying ranking of the characteristic modes in terms of their 'modal significance' including all aspects of antenna performance.

The most significant contributions of this thesis are developed in Chapters 5, 6 and 7. In Chapter 5, we will outline a concise design methodology one can use to control and excite unique sets of characteristic modes at independently operating antenna ports. In doing so, we maintain far-field orthogonality and thus low envelope correlation between the antenna ports – a principal requirement in MIMO antenna design. In particular, this methodology is outlined in section 5.4. Additionally, in section 5.5 and 5.6 we show methods in which one can ensure excellent impedance bandwidth while still maintaining the low envelope correlation requirement. We also discuss physical symmetry and Characteristic Modes, which has a very satisfying tie in to the material in Chapter 7. Lastly, in section 5.8, we consider a multitude of MIMO antenna design examples using the developed methodology, with experimentally verified results, showing the design methodology is sturdy in its approach.

In Chapter 6, we consider an alternative modal formulation known as Generalized Characteristic Modes (GCM), which define modal currents with far-field orthogonality relative to a specified weight. We derive a new set of GCMs that include the ability to specify polarization. One can set this weight equal to a PAS function which describes a more practical scattering environment. These PAS functions are based on experimentally measured data found in the literature, with few approximations needing to be conceded as a result. We then apply the same design methodology developed in Chapter 5, only with the newly distinct GCM currents, and the resulting design is a practical set of MIMO antennas with low envelope correlation relative to a practical scattering environment,

rather than the idealized perfect scattering environment of full angular spread (i.e. full sphere orthogonality).

In chapter 7, we show an application of Characteristic Port Mode theory to MIMO antenna design. This approach is similar to the previous mode theories in that we obtain orthogonality of antenna far-field patterns. However, what differs in this approach is that the modal quantities (currents and voltages) exist solely at pre-defined ports, forgoing the need to analyze the entire surface of the antenna. Moreover, the methodology allows for commercial codes to be used in the analysis process. Contrary to Chapters 5 and 6, we no longer have individual antennas, but a set of superimposed antennas, requiring additional circuitry to act as a 'modal decomposition network' or (MDN). In this section we also show how the physical symmetry of the antenna ports is directly related to the accessibility and practicality of the CPMs. We conclude the chapter with a comparison of various similar methodologies, and show under what conditions these formulations are equivalent, including a comparison between the CMs and CPM theory.

Finally, in chapter 8, we conclude with a list of the major contributions made throughout this thesis. We will also comment on the future potential of characteristic mode concepts applied to MIMO antenna design.

Chapter 2

OVERVIEW OF THEORY

2.1 – Introduction

In this chapter we will discuss the various theoretical frameworks necessary for the design of MIMO antennas using Characteristic Mode Concepts. In section 2.2 we will briefly consider MIMO from the signal's perspective but focus mainly on the electromagnetics, namely the design requirements of MIMO antennas. We will show that there are two important antenna design criteria: envelope correlation and mean effective gain. In section 2.3, we will consider the theory of characteristic modes, the properties of these modes and the methods one can use to extract useful information from them. The modal formulations provide surface currents that exist over the entire analyzed structure and have enticing far-field properties. We will consider various formulations, beginning with the Characteristic Modes (CM), and continuing with the newly defined lossy characteristic modes (LCM). The CM and LCM formulations yield modes that have orthogonality over the entire far-field sphere, which is a tantalizing property for MIMO antenna design. We will also introduce the Generalized Characteristic Modes (GCMs), and show the CMs are related to the generalized modes GCMs in a simple manner. These GCM modes have far-field orthogonality relative to a chosen weight function rather than the entire far-field sphere. Lastly, we consider the Characteristic Port Modes (CPM) which have the same orthogonality properties as the CMs and LCMs only the modes exist in the form of currents or voltages solely at a finite number of pre-defined antenna ports. Lastly, we conclude in section 2.4 with an overview of moment methods applied to electromagnetics, and consider a surface patch formulation using RWG basis functions, which we will use in the computation of both modal and MIMO quantities.

2.2 – MIMO Systems

2.2.1 – Introduction

In recent years MIMO communications has had an exponential increase in interest as evident by the eruption of papers published on the topic. A simplified definition for MIMO is as follows:

> *MIMO stands for Multiple-Input, Multiple-Output: the use of multiple transmitters and multiple receivers in a communications environment allows for a significant increase in noise immunity and thus data throughput, provided the environment allows for uncorrelated fading of the transmitted signals.*

The biggest advantage that MIMO has over other types of communication schemes (SISO, SIMO, MISO) is the fact that MIMO takes advantage of multipath fading within the communications link. Fading, in its simplest definition, is any mechanism that distorts the transmission of electromagnetic energy (i.e. scatterers, diffractions). This is contrary to previously held beliefs about communications environments, since these types of obstacles degrade performance by reducing received power (thereby decreasing SNR) by introducing noise in the form of destructive interference and otherwise making life miserable for those stuck in the SISO days.

MIMO is not restricted to any physical form of communications link, and the concepts work just as well for wired approaches (Parallel wired communications, IDE cables) and wireless approaches using multiple transmit and receive antennas. Wired MIMO yield incredible advantages over the wireless approach (for reasons that will be explained later) but has the obvious crippling disadvantage of needing copper.

Consider a single transmit and receive antenna, built for SISO operation in Freespace. If one were to gauge the performance of the system in a noisy environment, one could characterize the signal-to-noise ratio by estimating the noise level at the receiver, and the

total received power via the Friis transmission formula. By introducing large scattering objects and other various fading affects, we can critically reduce the received power at the receiver such that the SNR is no longer acceptable.

Now consider introducing a second Tx and Rx antenna, thus making a 2 x 2 MIMO system. Place this system in a freespace environment, and depending on the spacing of the Tx and Rx pairs, one might increase the received power at the Rx terminals, but one might also destructively interfere with the signals from the antenna terminals and cause a reduction in received signal level, potentially dropping SNR.

Finally, introduce the scattering environment. With sufficient amounts of fading (uncorrelated fading to be precise) the signals transmitted can oft be recovered efficiently at the receiving end, provided information about the fading (i.e. the channel) is known. It is as though by experiencing unique paths of fading the transmitted information can be efficiently retrieved. Perhaps one might consider this phenomenon as though each transmitted signal has taken its own unique path (or set of paths) to the receiver, independent of others. This is the advantage of MIMO in a scattering rich environment: the greater the scattering, the greater likelihood the transmitted signals will fade independently of each other and a higher capacity results.

2.2.2 – The MIMO Channel

An important concept to understand in the theory of MIMO communications from the signal's perspective is the channel matrix. The basic MIMO architecture is as follows:

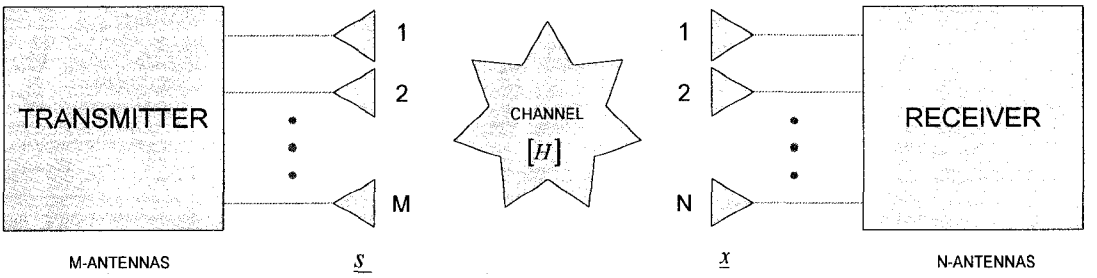

Figure 1 – MIMO Channel Block Diagram

The transmitter has M antennas, and thus is attributed to M signals:

$$\underline{s} = \begin{bmatrix} s_1 & s_2 & s_3 & \cdots & s_M \end{bmatrix}^T \tag{2.2-1}$$

The channel matrix H describes the environment, including scattering, diffraction, obstruction, and so forth. Each combination of Tx (m) and Rx (n) have their own transfer function h_{mn}, much like the transfer function for a SISO system. Together, these functions form the channel matrix:

$$[H] = \begin{bmatrix} h_{11} & h_{12} & \cdots & h_{1M} \\ h_{21} & h_{22} & \cdots & h_{2M} \\ \vdots & \vdots & \ddots & \vdots \\ h_{N1} & h_{N2} & \cdots & h_{NM} \end{bmatrix} \tag{2.2-2}$$

The receive antennas receive signals x, and is formed into a column vector as such:

$$\underline{x} = \begin{bmatrix} x_1 & x_2 & x_3 & \cdots & x_N \end{bmatrix}^T \tag{2.2-3}$$

We can also define the channel noise n in a similar manner:

$$\underline{n} = \begin{bmatrix} n_1 & n_2 & n_3 & \cdots & n_N \end{bmatrix}^T \tag{2.2-4}$$

The receive vector can be written in terms of the channel matrix, the transmitted signals and the noise:

$$\underline{x} = [H] \cdot \underline{s} + \underline{n} \tag{2.2-5}$$

One can state that the channel matrix forms a collection of the complex transfer functions between every possible Tx-Rx antenna pair. For example:

- h11 represents the transfer function between *transmitter* #1 and *receiver* #1
- h12 represents the transfer function between *transmitter* #1 and *receiver* #2
- The quantity h11 is not a type of self-transfer function. It is **not** akin to the scattering parameter S_{11}!

It should be noted that the most important concept to take away from this introduction that the channel matrix is defined by the combined effect of the environment, transmitter and receiver antennas. Thus, all electromagnetic effects such as near-field coupling are present and accounted for in the channel matrix [H].

By analyzing MIMO systems, Foschini and Teletar [1] made ground breaking research in this fledgling area of communication systems. They showed that with the knowledge of the channel matrix, one can quickly determine the maximum capacity of said communications link in the presence of some defined noise level ρ. Foschini and Teletar showed that channel capacity is defined by the following formula:

$$C = \log_2 \det\left(I + \frac{\rho}{n_T} HH^+ \right) \tag{2.2-6}$$

where I is the identity matrix, n_T is the number of transmitting antennas and C is the capacity, a measure of spectral efficiency [bits/s /Hz], H is the channel matrix and the symbol + is the conjugate transpose. These results are valid for the ideal scenario where the channel matrix is known, and is in an agreeable form for purposes such as inversion or eigenanalysis.

In this thesis we are interested in the antenna design requirements for MIMO antennas. The antenna designer must remain attentive to a multitude of details from the electromagnetics perspective, all of which will be discussed in the proceeding sections.

2.2.3 – Power Angular Spectrum

One classifies environments based on the nature of their scattering and the angular spread of the incident electromagnetic energy. The causes of this scattering can be attributed to buildings, terrain and vegetation. This "spread" of incident electromagnetic energy can be described, in general, as a function of azimuth(ϕ) and zenith(θ) angular components:

$$\text{Power Angular Spectrum} = P(\theta,\phi)$$

The most general power angular spectrum (PAS) one can consider is the perfectly scattering environment, described by an equally likely incidence of power from all angles over the entire sphere. This model is often used to determine potential MIMO performance of a set of antennas, as though they were in a perfect scattering environment [2]. In this case, the PAS function would be a constant:

$$P(\theta,\phi) = \text{constant}$$

A more reasonable, but still general PAS is described by the MCS, or Mobile Communication Scenario. As described by Vaughan [2], MCS is defined in terms of transverse spherical coordinates as:

$$P(\theta,\phi) = \text{constant for } 60^o \le \theta \le 90^o \text{ and } 0^o \le \phi \le 360^o$$

It is then assumed that incident power is equally likely from within this region, and zero everywhere outside of it. This is of course a simplification, but serves as refinement to the full angular spread approach (perfect scattering environment) and an excellent basis for designing more realistic MIMO antenna systems.

In practice, one finds that different types of environments have different PAS functions. Typically, one considers the rural, urban and indoor models when discussing

mobile communications of the mobile variety. As such, extensive experimental measurements have shown certain mathematical functions describe the PAS of urban and rural environments quite well.

For both rural, urban and indoor environments, the most common functions quoted to best represent the incident power distribution are *Gaussian* [3], *Laplacian* [4] and *Double Exponential* [5]. All three are functionally similar and we shall discuss them below:

The Gaussian, Laplacian and Double Exponential distributions are described as follows:

$$P(\theta,\phi) = P(\theta) = A\exp\left(-(\theta-\theta_o)^2/\sigma_\theta\right) \tag{2.2-7a}$$

$$P(\theta,\phi) = P(\theta) = A\exp\left(-|\theta-\theta_o|/\sigma_\theta\right) \tag{2.2-7b}$$

$$P(\theta,\phi) = P(\theta) = \begin{cases} A\exp\left(-|\theta-\theta_o|/\sigma_{\theta 1}\right) & \theta < \theta_o \\ A\exp\left(-|\theta-\theta_o|/\sigma_{\theta 2}\right) & \theta > \theta_o \end{cases} \tag{2.2-7c}$$

where:

- θ is the azimuth angle and θ_o the main elevation angle (i.e. the angle where maximum power is incident)
- σ_θ controls the spread of the function.
- A is the normalizing factor.

Notice that the PAS functions described are independent of the azimuth angle ϕ and are therefore only dependent on the elevation θ. We consider plots of these PAS distributions, for arbitrarily chosen values of θ_o and σ_θ in Figure 2.

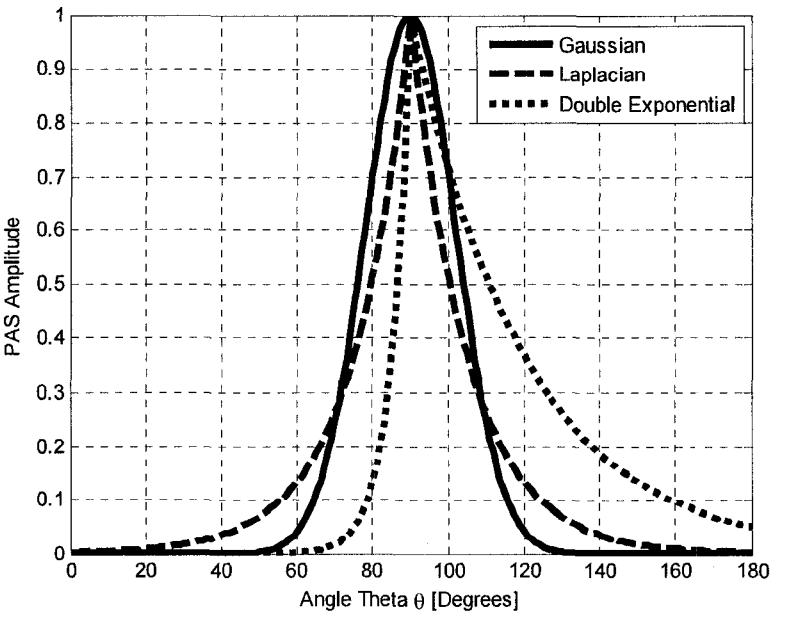

Figure 2 – Various PAS Distributions

Notice the Gaussian and Laplacian distributions are symmetric around $\theta = \theta_o$. In practice, this symmetry does not exist since the environment will yield far greater incident power from elevation angles above rather than below ground. A more suitable PAS is the double exponential found in [5] and shown in Figure 2. Based on experimental results, the authors determined the scaling factors $\sigma_{\theta 1}$ and $\sigma_{\theta 2}$ that best represent rural/urban environments and found $\sigma_{\theta 2}$ to be approximately 1.5 times the magnitude of $\sigma_{\theta 1}$. This implies far greater incident power density for less than 90 degree elevation (θ), which matches well with Vaughan's [2] defined MCS region.

We conclude the discussion on PAS distributions by comparing the double exponential to the MCS region in Figure 3. We do see good overlap between the double exponential and the MCS region, implying the MCS region is an excellent approximation to the incident power distribution one sees in practice.

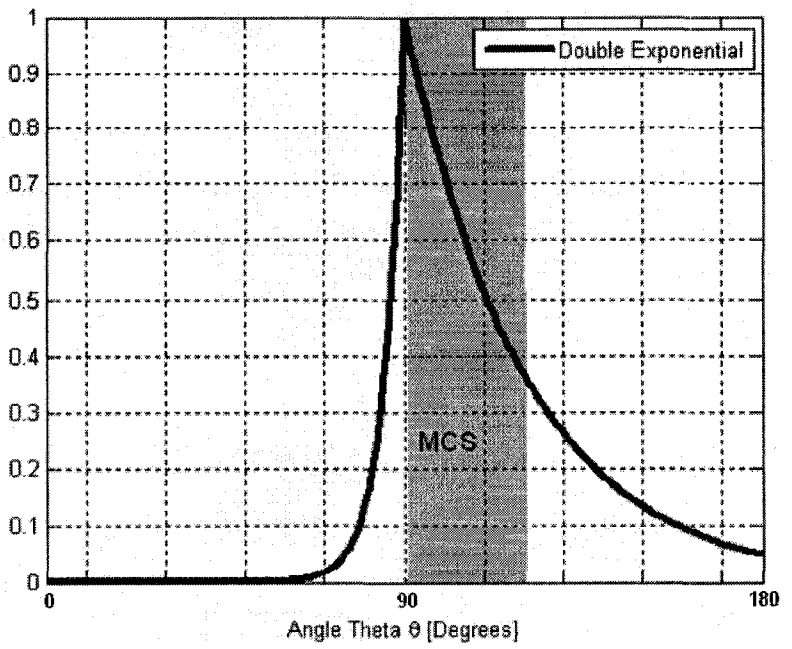

Figure 3 – Comparison of MCS to Urban Macrocell Double Exponential PAS

2.2.4 – Envelope Correlation

The term "correlation" can be considered as a measure of similarity between two quantities. In the strict mathematical sense, correlation is a measure of the strength and direction of a linear relationship between two random variables, random signals and so forth [6]. A similar concept arises in MIMO antenna design called envelope correlation [7]. It is a weighted measure of similarity between two antenna far-field patterns.

> Envelope correlation is a measure of pattern similarity. The lower the envelope correlation between antenna patterns, the less chance the incoming signals will be correlated and the higher the channel capacity.

Most importantly, it connects the concepts of power angular spectrum (PAS) with the antenna's patterns and measures the suitability of the antenna patterns for MIMO operation for a chosen PAS.

Envelope correlation is by far the most important antenna related quantity for MIMO antenna design, and will therefore become one of the main focuses of our attention throughout the thesis. The envelope correlation between any two far-field patterns relative to a chosen weighting function is expressed as follows:

$$\rho_{env}(i,j) = \frac{\left| \iint_{4\pi} P(\theta,\phi)\left[\underline{F}_i(\theta,\phi)\cdot\underline{F}_j^*(\theta,\phi)\right]d\Omega \right|^2}{\iint_{4\pi} P(\theta,\phi)\left|\underline{F}_i(\theta,\phi)\right|^2 d\Omega \iint_{4\pi} P(\theta,\phi)\left|\underline{F}_j(\theta,\phi)\right|^2 d\Omega} \tag{2.2-8}$$

where:

- $\underline{F}_n(\theta,\phi)$ and $\underline{F}_m(\theta,\phi)$ are the far-field patterns of the n^{th} and m^{th} antennas.
- $\underline{P}(\theta,\phi)$ is the power angular spectrum or PAS
- The envelope correlation is bound between: $0 \le \rho_{env}(i,j) \le 1$
- $\rho_{env}(i,j) = 1$ implies fully correlated beams, i.e. the same far-field pattern.
- $\rho_{env}(i,j) = 0$ implies uncorrelated patterns, i.e. orthogonal relative to $S(\theta,\phi)$

Various sources in the literature quote maximum acceptable values for the envelope correlation, ranging from 0.5 to 0.7 [2]. We shall err on the side of caution and consider the threshold of $\rho_{env} = 0.5$ to be the limit in which MIMO antennas can perform effectively. As mentioned in section 2.2.3, a PAS of $P(\theta,\phi) = \text{constant}$ is often used as a best-case-scenario measure of MIMO capabilities. Setting the PAS to a constant in Equation 2.2-8 allows us to write:

$$\rho_{env}(i,j) = \frac{\left| \iint_{4\pi} \left[\underline{F}_i(\theta,\phi)\cdot\underline{F}_j^*(\theta,\phi)\right]d\Omega \right|^2}{\iint_{4\pi} \left|\underline{F}_i(\theta,\phi)\right|^2 d\Omega \iint_{4\pi} \left|\underline{F}_j(\theta,\phi)\right|^2 d\Omega} \tag{2.2-9}$$

The interpretation of the envelope correlation is always the same, regardless of the chosen PAS distribution.

For lossless antennas, we can alternatively compute the full-sphere envelope correlation using the S-parameters of the N-antenna system. This formula is derived in [7] and is shown below:

$$\rho_{env}(i,j) = \frac{\left|\sum_{n=1}^{N} S_{i,n}^{*} S_{n,j}\right|^2}{\prod_{k=i,j}\left[1-\sum_{n=1}^{N} S_{k,n}^{*} S_{n,k}\right]} \tag{2.2-10}$$

This relationship is derived from energy conservation relationships between the S-parameters and far-fields, and hence does not apply when the antenna system is lossy. The above expression allows designers to quickly measure the envelope correlation without having to resort to the laborious task of measuring far-field patterns.

2.2.5 – Mean Effective Gain

The second key parameter for MIMO antenna design is the mean effective gain or MEG. It is defined in the literature [3], with a simplified definition as follows:

> *MEG is the ratio of the total received power by an AUT to the total received power of another reference antenna in the same environment. Typically, the reference antenna is chosen to be a circularly polarized isotropic antenna.*

The general expression for MEG is as follows:

$$MEG = \frac{\mathrm{P_{rec}\ by\ Antenna}}{\mathrm{P_{rec}\ by\ Isotropic\ \ CP\ Antenna}} = \frac{\int_{\Omega}\left(\left[P_1 p_\theta\right]G_\theta + \left[P_2 p_\phi\right]G_\phi\right)d\Omega}{\int_{\Omega}\left(\left[P_1 p_\theta\right] + \left[P_2 p_\phi\right]\right)d\Omega} \tag{2.2-11}$$

where p_θ and p_ϕ are the normalized distributions of incident power in both the theta and phi polarizations and P_1 and P_2 are constants that are simply weights that increase or decrease the total incident power. G_θ and G_ϕ are the gain patterns for the theta and phi

polarizations. Note that integration is over the entire sphere. Additionally, one can define XPR, which is a measure of how strong the theta polarization is relative to the phi polarization, and is simply equal to: XPR = P_1/P_2.

Ultimately, we wish to have MEG as high as possible since this would maximize the received power from the region of interest and thus potentially boost SNR. Additionally, we want the ratios of MEG between antennas to be approximately equal in order to have a balanced set of MIMO antennas. If we wish to measure MEG in an environment that has equal likelihood incidence from all angles over the entire sphere, we find $p_\theta = p_\phi = 1/4\pi$ and setting $P_1 = P_2 = P_o$, we find P_o cancels leaving us with MEG = 0.5, independent of the antenna gain pattern since the integral $\int_\Omega \left(G_\theta + G_\phi\right) d\Omega = 4\pi$ for any practically realizable antenna. If the antenna were lossy, we would simply find that MEG is equal to $e_{rad}/2$. Changing the incident power distribution to an azimuth and elevation dependent function makes the antenna gain pattern critical in determining the value for MEG, and hence greater attention is needed when designing for constrained regions of incident power such as the MCS region.

2.2.6 – MIMO Antenna Design Basics

It is evident from Equation 2.2-8 that a set of antennas whose far-field patterns are mutually orthogonal relative to the weighting function $P(\theta,\phi)$ are ideal for MIMO purposes. For the case of equal angular spread ($P(\theta,\phi) = \text{constant}$) the far-field patterns must be orthogonal relative to the entire far-field sphere. The same holds true for the MCS region, as well as the previous defined distributions (e.g. double exponential). It is not immediately evident how one would go about designing MIMO antennas, aside from perhaps optimization schemes that could be used to minimize the numerator of Equations 2.2-8 or 2.2-10. However, we wish to develop a fundamental understanding of MIMO antenna design, something an optimizer inevitably obscures.

For the case of full angular spread, we see from 2.2-10 that envelope correlation is zero when the numerator is zero. That is to say when the S-parameters of the system satisfy the following condition:

$$\left|\sum_{n=1}^{N} S_{i,n}^{*} S_{n,j}\right|^{2} = 0 \qquad (2.2\text{-}12)$$

In general, a multitude of different combinations of S-parameters can yield an envelope correlation equal to zero. Of greatest interest is when S-parameters cross terms of the form $S_{i,j}$ for $i \neq j$ (mutual coupling) are all equal to zero. For a system without mutual coupling, the antennas have zero envelope correlation. Therefore, for a lossless system with no mutual coupling, antenna patterns are orthogonal over the far-field sphere, and are therefore ideal for MIMO operation in an all angular spread scattering environment. Alternatively, if we consider different PAS environments, namely the MCS region or the double exponential distribution, we must abandon the S-parameter method and use the far-field integration scheme instead. One of the purposes of this thesis is to investigate methods one can use to design MIMO antennas for these arbitrary distributions since no structured methodology exists in the literature to do so.

2.2.7 – Summary of MIMO Theory

We have discussed the various concepts of MIMO wireless communications, and noted two critically important performance metrics for the antenna designer. Firstly, we considered envelope correlation, a measure of similarity between the different antenna patterns. This correlation is defined relative to particular regions of the far-field sphere such as the entire sphere or constrained regions and distributions. If envelope correlation is low, then channel capacity is maximized. Furthermore, we wish to have as much of the pattern point into the region of desired orthogonality, with the quantity MEG (mean effective gain) as a suitable measure of this property. We therefore want the mean effective gain as high as possible for maximum MIMO capacity. How we optimally design MIMO antennas for these particular parameters is the primary goal of this thesis.

2.3 – Theory of Characteristic Modes

2.3.1 – Introduction

The theory of characteristic modes is an invaluable tool for antenna analysis, from both the scattering and excitation perspective. The theoretical analysis determines an infinite set of modal currents with corresponding modal fields for any antenna structure. These currents are independent of excitation and form a basis of surface currents for the domain represented by the analyzed surface. Any conceivable surface current that can exist on the surface can be expanded using the basis formed by the modal currents. These modes have many desirable properties. Firstly, the modal fields are orthogonal over the sphere at infinity. Secondly, the modal surface currents share a weighted orthogonality. These properties give rise to many different applications, including antenna design, far-field pattern synthesis and feed placement. With such tantalizing properties such as orthogonality, there are likely many more electromagnetics related areas in which characteristic modes can be applied.

The theory of characteristic modes was first developed by Garbacz and Turpin [9], [10]. Their discoveries led to a fundamental, although impractical, theory for generalized scatterers. While critical in understanding the historical development of CM theory, the theory proposed by Garbacz will not be discussed as it detracts from the main topics of this thesis. The current working model for the theory of characteristic modes was proposed by Harrington and Mautz [11]. What gave Harrington's approach such an edge was a clear and concise derivation from straightforward electromagnetics principles with an accompanying method [12] with which one could use existing electromagnetics simulation tools to compute the characteristic modes. Using a moment method formulation and the discretized impedance matrix, one can determine the characteristic modes of any perfectly conducting structure. The properties of characteristic modes are what make this type of modal analysis so useful. Due to their orthogonality properties, and the fact that they form a basis that spans all possible radiation modes of the analyzed structure, characteristic modes gives fundamental insight into how antennas radiate.

2.3.2 – The Impedance Operator

Consider an arbitrary conducting surface S, situated within an impressed field E^i as shown in Figure 4.

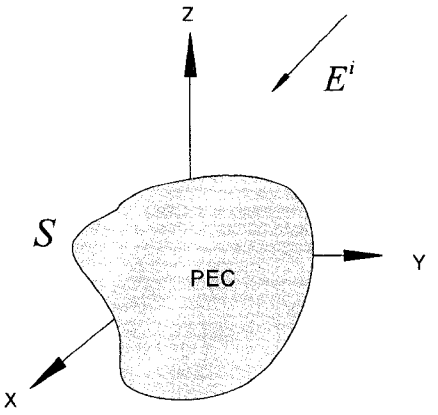

Figure 4 – Arbitrary Conducting Surface in an Impressed Field

On the surface of the conductor, the total tangential electric field must be zero. As such, the impressed electric field $\underline{E}^i$ must generate surface currents that force this boundary condition to hold. We define the surface current generated in this way using the operator relationship:

$$\left[L(\underline{J}) - \underline{E}^i\right]_{\tan} = 0 \tag{2.3-1}$$

The operator L acts on the surface current J and produces a tangential electric field on the surface S that exactly cancels the contribution of the tangential impressed field. The operator L is defined in the following manner:

$$\boxed{L(\underline{J}) = j\omega \underline{A}(\underline{J}) + \nabla\Phi(\underline{J})} \tag{2.3-2}$$

$\underline{A}(\underline{J})$ is the magnetic vector potential, defined by:

$$\underline{A}(\underline{J}) = \mu \iint_S J(r')\psi(r,r')\,ds' \tag{2.3-3}$$

$\Phi(\underline{J})$ is the electric scalar potential , defined by:

$$\Phi(\underline{J}) = \frac{j}{\omega\varepsilon} \iint_S \nabla' \cdot J(r') \psi(r,r') ds' \tag{2.3-4}$$

We consider r and r' to be field and source points, with ε, μ, and k as the permittivity, permeability and wave number of free space. Furthermore, we consider $\psi(r,r')$ being the Green's function of Freespace, defined as:

$$\psi(r,r') = \frac{e^{-jk|r-r'|}}{4\pi|r-r'|} \tag{2.3-5}$$

The operator in Equation 2.3-2 transforms a current density into an electric field quantity, and hence has dimension of impedance. As such, we introduce notation for the tangential operator L:

$$Z(\underline{J}) = \left[L(\underline{J})\right]_{\tan} \tag{2.3-6}$$

We can write the impedance operator in their real and imaginary parts:

$$Z = R + jX \tag{2.3-7}$$

Both R and X are real operators, and are also symmetric due to the symmetry of Z. Consider the inner product over complex space, defined as the surface integral:

$$\langle \underline{A}, \underline{B} \rangle = \iint_S \underline{A}^* \cdot \underline{B} dS \tag{2.3-8}$$

Consider the complex power balance of a given impressed surface current J on S.

$$\langle \underline{J}^*, Z\underline{J} \rangle = \langle \underline{J}^*, (R + jX)\underline{J} \rangle = \langle \underline{J}^*, R\underline{J} \rangle + j\langle \underline{J}^*, X\underline{J} \rangle \tag{2.3-9}$$

The term $\langle \underline{J}^*, R\underline{J} \rangle$ represents the radiated power associated with the total surface current J on S. This quantity cannot be negative as radiated power must be positive, and is always greater than zero for open structures (since every current radiates some measurable amount of power, however small). These conditions give rise to a positive semi-definite operator R. No further properties than real symmetry exist for the operator X, as reactance can take any value: positive, negative and zero.

2.3.3 – Generalized Eigenvalue Problem

Suppose we now consider our operator Z in the following generalized eigenvalue problem:

$$[Z][J_n] = \nu_n [M][J_n] \tag{2.3-10}$$

where Z is our impedance operator, J_n are the eigenvectors, ν_n are the eigenvalues and M is a suitably chosen weighting operator. If M were the identity operator, we would solve the following eigenvalue problem:

$$[Z][J_n] = \nu_n [J_n] \tag{2.3-11}$$

The eigenvalues and eigenvectors would in general be complex, and since [Z] is symmetric, the appropriate orthogonality properties on the surface S defined by [Z] hold. Alternatively, let us consider the operator R as our weighting function. Our eigenvalue problem becomes:

$$[Z][J_n] = \nu_n [R][J_n] \tag{2.3-12}$$

Expanding the operator Z and making the substitution $\nu_n = 1 + j\lambda_n$

$$[R + jX][J_n] = (1 + j\lambda_n)[R][J_n] \tag{2.3-13a}$$

$$[R][J_n] + j[X][J_n] = [R][J_n] + j\lambda_n [R][J_n] \tag{2.3-13b}$$

Canceling like terms, we arrive at the weighted eigenvalue problem:

$$[X][J_n] = \lambda_n [R][J_n] \tag{2.3-13c}$$

Since X and R are real symmetric operators, the resultant eigenvalues and eigenvectors will be purely real. We therefore consider the eigenvectors $[J_n]$ to be the modal currents or eigencurrents for the perfectly conducting surface S defined by the operator Z. The significance of the eigenvalues will be discussed shortly.

2.3.4 – Characteristic Modal Currents and Normalization

Since the operators R and X are real symmetric and hence Hermitian, we recognize the following orthogonality properties of the eigencurrents with respect to the *symmetric* and *inner products*:

$$\langle J_m, RJ_n \rangle = \langle J_m^*, RJ_n \rangle = 0 \tag{2.3-14a}$$

$$\langle J_m, XJ_n \rangle = \langle J_m^*, XJ_n \rangle = 0 \tag{2.3-14b}$$

$$\langle J_m, ZJ_n \rangle = \langle J_m^*, ZJ_n \rangle = 0 \tag{2.3-14c}$$

where $m \neq n$. Since eigenanalysis yields eigencurrents of indeterminant magnitude we wish to normalize the eigencurrents such that each modal surface current radiates 1 Watt. In order to accomplish this, we compute the scaling factor:

$$scale_n = \sqrt{\langle J_n, RJ_n \rangle} \tag{2.3-15}$$

which we divide into each corresponding current. This enforces the following equality:

$$\mathrm{P}_{rad,n} = \langle J_n^{norm}, RJ_n^{norm} \rangle = \langle J_n^{un-norm} / scale_n, RJ_n^{un-norm} / scale_n \rangle = 1 \tag{2.3-16}$$

If the characteristic mode currents are normalized, we can generalize the orthogonality relationships via:

$$\langle J_m, RJ_n \rangle = \langle J_m^*, RJ_n \rangle = \delta_{mn} \tag{2.3-17a}$$

$$\langle J_m, XJ_n \rangle = \langle J_m^*, XJ_n \rangle = \lambda_n \delta_{mn} \tag{2.3-17b}$$

$$\langle J_m, ZJ_n \rangle = \langle J_m^*, ZJ_n \rangle = (1 + j\lambda_n)\delta_{mn} \tag{2.3-17c}$$

where δ_{mn} is the Kronecker delta (0 if $m \neq n$, 1 if $m = n$). All subsequent derivations within this thesis assume normalized current.

2.3.5 – *Characteristic Fields*

We can derive the orthogonality properties of the modal fields using the complex Poynting theorem [13]. If we consider the far-field of the surface, the complex power for any modal surface current J on S is expressed as:

$$\begin{aligned} P &= \langle J^*, ZJ \rangle = \langle J^*, RJ \rangle + j \langle J^*, XJ \rangle \\ &= \iint_{S^\infty} \underline{E} \times \underline{H}^* \cdot dS + j\omega \iiint_{V^\infty} \left(\mu \underline{H} \cdot \underline{H}^* - \varepsilon \underline{E} \cdot \underline{E}^* \right) dV \end{aligned} \tag{2.3-18}$$

where S^∞ is the sphere at infinity enclosing S and V^∞ is the volume enclosed by S^∞. For our purposes, the far-field of the surface S approximates the sphere at infinity. When considering the modal currents, we derive a similar expression:

$$\begin{aligned} \mathrm{P} &= \langle J_m^*, RJ_n \rangle + j \langle J_m^*, XJ_n \rangle \\ &= \iint_{S'} \underline{E}_m \times \underline{H}_n^* \cdot dS + j\omega \iiint_{V'} \left(\mu \underline{H}_m \cdot \underline{H}_n^* - \varepsilon \underline{E}_m \cdot \underline{E}_n^* \right) dV' \\ &= \left(1 + j\lambda_n \right) \delta_{mn} \end{aligned} \tag{2.3-19}$$

which implies the following individual relationships hold:

Radiated Power *Net Stored Energy*

$$\boxed{\iint_{S'} \underline{E}_m \times \underline{H}_n^* \cdot dS = \delta_{mn}} \qquad \boxed{\iiint_{V'} \left(\mu \underline{H}_m \cdot \underline{H}_n^* - \varepsilon \underline{E}_m \cdot \underline{E}_n^* \right) dV' = \frac{\lambda_n}{\omega} \delta_{mn}} \tag{2.3-20a,b}$$

If we consider extending our surface of integration to the sphere at infinity, our fields take the form of purely outward traveling waves, with the form:

$$\underline{E}_n = \eta \underline{H}_n \times \hat{n} = \frac{-j\omega\mu}{4\pi r} e^{-jkr} \underline{F}_n(\theta, \phi) \tag{2.3-21}$$

We have introduced η, the intrinsic impedance of Freespace, r is the radial distance from the origin, $\hat{n}$ is the unit normal to the sphere at infinity and $\underline{F}_n(\theta, \phi)$ is the characteristic pattern or eigenpattern corresponding to the eigencurrents J_n. Adding Equation 2.3-19 to its conjugate with m and n interchanged gives us:

$$\frac{1}{\eta} \oiint_{S\infty} \underline{E}_m \cdot \underline{E}_n^* \cdot dS = \delta_{mn} \tag{2.3-22}$$

Similar, replacing $\underline{E}_n$ with $\eta \underline{H}_n \times \hat{n}$ we find:

$$\eta \iint_{S\infty} \underline{H}_m \cdot \underline{H}_n^* \cdot dS = \delta_{mn} \tag{2.3-23}$$

Both Equations 2.3-22 and 2.3-23 show that the *eigenfields* are orthogonal over the sphere at infinity.

2.3.6 – Modal Excitation

Given some arbitrary excitation, it is possible to determine to what extent each of the characteristic modes is excited. The excitation can come in the form of feeds or incident electromagnetic waves.

Any arbitrary excitation will yield a surface current over S. Since the modal currents are orthogonal over the surface S, we can expand the currents as follows:

$$J = \sum_{n=0}^{\infty} \alpha_n J_n \tag{2.3-24}$$

Recall the operator equation:

$$\left[Z(\underline{J}) - E^i \right]_{\tan} = 0 \tag{2.3-25}$$

Substituting in the summation expression for J and taking the inner product of the above expression with respect to J_m we find:

$$\left[\sum_{n=0}^{\infty} \alpha_n \langle J_m, ZJ_n \rangle - \langle J_m, E^i \rangle \right]_{\tan} = 0 \tag{2.3-26}$$

By the orthogonality properties of the modal currents, we end with:

$$\alpha_n\left(1+j\lambda_n\right)=\left\langle J_n, E^i_{\tan}\right\rangle \tag{2.3-27}$$

where we define the *modal excitation coefficient* as:

$$V^i_n=\oiint_S J_n\cdot E^i_{\tan}dS=\left\langle J_n, E^i_{\tan}\right\rangle \tag{2.3-28}$$

And the *modal expansion coefficient* as:

$$\alpha_n=\frac{\left\langle J_n, E^i_{\tan}\right\rangle}{\left(1+j\lambda_n\right)}=\frac{V^i_n}{\left(1+j\lambda_n\right)} \tag{2.3-29}$$

This allows us to express any arbitrary surface current and their respective field as expansions of the modal currents and fields:

$$J=\sum_{n=0}^{\infty}\alpha_n J_n=\sum_{n=0}^{\infty}\frac{V^i_n J_n}{\left(1+j\lambda_n\right)} \tag{2.3-30a}$$

$$E=\sum_{n=0}^{\infty}\alpha_n E_n=\sum_{n=0}^{\infty}\frac{V^i_n E_n}{\left(1+j\lambda_n\right)} \tag{2.3-30b}$$

$$H=\sum_{n=0}^{\infty}\alpha_n H_n=\sum_{n=0}^{\infty}\frac{V^i_n H_n}{\left(1+j\lambda_n\right)} \tag{2.3-30c}$$

2.3.7 – *Interpretation of Modal Properties*

It is key to understand the properties of the modes and what makes their existence meaningful for antenna design. Recall that the eigenvalue for the generalized eigenvalue problem can be expressed as:

$$\lambda_n = \frac{\omega W_{net,n}}{P_{rad,n}} \tag{2.3-31}$$

where $W_{n,net}$ is the net stored energy by the specified mode 'n'. This explicitly shows the following properties:

- If $\lambda_n > 0$, the mode can be considered to be an *inductive mode* since it predominantly stores magnetic energy.
- If $\lambda_n < 0$, the mode can be considered to be a *capacitive mode* since it predominantly stores electrical energy.
- If $\lambda_n = 0$, the mode has no net stored energy and is called *externally resonant*
- If $\lambda_n \to \infty$, the mode has no radiated power and is called *internally resonant*

If we are specifically trying to excite individual modes, we would like to excite modes with $\lambda_n \approx 0$ since these modes will have the lowest possible contribution to net stored energy and thus input reactance. Let us now consider the general excitation of a surface S. This will result in the excitation of multiple modes, each of which contributes to the overall net stored energy of the arbitrary PEC surface:

$$\omega W_{net} = \langle J^*, XJ \rangle = \left\langle \sum_{n=0}^{\infty} \alpha_n^* J_n, X \sum_{n=0}^{\infty} \alpha_n J_n \right\rangle = \sum_{n=0}^{\infty} \alpha_n^* \alpha_n \langle J_n, XJ_n \rangle = \sum_{n=0}^{\infty} |\alpha_n|^2 \lambda_n \tag{2.3-32}$$

Giving us the expressions for the total net stored energy:

$$\omega W_{net} = \sum_{n=0}^{\infty} \lambda_n |\alpha_n|^2 \tag{2.3-33}$$

And the individual contribution of each mode to the net stored energy:

$$\omega W_{net,n} = \lambda_n |\alpha_n|^2 \tag{2.3-34}$$

We can also expand the radiated power in a similar manner:

$$P_{rad} = \langle J^*, RJ \rangle = \left\langle \sum_{n=0}^{\infty} \alpha_n^* J_n, R \sum_{n=0}^{\infty} \alpha_n J_n \right\rangle = \sum_{n=0}^{\infty} \alpha_n^* \alpha_n \underbrace{\langle J_n, RJ_n \rangle}_{=1} = \sum_{n=0}^{\infty} |\alpha_n|^2 \tag{2.3-35}$$

Giving us the expressions for the total radiated power:

$$P_{rad,total} = \sum_{n=0}^{\infty} |\alpha_n|^2 \tag{2.3-36}$$

And the individual contribution of each mode:

$$P_{rad,n} = |\alpha_n|^2 \tag{2.3-37}$$

The aforementioned expression allows us to determine the amount of power radiated by mode 'n'. Using these expressions one can determine to what extent a mode is being excited as well as how detrimental the excitation is for stored energy and hence input reactance.

If we wish to excite individual modes, we can compute a quantity that will be defined as the *mode excitation efficiency, 'e'*. It is simply a measure of how efficient we direct the power into specific modes of the radiating structure:

$$e = \frac{P_{rad,m}}{P_{rad,total}} = \frac{|\alpha_m|^2}{\sum_{n=0}^{\infty} |\alpha_n|^2} \tag{2.3-38}$$

The expression 2.3-38 represents the percentage of power that is radiated by mode m.

We can also expand this expression to include multiple modes versus total power:

$$e = \frac{\mathrm{P}_{rad,m,p,\ldots q}}{\mathrm{P}_{rad,total}} = \frac{|\alpha_m|^2 + |\alpha_p|^2 + \ldots + |\alpha_q|^2}{\sum_{n=0}^{\infty} |\alpha_n|^2} \tag{2.3-39}$$

This will be helpful if we wish to excite a set of modes, possibly when using multi-mode excitation to balance to net stored energy to be near zero.

We can also state something about the significance of the modes based on the eigenvalue. Recall that surface current (and fields) can be expanded in terms of modal quantities as:

$$J = \sum_{n=0}^{\infty} \frac{V_n^i J_n}{(1 + j\lambda_n)} \tag{2.3-40}$$

The factor $\frac{1}{(1+j\lambda_n)}$ plays an integral role in "weighting" each mode appropriately. Note that for very large λ_n eigenvalues the factor becomes very small and hence makes the mode 'n' both insignificant and difficult to excite. Conversely, if the eigenvalue λ_n is very small, the expression above approaches 1, and is therefore a very significant mode in terms of expanding the currents and fields for any given excitation. It is for this reason that only a small number of modes are required to fully describe the radiation properties of any given near-resonant or resonant radiator. We will see however that this approach to determining modal significance is incomplete, and other factors, namely the magnitude of the normalized currents are important as well.

2.3.8 – Characteristic Modes of Lossy Conductors

The classical characteristic modes, as defined by Garbacz, Harrington and Mautz, assume a perfectly conducting surface. One can also define a surface that has finite conductivity and then consider defining a new set of modal currents for the lossy surface. Harrington briefly considers resistive loading on conducting surfaces, but continues with the assumption of purely reactive loading [14]. We shall colloquially call these modes Lossy Characteristic Modes (LCM).

The nature of the modes, from the surface and far-field perspective, will change due to the introduction of losses. We shall consider introducing finite conductivity into the impedance matrix using the methods devised by Johnson [15]. Let the impedance matrix be known as [Z] and the loading matrix responsible for finite conductivity as $[Z_L]$. Our eigenvalue problem becomes:

$$[Z + Z_L][J_n] = \nu_n [M][J_n] \tag{2.3-41}$$

We recognize the familiar eigenvalue form from the previous derivation, noting the additional Z_L term. We must first define the operator $[Z_L]$ which is responsible for the lossiness of the surfaces in question. As defined in [16], the entries of the discrete $[Z_L]$ operator are defined by:

$$[Z_L]_{mn} = \langle f_n, Z_s f_m \rangle \tag{2.3-42}$$

where f_n and f_m are the moment method expansion functions and Z_s is the surface impedance defined as $Z_s = (1+j)\sqrt{\omega\mu_o/2\sigma}$, where σ is the conductivity.

The choice of operator [M] plays an integral role in the nature of the modal currents. For our purposes, strictly MIMO applications, we wish to maintain far-field orthogonality of the modal fields. It can be shown that the operator [R] is the ideal weighting function for this goal, since it is the only operator in which far-field orthogonality is obtained.

Substituting [M] = [R] and $\nu_n = 1 + j\lambda_n'$:

$$[Z + Z_L][J_n] = (1 + j\lambda_n')[R][J_n] \tag{2.3-43}$$

Expanding out the [Z] operator:

$$[R][J_n] + j[X][J_n] + [Z_L][J_n] = [R][J_n] + j\lambda_n'[R][J_n] \tag{2.3-44}$$

Canceling like terms:

$$([X] - j[Z_L])[J_n] = \lambda_n'[R][J_n] \tag{2.3-45}$$

The left hand matrix $([X] - j[Z_L])$ is complex symmetric, but not Hermitian. Since both sides of the eigenvalue problem are symmetric, the eigencurrents have the same *symmetric product* orthogonality as the classical modes, but not necessarily *inner product* orthogonality. Ultimately, the 'lossy modes' determined by the eigenvalue problem in Equation 2.3-45 have far-field patterns that are orthogonal over the entire sphere [14]. Using this methodology, we can include lossy structures in our analysis for the design of MIMO antennas. It would also seem that this is the first time in the literature that lossy characteristic modes have been calculated and considered for design purposes. The eigenvalues now have a real and imaginary part, as evident by taking the inner product of the eigenvalue problem with respect to the m^{th} modal surface current:

$$[J_m][X][J_n] - j[J_m][Z_L][J_n] = \lambda_n[J_m][R][J_n] \tag{2.3-46}$$

which can be interpreted as:

$$P_{reac} - jP_{loss} = \lambda_n' P_{rad} \tag{2.3-47}$$

We can therefore consider the eigenvalue equal to: $\lambda_n' = \lambda_n - j\dfrac{1 - e_{rad}}{e_{rad}}$ where λ_n maintains the same meaning as it did in the PEC case, only we now have an additional term related to radiation efficiency. Note that due to the lack of Hermitian symmetry in

the eigenvalue problem, the characteristic modes are not orthogonal relative to the power lost to finite conductivity - the orthogonality only holds for the radiated power. Hence, we can always expand the far-field radiation patterns in terms of these characteristic modes but there is cross-coupling amongst the modes in terms of loss. Thus, the radiation efficiency factor can be thought of as a form of modal radiation efficiency – but not a general method to expand antenna losses.

2.3.9 – Generalized Characteristic Modes

The classical characteristic modes of the perfectly conducting variety, maintain orthogonality of far-field patterns over the entire sphere. While this is a useful property of the modes, it would be prudent to consider modes that are orthogonal over particular regions of the sphere, or weighted orthogonality relative to some defined function.

As defined by Vaughan [2] and discussed in section 2.2, there is a region of the far-field that is of particular interest to mobile communications known as the Mobile Communications Scenario or MCS. In terms of the angular spherical coordinates, it is defined as the region bounded by:

$$60^o \leq \theta \leq 90^o \text{ and } 0^o \leq \phi \leq 360^o$$

It is a logically defined region of the far-field, as incident electromagnetic power is typically confined to this region, with very little power incident directly above or below the handheld.

An alternative modal theory, similar to characteristic modes, was devised by Inagaki [17] and further investigated by Pozar [18] and Liu [19]. Their work defined a new operator, when used in eigenvalue problems, assured orthogonality over particular regions of the far-field rather than over the entire sphere. Furthermore, the theory is

general enough to have the orthogonality relative to a function that isn't necessarily constant over a region. This operator is defined as:

$$[H_{ij}] = \langle W(\theta,\phi)F_i(\theta,\phi), W(\theta,\phi)F_j(\theta,\phi)\rangle \tag{2.3-48}$$

where $W(\theta,\phi)$is a weighting function defined over the far-field, with $F_i(\theta,\phi)$ and $F_j(\theta,\phi)$ as the ith and jth moment method expansion functions far-field patterns. When this operator [H] is used in an appropriately defined eigenvalue problem, one finds the modal far-field are orthogonal with respect to the region or function defined by $W(\theta,\phi)$.

Two eigenvalue problems are defined, first the Inagaki Modes:

$$[Z^*][Z][J_n] = \lambda_n'[H][J_n] \tag{2.3-49}$$

Secondly, we consider the Generalized Characteristic Modes (Liu):

$$[X][J_n] = \lambda_n'[H][J_n] \tag{2.3-50}$$

Both methods yield modal surface currents that radiate far-fields that are orthogonal over the region defined by$W(\theta,\phi)$. However, one finds greater utility with the generalized modes since the eigenvalues have clear physical meaning, that being the ratio of reactive power to the radiated power into the region W. As an example, if we were to choose the weighting function to reflect the MCS, we would have:

$$W(\theta,\phi) = \begin{cases} 1 & 60^o \le \theta \le 90^o, 0^o \le \phi \le 360^o \\ 0 & else \end{cases} \tag{2.3-51}$$

The PEC surface would then have a defined set of surface currents whose far-field patterns would be orthogonal over the MCS. As discussed in section 2.2.4, far-field patterns that are orthogonal have zero envelope correlation. In Chapter 6 we will show a derivation that includes polarization sensitivity, and a direct application to MIMO antenna design for arbitrary PAS distributions yielding zero envelope correlation antennas.

2.3.10 – Characteristic Port Modes

As a final consideration, we will discuss Characteristic Port Modes (CPM), devised by Mautz [20]. All previously defined modal theories compute surface currents that yield orthogonal far-field patterns without defining a feeding location. When considering CPMs, one finds **port** currents or voltages that yield far-field patterns sharing the same orthogonality properties as the *entire surface* modes. We begin by considering a generic PEC surface, with N ports defined as shown in Figure 5.

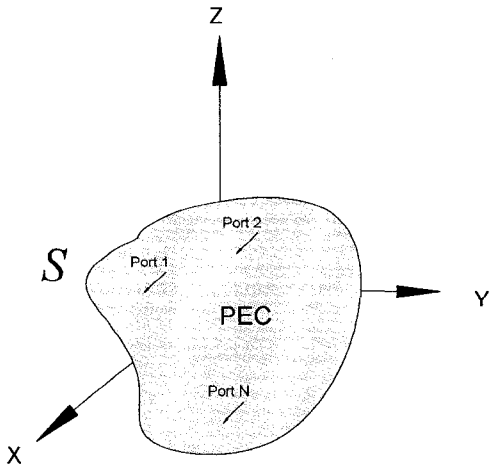

Figure 5 – Arbitrary Conducting Surface with Pre-defined Ports

Computing the Y or Z-parameters of the N-ports (self and mutual admittance and impedance terms) we can perform eigenanalysis on the resulting matrices. For the particular case, we consider the CPM voltages and compute the eigenvectors and eigenvalues in a very similar, but far more compact eigenvalue problem:

$$[B][V_n] = \mu_n [G][V_n] \tag{2.3-52}$$

where G and B are the real and imaginary parts of the Y-parameter admittance matrix. The eigenvectors $[V_n]$ are excitation vectors of length N (where N is the number of ports) and represent the necessary excitations in order to excite a specific CPM. The eigenvalue μ_n will not be used in the design process, and will not be discussed further.

The orthogonality properties of the CPM far-field patterns are the same as those found in the regular operator based CM theory:

$$\frac{1}{\eta} \oiint_{S\infty} \underline{E}_m \cdot \underline{E}_n^* \cdot dS = \delta_{mn} \tag{2.3-53}$$

where $\underline{E}_m$ and $\underline{E}_n$ are the far-field patterns associated with the excitation of the N ports using eigen-voltage vectors V_m and V_n.

The limitation to using CPM theory is the lack of forming a basis of far-field patterns over the far-field sphere, as we are clearly limited by the N-Ports. However, in applications not interested in forming a basis, namely those that are strictly concerned with orthogonality, CPM finds many uses.

As a final note of interest, the computation of CPM's is numerical method independent: all that is required is the Z / Y parameters which can be obtained from whatever resources are available. This is in contrast with the other modal formulations (CM and GCM), which as of writing this thesis, require a moment method formulation. One can use a moment method formulation to compute the CPM's. In this case, as the number of ports N approaches the number of moment method expansion functions M, the CPM's converge to be equivalent to the classical CM's.

2.3.11 – Summary of Characteristic Mode Theory

We have introduced various modal theories, all of which have the critical property of far-field orthogonality. All formulations can be cast into a moment method formulation, which will prove useful when analyzing and designing antennas with the modal theory.

In sections 2.3.1 through 2.3.7 we discussed the Characteristic Modes (or CM for short). Upon analyzing any arbitrary surface, the computed modes had far-field pattern orthogonality and the ability to expand any surface current on said structure using the modal currents. The modes are computed by solving a generalized eigenvalue problem. The eigenvalues form a useful diagnostic quantity that judges modes suitability for radiation purposes. Moreover, we discussed how one can compute the power radiated and net energy stored associated with each mode in the CM spectrum. This allows us to judge how well we distribute power among the modes given an arbitrary excitation.

Continuing with section 2.3.8 we discussed an alternative modal formulation similar to characteristic modes (CM) that included the effects of finite conductivity known colloquially as Lossy Characteristic Modes (LCM). We showed that the eigenvalues for this modal formulation now contain an imaginary part, which represents a quantity proportional to the modal radiation efficiency.

In section 2.3.9, we discussed another modal formulation known as Generalized Characteristic Modes (GCM) where we can arbitrarily define a weighted region of orthogonality rather than defining the entire far-field sphere.

Concluding in section 2.3.10, we considered the Characteristic Port Modes (CPM) which shares the same far-field orthogonality as the CMs, only we define the currents at a set of finite ports rather than over the entire surface.

We shall use these modal theories and their orthogonality properties in the design of MIMO antennas, with the design methodologies discussed in chapters 5, 6 and 7.

2.4 – Method of Moments

2.4.1 – Brief Overview of the Method of Moments

The method of moments is an invaluable numerical method used predominantly for antenna design and analysis [21]. The moment method solves an integral equation by discretizing the domain in which the solvable is defined. As is often the case, the unknown quantity in the method of moments is surface and/or volume currents. These currents can be the result of some chosen method of excitation, be it with a source defined somewhere on the surface or an incident field scattered by the object.

We can begin by defining a typical integral equation, as shown in [22]:

$$\int_a^b f(x')G(x,x')\,dx' = g(x) \text{ where } a \le x \le b \tag{2.4-1}$$

- $f(x')$ is the unknown function we wish to determine, and typically takes the form of a surface and/or volume current (but in the 1D case, it is a line current)
- $G(x,x')$ is known as the kernel of the integral equation. In electromagnetics, this function is almost always a Green's function that has a hand in describing the domain in which $f(x')$ is defined.
- $g(x)$ is known as a source function or driving function. It is considered the driving force behind the unknown function $f(x')$

In order to solve for the unknown $f(x')$, we expand the function in terms of a set of orthogonal expansion functions. This methodology is akin to Fourier expansion, and other types of orthogonal expansions.

$$f(x') = \sum_{n=1}^{\infty} a_n f_n(x') \tag{2.4-2}$$

Since we are using finite resources we must discretize the domain and hence use a finite number of expansion functions N to model the unknown $f(x')$.

$$f(x') \approx \sum_{n=1}^{N} a_n f_n(x') \tag{2.4-3}$$

This is where the approximation occurs when solving for $f(x')$ as it is a mathematical equivalence when using an infinite set, and an approximation (albeit a very good one!) when using a finite number of expansion function.

Our integral equation after substitution of the approximated unknown then becomes:

$$\int_a^b \left(\sum_{n=1}^{N} a_n f_n(x') \right) G(x,x')\,dx' \approx g(x) \tag{2.4-4}$$

Integral operators are linear, and hence we can write:

$$\sum_{n=1}^{N} a_n \int_a^b f_n(x') G(x,x')\,dx' \approx g(x) \tag{2.4-5}$$

We note that currently our only unknown is the coefficient a_n, so we are clearly on the right track to developing a numerical method to solve the integral equation.

Examining the above integral equation, we note that we have effectively discretized the kernel over x' by expanding the unknown using the expansion functions $f_n(x')$, but we still have the x portion of the kernel and the continuous function $g(x)$ that have yet to be discretized. We therefore define another set of orthogonal weighting functions $g_m(x)$ in which to expand $g(x)$. We choose these weighting functions to be the same as the expansion functions, yielding what is known as a Galerkin method. This is a very important concept for characteristic mode analysis, as a Galerkin method will produce a symmetric impedance matrix [Z], as required by CM theory [12].

We therefore set our weighting functions to be the same as the expansion functions, multiply and integrate both sides of the integral equation, noting the new set of indices.

$$\sum_{n=1}^{N} a_n \int_a^b \int_a^b f_n(x') G(x,x') f_m(x)\, dx' dx \approx \int_a^b g(x) f_m(x)\, dx \tag{2.4-6}$$

We still have but one unknown and now have all known functions discretized over the domain. We can now consider the above expression as a system of linear equations, and group terms in matrix form as shown below:

$$\sum_{n=1}^{N} a_n \underbrace{\int_a^b \int_a^b f_n(x') G(x,x') f_m(x)\, dx' dx}_{Z_{mn}} \approx \underbrace{\int_a^b g(x) f_m(x)\, dx}_{V_m} \tag{2.4-7}$$

Allowing us to write:

$$\sum_{n=1}^{N} a_n Z_{mn} \approx V_m \tag{2.4-8}$$

This expression is of course equivalent to the matrix expression:

$$\begin{bmatrix} Z_{11} & \cdots & Z_{1N} \\ \vdots & \ddots & \vdots \\ Z_{N1} & \cdots & Z_{NN} \end{bmatrix} \begin{bmatrix} a_1 \\ \vdots \\ a_N \end{bmatrix} = \begin{bmatrix} V_1 \\ \vdots \\ V_N \end{bmatrix} \tag{2.4-9}$$

where the column vector $\begin{bmatrix} a_1 & \cdots & a_N \end{bmatrix}^T$ is the collection of unknowns to be solved.

We have considered a 1D domain, but the same method can be extended to 2 and 3 dimensions, with newly defined integral equations in which to solve.

The moment method is a general methodology used to solve electromagnetics problems, and the details change depending on the formulation. The expansion function can exist over discretized portion over the domain or possibly over the entire domain. The properties of the expansion functions change depending on the application, and are especially dependent on the function being approximated.

Three high level categories can be considered for moment method expansion functions, namely wire-type, surface-type and volumetric-type. As their names imply, the expansion functions are application specific. For our purposes, we shall employ surface-type or triangular patch expansion functions.

2.4.2 – Moment Method Formulation using RWG Elements

Many commercial software tools are available that use a Moment Method formulation, but access to the details of the formulation, namely the impedance matrix [Z] is typically restricted. For the purposes of eigenanalysis, we require access to [Z]. An ideal solution was found using the moment method engine designed by Makarov [23]. With the Moment Method formulation in hand, we were able to design the additional software components required for eigenanalysis, as well as further tools used for antenna analysis and MIMO related performance metrics. The expansion functions used on Makarov's formulation are known as RWG edge elements. They were first proposed by Rao, Wilton and Glisson [24] from which the expansion functions' name is derived.

An example expansion function is shown below:

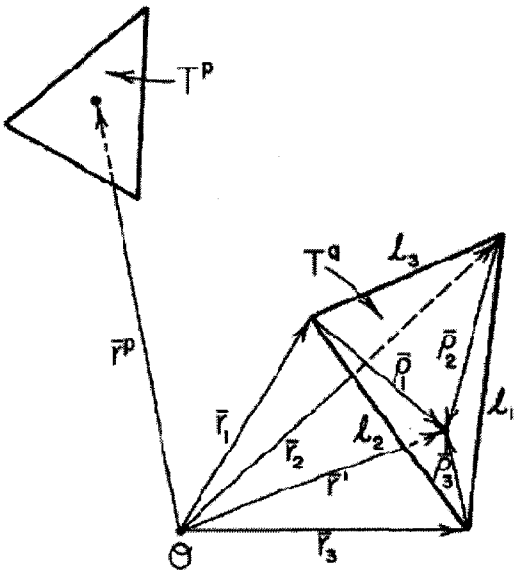

Figure 6 - RWG Expansion Function, After [24]

The surface that defines our antenna is discretized into triangles, with every pair of triangles sharing a common edge forming an RWG edge element. One can think of each edge as an equivalent elementary dipole of current, and the Z matrix as the description of the mutual and self interactions of these dipoles. From this perspective, we can approximate the current across each edge using these edge elements, and subsequently determine various quantities such as input impedance, radiation efficiency and far-field patterns. More importantly, we can compute the characteristic modes of the meshed structure using the impedance operator [Z], which we shall discuss in Chapter 3.

Another enormous advantage to using the MATLAB formulation devised by Makarov is the freedom to use many different meshing tools, including FEMLab™, PDETool™ and our own customized meshing software designed with MATLAB™.

We restrict our designs to be infinitesimally thin conducting surfaces, thereby forgoing the need to design with volumetric RWG elements. That being said, we are not limited to two dimensions as we can construct 3D objects provided they are hollow.

2.4.3 – Conclusions

In section 2.4 we discussed the moment method formulation used to solve integral equations. The integral equations that appear in the characteristic mode theory can ideally be solved using a moment method approach, and in fact was formulated explicitly for this purpose.

In section 2.4.1 we went through the derivation of a 1D moment method formulation of an integral equation, showing how one discretizes a domain and then applied weighting and expansion functions to model the resulting solution. We also pointed out the need for the weighting functions to be equal to the expansion function in order to have a Galerkin formulation, which is necessary for characteristic mode computations. In section 2.4.2 we discussed the details of the surface patch formulation we shall use which allows us to model surfaces using triangular patch elements of the RWG variety.

2.5 – Concluding Remarks

In the preceding chapter we discussed the various mathematical formulations necessary for the design of MIMO antennas using Characteristic Mode concepts.

In section 2.2 we discussed the theoretical underpinnings of the MIMO communications theory. We did not dwell long on the signal's perspective and focused primarily on the electromagnetics, namely the design requirements of MIMO antennas. We noted two important antenna design criteria: envelope correlation and mean effective gain, the former we wish to minimize and the latter we wish to maximize.

Throughout section 2.3, we considered the theory of characteristic modes. The modal formulations yield surface currents that subsist over the entire analyzed structure and have appealing far-field properties. We considered various formulations, beginning with the Characteristic Modes (CM), and continuing with the 'lossy' modes (LCM). The CM and LCM formulations produce modes that have orthogonality over the full far-field sphere, which we showed is a tantalizing property for MIMO antenna design. We also introduced the Generalized Characteristic Modes (GCMs), and showed a simple relationship between the CMs and GCMs. These GCM modes have orthogonality in the far-field relative a chosen weighting function rather than the full far-field sphere. Lastly, we consider the Characteristic Port Modes (CPM) which have the same orthogonality properties as the CMs and LCMs. The CPM modes exist in the form of currents or voltages solely at a finite number of pre-defined ports.

Finally, we concluded with a basic outline of a moment method formulation applied to electromagnetics, and considered a surface patch formulation involving RWG basis functions. We will use a moment method framework in the computation of modal and MIMO quantities, the formulation for which we will discuss in the next chapter.

CHAPTER 2 REFERENCES

[1] G.J. Foschini, M.J. Gans, "On the Limits of Wireless Communications in a Fading Environment when using Multiple Antennas," *Wireless Personal Communications*, Vol. 6, No. 3, pp. 311 – 335, March 1998.

[2] R.G. Vaughan, J.B. Andersen, "Antenna Diversity in Mobile Communications," *IEEE Transactions on Vehicular Technology*, Vol. VT-36, No. 4, pp. 149 – 172, November 1987.

[3] T. Taga, "Analysis for Mean Effective Gain of Mobile Antennas in Land Mobile Radio," *IEEE Transactions on Vehicular Technology*, Vol. 39, No. 2, pp 117 – 131, May 1990.

[4] T. Svantesson, "Correlation and Channel Capacity of MIMO Systems Employing Multimode Antennas," *IEEE Transactions on Vehicular Technology*, Vol. 51, No. 6, pp. 1304 – 1312, November 2002.

[5] Kalliola et al., "Angular Power distributions and Mean Effective Gain of Mobile Antenna in Different Propagation Environments", *IEEE Transactions on Vehicular Technology,* Vol. 51, No. 5, pp. 823 – 838, September 2002.

[6] Peyton Z. Peebles, *Probability, Random Variables and Random Signal Principles,* 4th Edition. New Jersey: McGraw-Hill, 2001.

[7] J. Thaysen, K.B. Jakobsen, "Envelope Correlation in (N, N) MIMO Antenna Array from Scattering Parameters," *Microwave and Optical Technology Letters*, Vol. 48, No. 5, pp.832 – 834, May 2006.

[8] C. Chiau, X. Chen, G. Parini, "A Compact Four Element Diversity Antenna Array for PDA Terminals in a MIMO System," *Microwave and Optical Technology Letters*, Vol. 44, No. 5, pp.408 – 412, March 2006.

[9] R. Garbacz, "Modal Expansions for Resonance Scattering Phenomena," *Proceedings of the IEEE*, pp. 856 – 864, August 1965.

[10] R. Garbacz, R. Turpin, "A Generalized Expansion for Radiated and Scattered Fields", *IEEE Transactions on Antennas and Propagation*, Vol. AP-19, No. 3, May 1971.

[11] R.F. Harrington, J Mautz, "Theory of Characteristic Modes for Conducting Bodies", *IEEE Transactions on Antennas and Propagation*, Vol. AP-19, No. 5, Sept 1971.

[12] R. F. Harrington, J. Mautz, "Computation of Characteristic Modes for Conducting Bodies", *IEEE Transactions on Antennas and Propagation*, Vol. AP-19, No. 5, pp. 629 – 639, September 1971.

[13] David M. Pozar, *Microwave Engineering,* 3rd Edition. New Jersey: John Wiley & Sons, 2005.

[14] R. F. Harrington, J. Mautz, "Control of Radar Scattering by Reactive Loading", *IEEE Transactions on Antennas and Propagation*, Vol. AP-20, No. 4, pp 446 – 454, July 1972.

[15] W.A. Johnson, D.R. Wilton, R.M. Sharpe, "Modeling Scattering from and Radiation by Arbitrary Shaped Objects with Electric Field Integral Equation Triangular Surface Patch Code," *Journal of Electromagnetics*, Vol. 10, pp. 41-63, 1990.

[16] T.B.A. Senior, "Impedance Boundary Conditions for Imperfectly Conducting Surfaces", *Applied Scientific Research*, Section B, Vol. 8, pp. 418 – 436, July 1960.

[17] N. Inagaki, R. Garbacz, "Eigenfunctions of Composite Hermitian Operators with Application to Discrete and Continuous Radiating Systems", *IEEE Transactions on Antennas and Propagation*, Vol. AP-30, No. 4, pp 571 – 575, July 1982.

[18] D. Pozar, "Antenna Synthesis and Optimization Using Weighted Inagaki Modes", *IEEE Transactions on Antennas and Propagation*, Vol. AP-32, No. 2, pp 159 – 165, February 1984.

[19] D. Liu, R. Garbacz, D. Pozar, "Antenna Synthesis and Optimization Using Generalized Characteristic Modes", *IEEE Transactions on Antennas and Propagation*, Vol. 38, No. 6, pp 862 – 868, June 1990.

[20] J. Mautz, R.F. Harrington, "Modal Analysis of Loaded N-Port Scatterers", *IEEE Transactions on Antennas and Propagation*, Vol. AP-21, No. 2, March 1973.

[21] Roger F. Harrington, *Field Computation by Moment Methods,* Wiley-IEEE Press, 1st Edition, 1993.

[22] Derek A. McNamara, Course Notes: *ELG7100D Moment Method Applied to Electromagnetics*, University of Ottawa, Fall 2007.

[23] Sergey N. Makarov, *Antenna and EM Modeling with MATLAB®*. New York: John Wiley & Sons, 2002.

[24] S. Rao, D. Wilton, A. Glisson, "Electromagnetic Scattering by Surfaces of Arbitrary Shape", *IEEE Transactions on Antennas and Propagation*, Vol. AP-30, No. 3, May 1982.

Chapter 3

Characteristic Mode Analysis Software

3.1 – Introduction

The main goal of this chapter is to discuss the software formulation we shall use to compute, analyze and ultimately design with characteristic modes. In section 3.2 we discuss how a moment method formulation is the ideal formulation to use, since the required impedance operator is discretized in such formulations. In section 3.3 we outline the moment method formulation we develop, using RWG function as our basis functions. This allows us to model surfaces rather than simply wire grids.

In section 3.4 we thoroughly validate the characteristic mode analysis software by measuring the symmetry of the discrete impedance operator using a novel measurement technique. We proceed with further validation by comparing the computed characteristic modes for a perfectly conducting sphere with closed-form values – the only known closed-form quantities one can compare to with characteristic mode theory. We also consider the characteristic modes of a strip dipole and compare the results to published work and make logical conclusions based on the results.

Lastly, in section 3.5, we consider the validation of the finite conductivity (or surface impedance) formulation. We show that our methodology yields radiation efficiencies that are at all times worse than those predicted by a popular commercial code, giving us a worst-case result we can use with confidence. Furthermore, we show that as the conductivity increases to arbitrarily large values the modal formulation for lossy conductors converges to that of the perfectly conducting modes, showing a self-consistency within the software formulation.

3.2 – Characteristic Modes and Method of Moments

When dealing with antenna problems, the integral equation that needs to be solved is none other than the impedance operator Z defined by the EFIE (electric field integral equation) [1]. The operator is defined in the following manner:

$$Z(\underline{J}) = j\omega \underline{A}(\underline{J}) + \nabla\Phi(\underline{J}) \tag{3.2-1}$$

$\underline{A}(\underline{J})$ and $\Phi(\underline{J})$ is the magnetic vector and electric scalar potentials respectively , defined by:

$$\underline{A}(\underline{J}) = \mu \iint_S J(r')\psi(r,r')\,ds' \text{ and } \Phi(\underline{J}) = \frac{j}{\omega\varepsilon} \iint_S \nabla' \bullet J(r')\psi(r,r')\,ds' \tag{3.2-2}$$

We consider r and r' to be field and source points, and ε, μ, and k to be the permittivity, permeability and wave number of free space. Furthermore, we consider $\psi(r,r')$ as the Green's function of freespace, defined as:

$$\psi(r,r') = \frac{e^{-jk|r-r'|}}{4\pi|r-r'|} \tag{3.2-3}$$

Written out in full, we have the following integral equation:

$$Z(J) = j\omega\mu \iint_S J(r')\psi(r,r')\,ds' + \nabla \frac{j}{\omega\varepsilon} \iint_S \nabla' \bullet J(r')\psi(r,r')\,ds' \tag{3.2-4}$$

We have defined our integral equation in which to solve using the method of moments, with the unknown being the surface currents on S and the kernel is equal to the Green's function of freespace and our domain is 3D-space.

Since the method of moments discretizes the domain in which we solve for the current, we discretize the impedance operator Z over the surface S [2]. As shown in the previous section, the discretized impedance operator is then represented by the matrix of values Z_{mn}. One can then define an excitation that is discretized using appropriate

expansion functions in the form of the excitation vector V_m, and the resulting currents can be solved for via matrix inversion $[I] = [Z]^{-1}[V]$.

Alternatively, one can determine source-free currents by performing eigenanalysis on the operator [Z] (now in discrete form). This eigenvalue problem can be setup in a multitude of ways, and can yield very useful modal results for antennas in general.

For the purposes of characteristic mode analysis, we are interested in computing the discrete impedance operator [Z] and recalling [R] and [X] as the real and imaginary parts of [Z] and setting up the eigenvalue problem:

$$[X][J_n] = [\lambda_n][R][J_n] \tag{3.2-5}$$

where: $J_n = \sum_{i=1}^{N} I_i W_i$,

Giving us the discrete eigenvalue problem:

$$\sum_{i=1}^{N} [X][I_i W_i] = [\lambda_n] \sum_{i=1}^{N} [R][I_i W_i] \tag{3.2-6}$$

with $[R] = \left[\langle W_i, RW_j \rangle\right]$ and $[X] = \left[\langle W_i, XW_j \rangle\right]$

3.3 – Characteristic Mode Analysis Software Formulation

3.3.1 –Characteristic Modes of PEC Objects

Using Makarov's [3] moment method formulation which is based in MATLAB [8], we have access to the discretized impedance operator, which implies we already have access to both the R and X operators for the surface that is being analyzed. We immediately consider computing the eigenvalues and eigenvectors for the problem $[X][J_n]=[\lambda_n][R][J_n]$ using the built-in MATLAB routine 'eig'. Since the moment method formulation is approximate we must take care when consider the results of the eigenvalue solver. Due to the numerical inaccuracies, and the lack of perfect symmetry in the matrices [R] and [X], not all eigenvalues and eigenvectors are purely real. However, the nature of eigenvalue solvers allows us to extract the lowest magnitude eigenvalues and be assured their values are accurate. As we move up in eigenvalue magnitude (here-after called 'higher-order' modes) the accuracy decreases and imaginary parts begin to appear.

A simple method of determining the limit of the number of accurately computed modes begins by normalizing the currents as described in section 2.2.4. With the currents normalized, one can then compute the weighted inner product between modes, relative to the operator [R]. The properties of characteristic modes states that any two distinct modal surface currents are weighted orthogonal and hence will result in a zero weighted inner product. The order of the mode in which this property breaks down is precisely the point in which the computed modes are no longer valid. By setting some form of threshold, the collection of valid characteristic modes can be found by limiting access to the modes that meet the above criteria for inner product.

Clearly, by increasing the segmentation of the surface in question (i.e. increasing the number of unknowns), a greater number of accurately computed modes will result. Note that the number of modes is always infinite, but the number of accurately computed modes is always finite.

Furthermore, if we wish to feed the structure using the moment method, we compute the desired excitation matrix [V], which in turn forms the matrix equation:

$$[V] = [Z][J] \tag{3.3-1}$$

which we can then use matrix inversion techniques (built-in MATLAB functionality) to compute the resulting currents [J] on [Z] due to [V]. Note that MATLAB does not compute the inverse directly, but rather uses much faster computational methods to solve systems of equations.

We now have the resulting surface current due to excitation, whether by voltage-gap feed or possibly incident plane wave(s). According to characteristic mode theory, we can expand this surface current in terms of the characteristic modal currents. We can compute to what extent each mode is being excited by computing the modal excitation coefficient:

$$V_n^i = \oiint_S J_n \cdot E_{\tan}^i dS = \left\langle J_n, E_{\tan}^i \right\rangle = [J_n][V] \tag{3.3-2}$$

And subsequently the modal expansion coefficient:

$$\alpha_n = \frac{\left\langle J_n, E_{\tan}^i \right\rangle}{(1 + j\lambda_n)} = \frac{V_n^i}{(1 + j\lambda_n)} \tag{3.3-3}$$

the latter of which can be used to directly compute the amount of power that is being sent into each mode, which is an effective means of determining how distinctly we excite unique sets of characteristic modes as we change the location of excitation. In MATLAB, this computation is performed in the discrete domain simply by matrix multiplication:

$$\alpha_n = \frac{[J_n][V]}{1 + j\lambda_n} \tag{3.3-4}$$

where [Jn] is the n^{th} modal current and [V] is our excitation vector.

We can alternatively write this as:

$$\alpha_n = \frac{[J_n][Z][J]}{1 + j\lambda_n} \tag{3.3-5}$$

which shows that we can compute the mode expansion factor from the known surface current. The quantity α_n is in general a complex number, with its magnitude squared equal to the power radiated by the n'th mode.

Furthermore, we can use the results of the modal excitation factors as a guideline in determine the optimal feed locations, as well as a measure of how well certain designs perform relative to others.

3.3.3 – Generalized Characteristic Modes

For the generalized characteristic modes, we wish to compute the matrix [H], which is used to compute surface currents that will yield orthogonal far-field patterns over constrained regions of the far-field.

By looping through the surface patch edges, we can force the current across the edge to be unity, and measure the resulting far-field pattern. In doing so, we determine the far-field patterns of these small elements of currents. These patterns represent the fields of the moment method expansion functions.

Subsequently, we perform surface integration on a far-field sphere between every pair of moment method expansion function far-field patterns, both of which are weighted by the desired region of orthogonality. The surface integration is performed by using a densely meshed sphere, with points evenly spread around the surface rather than bunched near the poles. Each meshed triangle has a prescribed area, which we consider to be the differential element of surface, and the field is averaged over the triangle, multiply the two and adding over all parts of the sphere gives us the resultant surface integral. If we

are interested in solid angle integration rather than surface, we simply divide by the radius squared to get our result.

Each computation results in an entry in the desired [H] matrix, which is then used in either of the eigenvalue problems: $[Z^*Z][J_n] = \lambda_n'[H][J_n]$ or $[X][J_n] = \lambda_n'[H][J_n]$. Either formulation will yield orthogonal far-fields, with the advantages of each formulation discussed later.

3.3.4 – Surface Integration Used in Performance Index Computations

Using the methodology for surface and solid angle integration described in the previous section, we can compute the following quantities:

- Mean Effective Gain, or MEG
- Envelope Correlation, ρ_{env}
- Power Radiated, and thus Efficiency
- Power Radiated Figure of Merit (% of power radiating into a desired region of the far-field)

3.3.5 – Meshing Routines

In order to test a wide range of potential handheld chassis designs, we consider various plate sizes, orientations and physical layouts. The meshing function including with Makarov's formulation is capable of meshing a plate of any given dimension to any chosen segmentation density. However, numerous features were added to give us design flexibility:

- Rotate plate using Euler transformation coordinates, allowing us to rotate handheld in more natural 'talk' positions

- Translation using simply Cartesian coordinate displacement allowing us to create clamshell-type handheld chassis
- The ability to add any number of meshed objects together, which gave us the flexibility when designing flip phones.

MATLAB's PDETool was used for altering the physical layout of the plates, such as adding slots, removing metallization and generally shaping the handheld into more reasonable and recognizable shapes.

3.3.6 – Secondary Parameter Computation

Finally, the ability to measure various network related parameters, including Z, Y and S-parameters were coded to make analysis far simpler.

The simplest approach to compute network parameters using a moment method formulation begins with computing Y-parameters. Since the default state of all ports in a moment method formulation is shorted, the condition for measuring Y-parameter is by default already in place. By shorting all ports but one and exciting the remaining port using an ideal voltage source, we can compute the desired currents, and hence the desired Y-parameters.

With the ability to compute currents due to applied voltages, it is possible to excite a port (an RWG edge) and compute the port current. From this result one can compute input impedance. Furthermore, using standard conversion formulas [6] one can quickly convert from the Y-parameters into the more common Z- or S-parameters.

3.4 – Validation of Characteristic Mode Software

3.4.1 – Symmetry of the Impedance Operator

We can trust implicitly the moment method formulation devised by Makarov since he performed extensive validation studies [3]. The impedance operator [Z], and all parameters derived from it including surface currents, far-field patterns, and input impedance is assumed to be validated. What is not validated is the symmetry of the operator [Z] and various other characteristic mode dependent properties. Makarov's method is Galerkin by definition and will thus produce nearly symmetric impedance matrices [Z]. However, we must confirm there is enough symmetry for the purposes of eigenanalysis.

Some authors [2] force the impedance operator to be symmetric by setting the cross-terms equal to the average of the asymmetric values. This approach is likely valid for smaller impedance matrices, where the asymmetry rears its ugly head in a more apparent manner, but for larger matrices (denser meshes) one finds this approach yields no appreciable benefit in eigenanalysis.

A symmetric matrix A has the property $A = A^T$. For the case of the impedance operator Z, we have $Z = Z^T$ or more specifically in terms of the real and imaginary parts: $R = R^T$ and $X = X^T$. For the computed matrices, we would like to see these properties hold true, but due to numerical inaccuracies, the matrices will not be perfectly symmetric. One way to measure the level of symmetry of X and R, we define two "error" matrices:

$$r = R - R^T \text{ and } x = X - X^T \tag{3.4-1}$$

Ideally 'r' and 'x' would be null matrices, with our goal being a measure of the deviation from this ideal. The problem with this approach is as mesh density increases, the entries of R and X tend to shrink in size. Clearly some form of normalization is required such that the measurement of similarity can be achieved regardless of the size of the

impedance matrix. The solution is found using a correlation measurement, similar in form to the envelope correlation used for MIMO discussed in Section 2.2. The correlation measurement we speak of is defined as:

$$Corr(A,B) = \frac{\sum_i \sum_j \left(A_{ij} - \overline{A}\right)\left(B_{ij} - \overline{B}\right)}{\sqrt{\left(\sum_i \sum_j \left(A_{ij} - \overline{A}\right)^2\right)\left(\sum_i \sum_j \left(B_{ij} - \overline{B}\right)^2\right)}} \tag{3.4-2}$$

where $-1 \le Corr(A,B) \le 1$ with $\overline{A}$ and $\overline{B}$ as the means of the matrices A and B. MATLAB has a built in function "corr2" that computes this exact quantity. Note that if A and B are equal (the entries of A are equal to the entries of B) then the value of the correlation function corr(A,B) is precisely 1. If the A and B are anti-symmetric (skew-symmetric) the correlation function has value -1. Thus, the correlation function is normalized and does not depend on the magnitudes of the entries in A or B.

We now consider the correlations and thus the measure of similarity between the matrices X and R and their transposes. For the case of a half-wavelength squared PEC plate, we find correlation (i.e. measure of matrix symmetry) in Figure 7 as a function of mesh density. We see the correlation is extremely high, even in the lower mesh densities. Note that we are not considering accuracy of the eigenanalysis formulation, just the measure of symmetry of X and R. We consider an electrically larger plate, 2 wavelengths squared in Figure 8. We see the correlation converges to the ideal value of 1.00, but in contrast to the previous example, the electrically larger plate requires a higher mesh density to achieve similar high levels of correlation.

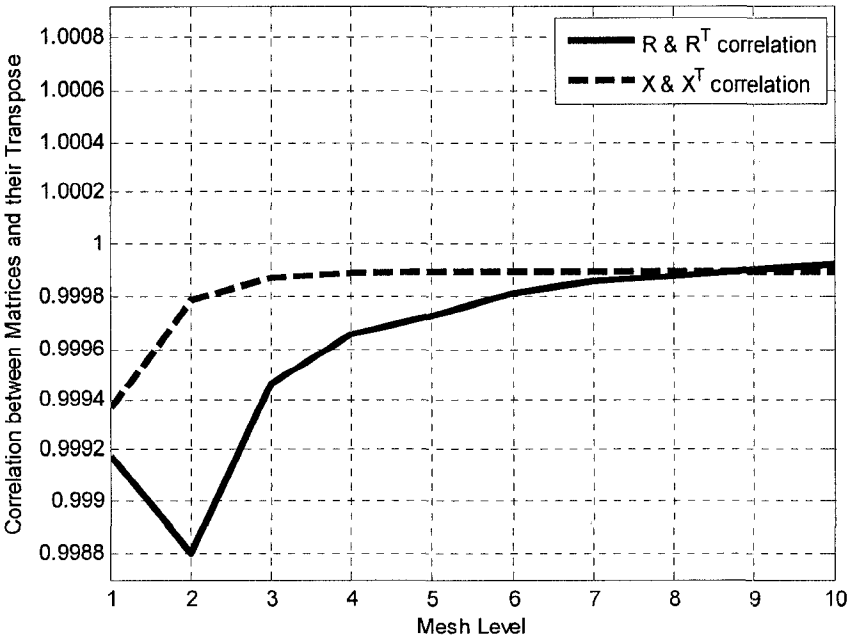

Figure 7 –Impedance Matrix Symmetry as a Function of Mesh Density, Half-Wavelength Square Plate

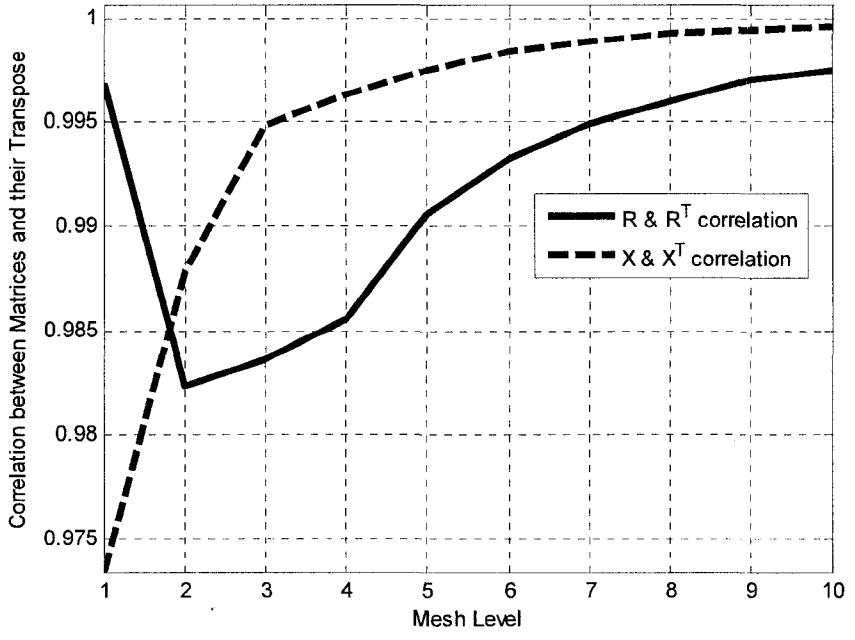

Figure 8 - Impedance Matrix Symmetry as a Function of Mesh Density, Two-Wavelength Square Plate

Lastly, we consider a fixed mesh sphere, vary the frequency, and compute the correlation between the matrices and their transposes, as shown in Figure 9. We clearly see the correlation between the matrices decreasing with frequency, implying a need for greater mesh density. However, one finds the drop in matrix symmetry to be quite small and as such the limiting factor(s) in accurate computation of modal properties does not rely on the matrix symmetry for our moment method formulation.

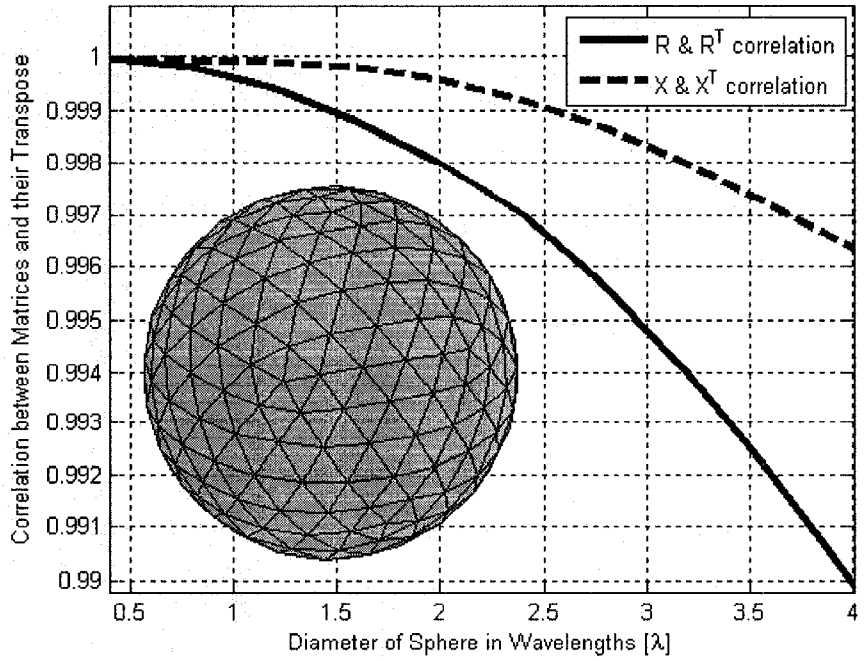

Figure 9 – Matrix Symmetry as a Function of Frequency for a Fixed Mesh Density

3.4.2 – Characteristic Modes of the Perfectly Conducting Sphere

It is difficult to state whether or not a set of eigenvalues and eigen-currents are indeed accurately computed, as closed form expressions do not exists for these quantities for arbitrarily defined surfaces. However, we are fortunate since a closed form expression for the eigenvalues of the perfectly conducting sphere does exist, and amounts to a simple ratio of Bessel-type functions [2]. These closed-form expressions exist due to the connection between characteristic modes and the spherical wave expansion functions. Using the characteristic mode analysis software we developed, we can simulate a perfectly conducting sphere and compute the eigenvalues, comparing them with the closed-form values in Table 1.

Table 1 – Convergence Data: Eigenvalues of the Perfectly Conducting Sphere

Sphere Radius a = 0.2 lambda, Unaltered [Z] matrix					
	Eigenvalue λ_n				
Mode	**Exact**	**Approx L1**	**Approx L2**	**Approx L3**	**% Error for L3**
TM01	-1.082	-1.129	-1.0876	-1.0806	-0.13
TE01	2.673	2.8849	2.6899	2.6577	-0.57
TM12	-11.00	-14.702	-11.4892	-10.9533	-0.42
TM22	-11.00	-14.827	-11.5061	-10.9563	-0.40
TE02	21.60	24.824	21.8566	21.378	-1.03
TE12	21.60	24.843	21.8566	21.378	-1.03
TE22	21.60	24.8434	21.8566	21.378	-1.03
TM03	-284.40	373.131	-313.0159	-284.3753	-0.01
L1 = 80 Triangles, L2 = 320 Triangles, L3 = 1280 Triangles					

We can make the following conclusions based on our simulation results:

- For low mesh densities, only the very lowest eigenvalues have acceptable error.
- As the mesh density increases the convergence of eigenvalues, including higher-order modes, converge to the expected value.

The total surface area of the sphere is approximately: $0.377\lambda^2$ where the mesh densities used in terms of wavelength are as follows: *L1*: 80 triangles, or approximately $0.0047\lambda^2$/ triangle. This equates to an approximate linear mesh density of 0.07λ / element. *L2*: an approximate 0.035λ / triangle and *L3*: an approximate 0.017λ / triangle.

The general rule for method of moments mesh density is approximately 0.05λ to 0.1λ per triangle edge or better. We meet this criterion for the L2 and L3 mesh densities, with the resulting accuracy apparent in the eigenvalues. We shall therefore ensure mesh densities on the order of 0.1λ to 0.05λ or smaller to ensure low error in computation of characteristic modes.

Other methods were considered for increasing the accuracy of the eigenvalue results, including pre-conditioners and creating smaller subsets of matrices in which to solve eigenvalues for, but the increase in accuracy was on the order of 0.01% to 0.1% for the eigenvalues and is therefore insignificant when considering the substantial increase in computation time.

3.4.3 – Characteristic Modes of the Strip Dipole

The ubiquitous antenna is the resonant dipole, and no antenna software validation is complete without it. We begin by computing the characteristic modes of a 75mm long strip dipole at various frequencies. This dipole has its first resonance around 2 GHz, with higher frequency resonances spaced at the usual intervals. Near resonance the dominant characteristic mode has its eigenvalue near zero, which is the principle reason for near-zero input reactance at resonance. Furthermore, we plot the corresponding modal currents on the dipole for select few of the dipole resonances, including the lowest resonance, as shown in Figure 10. The resulting modal currents agree well with the results published by Akkerman [7]. We can see that as the frequency increases, the current oscillates more rapidly, as expected for electrically larger dipoles.

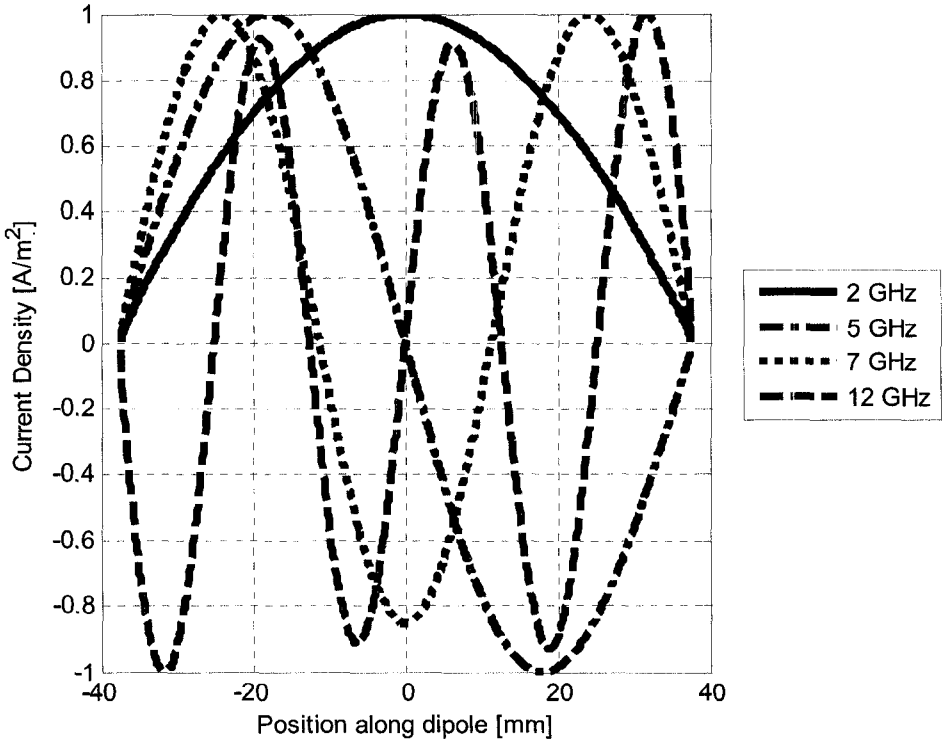

Figure 10 (a) – Selection of Externally Resonant Dipole Modes

Furthermore, we can consider the eigenvalue behaviour over frequency. We plot the magnitude of the eigenvalue in logarithm scale in Figure 11 using $10\log_{10}|\lambda_n|$. We clearly see the source of the multiple resonances of the dipole as frequency increases. As if taking turns, each mode's magnitude drops sharply at evenly spaced frequencies. These frequencies represent the resonances that occur for dipole electrical lengths that are integer multiples of half a wavelength. Notice the anti-resonances (occurring at integer multiples of one wavelength) are not apparent from the eigenvalue behaviour.

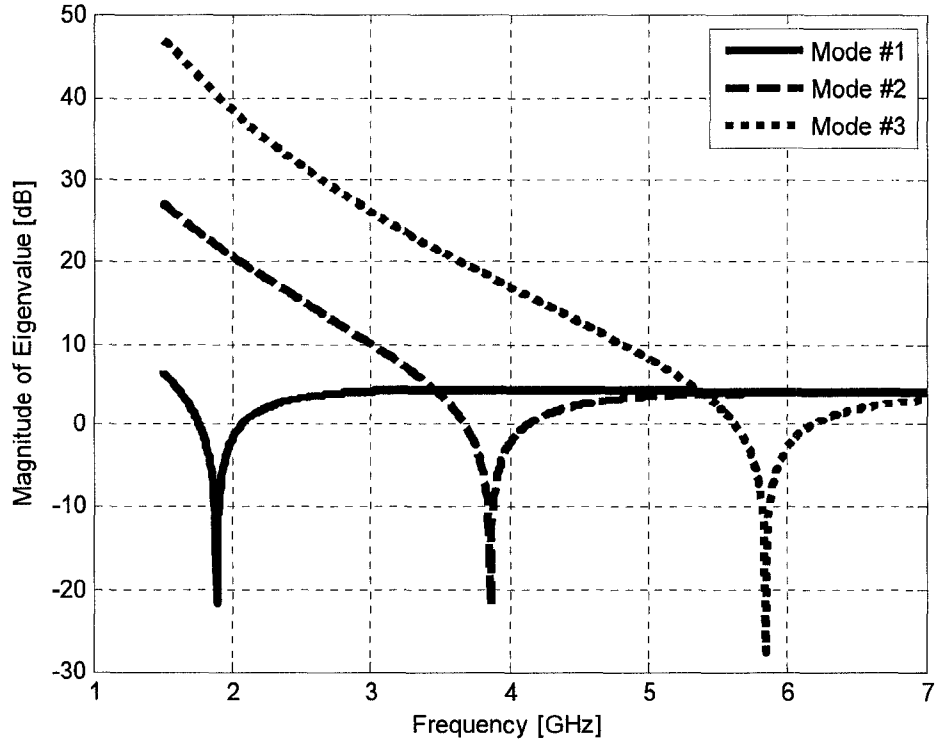

Figure 11 – Frequency Behaviour of the Eigenvalues of a Strip Dipole

3.5 – Validation of Surface Impedance Formulation

The lossy characteristic mode formulation is very similar to the classical case, with the exception being appending to the original impedance operator [Z] with a loading operator [Z_L] and a re-interpretation of the eigenvalues, as discussed in Chapter 2.

The lossy surface formulation allows us to compute the loading operator [Z_L] by computing the inner product between the moment method expansion functions, weighting by defined surface impedance. In our formulation we define the surface impedance to be constant over the entire structure, but the formulation does not forbid a positional dependence on the impedance.

Using the simplifications by Johnson [4], as discussed in section 2.2.8, it is possible to compute the required inner product $[Z_L]_{mn} = \langle f_n, Z_s f_m \rangle$ in closed form. Thus, we compute the matrix [Z_L] and compute the eigenvalues, expansion coefficients and far-field patterns in much the same way as the classical case.

3.5.1 – Computed Radiation Efficiency of a Lossy Dipole Antenna

We begin by computing the radiation efficiency of a strip dipole and compare the results to a comparable simulation using the commercial electromagnetic simulation software FEKO [9].

The physical size of the dipole is 100mm long and 1mm wide, with sufficient and similar meshing in both the modal software and commercial code. The commercial code has the additional ability to specify the thickness of the copper material, which certainly plays a role in the computed value of radiation efficiency.

We consider three cases of copper thickness (0.02 OZ, 0.1 OZ and 0.5 OZ) chosen within the FEKO simulation and compare to the results from our simulation code (where thickness must always be zero) in Figure 12. We see that in all cases the radiation efficiency predicted by the thesis code is less than the efficiency predicted by FEKO. We notice similar behavioral trends for the efficiency curves, with the thesis formulation being a worst-case-scenario lower bound on predicting efficiency.

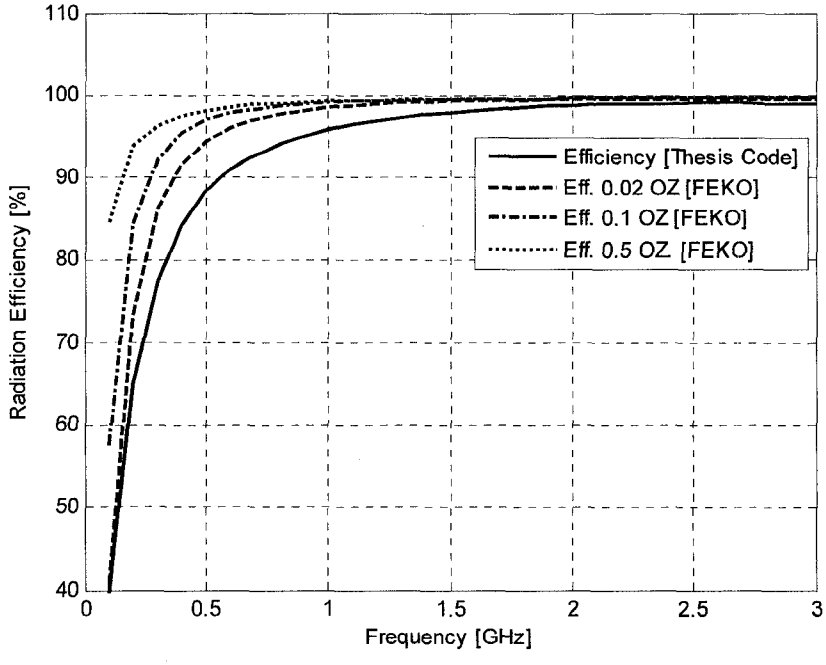

Figure 12 – Comparison of Radiation Efficiency Curves for Commercial and Thesis Code

3.5.2 – Convergence of Lossy Characteristic Modes to the PEC Case

Additionally, we consider the convergence of the characteristic modes of lossy conductors as the conductivity is increased. One would expect these "lossy" modes would converge such that the imaginary part would disappear (i.e. 100% radiation efficiency) and the real part of the eigenvalue would be equal to the characteristic mode of the perfect conductor counterpart. We consider a quarter wavelength by quarter wavelength finitely conducting plate and plot the imaginary parts of the first ten modes as a function of conductivity, as shown in Figure 13. We see in all cases the imaginary part is negative (as expected from modal theory) and furthermore, the convergence shows a distinct trend towards zero imaginary part.

We conclude the validation of the finite conductivity formulation by considering the percentage difference between the real part of the eigenvalue for the finite conductivity case versus the eigenvalue of the PEC case in Figure 14. We see the percentage difference is quite low to begin with, and drops even lower (below 0.01%) as the conductivity increases. We therefore conclude that as the conductivity increases, the finite conductivity modal formulation converges to the perfectly conducting modal formulation, which in turn was properly validated.

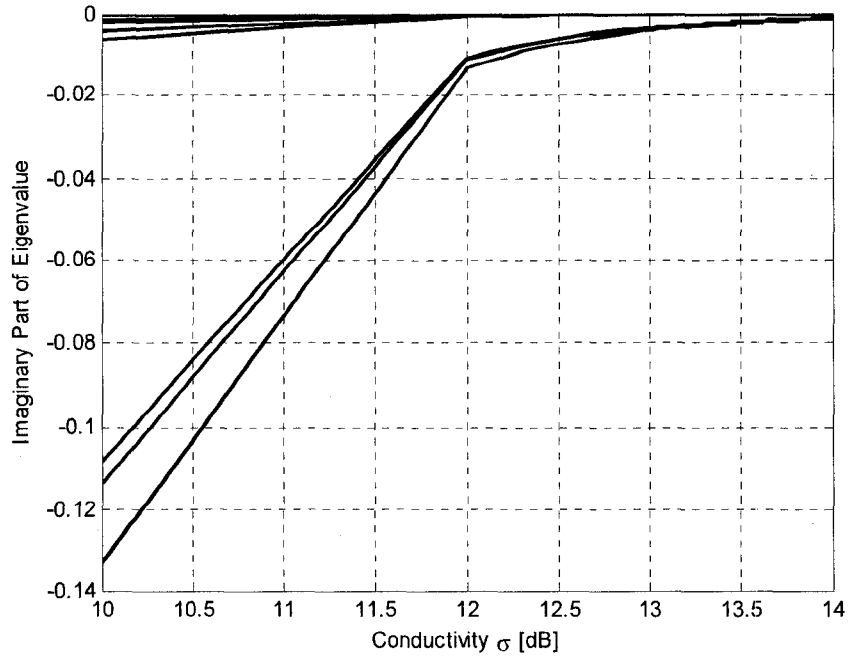

Figure 13 – Imaginary Part of the Eigenvalues of the Lossy Plate as a Function of Conductivity

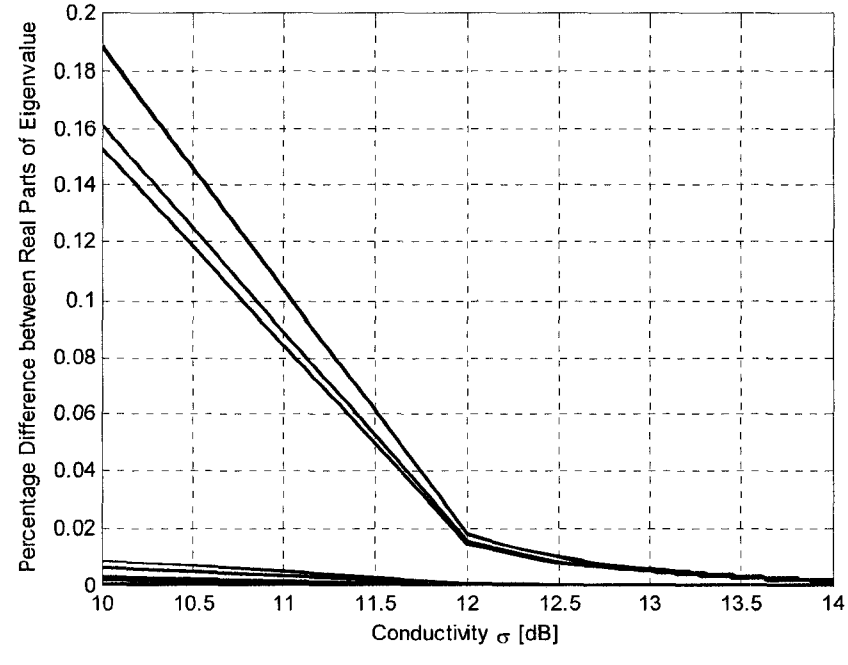

Figure 14 – Percentage Difference between Real Part of Eigenvalues of the Lossy Plate and PEC Equivalent

3.6 – Concluding Remarks

In the preceding chapter we discussed the software formulation we intend to us in the computation, analysis and ultimately MIMO antenna design with characteristic modes. In section 3.2 we discussed how moment method formulations are the ideal formulations to use, since the required impedance operator is inherently discretized in such formulations, allowing us to cast the required eigenvalue problem. In section 3.3 we outlined the details of moment method formulation where we used RWG basis function to solve for the necessary surface currents.

Throughout section 3.4 we thoroughly validated the characteristic mode analysis software. The first step was to measure the symmetry of the discrete impedance operator using a novel measurement technique involving matrix correlations. We proceeded with further validation by comparing the simulated characteristic modes of a perfectly conducting sphere with closed-form parameters – the only known closed-form quantities one can compare with characteristic mode theory. We also considered the characteristic modes of a dipole and compared the results with published work, showing good agreement.

Concluding in section 3.5, we considered the validation of the finite conductivity (or surface impedance) formulation. We showed that our methodology yields radiation efficiencies that are at all times worse than those predicted by popular commercial codes, giving us a worst-case result we can quote with confidence since it will never be an over-estimate. Lastly (and most importantly), we show that as conductivity increases to arbitrarily large values, the modal formulation for lossy conductors converges to that of the perfectly conducting modes, showing the necessary self-consistency within the software formulation.

CHAPTER 3 REFERENCES

[1] R.F. Harrington, J Mautz, "Theory of Characteristic Modes for Conducting Bodies", *IEEE Transactions on Antennas and Propagation*, Vol. AP-19, No. 5, Sept 1971.

[2] R. F. Harrington, J. Mautz, "Computation of Characteristic Modes for Conducting Bodies", *IEEE Transactions on Antennas and Propagation*, Vol. AP-19, No. 5, pp. 629 – 639, September 1971.

[3] Sergey N. Makarov, *Antenna and EM Modeling with MATLAB®*. New York: John Wiley & Sons, 2002.

[4] W.A. Johnson, D.R. Wilton, R.M. Sharpe, "Modeling Scattering from and Radiation by Arbitrary Shaped Objects with Electric Field Integral Equation Triangular Surface Patch Code", *Journal of Electromagnetics*, Vol. 10, pp. 41-63, 1990.

[5] T.B.A. Senior, "Impedance Boundary Conditions for Imperfectly Conducting Surfaces", *Applied Scientific Research*, Section B, Vol. 8, pp. 418 – 436, July 1960.

[6] David M. Pozar, *Microwave Engineering*, 3rd Edition. New Jersey: John Wiley & Sons, 2005.

[7] K. Akkerman, "Characteristic Modes for Planar Structure Feed Design", *Antennas and Propagation Society International Symposium*, Volume 2B, pp. 503-506, July 2005.

[8] The MathWorks, Inc. 3 Apple Drive, Natick, MA 01760-2098, USA. *MATLAB™ (Mathematical Laboratory)*.

[9] EM Software & Systems (USA) Inc. Langley Research Park, 144 Research Drive, Hampton, VA 23666. (*FEKO Electromagnetics Simulator*)

Chapter 4

Fundamental Studies of Characteristic Mode Properties

4.1 – Introduction

In order to use the characteristic modes to their full potential it is a good idea to get a better understanding of their properties. In Chapter 2, we summarized the theory regarding characteristic modes [1] that is already well known in the literature. An exception to this is the consideration of the lossy characteristic modes, which we shall discuss in a later section.

Most importantly, we must investigate what significance the modes have in describing antenna performance. A claim found in the literature [2] is the eigenvalue λ_n obtained through eigenanalysis is the determining quantity in modal significance. We will show that this claim is not true and in fact, can be very misleading in classifying modes as either significant or insignificant.

Lastly, we will compute and analyze the characteristic modes of various common PEC scatterers, and show that the modes confirm already well-known properties and phenomena, and that new phenomena can be derived as well.

4.2 – Useful Figures of Merit for Characteristic Modes

The typical approach using characteristic mode analysis involves ranking the modes based on their eigenvalue (with the smallest magnitude implying 'modal dominance'). In particular, there is the proposed notion that the factor $1/(1+j\lambda_n)$ can be considered to be a form of measured "modal significance" for the n'th mode. The argument is that since the modal excitation $\alpha_n = \langle J_n, E^i \rangle / (1+j\lambda_n)$ contains the term $1/(1+j\lambda_n)$, all excitation factors are scaled by this quantity.

However, this is an incomplete interpretation of characteristic modes, since the modal currents and their corresponding normalized magnitudes play an important role in modal significance. The numerator for the expression α_n contains the normalized surface current J_n which can be quite large in some instances. Even for large λ_n, a large J_n can balance the scale factor $1/(1+j\lambda_n)$ yielding a significant excitation of a particular mode.

Here we shall consider figures of merit that will take in account all facets of the characteristic mode: both eigenvalue and eigencurrent. Recall that the complex power associated with an arbitrary excitation can always be written in terms of the characteristic modes as:

$$S = P + jQ = \sum_{n=1}^{N} |\alpha_n|^2 (1+j\lambda_n) \tag{4.2-1}$$

where

$$\alpha_n = \langle J_n, E^i \rangle / (1+j\lambda_n) \tag{4.2-2}$$

For the case of excitation via a single port, the impressed electric field E^i can be thought of as the port voltage. In this case, the inner product in the numerator of α_n becomes a multiplication of the excitation E^i, now denoted $V^{port\ m}$ and the modal current at that port, denoted: $J_n^{port\ m}$. This concept can easily be extended to include excitation via multiple ports, but the single port excitation will suffice for our purposes.

For an arbitrary excitation at port m, we can express the magnitude squared excitation coefficient as:

$$|\alpha_n|^2 = \frac{\left(J_n^{port\ m} V^{port\ m}\right)^2}{1+\lambda_n^2} \tag{4.2-3}$$

Allowing us to express the complex power in terms of the characteristic modes:

$$S = \sum_{n=1}^{N} \frac{\left(J_n^{port\ m} V^{port\ m}\right)^2}{1+\lambda_n^2}\left(1+j\lambda_n\right) \tag{4.2-4}$$

For a surface that is meshed with triangles yielding N edges, there are N ports in which to excite. Each port m when excited with magnitude V^{port} routes both real and imaginary power into various modes. Since we are exciting the structure at a single port, this allows us to remove the excitation from the summation:

$$S = \left(V^{port\ m}\right)^2 \sum_{n=1}^{N} \frac{\left(J_n^{port\ m}\right)^2}{1+\lambda_n^2}\left(1+j\lambda_n\right) \tag{4.2-5}$$

If we normalize the port excitation to be $V^{port} = 1$ at all ports, we can then compare the complex power associated with every port. We could also just consider that the magnitude of the port voltage scales all modal excitation equally.

Considering Equation 4.2-5 we can state that the port having maximum modal current will invariably yield the highest magnitude real and imaginary parts of complex power. We therefore consider two important figures of merit. The first being:

$$FIG_n^{radiation} = \frac{\max_{\bar{r}} \forall \left|J_n(\bar{r})\right|^2}{1+\lambda_n^2} \tag{4.2-6}$$

This figure of merit considers modes that contribute significantly to radiated power. This quantity can be calculated for each mode, normalized relative to the maximum value and then ranked in order of magnitude. The modes with the largest figures of merit

contributed the most to radiated power. A cut-off can be stated with modes having figures of merit below this cutoff consider insignificant in terms of radiated power.

$$FIG_n^{reactive} = \frac{\max_{\bar{r}} \forall \left|J_n(\bar{r})\right|^2 |\lambda_n|}{1+\lambda_n^2} \tag{4.2-7}$$

This figure of merit is similar to the quantity previously defined; only this quantity considers reactive power. The same normalization, cut-off and judgment on whether a mode is significant holds for this figure of merit as well. In order to remain consistent, we notice the following ratio:

$$\frac{FIG_n^{reactive}}{FIG_n^{radiation}} = \frac{\dfrac{\max_{\bar{r}} \forall \left|J_n(\bar{r})\right|^2 |\lambda_n|}{1+\lambda_n^2}}{\dfrac{\max_{\bar{r}} \forall \left|J_n(\bar{r})\right|^2}{1+\lambda_n^2}} = |\lambda_n| \tag{4.2-8}$$

This result shows that the eigenvalue λ_n, irrespective of the chosen port and modal current magnitude, can be used to judge whether a mode will radiate significant power or rather store significant energy. However, it cannot be used to judge whether a mode will be insignificant in terms of antenna performance, since a highly reactive mode is undesirable, and will clearly be a detriment to antenna performance in the form of very large reactive impedances.

We can further combine these quantities together in a single figure of merit since the total complex power attributed to a mode for a given port can be written as:

$$S_n = \frac{\left(J_n^{port\ m}\right)^2}{1+\lambda_n^2} + j\lambda_n \frac{\left(J_n^{port\ m}\right)^2}{1+\lambda_n^2} \tag{4.2-9}$$

which has a magnitude of:

$$|S_n| = \sqrt{\left[\frac{\left(J_n^{port\ m}\right)^2}{1+\lambda_n^2}\right]^2 + \left[\lambda_n \frac{\left(J_n^{port\ m}\right)^2}{1+\lambda_n^2}\right]^2} = \frac{\left(J_n^{port\ m}\right)^2}{1+\lambda_n^2}\sqrt{1+\lambda_n^2} = \frac{\left(J_n^{port\ m}\right)^2}{\sqrt{1+\lambda_n^2}} \tag{4.2-10}$$

Thus, for an arbitrary radiating structure, we can consider the maximum surface current as yielding our figure of merit associated with mode n:

$$FIG_n^{total} = \frac{\max_{\bar{r}} \forall \left| J_n(\bar{r}) \right|^2}{\sqrt{1+\lambda_n^2}} \tag{4.2-11}$$

This figure of merit combines both the radiative and reactive parts of the complex power. This quantity is the most useful of the three newly defined quantities, since it can be used to rank modes in terms of both radiative and reactive properties *simultaneously*. Modes that have figures of merit below a defined cutoff using this measurement quantity are insignificant from all aspects of antenna performance, and do not contribute to either radiated power or net stored energy and are therefore contribute negligibly to input resistance and input reactance.

The goal of this newly defined quantity is to point out that modal significance in terms of antenna performance cannot be solely judged by the modes' eigenvalue, and one must additionally consider the modal current magnitude before any conclusions can be made.

These results do not change the fact that mainly low magnitude eigenvalue modes contribute to radiated power – this fact still holds true as evident in Expression 4.2-6. That being said, an antenna's performance is very much dependent on input reactance, something which the eigenvalue alone cannot predict.

We shall denote this quantity FIG_n^{total} as another accurate measure of modal significance, denoted as:

$$\chi(n) = \frac{\max_{\bar{r}} \forall \left| J_n(\bar{r}) \right|^2}{\sqrt{1+\lambda_n^2}} \tag{4.2-12}$$

4.3 – Figure of Merit for Typical Antenna and Scattering Structures

4.3.1 – Modal Significance of the Resonant Dipole

We consider computing these figures of merit for a resonant dipole. The first two figures of merit we consider are the radiative and reactive measurements defined by Equations 4.2-6 and 4.2-7 and computed as shown in Figure 15. Not surprisingly, we find the first mode of the dipole to be the only dominant mode for radiation. This is because the eigenvalue is such a low eigenvalue mode, while the remaining modes (for $n > 1$) all have large magnitude eigenvalues.

What is of interest is the modal significance in terms of reactive power (or net stored energy). Clearly, the dominant mode $n = 1$ has negligent reactive modal significance since the eigenvalue is approximately zero. However, some of the higher order modes have significant contributions to reactive power. These modes are the source of input reactance when one feeds a dipole off-center.

Notice also some further insight into the dipole behaviour: only mode 1 is significant for radiation, and only modes 2, 3 and 6 are significant for stored energy. One can conclude that the dipole's behaviour can be solely described by these four modes, regardless of the chosen location of excitation. This is an interesting result since it has been shown in the literature that CMs can serve as basis functions for increasing the computational efficiency of some antenna related calculations [3]. These figures of merit should allow these approaches to further reduce the number of necessary modes utilized by the computational procedures.

Previous approaches in defining modal significance fail to take into account the effects of the normalized modal currents. By including these effects, we can show that modes that would otherwise be deemed insignificant are in fact important to fully describe an antenna's performance.

Next we consider the two figures of merit. The *previously* quoted modal significance:

$$FIG = \frac{1}{\sqrt{1+\lambda_n^2}} \tag{4.3-1}$$

The *newly* defined modal significance:

$$\chi(n) = \frac{\max_{\bar{r}} \forall \left| J_n(\bar{r}) \right|^2}{\sqrt{1+\lambda_n^2}} \tag{4.3-2}$$

We then compute and plot this new modal significance as shown in Figure 16.

We can clearly see mode 2, 3 and 6 becoming significant in terms of their normalized figure of merit. The original approach would not consider these modes as important, but the newly defined figure of merit, $\chi(n)$ is able to determine these modes of significance. It should be noted that even with our newly defined figure of merit, these higher order modes are low in magnitude relative to the dominant mode. This is evidence of simplistic nature of the dipole antenna.

Some further investigations find that more complicated antenna structures yield drastically different results depending on which figure of merit one uses, lending credence to the newly defined approach.

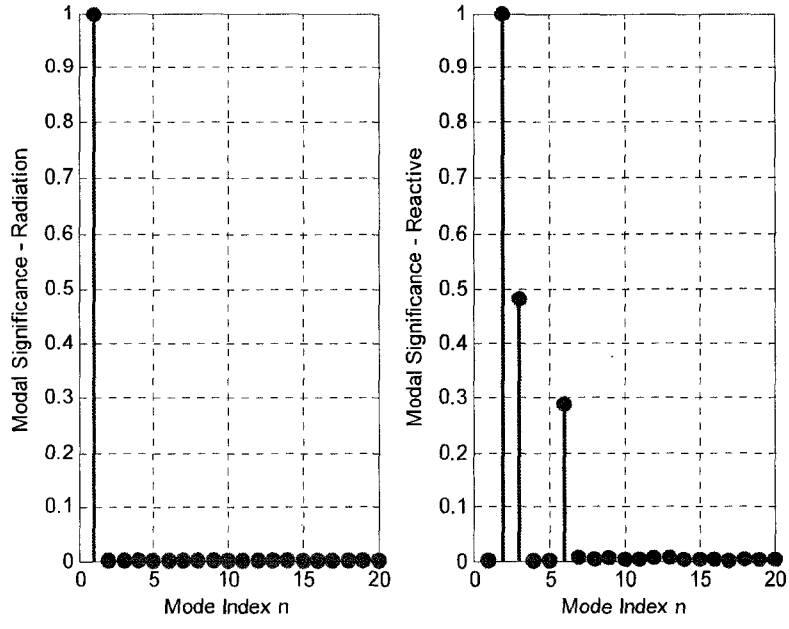

Figure 15 – Radiative and Reactive Modal Significances for a Dipole Antenna

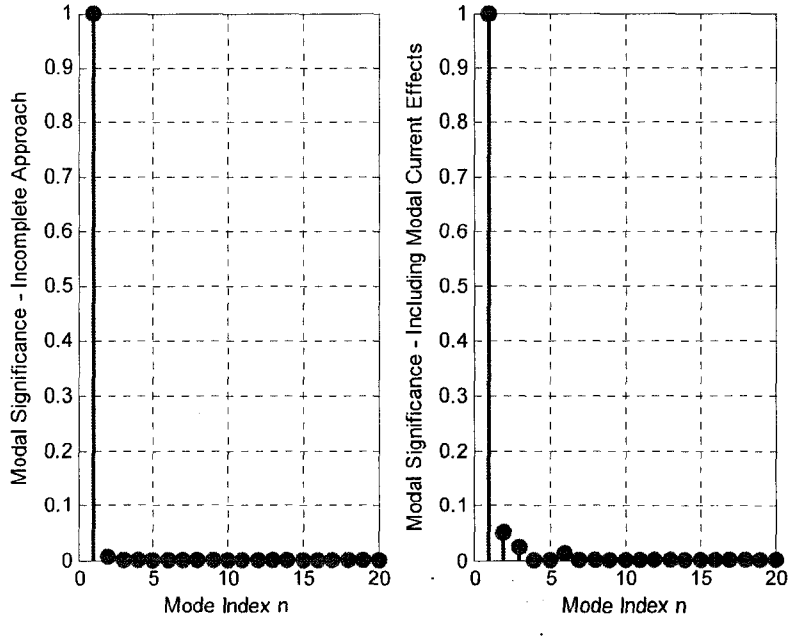

Figure 16 – Comparison between Incomplete and Newly Defined Modal Significance, Dipole Antenna

4.3.2 – Modal Significance of a Loop Antenna

Next we consider the characteristic modes of a perfectly conducting resonant loop antenna, slightly more complicated than the dipole antenna, with the modal significance considered in Figure 17 and Figure 18.

As expected, the only significant modes for radiation are modes 1 and 2, which are the two dominant orthogonal modes of the loop antenna. We also see modes 3, 4, 5, 11 and 12 are significant in terms of input reactance. Again, we find that the newly defined functions predict significant modes that would otherwise be overlooked by the usual modal significance definitions.

We find that modes 4, 5, 6 and 7 (and to a lesser extent mode 11 and 12) are notably more significant than the typical measure would imply. Like the dipole, the loop is a relatively simple structure and the advantage of using the newly defined modal significance does become apparent.

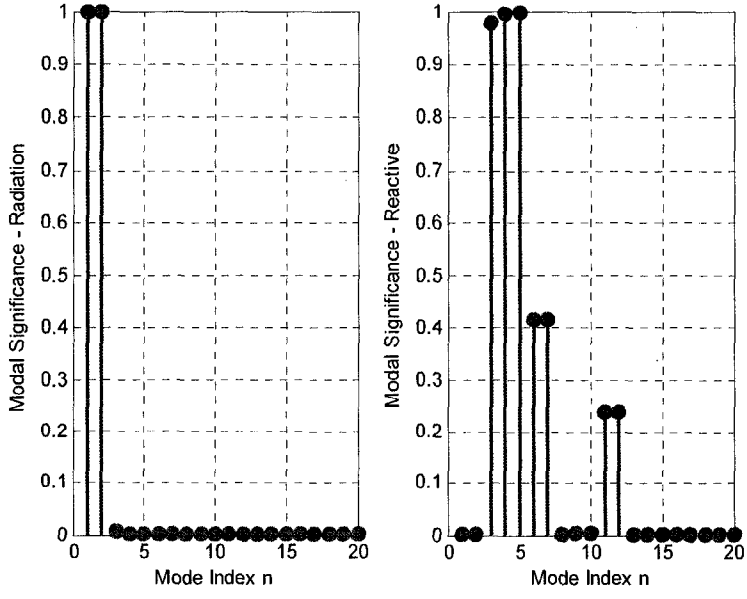

Figure 17– Radiative and Reactive Modal Significances for a Loop Antenna

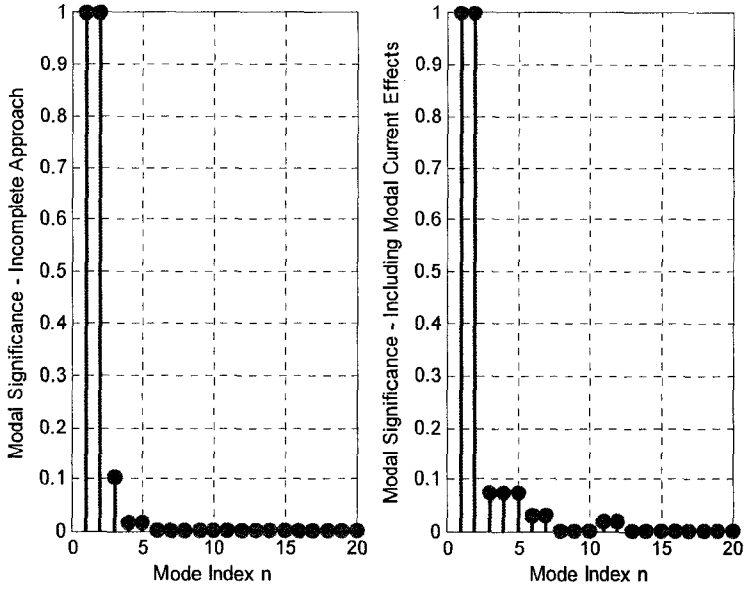

Figure 18 – Comparison between Incomplete and Newly Defined Modal Significance, Loop Antenna

4.3.3 – Modal Significance of a PEC Plate

We consider the characteristic modes of a perfectly conducting 1λ by 0.5λ plate, representative of typical cell phone chassis' at wireless LAN frequencies, and plot the modal significances in Figure 19.

Notice that the conventional method for determining modal significance predicts four dominant modes. However, there is no feeding mechanism by which to practically excite these modes, making these dominant modes inaccessible. We can conclude that the modal significance in this case is of minimal practical use.

Conversely, using the newly defined formula for modal significance, we find that the spread of modal significance is quite wide, with no apparent dominant modes. This lack of dominant modes likely implies a lack of decent radiation abilities, as is the case for a basic unaltered PEC plate without an inherently obvious feeding mechanism.

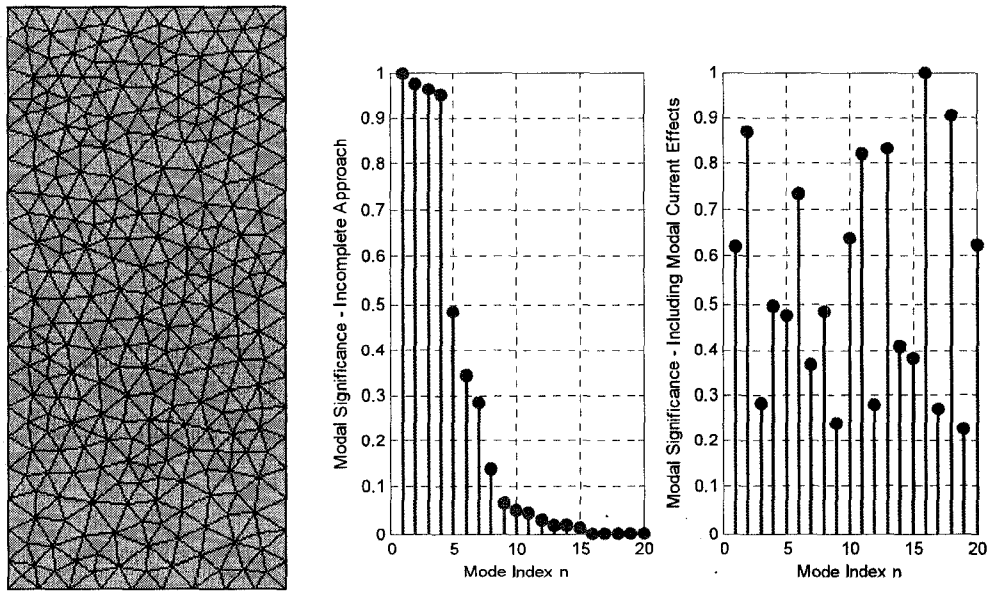

Figure 19 – Comparison of Modal Significances for Rectangular PEC Plate

If we introduce a half-wavelength slot, center fed, into the PEC plate, we are very clearly setting up a feed location on the structure under analysis. However, since the figure of merit does not define a feed location, we do not analyze the structure as though there were a feed. Nevertheless, we find the figures of merit as shown in figure 20.

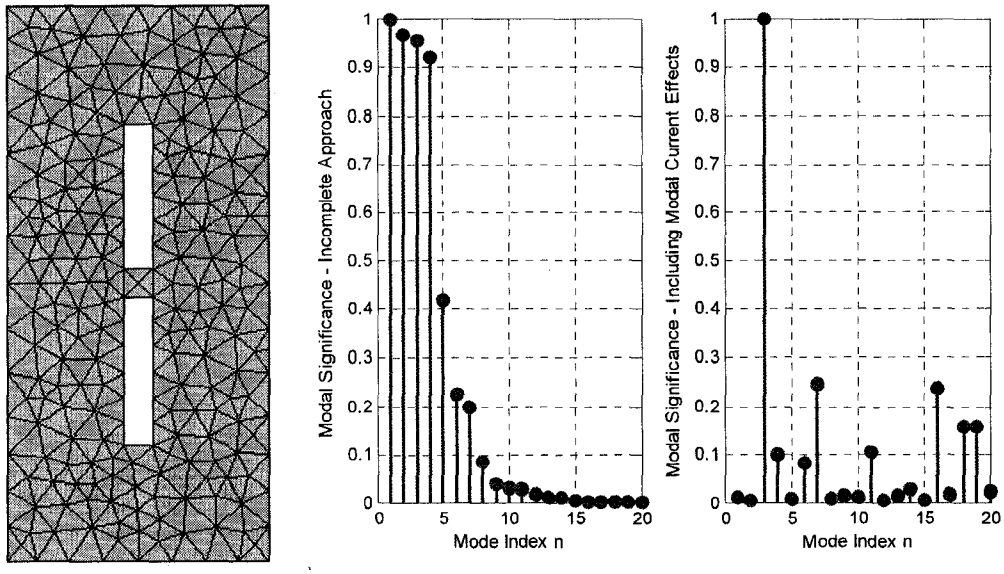

Figure 20– Comparison of Modal Significances for Rectangular PEC Plate with Added Slot

Because of the introduction of the slot, we find a dominant mode (mode 3) appears in the newly defined figure of merit. Conversely, in the original modal significance computation approach, one sees very little difference between the figures of merit of the unaltered plate and the plate with a slot. Notice that the incomplete approach predicts four dominant modes, whereas the new approach predicts a single mode, corresponding to the excitation of the slot antenna. Due to a lack of feeding mechanisms, three of the four modes are inaccessible. The new approach allows one to filter the modes in such a way that determines the modes that can practically be excited.

Keep in mind that we have not defined a feed location, yet we can predict to some degree that this structure has a dominant mode for radiation (mode 3) – something the original figure of merit *cannot* predict.

The reader might suggest that since we have analyzed a structure with a very obvious feeding location, the modal significance does not tell us anything new regarding the analyzed antenna. This statement is indeed true; however, one can envision relatively complicated structures where feed locations are not quite obvious, allowing one to quickly determine whether a structure has accessible mode(s) like the slot antenna or inaccessible modes like the unaltered PEC plate.

Furthermore, optimization routines can take advantage of the newly define modal significance, since optimizing the slot / plate combination such that mode 3 is as significant as possible while other modes remain insignificant would yield a structure with minimal stored energy, since higher order modes would be suppressed.

4.3.4 – Modal Significance of a Wideband Radiating Slot

Lastly, we consider a wideband radiating slot. We compute the modal significance of the wideband radiating slot at 1 GHz (within the operating bandwidth of the wideband slot) and compare the previously defined function to our newly defined modal significance as depicted in Figure 21.

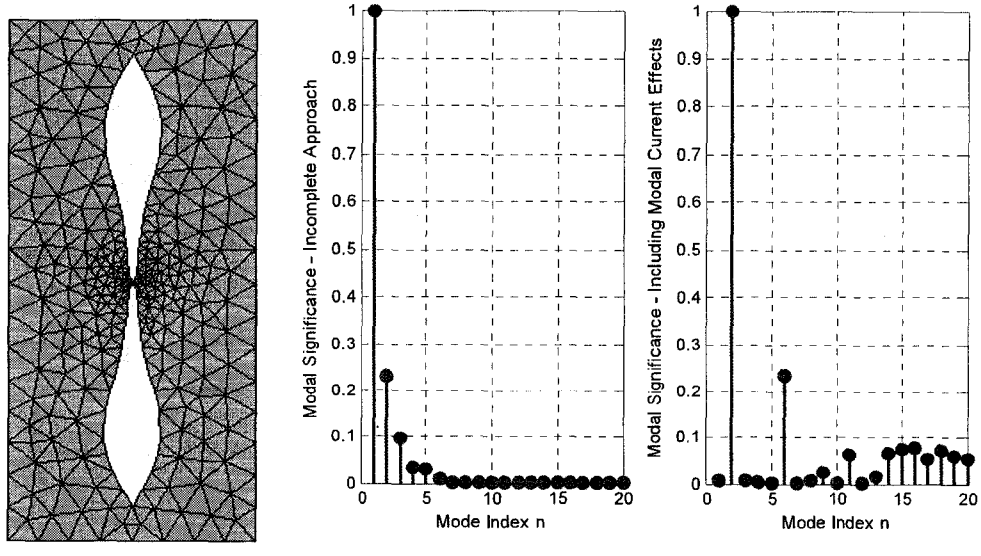

Figure 21– Comparison of Modal Significances for Wideband Radiating Slot

Quite surprisingly, the two approaches predict entirely different modal significance. What we claim as the incomplete approach considers mode 1 to be the most significant, while our newly defined function considers mode 2 to have the greatest significance. Furthermore, our approach even goes as far to say mode 1 is entirely insignificant for judging antenna performance. Obviously we need to sift out the details as to why this difference occurs. We begin our investigation by considering the modal surface currents and eigenvalues of modes 1 and 2, which is where the discrepancy lies. We plot the eigencurrents in dB scale as shown in Figure 22.

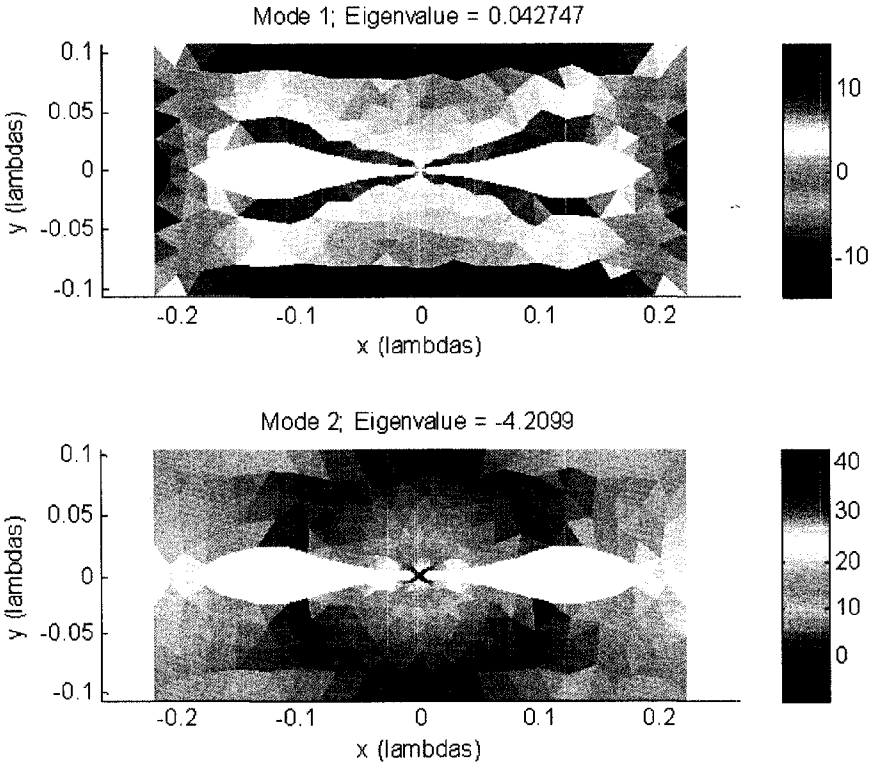

Figure 22 – First Two Low-Eigenvalue Characteristic Modes for Wideband Radiating Slot

Consider that mode 1 has a very low eigenvalue, nearly zero while mode 2 has a magnitude around 4.2. This is why the factor $1/\sqrt{1+\lambda_n^2}$ is so large for mode 1 compared to the same measurement of mode 2. Of equal importance we notice the scale of the normalized surface currents. Mode 1 has a normalized maximum current density of around 10dB while mode 2 is around 40 dB.

Finally, we note the location of the current density peaks on the surface of the radiator. The logical feeding location of this structure is the center gap where we find that mode 1 has a modal current of around 0 dB whereas mode 2 has a much larger 40 dB of current. Therefore, any practical use of this antenna would predominantly excite mode 2, while mode 1 would remain insignificant. This is where our modal significance definition is quite useful, as it predicts this exact phenomenon via: $\chi(n) = \max_{\bar{r}} \forall \left| J_n(\bar{r}) \right|^2 / \sqrt{1+\lambda_n^2}$

That being said, we do not imply mode 1 can never be excited. One can imagine incident radiation that would predominantly excite mode 1. However, this would make little difference at the antenna port since the modal currents are so low at this optimal feeding location. In this sense, it is likely that mode 1 can be excited but only from incident power in the nulls of the antenna, making very little power appear at the antenna terminals.

Additionally, if one considers elements that couple to this structure such as a dipole or a loop, then mode 1 can also become significant. This is the reason why handheld chassis play a significant role in radiation – not by their direct excitation, but rather, through the coupled excitation using separate radiating elements. Through the course of this thesis we shall consider modal excitation via direct excitation, as this method considers both the radiator and the feed in the design approach.

Taking stock of the discussion in the preceding section, we make the following conclusions:

- A low eigenvalue mode does not guarantee it is a "useful" mode, since it might be inaccessible via excitation. Ranking the characteristic modes by eigenvalue alone is not always an appropriate method of determining modal significance.
- This concept can be applied separately by considering the modal contributions to power radiated and net energy stored. One can then consider which modes contribute the most the radiated power (i.e. the modes we want to excite) and note the modes that store the most net energy (i.e. the modes we want to avoid). These figures of merit could easily be integrated into optimization routines.

4.4 – Parametric Study of PEC Rectangular Plates

We consider the lowest magnitude eigenvalue for various sizes of rectangular PEC plates, as shown in Figure 23. We vary the *area of the plate* and the *ratio of length to width* and plot the dominant lowest magnitude eigenvalue (log scale) in a 2D plot. We see an interesting set of curves, rings and regions where the eigenvalues are effectively zero. These regions we shall consider as externally resonant regions in which the given plate dimensions yield (at the very least) a single dominant eigenvalue for radiation (albeit more than one dominant eigenvalue can exist). We also note that two distinct regions are immediately obvious: region 1 has eigenvalues that are mostly greater than 0 dB in magnitude, where region 2 has the majority of eigenvalues less than 0 dB. Separating these two regions is a braided curve representing resonant modes. These two regions can be thought of as the fundamental limits of energy storage versus radiation for the possible dimensions of PEC plates. Furthermore, results such as these can be used as a design guide, since plates in region 1 at resonance would be far more sensitive to frequency changes than region 2, since the eigenvalues are mostly large in magnitude.

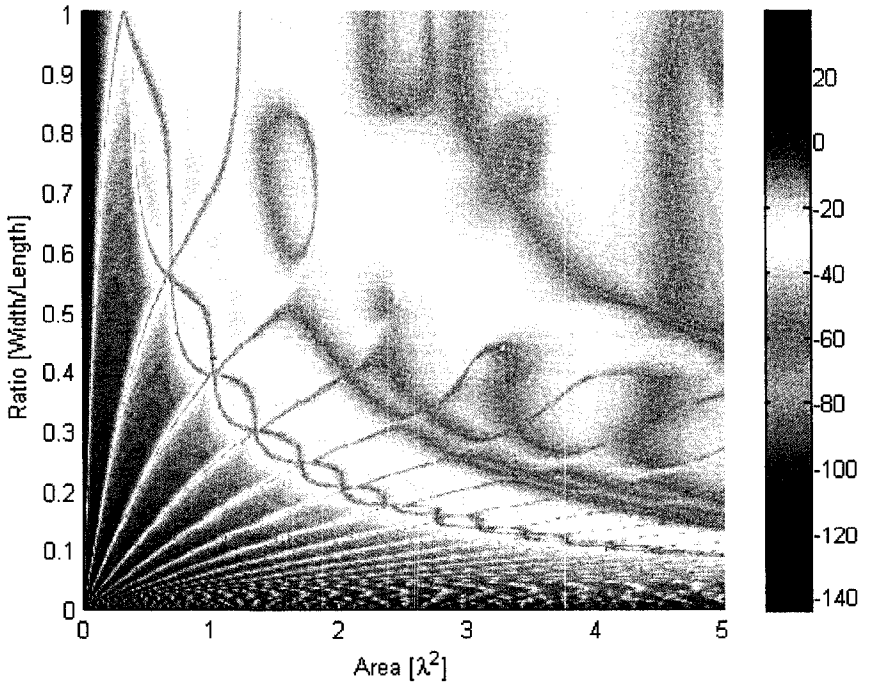

Figure 23 – Parametric Analysis of the Eigenvalues of Perfectly Conducting Plates

4.5 – Characteristic Modes of Lossy Conductors

We conclude our investigation of modal significance with a look at the properties of lossy characteristic modes. No longer are the eigenvalues purely real in the lossy formulation. The real part maintains the same meaning as the PEC modes, but an imaginary part materializes, being proportional to the radiation efficiency of the mode.

The plate size we consider is 111mm x 61mm operating at 2.5 GHz, which represents the typical size of a handheld mobile device. Firstly, we consider the characteristic modes of the PEC plate in Figure 24. Next we consider the modes of a finite conductivity plate. We choose the conductivity to be that of copper: $\sigma = 5.8 \times 10^7$ S/m and simulate the corresponding lossy modes as shown in Figure 25. From visual inspection alone, the lossy modes appear identical to the PEC classical characteristic modes. The modal current magnitudes are similar, as well as the real parts of the eigenvalues. We summarize these results in Table 2.

Table 2 – Comparison between Classical and Lossy Eigenvalues for Wide Plate

	Eigenvalue Mode 1	Eigenvalue Mode 2	Eigenvalue Mode 3	Eigenvalue Mode 4	Eigenvalue Mode 5	Eigenvalue Mode 6
PEC	-0.18108	0.27182	-0.30632	-0.32732	1.7989	-3.9180
Copper	-0.18018 -9E-4i	0.27223 -4.1E-4i	-0.30571 -6.1E-4i	-0.32627 -1.04E-3i	1.7999 - 1E-3i	-3.9142 -3.8E-3i

We see two trends appear. Firstly, the real part of the eigenvalues does not change drastically. They do however all see a positive increase, which is due to the reactive loading (inductive) that ohmic losses introduce to the surface. Regardless, the change is minor, implying very little difference between the PEC and lossy case in terms of excitation of modes for the unaltered plate. Secondly, the imaginary part of the eigenvalue is always negative, as it should be, and is extremely small. This implies the lossy modes have relatively high radiation efficiency. Furthermore, there is a tendency

for the imaginary part to increase as the mode order increases, implying that mode radiation efficiency decreases for the higher order modes. The efficiency varies between 99.91% and 99.62%.

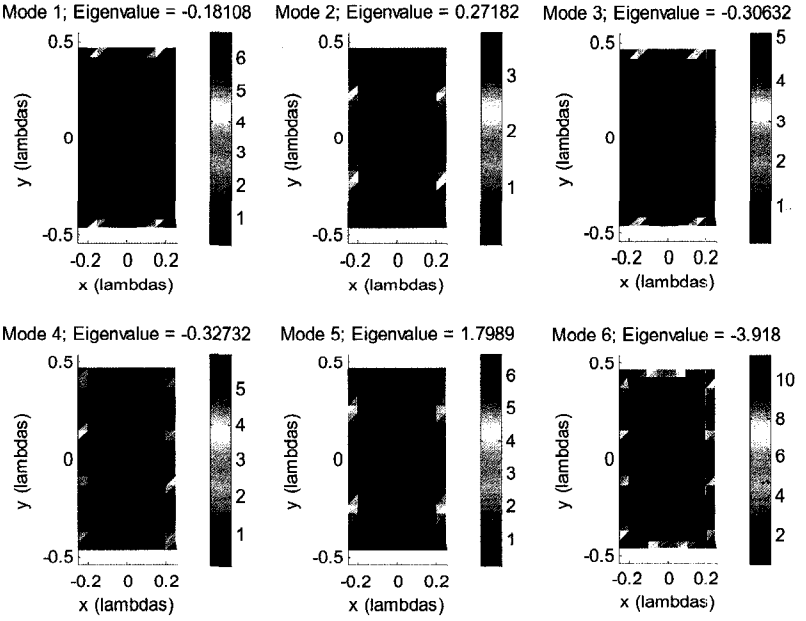

Figure 24 – Characteristic Mode Currents for Wide Plate

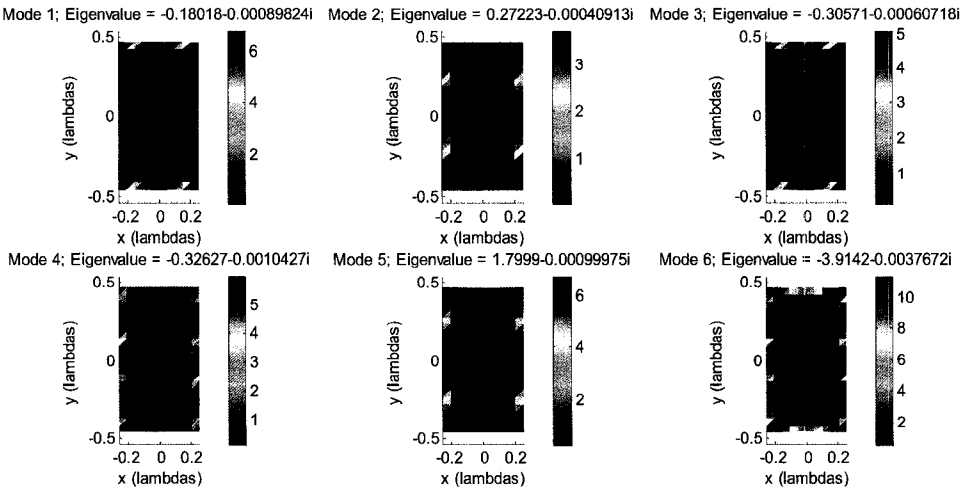

Figure 25 – Lossy Characteristic Mode Currents for Wide Plate

We see another reason to use our newly defined modal significance function. If one were to take this finite conductivity plate, and attempt to excite it using a voltage gap feed, one would expect to find very low input resistance and possibly very low radiation efficiency. Simulating this finite conductivity plate and determining the highest achievable efficiency using voltage gap feeds, one finds this to be the case as a maximum radiation efficiency of 80% is achieved.

Yet when one considers the first six modes as shown, one would say the efficiency should be quite high since their efficiencies are 99.6% or higher. Where does the discrepancy occur? Clearly the eigenvalues do not tell the entire tale – enter the properly defined modal significance definition.

If one refers back to section 4.3.3 where we considered a PEC plate of equal dimension, note how in reality many higher order modes are significant in terms of antenna performance. We therefore compute the eigenvalues, specifically showing the modal efficiency derived from the eigenvalue as shown in Figure 26.

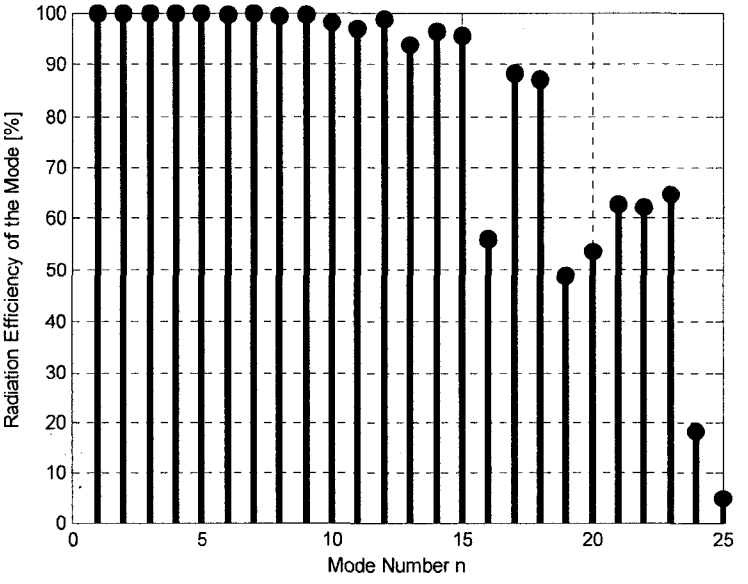

Figure 26 – Modal Radiation Efficiencies of Rectangular Plate

Notice that the higher order modes, specifically starting around mode 16 and later have very low radiation efficiencies. Referring back to Figure 26, we find mode 16 is a significant mode for the plate with the modal efficiency below 60%. Any significant excitation of this mode will certainly result in appreciable radiation losses. We have therefore shown when introducing losses, modes that would be judged insignificant solely by their eigenvalue are in fact major contributors to radiation losses.

4.6 – Concluding Remarks

In this chapter we have derived a fundamentally important figure of merit, which we denoted as the modal significance. As derived in section 4.2, one can use this measurement quantity to compute the significance of characteristic modes in terms of antenna performance. This performance can be categorized as significance for radiated power, net stored energy or a combination of both. The newly defined figure of merit was applied to various canonical antennas, where we showed the modal significance predicted well known results, but also showed that some higher-order modes, previously deemed negligible, are in fact important to fully describe antenna performance.

Most importantly, in section 4.3, we applied the modal significance concept to a wideband radiating slot, and found the modal significance as defined in the literature incorrectly predicts a single dominant mode that is entirely inaccessible via excitation. On the other hand, the newly defined modal significance correctly predicts the significance of a higher-order mode that despite its larger eigenvalue is the true dominant characteristic mode of the antenna structure.

Furthermore, we applied this concept to the characteristic modes of lossy structures in section 4.5, and found the same insufficient nature of the eigenvalues alone at predicting antenna properties. We observed low radiation efficiency for a particular antenna, and noted the responsible modes are higher order modes that would otherwise be deemed insignificant, further showing the usefulness of a well defined modal significance.

Chapter 4 References

[1] R.F. Harrington, J Mautz, "Theory of Characteristic Modes for Conducting Bodies", *IEEE Transactions on Antennas and Propagation*, Vol. AP-19, No. 5, Sept 1971.

[2] M. Cabedo-Fabres, E. Antonino-Daviu, A. Valero-Nogueira, M. Bataller, "The Theory of Characteristic Modes Revisited: A Contribution to the Design of Antennas for Modern Applications," *IEEE Antennas and Propagation Magazine*, Vol. 49, No. 5, October 2007.

[3] M. Cabedo-Fabres, E. Antonino-Daviu, A. Valero-Nogueira, M. Bataller, "On the Application of Characteristic Modes for the Analysis of Large Scale Antenna Problems," *EuCAP 2007, 2nd European Conference on Antennas and Propagation,* pp. 1-7, November 2007.

Chapter 5

Characteristic Mode Theory Applied to MIMO Antenna Design

5.1 – Introduction

The goal of this chapter is to control the excitation of characteristic modes of perfectly conducting structures, for the expressed purpose of MIMO antenna design. Thus far, the literature has discussed analyzing objects for their suitability as good radiators [1], considered the use of discrete loading to optimize scattering [2], determined the optimal surfaces that have externally resonant modes [3] and performed comprehensive analysis on various conducting shapes and sizes [4]. Furthermore, there have been numerous successful attempts at optimizing pattern synthesis techniques using antenna arrays [5, 6, 7]. Recently, a great deal of research has been performed on the analysis of handheld and mobile chassis using conventional antenna analysis techniques as well as characteristic mode approaches. The discussions in the literature consider determining the frequencies in which mobile chassis' resonate [8] as well as pointing out the availability of multiple low eigenvalue modes at wireless frequencies [9]. In a more recent paper by Chaudhury & Schroeder [10] an attempt is made to excite the characteristic modes of a conducting plate, but shows a difficulty in obtaining reasonable impedance bandwidth. More importantly, the claims of exciting individual characteristic modes are questionable given the complete lack of evidence in the paper. What we wish to accomplish in this chapter is the *intentional* control of characteristic modes for the expressed purpose of MIMO antenna design and show unquestionably that we are exciting individual or groups of unique characteristic modes.

In section 5.2 we shall investigate the properties of characteristic modes that lead to direct application in MIMO antenna design, namely the far-field orthogonality of the modes. We show that if one can design a set of antennas where each antenna excites a unique set of CMs (among the possible CMs of the structure) far-field orthogonality and thus zero envelope correlation is maintained between all antennas pairs. We also derive a very useful expression where one can compute envelope correlation in terms of modal quantities. We will then consider typical mobile phone chassis in section 5.3.

After deciding on the physical model of the cell phone chassis, we analyze the characteristic modes of said chassis in section 5.4. In this section we will compute the CMs, consider their eigenvalues and most importantly, their surface current distributions. From their modal current distributions, we will outline a very straightforward method one can use to excite particular CMs of interest, based solely on the locations of modal current maxima. In section 5.4, we will use voltage gaps to excite the modes of the mobile phone chassis, but recognize that the input resistance is too low and input reactance too large. A solution is discussed in section 5.5 by extending the voltage gap in the form of a slot, thereby improving impedance matching significantly, while still maintaining the desirable modal excitation properties. These slots are meticulously placed in a structured manner, as outlined in section 5.6, using the modal properties in each step. We conclude by generalizing the methodology and summarize the findings with a step by step approach. Additionally, an interesting alternative route to modal control is discussed section 5.7, where one can take advantage of physical symmetry, exciting similar modes but still maintaining far-field orthogonality.

Lastly, in section 5.8 we consider four example designs applying the newly developed modal design approach. We first consider a MIMO antenna design on a bar-type mobile phone chassis. We next consider an alternative design using a similar chassis, only with different antenna structures, showing that the method is not limited to only slot antennas. We subsequently consider a design building on the modal symmetries derived in section 5.7. We conclude with a MIMO antenna design example where the starting structure involves an arbitrarily shaped structure and designing a set of ideal MIMO antennas.

5.2 – Characteristic Modes and MIMO

The most important property derived from the theory of characteristic modes (for our purposes) is that the individual modes have far-field patterns that are mutually orthogonal over the sphere at infinity. This property can be expressed as:

$$\frac{1}{\eta}\oiint_{S\infty}\underline{E}_m\cdot\underline{E}_n^*\cdot dS=\delta_{mn} \tag{5.2-1}$$

where Em and En are the m'th and n'th characteristic mode fields generated by the surface current Jm and Jn, respectively.

Let us assume we excite an arbitrary surface S using two distinct feeding mechanisms. Assume also that the first feeding mechanism excites the set of modes A and the second excites the set of modes B. Let us denote the far-field patterns expanded in terms of modal fields, which is possible by the orthogonality property, in the following way:

$$E_A=\alpha_{A1}E_{A1}+\alpha_{A2}E_{A2}+\ldots+\alpha_{AN}E_{AN}=\sum_{n=1}^{N}\alpha_{An}E_{An} \tag{5.2-2a}$$

$$E_B=\alpha_{B1}E_{B1}+\alpha_{B2}E_{B2}+\ldots+\alpha_{BN}E_{BN}=\sum_{n=1}^{N}\alpha_{Bn}E_{Bn} \tag{5.2-2b}$$

Each collection of modes $\{A_1, A_2, \ldots A_N\}$ and $\{B_1, B_2, \ldots B_N\}$ refer to uniquely indexed characteristic modes. Let us now consider the integration of E_A and E_B over the sphere at infinity, in the following integral:

$$\frac{1}{\eta}\oiint_{S_\infty}\underline{E}_A\cdot\underline{E}_B^*dS \tag{5.2-3}$$

If we make the substitution for E_A and E_B into the above integral, we find:

$$\frac{1}{\eta}\oiint_{S_\infty}\left(\alpha_{A1}E_{A1}+\alpha_{A2}E_{A2}+\ldots+\alpha_{AN}E_{AN}\right)\cdot\left(\alpha_{B1}E_{B1}+\alpha_{B2}E_{B2}+\ldots+\alpha_{BN}E_{BN}\right)^*dS \tag{5.2-4}$$

By considering the expansion of the multiplications term by term, we then have the following integrals:

$$\frac{1}{\eta}\iint_{S_\infty}\alpha_{A1}E_{A1}\left(\alpha_{B1}E_{B1}\right)^{*}dS+\frac{1}{\eta}\iint_{S_\infty}\alpha_{A1}E_{A1}\left(\alpha_{B2}E_{B2}\right)^{*}dS+\ldots \tag{5.2-5}$$
$$+\frac{1}{\eta}\iint_{S_\infty}\alpha_{A2}E_{A2}\left(\alpha_{B1}E_{B1}\right)^{*}dS+\ldots+\frac{1}{\eta}\iint_{S_\infty}\alpha_{AN}E_{AN}\left(\alpha_{BN}E_{BN}\right)^{*}dS$$

Notice that the paired subscript for each integral will never share the same integer, and hence Equation 5.2-1 the sum of the above integrals is precisely zero. This conclusion can be argued from practical reasoning: since integration is a linear operator, and the modes are orthogonal, then unique sets of modes are also mutually orthogonal.

This shows that two (or more) unique sets of characteristic modes are mutually orthogonal. This is precisely what drives us to control the characteristic modes as the excitation of unique sets of modes will yield antenna patterns that are orthogonal over the sphere at infinity: an attractive property for MIMO antenna design.

Let us now turn to the expression for envelope correlation in terms of far-field patterns, derived in Chapter 2:

$$\rho_e\left(i,j,N\right)=\frac{\left|\iint_{4\pi}\left[F_i\left(\theta,\phi\right)\bullet F_j^{*}\left(\theta,\phi\right)\right]d\Omega\right|^2}{\iint_{4\pi}\left|F_i\left(\theta,\phi\right)\right|^2 d\Omega\iint_{4\pi}\left|F_j\left(\theta,\phi\right)\right|^2 d\Omega} \tag{5.2-6}$$

We recognize that any far-field pattern can be expanded in terms of the characteristic mode fields. This property can be expressed as:

$$F_i\left(\theta,\phi\right)=\sum_{n=1}^{N}\alpha_{n,i}E_n\left(\theta,\phi\right) \tag{5.2-7}$$

If we substitute this field expansion into the numerator of the envelope correlation Equation 5.2-6, we find the following:

$$\left|\iint_{4\pi}\left[F_i(\theta,\phi)\bullet F_j^*(\theta,\phi)\right]d\Omega\right|^2=\left|\iint_{4\pi}\left[\left(\sum_{n=1}^{N}\alpha_{n,i}E_n(\theta,\phi)\right)\bullet\left(\sum_{n=1}^{N}\alpha_{n,j}^*E_n^*(\theta,\phi)\right)\right]d\Omega\right|^2 \quad (5.2\text{-}8)$$

Since the modes exist on the same structure (or equivalently in the same system) we can easily show that the dot product between summations can be greatly simplified. The integration is zero whenever the value of n between the two summations is not the same, due to orthogonality of the modal fields.

$$\begin{aligned}\left|\iint_{4\pi}\left[F_i(\theta,\phi)\bullet F_j^*(\theta,\phi)\right]d\Omega\right|^2&=\left|\iint_{4\pi}\left[\left(\sum_{n=1}^{N}\alpha_{n,i}E_n(\theta,\phi)\right)\bullet\left(\sum_{n=1}^{N}\alpha_{n,j}^*E_n^*(\theta,\phi)\right)\right]d\Omega\right|^2\\&=\left|\alpha_{1,i}\alpha_{1,j}^*\iint_{4\pi}|E_1|^2\,d\Omega+\alpha_{2,i}\alpha_{2,j}^*\iint_{4\pi}|E_2|^2\,d\Omega+\ldots+\alpha_{N,i}\alpha_{N,j}^*\iint_{4\pi}|E_N|^2\,d\Omega\right|^2\\&=\eta^2\left|\sum_{n=1}^{N}\alpha_{n,i}\alpha_{n,j}^*\right|^2\end{aligned} \quad (5.2\text{-}9)$$

If we then consider the denominator of the expression for envelope correlation, we find:

$$\iint_{4\pi}|F_i(\theta,\phi)|^2\,d\Omega\iint_{4\pi}|F_j(\theta,\phi)|^2\,d\Omega=$$
$$\eta\left(\sum_{n=1}^{N}|\alpha_{n,i}|^2\right)\eta\left(\sum_{n=1}^{N}|\alpha_{n,j}|^2\right)=\eta^2\left(\sum_{n=1}^{N}|\alpha_{n,i}|^2\right)\left(\sum_{n=1}^{N}|\alpha_{n,j}|^2\right) \quad (5.2\text{-}10)$$

Combining the expressions for numerator and denominator, we find the expression for envelope correlation written in terms of characteristic modal quantities as:

$$\rho_e(i,j)=\frac{\left|\sum_{n=1}^{N}\alpha_{n,i}\alpha_{n,j}^*\right|^2}{\sum_{n=1}^{N}|\alpha_{n,i}|^2\sum_{n=1}^{N}|\alpha_{n,j}|^2} \quad (5.2\text{-}11)$$

where $\alpha_{n,i}$ and $\alpha_{n,j}$ are the modal current excitation factors for the ith and jth excitation. This expression has significant implications for MIMO antenna design. Simply stated, we find that the envelope correlation is minimized if the numerator of Equation 5.2-11, i.e. the expression $\left|\sum_{n=1}^{N}\alpha_{n,i}\alpha_{n,j}^*\right|^2=0$, is also minimized. If the modes excited by the ith and

j^{th} excitation are unique, that is to say the modal indices attributed to the i^{th} and j^{th} excitation do not overlap, then the numerator $\left|\sum_{n=1}^{N}\alpha_{n,i}\alpha_{n,j}^{*}\right|^{2}=0$ is zero and hence envelope correlation is zero between antennas. This is the precise reason for using characteristic mode analysis for the purposes of MIMO antenna design.

Notice also that Equation 5.2-11 is very similar in form to Equation 2.2-10 which computes envelope correlation in terms of S-parameters. The limitation of the S-parameters method is that is breaks down in the presence of antenna losses [11], where as the newly defined expression for correlation Equation 5.2-11 holds for both lossless and lossy structures, provided the modal formulation includes the effects of losses.

That being said, the S-parameter method is still an excellent practical approach for antennas with low loss, as it can be used to estimate envelope correlation without measuring field quantities. It is important to note that the far-field orthogonality must be measured as embedded patterns, that is to say, the ports must be properly terminated and then the patterns measured for orthogonality.

There is another distinct advantage to using characteristic mode analysis that involves conclusions one can make about the effect of termination. If two feeds each distinctly excite unique sets of characteristic modes, we know that the surface currents generated by one feed will not generate appreciable currents at other feeds. This fact is evident by the definition of modal excitation: $V_n^i=\oiint_S J_n\cdot E_{\tan}^i dS=\left\langle J_n,E_{\tan}^i\right\rangle$ where E_{tan} is the impressed tangential electric which can then be converted into an equivalent voltage source that excites the chosen feed location. If an excitation does not excite a particular mode J_n, it immediately implies that the surface current J_n must be zero (or negligible) at the defined feed. Thus, the introduction of port termination does not significantly affect a system that excites unique sets of characteristic modes. This is equivalent to saying that a system with negligible *mutual coupling* for a given choice of termination will have low *mutual coupling* for all choices of termination. That is not to say input reflection coefficients will be independent of termination – only the cross-terms S-parameters.

5.3 – The Mobile Phone Chassis

We begin with the simplest possible chassis design: a perfectly conducting plate. The plate represents the ground plane or structural supporting plate in a handheld device. The approach is clearly an approximation, since we do not consider the obvious effects of having onboard electronics, RF shielding, the handheld plastic casing and the users' head and hands. However, one must begin with the simplest case to build a thorough understanding of the problem at hand. Some example mobile phone dimensions are shown in Table 3. We choose an operating frequency of 2.5 GHz as this represents the most likely carrier frequency for next generation handheld devices. As with most antenna devices, a minor change in frequency (for example, down to 2.4 GHz) will result in a direct linear scaling of the device dimensions, making the precise frequency we design at less of an issue. While we are considering perfectly conducting plates that represent cell phone chassis, one can imagine these chassis can represent other devices such as laptops, PDAs and any electronic device in which MIMO is an attractive communications protocol. It can also be stated that the methodologies developed in this thesis can be applied to base stations, mobile vehicles and the like since the theory is general and not specific the handheld devices.

Table 3 – Chassis Dimensions for Common Mobile Phones

Wide Plate	Narrow Plate	Flip-Phone
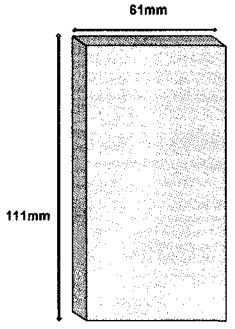	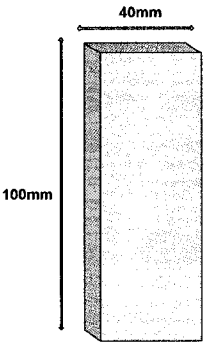	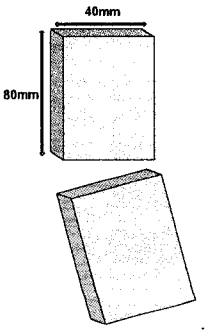
Real-world examples:	*Real-world example:*	*Real-world examples:*
iPhone, Blackberry	Samsung SGH-T629	Nokia v186, Razr i3

5.4 – Modal Control of Perfectly Conducting Plates

Let us consider the characteristic modes of a perfectly conducting rectangular plate, with dimensions representative of current popular handheld communications / media devices.

Physical Dimensions of Plate: 111mm x 61mm

Electrical Dimensions of Plate: $0.925\lambda \times 0.508\lambda$ (2.5 GHz)

We begin our analysis by computing the first six characteristic modes of the aforementioned PEC plate. The surface current density, with units of [A/m], is plotted in Figure 27.

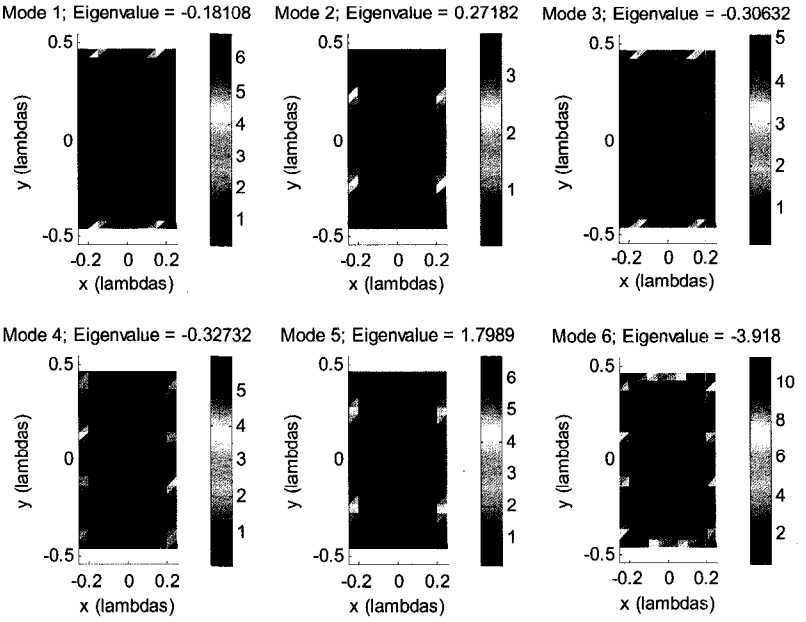

Figure 27 – Characteristic Modes of PEC Plate, Example #1, Current in Linear

We see that the surface currents are predominant in magnitude along the edges of the plate. This is as expected, given the well known edge condition of surface currents. The total surface area is approximately $0.47\lambda^2$, with a total mesh density equal to 400 triangles. This yields a triangle surface area of $0.001\lambda^2$ / triangle, which meets the required mesh density, as determined in Chapter 3.

We shall consider developing a modal control scheme using the perfectly conducting plate. The theory we develop will be general enough such that it can be applied to any reasonably shaped conducting surface.

All excitation methods will utilize voltage gaps. The gap will have an arbitrary potential applied, with a measurable input current. Together, these two quantities yield the input impedance attributed to the port. Furthermore, by setting the excitation of the gap we also have the ability to compute the relative excitations of each characteristic mode. By knowing the "spectrum" of modes being excited, we are able to ascertain how well single or unique groups of modes are being controlled and excited.

In Figure 28 we consider the modes of the conducting plate and emphasize the locations of each mode where the current is maximum, and where it is believed the modes will be predominantly excited.

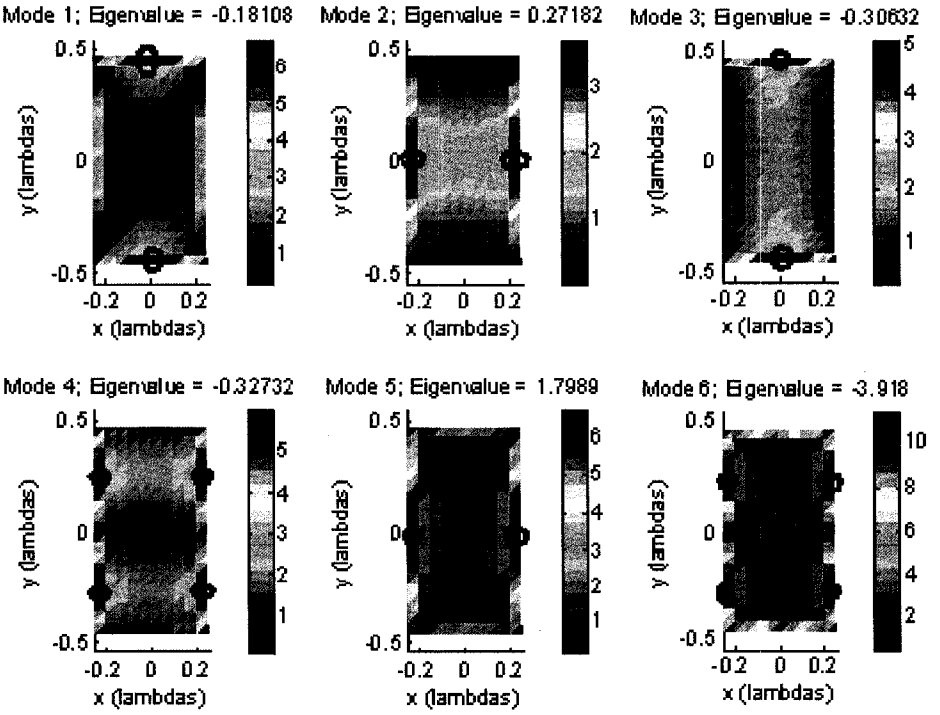

Figure 28 – Ideal Modal Excitation Locations for Design Example #1, Current in Linear

From Figure 28 we find the following properties:

- Modes 1 & 3, 2 & 5, and modes 4 and 6 in a pair wise manner share similar modal current maximum, and thus potentially similar modal excitations.

- Notice that Mode 1 also shares similarities with Modes 2 and 5. We would therefore expect interactions between the feeding mechanisms that excite mode 1 and 3 and the mechanisms that excite modes 2 and 5.

We would therefore expect to be capable of exciting three unique 'sets' of modes, given the nature of the current distributions. We shall denote modes 1 and 3 as Set #1, modes 2 and 4 as Set #2 and modes 3 and 6 as Set #3.

In order to excite the perfectly conducting plate, we use feeds in the form of voltage gaps. It is simple a feed mechanism that forces the tangential electric field over the gap to be a specific value. In a sense, it is very similar to an aperture problem, albeit an electrically small aperture.

An example voltage gap feed can be visualized in Figure 29. All feeding mechanisms in this section, as well as throughout the thesis will use a similar format. This method allows for a very simple feeding structure that can easily be moved without actually changing the physical device. It is important to note that this feeding mechanism can be implemented in practice using a coaxial cable, with the inner conductor connected to one edge, and the outer conductor to the remaining edge. If the coax and connector are electrically small relative to the antenna, then the cable can be connected directly. When the feed mechanism becomes comparable to the antenna size, as is often the case for dipole antennas, a balun is required to prevent the feed network from radiating.

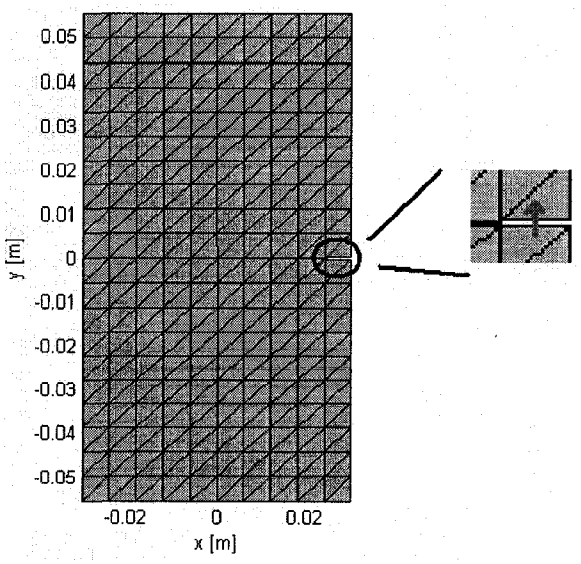

Figure 29 – Voltage Gap Model

Feeding the top and bottom edges of the plate shown in Figure 28 we expect to excite mode 1 and 3. We first attempt to excite only one edge at a time as shown in Figure 30 (a) – (b). We see exactly what we expect: mode 1 and 3 predominantly excited. Notice that mode 6 and 7 are also excited but these are higher order modes with much smaller excitation coefficients that we will neglect for arguments sake. Let us now consider the simultaneously excitation of both the top and bottom feeds, considering both the in-phase excitation Figure 30 (c) and 180° out of phase excitation Figure 30 (d). We find excitation in phase yields the predominant and near perfect unique excitation of mode 1, whereas out-of-phase yields predominantly excites mode 3.

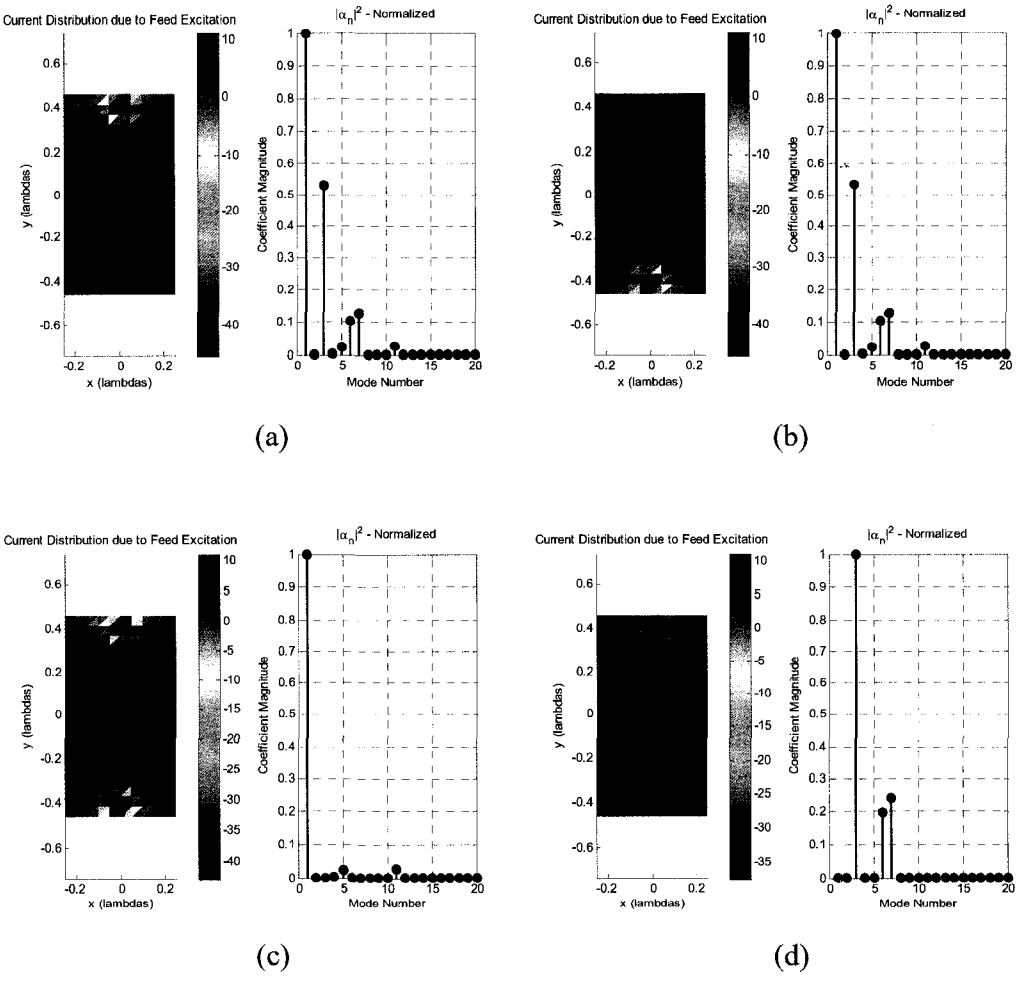

Figure 30 – Rectangular Plate Excited via Voltage Gap, (a) Top Edge, (b) Bottom Edge, (c) Both Edges, In Phase, (d) Both Edges, 180° Out of phase.

We perform similar simulations, only we now consider the left and right edges of the plate (long edges), as shown in Figure 31. We now see modes 1, 2 and 5 predominantly excited. We also consider the simultaneous excitation of the edges. We see mode 2 is predominantly excited via in-phase feeds, and mode 1 and 5 through out of phase feeding. Of interest here is to point out that out of phase excitation for the side edges excites mode 1 which conflicts with the resulting modal excitation of the top / bottom excitation in phase since it excites mode 1 as well. However, other combinations clearly exist where there is no overlap between which modes are excited.

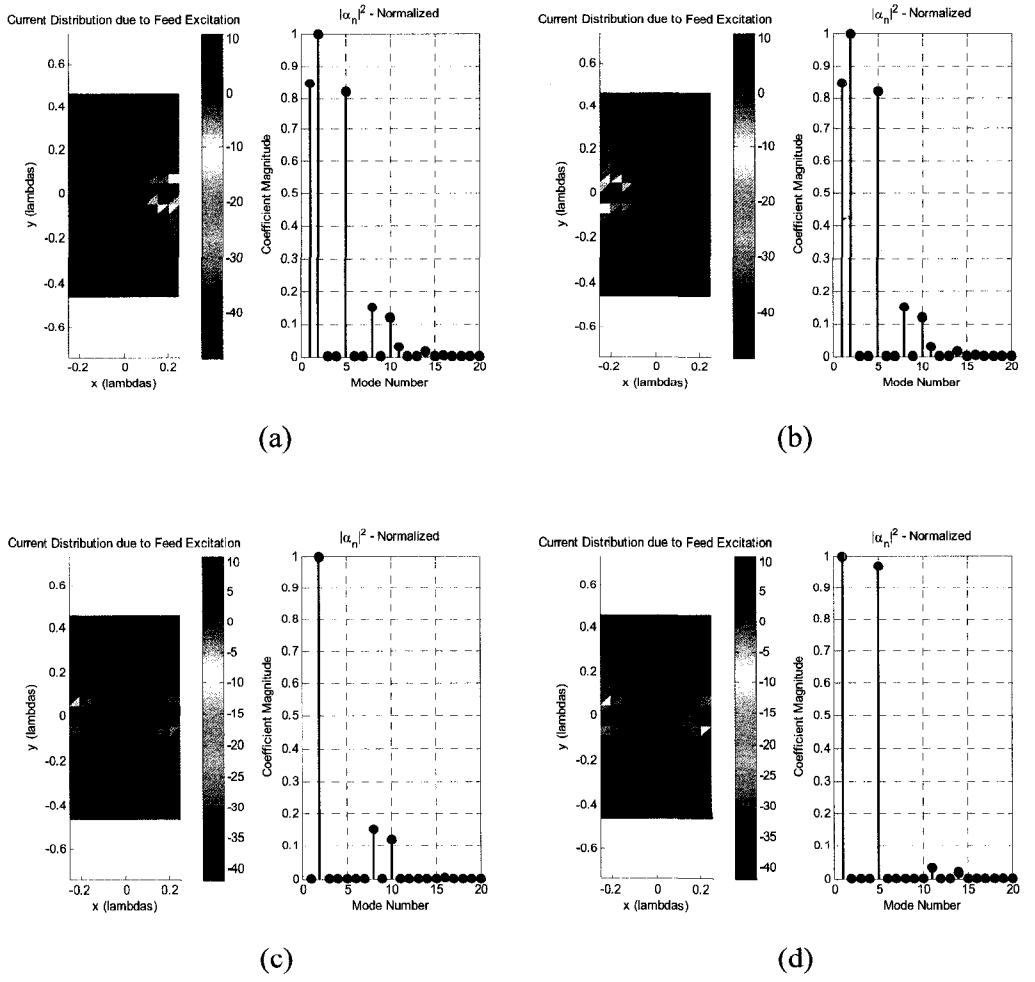

Figure 31– Rectangular Plate Excited via Voltage Gap, (a) Right Edge, (b) Left Edge, (c) Both Edges, In Phase, (d) Both Edges, 180° Out of phase.

Another set of feeding locations are possible as evident in the current distribution of mode 4 in Figure 32. We shall denote these locations as the diagonal feed positions. Regardless of the chosen feed location of the four diagonal positions, we see the same excitation of mode 4. This is an obvious result from symmetry considerations.

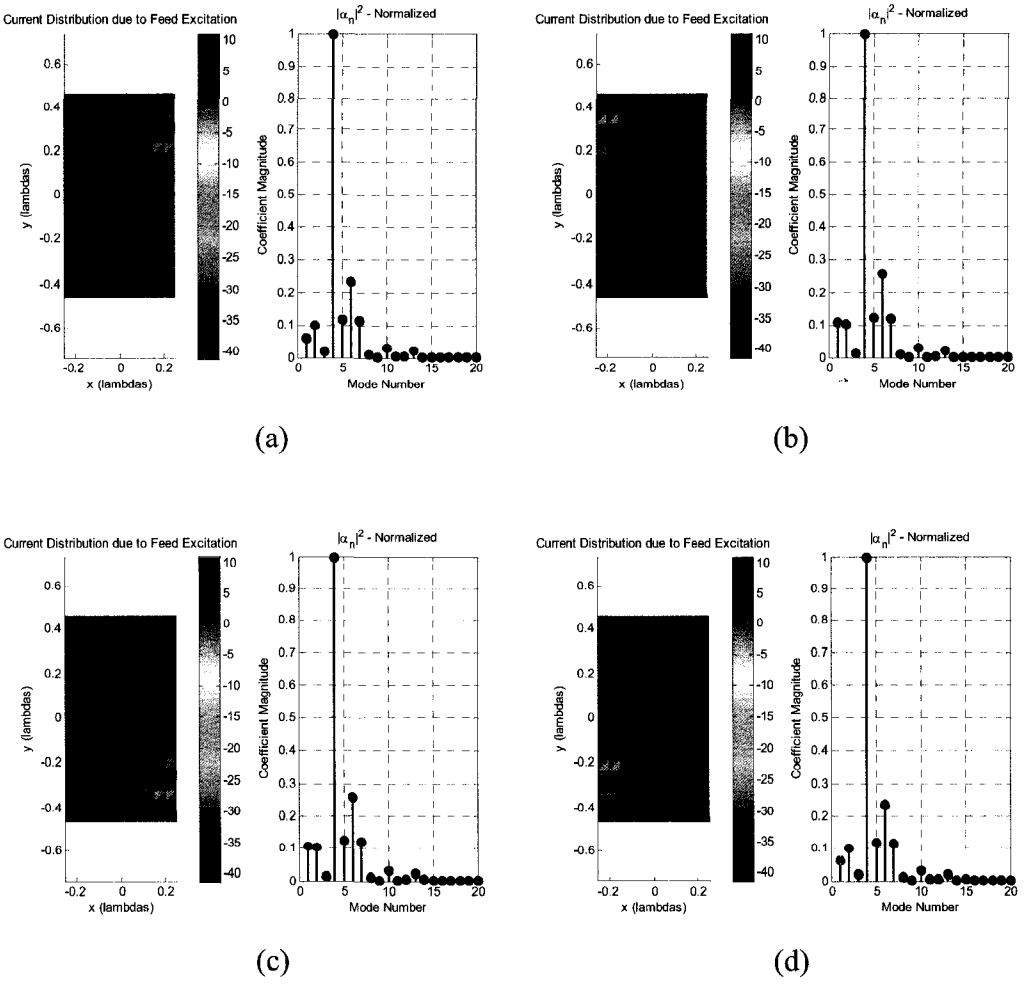

Figure 32– Rectangular Plate Excited via Voltage Gap, (a) Diagonal Top Right Edge, (b) Diagonal Top Left Edge, (c) Diagonal Bottom Right Edge, (d) Diagonal Bottom Left Edge

We also consider the simultaneous feeding in pairs, in phase as shown in Figure 33 (a),(c),(e) and 180° out of phase in Figure 33 (b),(d),(f). Single modes excitations can be seen in Figure 33 (a), (c) and (f).

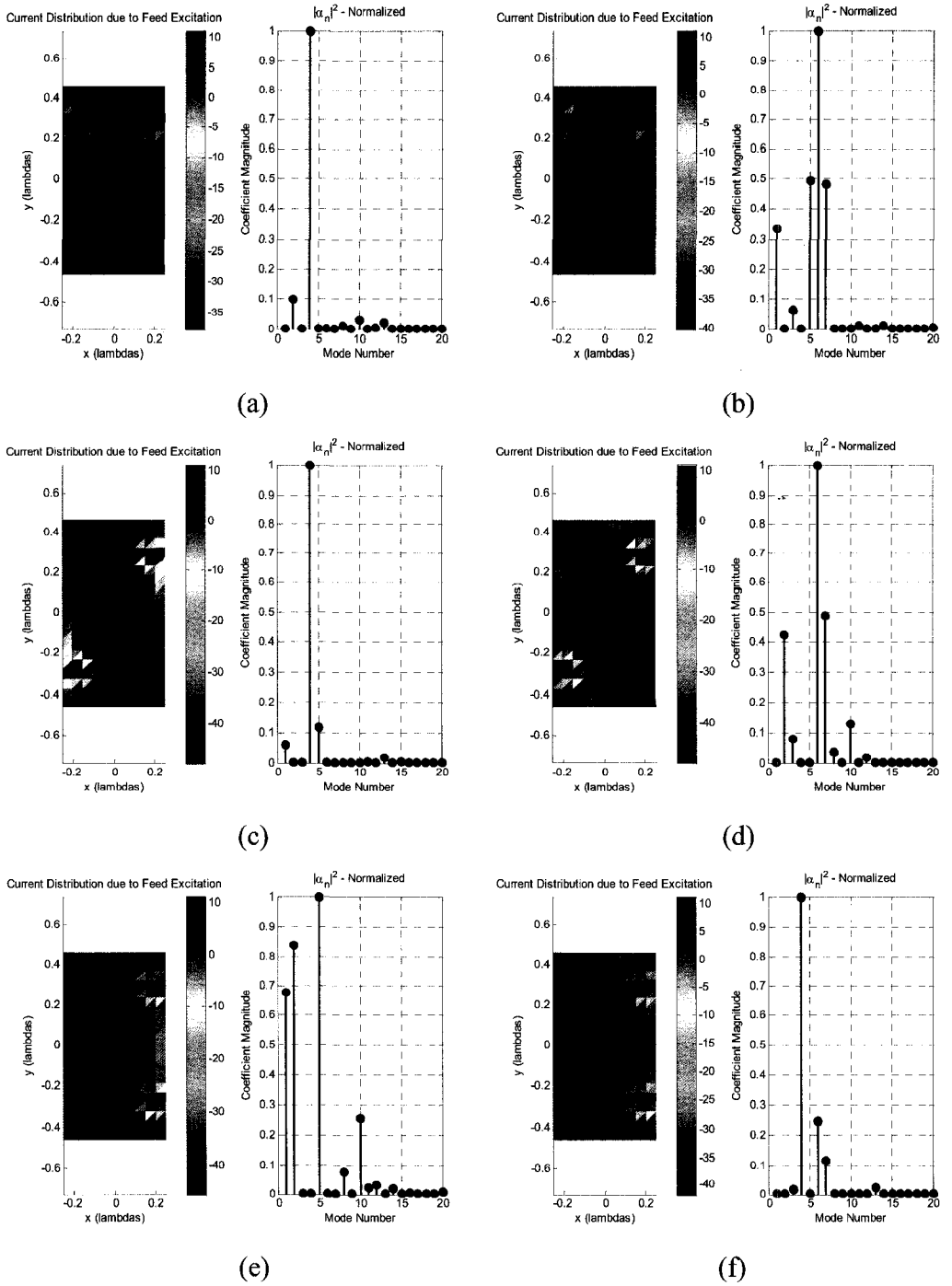

Figure 33– Rect. Plate Voltage Gap, (a) Both Top In Phase, (b) Both Top 180° Phase, (c) Both Diagonal In Phase, (d) Both Diagonal 180° Phase, (e) Both Edge In Phase, (f) Both Edge 180° Phase

We summarize these finding in Table 4, listing the relevant modal excitations, orientations and input impedances. As the above table shows, it is possible to excite unique sets of characteristic modes using the appropriate feeding locations and orientations. One possible antenna excitation scheme would be to operate three simultaneous feeding layouts (antennas) as follows:

- **Antenna #1**: Excite Top / Bottom using the opposite orientation, yielding a dominant Mode 1, Secondary Mode 5 and 11
- **Antenna #2**: Excite Left / Right using the same orientation, yielding a dominant mode 2, Secondary Mode 8, 10 and 16
- **Antenna #3**: Excite the diagonals using the same orientation, yielding a dominant mode 4, Secondary Mode 2 and 13.

Notice that each feeding scheme and hence antenna excites a unique set of characteristic modes. This invariably leads to far-field orthogonality of the antenna patterns.

Table 4 – Summary of Unaltered Plate Excitation via Dual Voltage Gaps

Set of Ports	Orientation	Dom. Modes	Sec. Modes	Input Impedance
Left / Right	Same	2	8, 10, 16	3.20 + 71.68i
Left / Right	Opposite	1 + 5	11, 14	4.18 + 70.7i
Top / Bottom	Opposite	1	5, 11	7.25 + 70.05i
Top / Bottom	Same	3	6, 7	5.58 + 72.50i
Diagonal, both top	Same	4	2, 13	7.11 + 71.58i
Diagonal, Both edge	Opposite	4	5	9.42 + 74.97i
Diagonal, across	Same	4	6, 7	7.50 + 71.46i

Strictly speaking, we have three feeding schemes that can be viewed as three independent antennas and since each 'antenna' predominantly excites a unique characteristic mode (or a unique set of characteristic modes); the far-field patterns associated with each antenna would have very low mutual envelope correlation.

Alternatively, let us consider the cases where a single voltage gap feed is used, as summarized in Table 5.

Table 5– Summary of Unaltered Plate Excitation via a Single Voltage Gap

Set of Ports	Dom. Mode(s)	Sec. Modes	Input Impedance
Top or Bottom Edge	1	3	7.25 + 70.05i
Left or Right Edge	2	1, 3	4.18 + 70.7i
Diagonal (any of four possible edges)	4	6	7.11 + 71.58i

From Table 5 we see another three possible simultaneous feeding schemes where single modes are excited. Thus, our current methodology for exciting single characteristic mode involves:

- analyzing the given structure for the modal currents,
- determining where the modal current maxima reside,
- placing voltage gap feeds at these locations

In doing so, we predominantly excite the modes associated with the current maxima and therefore obtain antennas with very low envelope correlation. However, we see a *serious flaw* in this design approach. Since the feeding gap is shorted by metallization on all sides, the input resistance is very low. In practice, it would be very difficult to match a generator to these ports, as well as being very inefficient antennas since the radiation loss resistance would constitute a major portion of the input resistance. Clearly, we need an alternative feeding mechanism to increase the input resistance, as well as to tune out the input reactance, all the while maintaining the unique excitation of characteristic modes.

As a last investigation of perfectly conducting unaltered plates, we consider the identically sized plate in the preceding examples, but we compute the characteristic modes at 900 MHz. The plate is now $0.33\lambda \times 0.18\lambda$, very near the electrically small realm. The first six characteristic modes are shown in Figure 34 with similar current distributions as the modes at the higher frequencies but we note distinctly larger eigenvalues. These larger eigenvalues imply large amounts of net stored energy, leading to large reactive input impedances. Figure 35 (a) – (d) shows that single modes (e.g. 1, 2, 3 or 5) can certainly be excited on electrically small plates, but we run into the same problem of large reactance, significantly larger than those found in Tables 4 and 5. At these electrical sizes, it is difficult if not impossible to match with any appreciable impedance bandwidth without a matching network. Moreover, we find it also very difficult to excite modes using only single voltage gaps, requiring us to use multiple feeds, something we wish to avoid if possible.

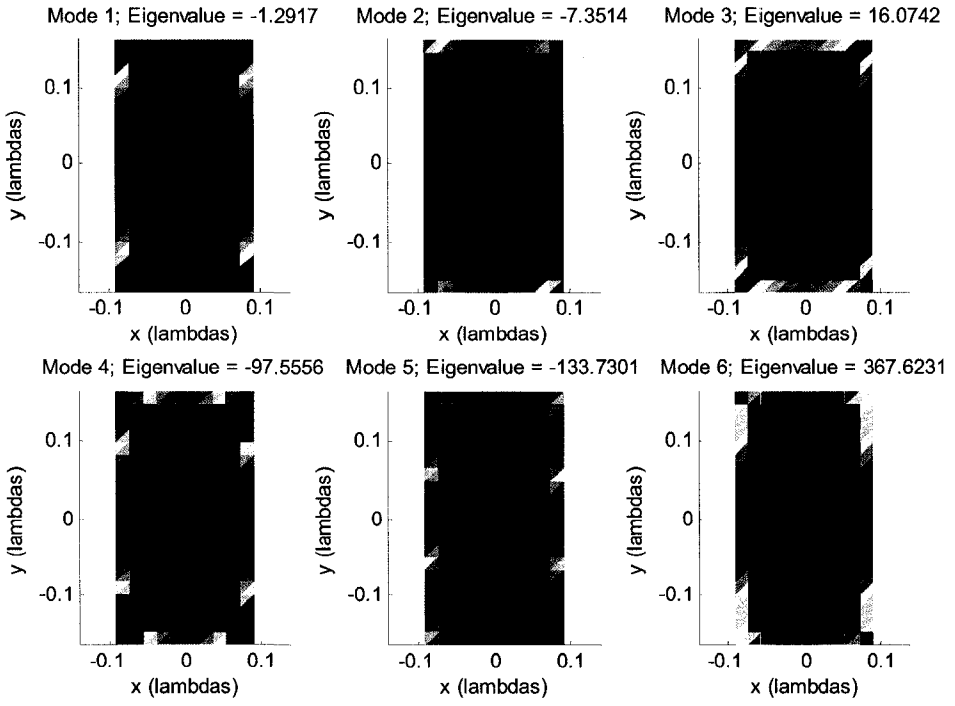

Figure 34 – Characteristic Mode Currents of Electrically Small Plate

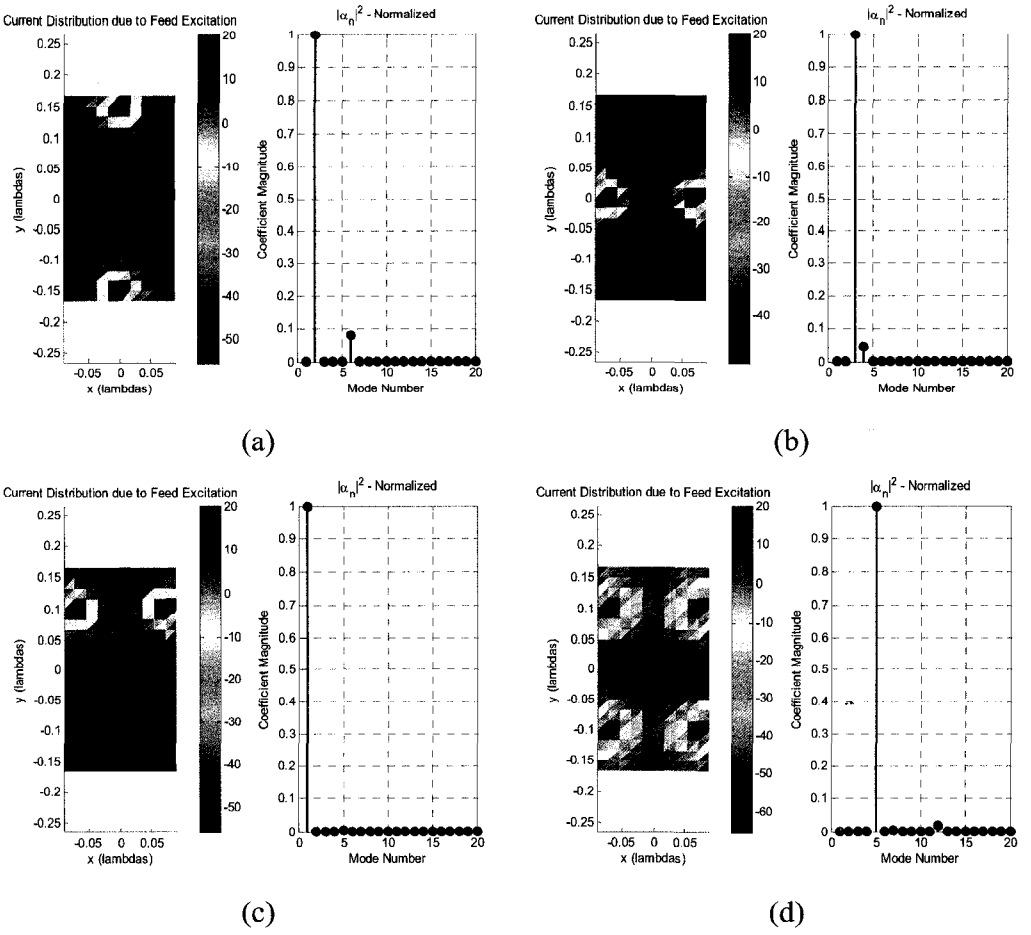

Figure 35 – Voltage Gap Excitation of Electrically Small Plate, (a) Top and Bottom Edges, (b) Side Edges, (c) Top Diagonal, (d) All Four Diagonals – Current in dB

5.5 – Practical Feeding Mechanisms for Modal Control

Intuitively, we know in order to increase the input impedance we must prevent the voltage gap from being shorted by metallization in the vicinity. We see a possible example in Figure 36 of how one can prevent the feed shorting effect. By preventing the current from looping back into the feed, as shown in Figure 36 we significantly increase the input resistance since the current is unable to loop back onto itself. Of course, such an example doesn't correspond to a current maximum shown in Figure 28 but it serves the purpose of showing how one increases input resistance using voltages gaps. Through a multitude of simulations, it was found any such narrowing in the vicinity of the modal current maxima both predominantly excites unique sets of modes, and also increases input resistance. Furthermore, it was found that the procedure also allows for tuning of the feeding mechanism to remove input reactance. If one has a matching network capable of dealing with input resistances between 20 – 100 ohms, the flexibility in the chosen feeding mechanism is vast. However, we shall consider the typical RF and microwave system, with characteristic reference impedance of Z_o = 50 Ohms. If such a system is chosen, it was found that **slot antennas** yield ideal input resistances as close as possible to 50 ohms.

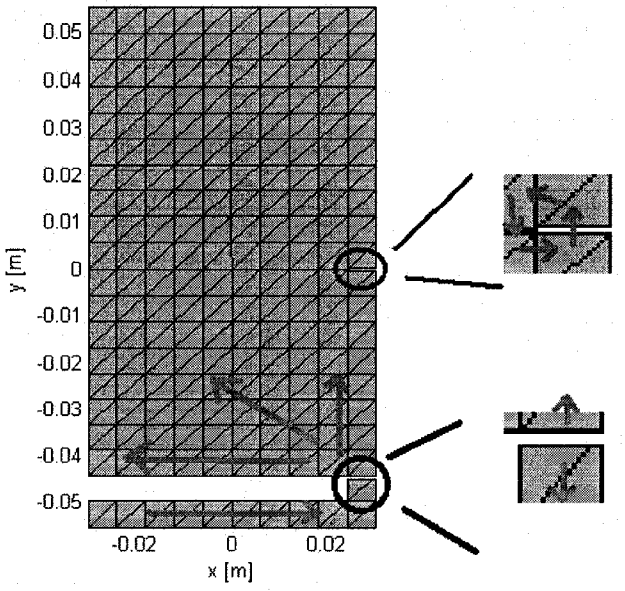

Figure 36 – Alternative Method of Excitation via Voltage Gap

5.6 – Design Methodology for the Excitation of Unique Groups of CMs

The first step of the methodology for exciting unique groups of characteristic modes was outlined in section 5.4, where we demonstrated placing a voltage gap at a modal current maximum predominantly excited the mode(s) associated with that maximum. There was but one problem remaining: low input resistance and high input reactance. A proposal was made in section 5.5 to solve this dilemma, in the form of preventing the surface currents from looping back onto the voltage gap, which is the cause of the low input resistance. A multitude of different antennas and feeding schemes were considered, with the majority showing less than ideal input impedances for matching to 50 ohms. It was found through these simulations that slot antennas provided the best match to 50 ohms, while still maintaining the necessary excitation of unique groups of characteristic modes. Furthermore, we found that slot antennas can have their overall shape altered (bent) to improve matching further while leaving modal excitation properties unchanged.

We consider the excitation of the lowest eigenvalue mode using two different slot antennas, shown in Figure 37. Recall that we predominantly excited this mode in Figure 30 (a) using a voltage gap (which is equivalent to a very short slot). We therefore place a slot in the same location and orientation as the voltage gap used in Figure 30. In some sense, we are extending the voltage gap to achieve better input impedance matching. The first example (Figure 37 a) has a relatively high input resistance of 85 ohms. By introducing a bend in the slot antenna (Figure 37 b) one finds the input impedance drops to around 55 ohms, offering an excellent match for 50-ohm microwave systems. Both examples slot designs are resonant (X_{IN} = 0) at our design frequency of 2.5 GHz. Additionally, it is clear that both feeding mechanisms work well for single mode excitation, with (Figure 37 a) having noticeably better single mode excitation since (Figure 37 b) excites mode 1 and mode 4. This reference impedance of $Z_o = 50\Omega$ was chosen for experimental measurements, since $Z_o = 50\Omega$ for most vector network analyzers and their corresponding calibration kits.

Having shown good single mode excitation with the top fed slot antenna, we re-compute the characteristic modes of the altered PEC plate. It should be noted that the CM theory does not consider the slot antenna as an individual radiator with the feed unknown to the modal formulation. Its presence will certainly change the modes to some degree, and it is our goal at this point to consider the newly computed CMs in and how one might go about exciting an additional set of unique characteristic modes. After observing the characteristic modes, we find the dominant mode of interest, as shown in Figure 38. It is clear in Figure 38 where one must place a voltage gap feed to excite said mode. We then apply the same argument of extending the voltage gap to form a slot, only the slot is now horizontal and does not require a bend for matching to 50 ohms.

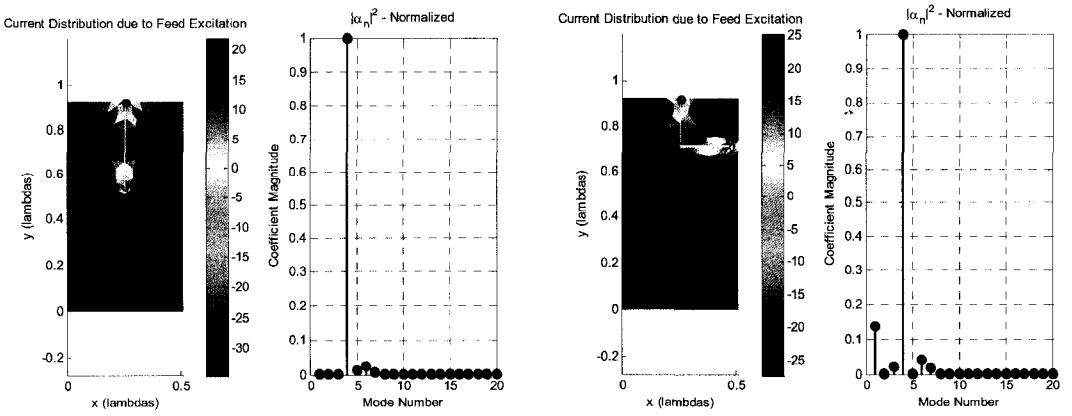

(a) **(b)**

Figure 37 – First MIMO Antenna, Single Mode Excitation, (a) Straight Slot, (b) Bent Slot

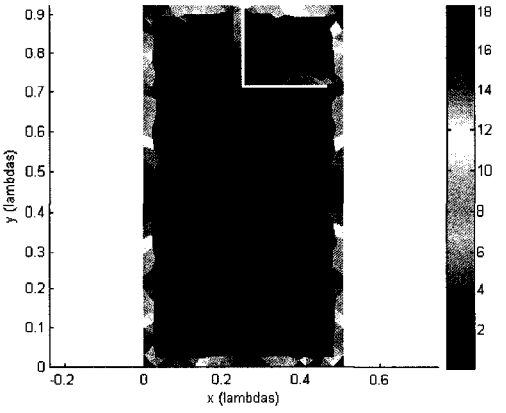

Figure 38 – Dominant Characteristic Mode After Bent Slot Antenna is Included

We introduce the second slot and in doing so we ensure a second MIMO antenna with low envelope correlation with respect to the first antenna. We excite each slot individually, with the remaining slot terminated in a matched load and measure the modal excitation of both ports, as shown in Figure 39 [*Note*: Current is measured in dB]. We see the top slot excites mode 3, and the side edge slot excites modes 5 and 8. We now have two antennas where each excites unique sets of characteristic modes, thereby maintaining orthogonality of the far-field. While we could measure the envelope correlation between the antennas using field integration, there is no need: we know that unique modal excitation will yield far-field orthogonality. We will of course confirm this using field integration in subsequent sections. Both feeds have input impedances around 55 – 57 ohms. Note the dimensions of the top feed do not need to change when introducing the second feed, which is a testament to the nature of unique modal excitation: the second feed does not affect the first feed in any appreciable manner.

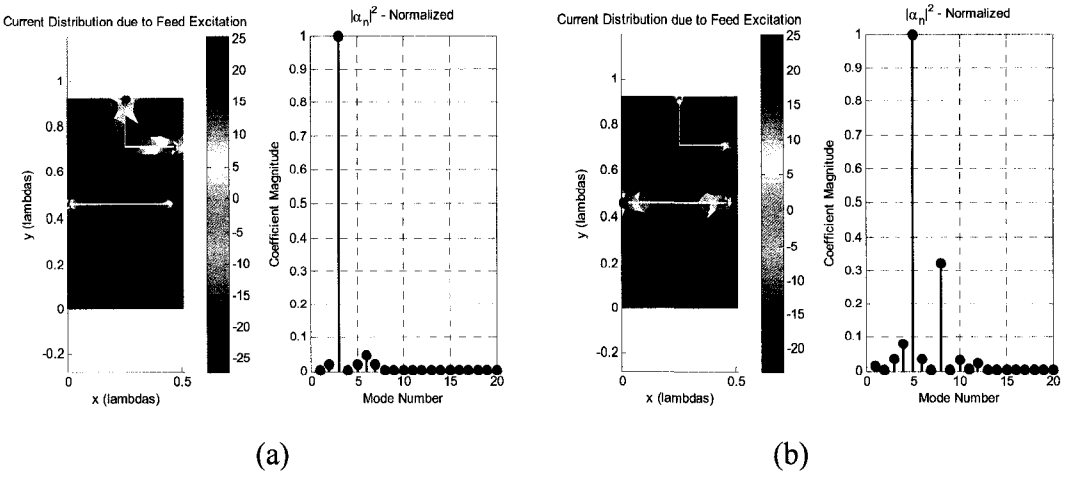

Figure 39 – Excitation of Unique Groups of CMs, Two MIMO Antennas, (a) top slot excited, (b) side slot excited

We continue with our design procedure, re-computing the CMs in the presence of both slot antennas, and then consider the surface currents of the modes. We find the CM of interest, as shown in Figure 40, implying that a voltage gap placed at the bottom of the plate will excite a unique set(s) of modes. Once again, in order to maintain reasonable input impedance, we extend the voltage gap in the form of a bent slot antenna.

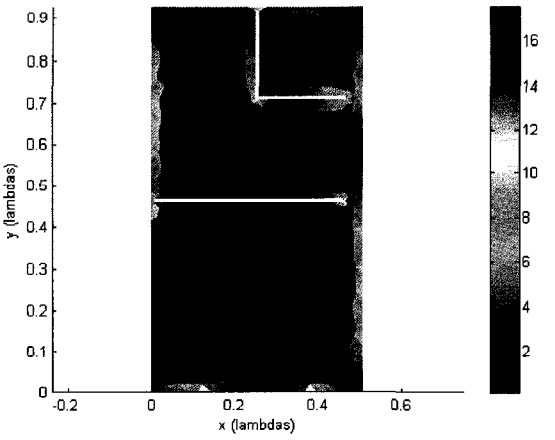

Figure 40 – Dominant Characteristic Mode Currents, Including Two Slot Antennas

What is of importance to note for this third antenna is to not copy the exact layout of the first antenna, otherwise we will yield a symmetric device and obtain the addition and subtraction phenomena discussed in the next section 5.7. While this would still yield a set of antennas with orthogonal far-field patterns, it relies heavily on the symmetry of the device, a requirement that is difficult to keep and all too easy to break. In order to ensure a lack of symmetry, the dimensions of the third slot will remain distinct from the first bent slot, as shown in Figure 41 (c). The top slot continues to excite mode 3, the edge slot (horizontal) excites mode 6 and 8 and the newly added bottom slot excites mode 2. Again, we find unique sets of characteristic modes excited at each port, which will prove critical in MIMO antenna design. It is very important to recognize that as we transitioned from an unaltered plate to a plate with one slot to a plate with two slots, and finally to a plate with three slots, the characteristic modes of each step are distinct from each other. Similarities will inevitably exist, but one cannot equate mode 1 of the unaltered plate to mode 1 of the final altered plate with the accompanying three slots.

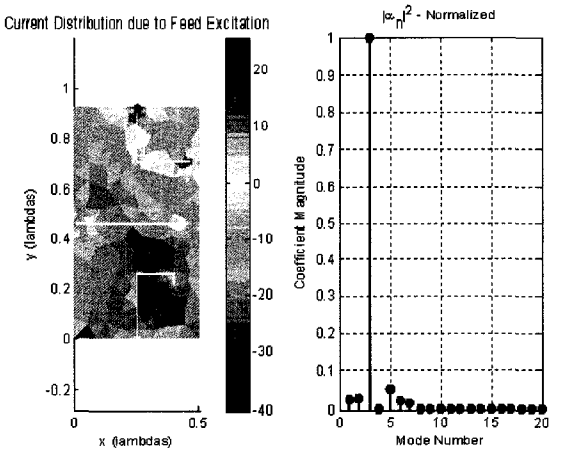

(a)

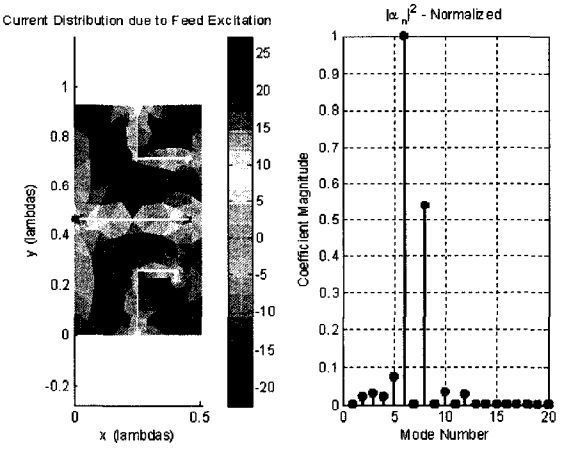

(b)

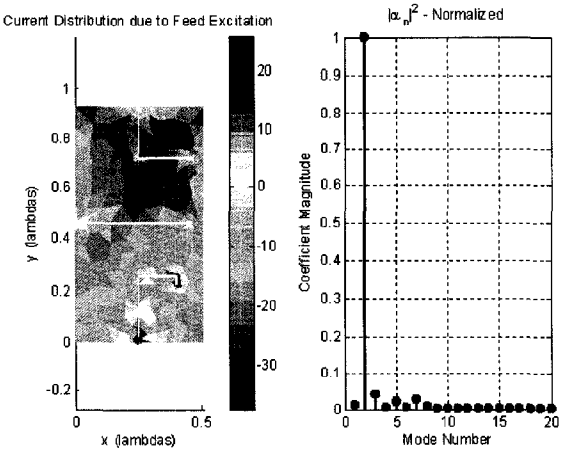

(c)

Figure 41 – characteristic Mode Spectrum for (a) Antenna 1, (b) Antenna 2, (c) Antenna 3

We summarize the developed methodology for the excitation of unique groups of characteristic modes as follows:

Step 1: Select a starting PEC structure, such as a mobile phone chassis. The model can, in general, take any shape.

Step 2: Compute the characteristic modes of the chosen structure and order the modal currents by their eigenvalue. Visually inspect the lowest order modes for their surface current maxima and note their locations (e.g, Figure 28).

Step 3: Starting with the dominant mode of the structure (lowest eigenvalue mode) introduce a slot[1] antenna in the vicinity of the modal current maximum of the dominant mode such that the feed of the slot is co-located with the modal current maximum. If multiple maxima exist for the given mode, choose whichever maximum is convenient.

Step 4: The antenna can be tuned to optimize impedance matching, provided the physical layout of the antenna is mostly restricted to the region of interest where the modal current maximum resides.

Step 5: Compute the characteristic modes of the altered structure that now includes the newly added antenna, and order them based on their eigenvalues. Return to Step 3 and repeat as necessary. However, one must consider modes that interact minimally with the antenna(s) from the previous steps (i.e. the modes that the other antennas do not excite).

Caveat: A shortcut exists for this methodology. If one determines multiple locations of the maxima (e.g. Figure 28) one can design all the desired antennas simultaneously without having to design each antenna and re-compute the modes every step. However, the most structured approach includes **all** steps mentioned above.

---

[1] *Clarification*: antennas capable of maintaining a feed location that is co-located with the current maximum will suffice for the modal design procedure. These include IFAs, monopoles, and the like. However, slot antennas (and structures resembling slot antennas) were found to yield the best match to $Z_o = 50\Omega$ as well as much wider operating bandwidth.

5.7 – Physical Symmetry and Characteristic Modes

It should be noted that the previously discussed design has no symmetry in its physical layout. What is critical to unique modal excitation is precisely this concept: lack of symmetry in excitation schemes leads to better possibilities of different modes excited by each port.

However, there exists another method one can use to achieve low envelope correlation despite exciting identical modes at different ports. This is contrary to our previous discussion, since a port that shares excitation of a mode should be coupled. Consider an arbitrary two antenna system where the excitation of each antenna excites modes 'm' and 'n' with all other modes negligible (valid possibility given some previous results). The fields produced by each antenna can be expanded in terms of the modal fields as:

$$E_{port\ 1} = \left(\alpha_{m,port\ 1}\right) E_m + \left(\alpha_{n,port\ 1}\right) E_n \tag{5.7-1}$$

and

$$E_{port\ 2} = \left(\alpha_{m,port\ 2}\right) E_m + \left(\alpha_{n,port\ 2}\right) E_n \tag{5.7-2}$$

Let us assume now that the excitation of mode m and n is roughly the *same in magnitude, but opposite in sign,* giving us the following excitation coefficients:

$$\alpha_{m,port\ 1} \approx \alpha_{m,port\ 2} \quad \text{and} \quad \alpha_{n,port\ 1} \approx -\alpha_{n,port\ 2} \tag{5.7-3}$$

Let us assume:

$$\alpha_m = \alpha_{m,port\ 1} = \alpha_{m,port\ 2} \text{ and } \alpha_n = \alpha_{n,port\ 1} = -\alpha_{n,port\ 2} \tag{5.7-4}$$

Thus, we can write:

$$E_{port1} \approx \alpha_m E_m + \alpha_n E_n \quad \text{and} \quad E_{port2} \approx \alpha_m E_m - \alpha_n E_n \tag{5.7-5}$$

We can therefore state that port 1 excites the sum of the modes m and n, and port 2 excites the difference of modes m and n. If we consider the numerator in Equation 5.2-11 the expression for envelope correlation, we can substitute in the values for the electric fields:

$$
\begin{aligned}
&\iint_S [\alpha_m E_m + \alpha_n E_n][\alpha_m E_m - \alpha_n E_n]^* \, dS \\
&= \iint_S \left(|\alpha_m|^2 |E_m|^2 - |\alpha_n|^2 |E_m|^2 + \alpha_n \alpha_m^* E_n E_m^* - \alpha_m^* \alpha_n E_m^* E_n \right) dS \\
&= \iint_S \left(|\alpha_m|^2 |E_m|^2 - |\alpha_n|^2 |E_n|^2 \right) dS \\
&= |\alpha_m|^2 \iint_S \left(|E_m|^2 \right) dS - |\alpha_n|^2 \iint_S \left(|E_m|^2 \right) dS \\
&= \eta \left(|\alpha_m|^2 - |\alpha_n|^2 \right) \\
&\approx 0
\end{aligned}
\tag{5.7-6}
$$

Therefore, if the excitation coefficients α_n and α_m are approximately equal in magnitude, the envelope correlation between the ports is very near zero. To have the coefficients approximately equal in magnitude but opposite in sign we merely need to have symmetry in the physical structure. This property is summed up below:

> The sum and difference of equally excited modes are mutually orthogonal. That is to say, $E_n + E_m$ and $E_n - E_m$ are orthogonal for $m \neq n$. This property can be exploited through symmetry arguments in the feeding mechanisms of the radiating structure.

This concept can be extended to scenarios where more than two modes are excited, as well as structures that have more than one axis of symmetry. An example design exploiting such a scenario is shown in Figure 42. We consider two slots, both resonant at 2.5 GHz, placed at the top and bottom of the PEC plate. We see both slots excite the same two modes, 2 and 4, with the magnitude of excitation approximately equal for both modes. We find that the excitation of the top feed excites the addition of mode 2 and 4 while the excitation of the bottom feed excites the subtraction of modes 2 and 4. This results in the following relationships between the modal excitations:

$$
\alpha_{2,port\ 1} \approx \alpha_{2,port\ 2} \quad \text{and} \quad \alpha_{4,port\ 1} \approx -\alpha_{4,port\ 2} \tag{5.7-7}
$$

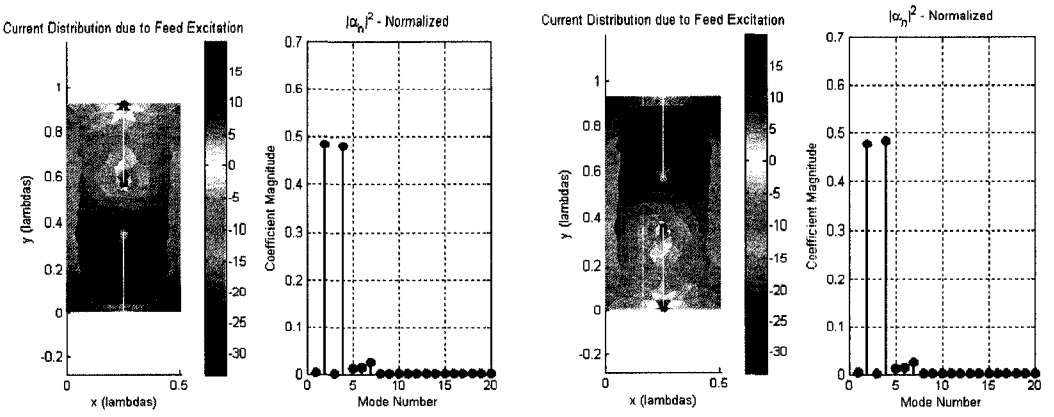

Figure 42 – Physical Symmetry and Characteristic Modes

We neglect the higher order modes (namely modes 5, 6 and 7) since they constitute less than 2% of the total radiated power associated with each port. We can therefore expand the fields from each port as follows:

$$E_{port\ 1} = \alpha_2 E_2 + \alpha_4 E_4 \quad \text{and} \quad E_{port\ 2} = \alpha_2 E_2 - \alpha_4 E_4 \qquad (5.7\text{-}8a,b)$$

Computing the inner product between these fields

$$\begin{aligned} \iint_S [\alpha_2 E_2 + \alpha_4 E_4][\alpha_2 E_2 - \alpha_4 E_4]^* \, dS &= \iint_S \left(|\alpha_2|^2 |E_2|^2 - |\alpha_4|^2 |E_4|^2 \right) dS \\ &= |\alpha_2|^2 \underbrace{\iint_S \left(|E_2|^2 \right) dS}_{=\eta} - |\alpha_4|^2 \underbrace{\iint_S \left(|E_4|^2 \right) dS}_{=\eta} \\ &= \eta \left(|\alpha_2|^2 - |\alpha_4|^2 \right) \end{aligned} \qquad (5.7\text{-}9)$$

The above expression is zero if the magnitude of α_2 was equal to the magnitude of α_4. This is the case for this design, as evident in the modal excitation coefficients shown in Figure 42 since $|\alpha_2|^2 \approx |\alpha_4|^2$. Tuning of the dimensions of the slot and / or the plate balances the excitations as desired. What is important to note is this procedure is sensitive to symmetry. By breaking symmetry, the modal excitation factors will change, and the modal addition / subtraction property no longer holds. That being said, if we use the modal currents themselves to break the symmetry, we excite unique sets of characteristic modes, something we shall discuss in the next section.

5.8 – MIMO Antenna Design Examples Using CM Theory

5.8.1 – Single Plate, Bar-Type Chassis

In this section we consider the CM based design developed in Section 5.6 whose physical dimensions are shown in Figure 43 and analyze the resulting modal excitations factors (shown in Figure 44) and MIMO related performance indices.

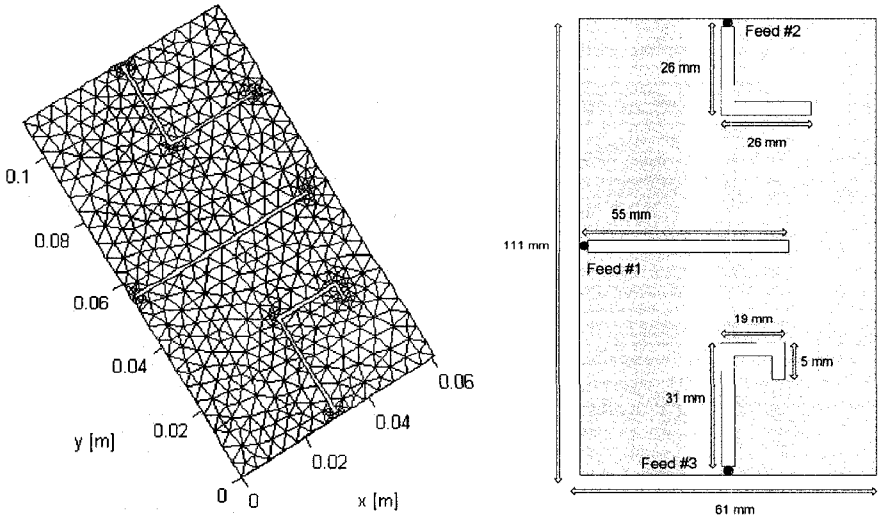

Figure 43 – Single Plate, Bar-type Chassis Three Antenna Design, Mesh and Physical Dimensions

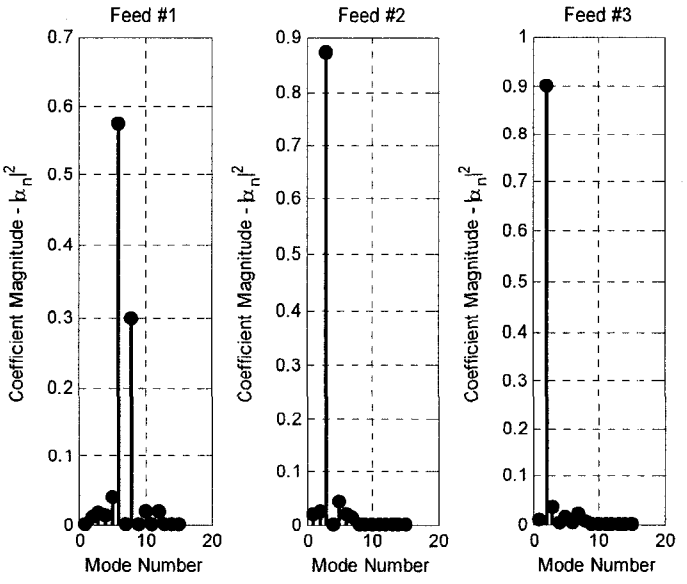

Figure 44 – Mode Spectrum of Three Antenna Design

We note that Port #1 predominantly excites mode 6 and 8, Port #2 excites mode 3 and Port #3 excites mode 2. We can compute the % of power distributed into the dominant modes for each port, as shown in Table 6. However, the preceding table only considers the dominant modes. We can also consider the higher order modes that are unique to each antenna that contribute a good portion of the remaining radiated power. We therefore consider the ports to excite modes as follows:

- Port #1 predominantly excites modes 6 & 8, and to a lesser extent modes 5, 10 and 12.
- Port #2 predominantly excites mode 3 and to a lesser extent modes 1 and 7
- Port #3 excites mode 2 with negligible higher order modes.

Since no modes overlap and 90%+ of the input power is radiated by the associated unique modes, we expect the far-field patterns of each antenna (each port) to be nearly orthogonal and thus have low envelope correlation. Additionally, the radiation efficiencies are very high, implying that we can use the S-parameters to estimate the envelope correlation, since the S-parameter method requires a lossless antenna system.

Table 6 – Summary of Excitation Parameter for Three Antenna Design

Port #	Dominant Mode(s)	% Rad. Power	Higher Order Modes	Adjusted % Power	Radiation Efficiency
1	6 & 8	87.7%	5, 10, 12	95.5%	98.6 %
2	3	87.3%	1, 7	90.7%	99.1 %
3	2	90.2%	None	90.2%	98.1 %

Let us first consider the *simulated* S-parameters ($Z_o = 50\Omega$) for the three antenna design as shown in Figure 45 (a) & (b). We see an excellent match at our design frequency, with a worst case 14% 10dB RL bandwidth, and even wider 50% 10dB RL bandwidth for ports 2 and 3. Consider also that the mutual coupling parameters are nearly all below -15 dB over the entire measured range of frequencies.

Moreover, we can use the simulated S-parameters to compute the envelope correlation, as shown in Figure 46. We see a very wide bandwidth (> 36%) over which the envelope correlation is less than 0.1. Notice also that the envelope correlation has a minimum at the center frequency of 2.5 GHz. This is caused primarily by the very high unique modal excitation at each port. This modal property inevitably leads to very low mutual coupling which will invariably reduce the envelope correlation. Furthermore, outside the well matched region we still maintain low envelope correlation due to the low mutual coupling between the ports

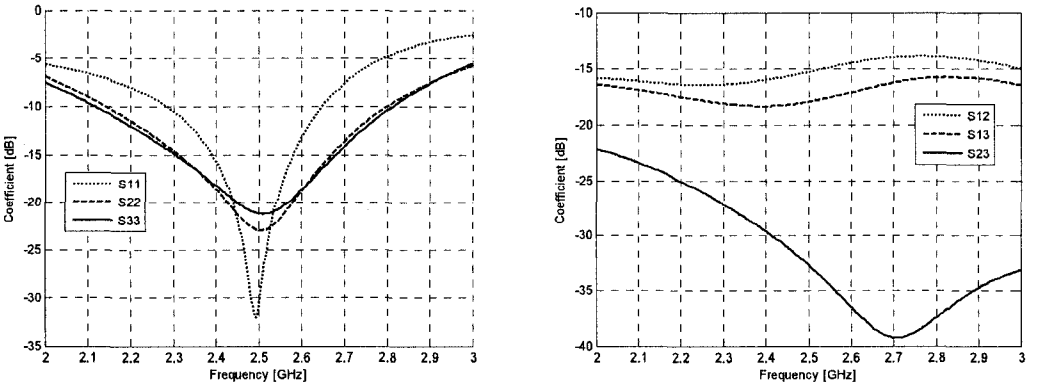

Figure 45 – Simulated S-parameters of Bar-type Mobile Chassis Three Antenna Design

Since the envelope correlation is quite low over a wide bandwidth, it is of interest to consider the envelope correlation over an even wider band, well outside the operating range, in order to distinctly visualize the region of low envelope correlation. We therefore compute the envelope correlation from 0.5 GHz to 5 GHz as shown in Figure 47. We see a very sharp and distinct region of low envelope correlation operation, evidently from 1.5 GHz to 3 GHz. Over the low envelope correlation region the characteristic modes

associated with each port do not change drastically, allowing the unique modal excitation to be maintained for more than a single frequency. Additionally, the envelope correlation is measured using field integration, and no perceivable difference is seen between both methods, confirming our assertion that the losses shown in Table 6 are low enough to use the S-parameter approach in computing the envelope correlation.

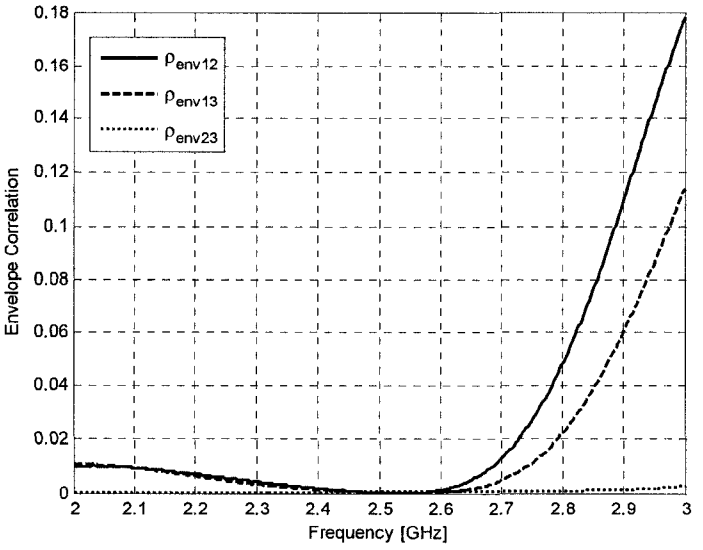

Figure 46 – Envelope Correlation for Bar-type Mobile Chassis Three Antenna Design

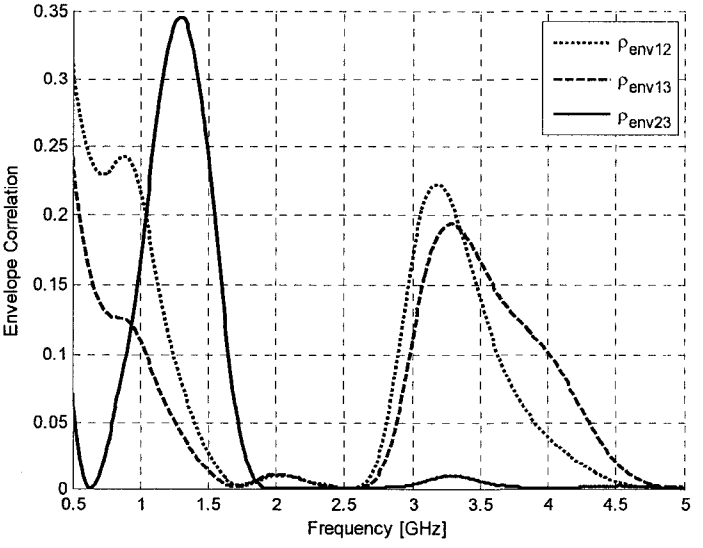

Figure 47– Envelope Correlation Measured over Wide Range of Frequencies

For illustrative purposes, we show these embedded far-field patterns (normalized electric field) in the form of 3D polar plots shown in Figure 48 (a), (b) and (c). These plots are not intended to give detailed field information, but rather give the reader a qualitative look at the far-field patterns. Notice that in some cases the patterns shown in Figure 48 have electric field maxima in the same direction. In these cases, the fields are either 180° out of phase, or oppositely polarized.

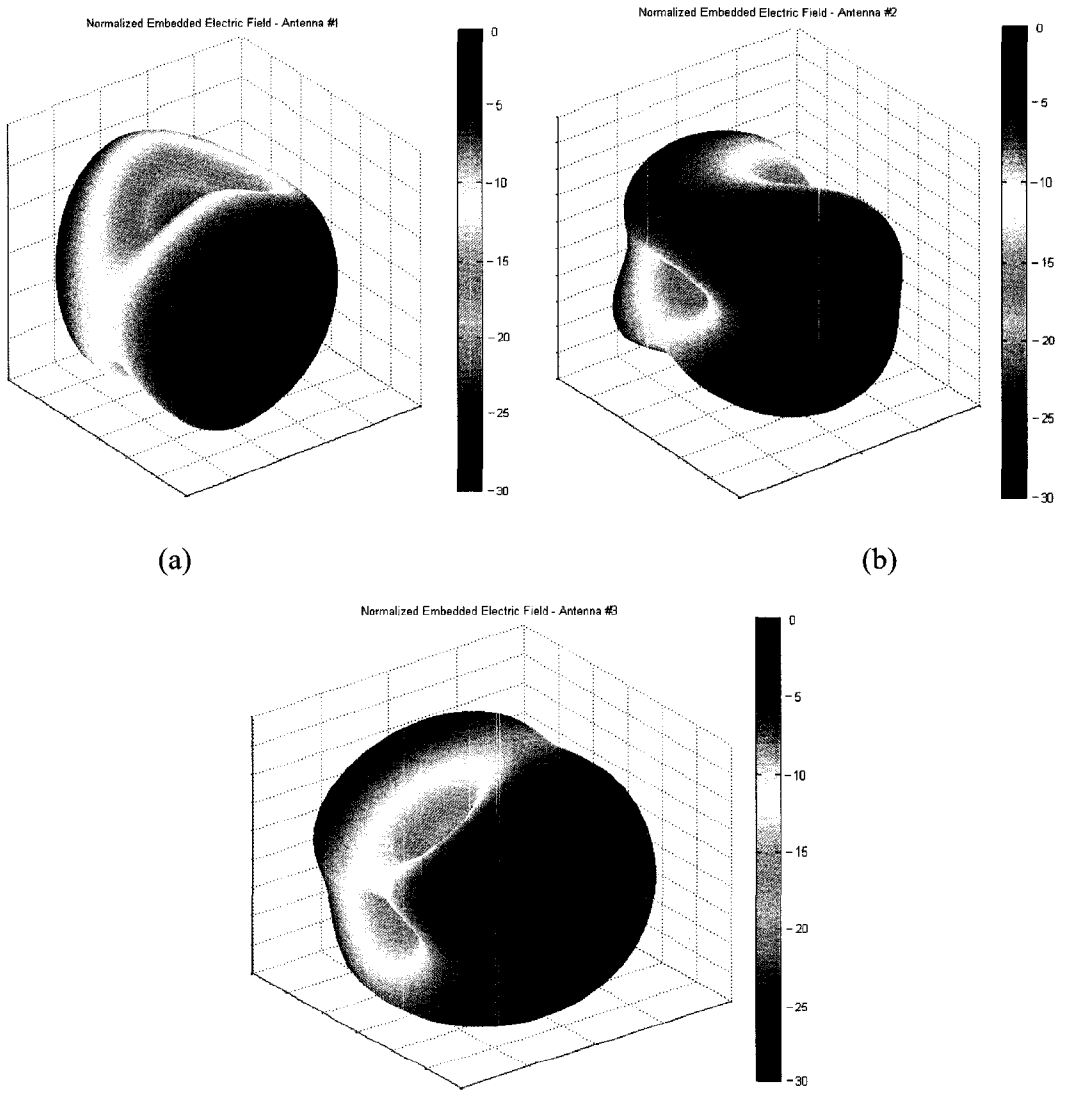

Figure 48 – Normalized Electric Field, 3D Far-field Polar Plot for (a) Antenna 1, (b) Antenna 2 and (c) Antenna 3

In order to properly validate our design, we must compare experiment with simulation. We choose to construct a physically scaled-up version of the handheld design, with a scale factor of around 1:4.15. This allows us to measure the S-parameters at a center frequency of 603 MHz, rather than at 2.5 GHz. As such, minor errors in construction will not drastically affect the final result. An image of the final experimental design is shown in Figure 49.

As shown in Figure 49, the feeding mechanism used to achieve a voltage gap is a coaxial connector, with the outer conducting soldered to one side of the feed and the center pin soldered to the remaining side. Orientation does not change the measured S-parameters. We are able to feed the ports without a balun because the feeding structure (coax SMA connector, sheath and pin) are significantly smaller than a wavelength at the operating frequency. At our operating frequency, the coaxial cable feeding scheme occupies a maximum linear dimension of 15mm, or around 2.5% of a wavelength.

At the true operating frequency of 2.5 GHz, the feeding structure would be 13% of a wavelength, and thus potentially significant in terms of radiation properties. In this situation, a balun would certainly be required.

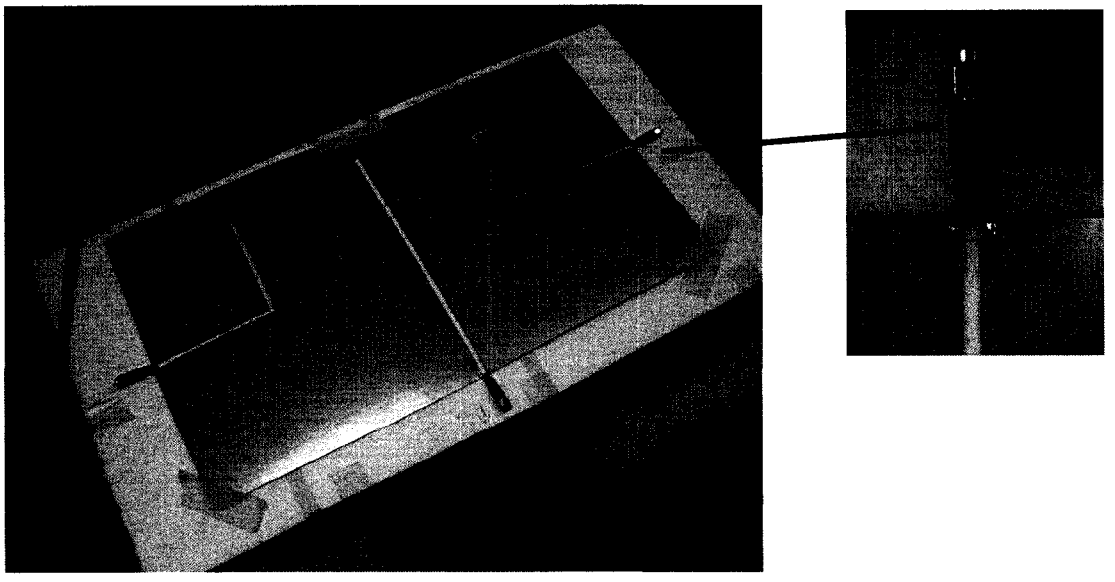

Figure 49 – Photograph of Three Antenna Experimental Design

We compare the simulated S-parameters with the experimentally determined values in Figure 50. We find reflection coefficient measurements match well with experiment and in all cases the measured 10 dB RL bandwidth is greater than or equal to the simulated results. Additionally, the mutual coupling parameters have similar trends between simulation and experiment.

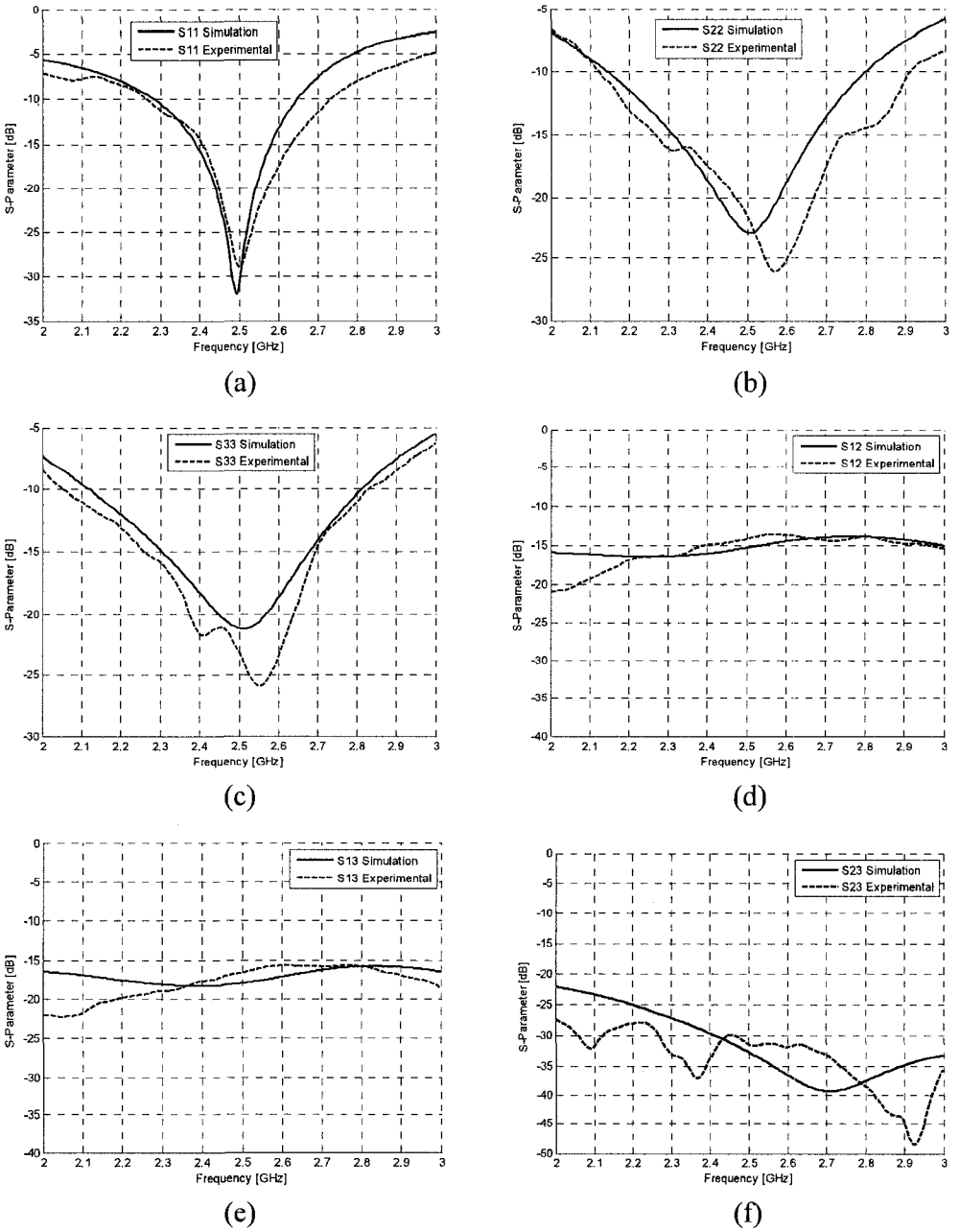

Figure 50 – Comparison of Simulated and Experimentally Measured S-Parameters

With the experimentally determined the S-parameters, we can compute an approximation to the envelope correlation using this measured data. We must consider the experimental calculation as an approximation because the experimental data includes the effects of loss and the formula for envelope correlation in terms of S-parameters assumes a lossless antenna. Since the experimental antenna efficiency is likely very high, we compare the experimentally determined envelope correlation with the simulated data in Figures 51 and 52.

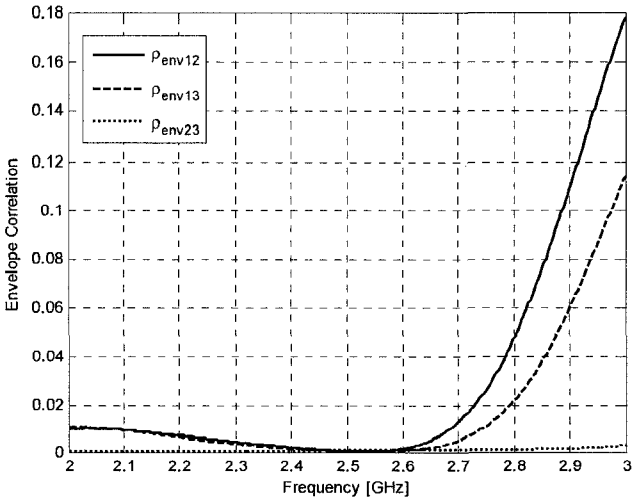

Figure 51 – Simulated Envelope Correlation, Computed Using S-parameters

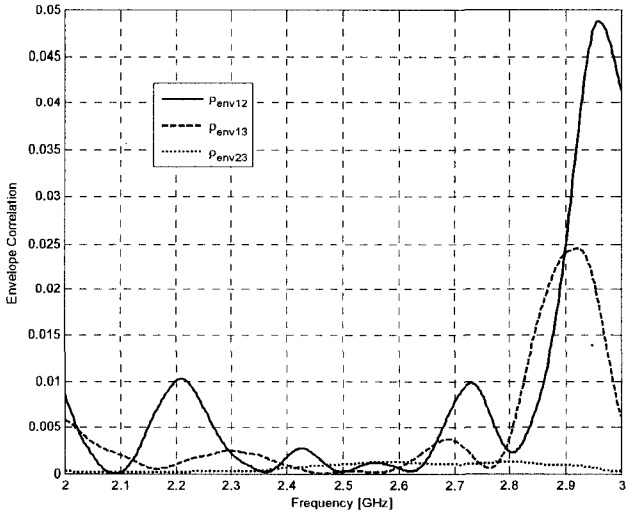

Figure 52– Experimentally Determined Envelope Correlation, Computed Using S-parameters

We note that again a behavioral trend appears between experiment and simulation Experiment shows much lower envelope correlation values which is primarily due to the lower than predicted mutual coupling between the antenna ports. Notice that ρ_{23} is insignificant over the entire frequency range as predicted through simulation, and ρ_{12} / ρ_{13} increase around 2.75 GHz, also predicted by the simulation results.

We see that in general, the envelope correlation trend does match well between simulation and experiment. In the cases where there is discrepancy, one finds the measured values drop well below the simulated values. This is expected since the experimentally determined mutual coupling and matching parameters were lower in most cases than predicted by simulation.

Of course the running assumption is the validity of the computation of envelope correlation via S-parameters, which requires a lossless structure. Since our structures are electrically resonant, and very well matched with large bandwidths, as well as simulation predicted greater than 98% radiation efficiency, we can safely assume the efficiencies are high enough to make the envelope computation approach valid.

The far-field patterns will not be measured experimentally as they are omni-directional and broad patterned and thus difficult to measure. Rather, we shall rely on the measured S-parameters which are far more sensitive quantities than an omni-directional far-field pattern since they are near-field derived parameters.

The validation procedure is not complete without comparison to existing designs. MIMO antenna design is a relatively new area of research, with very few direct comparisons found in the literature. One design we shall consider is by Thaysen [12]. Their design consisted of three antennas on a ground plane, mimicking a handheld chassis. Their design was specifically for 1.8 GHz operation, whereas our design is design for 2.5 GHz, but one can safely compare % bandwidth values.

The simulated and measured envelope correlation in Thaysen's design is shown in Figure 53. From this figure one can estimate an operating bandwidth of around 8% for all envelope correlation to be less than 0.1. Compare this quantity to our value of approximately 35% or greater. Furthermore, our poorest performing antenna has an impedance bandwidth of 14%, which is larger than Thaysen's best performing antenna. That being said, Thaysen's design occupies less electrical area than our design, but requires the third dimension (volume) to implement their PIFA antennas, albeit in a low-profile manner.

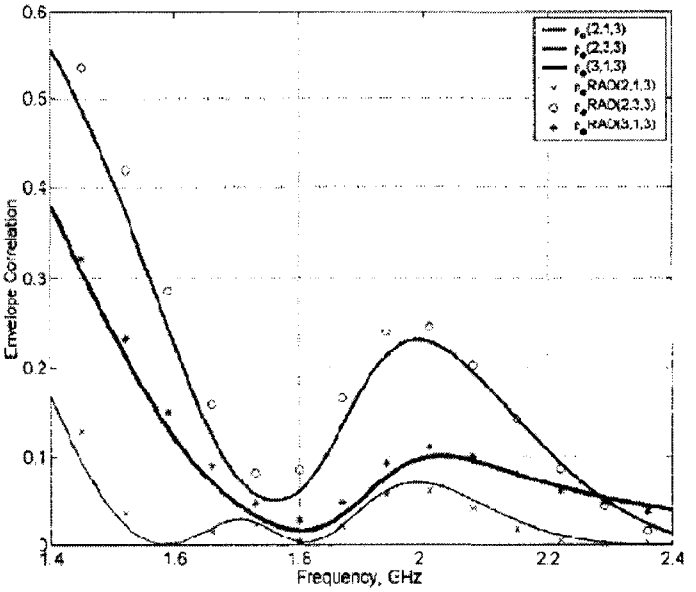

Figure 53 – Envelope Correlation of Three Antenna Design, After Thaysen [12]

Another possible comparison involves a set of three resonant dipole antennas. The ideal distance separating these antennas is half a wavelength, with their resonant length the usual half-wavelength. These dipoles would therefore occupy roughly the same area $(1\lambda \times 0.5\lambda)$ that our handheld occupies $(0.925\lambda \times 0.508\lambda)$. We compute the S-parameters over the same frequency span as our MIMO antenna design, referenced to $Z_o = 80\Omega$. We consider the input matching coefficients and the corresponding envelope correlations between the dipoles in Figure 54. We find the dipoles are well matched (as expected) with a minimum 12% 10dB RL bandwidth. Compare this bandwidth to our lowest

impedance bandwidth of 14% in simulation, 15% in experiment. Additionally, we find a best case envelope correlation bandwidth of 8% or $\rho_{env} < 0.1$, significantly poorer by comparison to our design result of 35%. Changing the orientations of the dipoles and minor changes in their positions does not improve the correlation or impedance matching. Unless the dipoles are separated a very large electrical distance from each other, our design is superior in both impedance matching and envelope correlation, with the latter quantity more than double in usable bandwidth. That is not to say that the dipoles do not form a decent MIMO antenna system. However, we do note the slot antennas are far easier to integrate into a handheld than a set of dipole antennas, with the added bonus of improved performance.

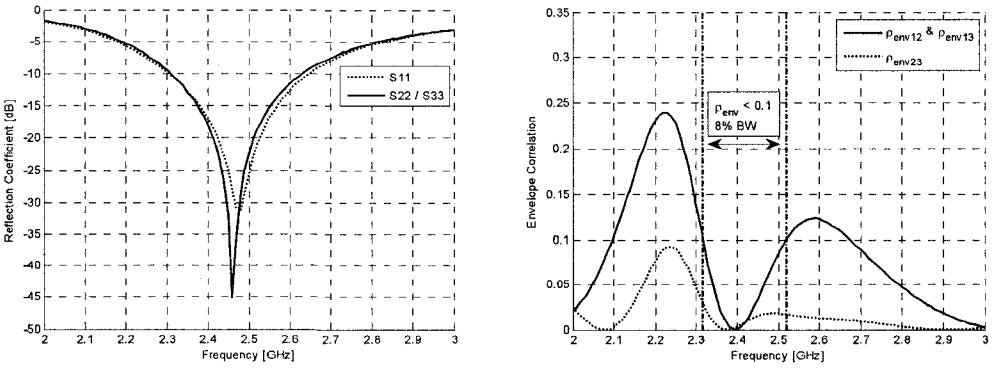

Figure 54 – Impedance Matching and Envelope Correlation of Three Dipoles

In any reasonable comparison, our impedance bandwidth is more than acceptable. Furthermore, we find the envelope correlation is well below 0.5 (the maximum allowed for beneficial diversity [13]) over the entire measured frequency span and below 0.1 over the impedance bandwidth. The envelope correlation was experimentally shown to be below 0.1 over the entire measure frequency span. We conclude that our design is indeed suitable as a system of antennas for MIMO communications.

5.8.2 – Alternative Design for Wide Plate

We next consider an alternative design for the same dimensions of plate. The same methodology of computing the characteristic modes, placing slots (and in this case using an alternative feeding mechanism) and exciting unique sets of CMs is used. The resulting design is shown in Figure 55. Moreover, we calculate the input impedances at each of the ports, under various loading conditions. In Table 7 we show that the input impedances are mostly insensitive to the choice of port termination which is indicative of the fact that when one antenna is excited, the resulting current density at the location of the other antenna ports is very small. Additionally, we see reasonable input impedances that are easily matched using standard microwave amplifiers. For this reason we choose characteristic impedances of 60Ω, 100Ω and 60Ω (respectively) for the three ports and compute the S-parameters using these distinct references.

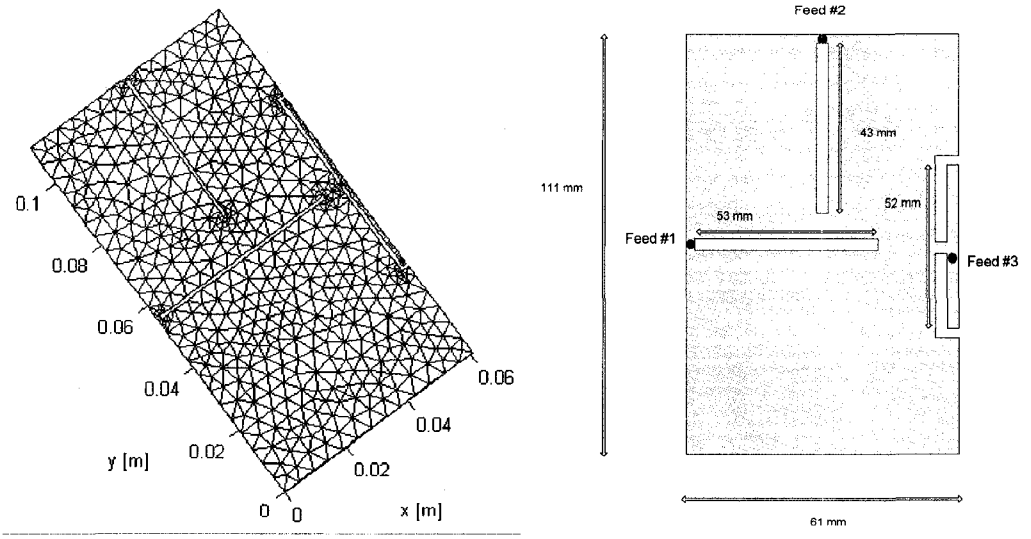

Figure 55 – Alternative Bar-type Chassis Three Antenna Design Mesh and Physical Dimensions

Table 7 – Input Impedances For Various Port Terminations

Antenna	0Ω Load	50Ω Load	100Ω Load
1	$58.7 - j1.6$	$63.4 - j1.4$	$59.1 - j1.5$
2	$91.2 + j3.9$	$93.6 + j2.3$	$96.9 + j2.1$
3	$57.3 - j5.2$	$54.6 - j1.8$	$58.8 - j2.3$

We next consider the modal excitation and where the power is diverted in each of the feeds. The modal excitation factors are shown in Figure 56 and the details summarized in Table 8. We find the modal excitations and % power into each set of the modes do not perform as well as the previous example in section 5.8.1. The distribution of the modes is not as "clean" as the previous example in that each port excites numerous modes rather than one or two at most shown previously. However, the large number of modes excited does not imply poor performance - we shall see the envelope correlation is nonetheless low enough for MIMO communications, since the modes excited are unique in each case.

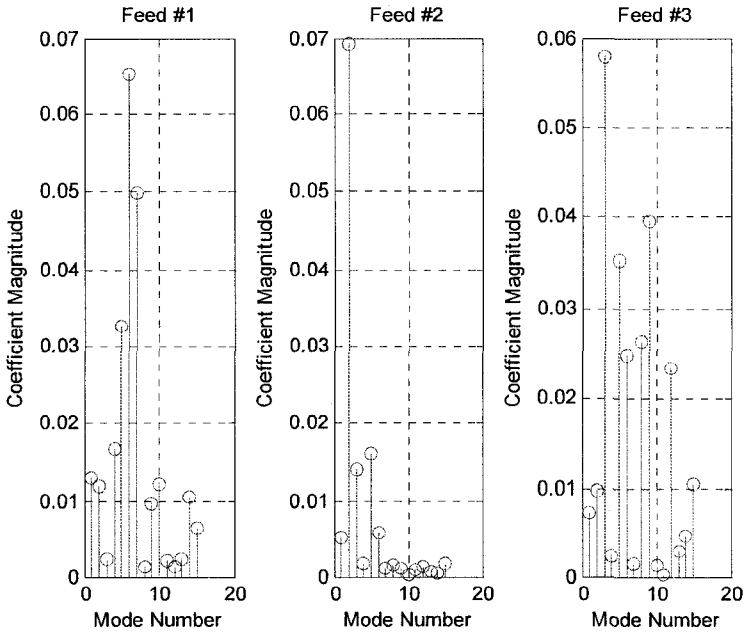

Figure 56 – Modal Excitation Coefficients for Three Antenna Design

Table 8 – Various Antenna and Modal Parameters of Alternative Three Antenna Design

Port #	Dominant Mode(s)	% Rad. Power	Radiation Efficiency
1	1, 4, 6, 7, 10, 14, 15	87.74%	98.66%
2	2	91.64%	98.18%
3	3, 5, 8, 9, 11, 12	89.17%	89.41%

In Figure 57 we consider the matching and coupling S-parameters of the design. At worst, the three antennas maintain a reasonable 11% 10dB RL. Additionally, we note that all mutual coupling parameters are less than -15dB at the center frequency. Lastly, we consider the envelope correlation behaviour over frequency in Figure 58. We see the envelope correlation is below 0.1 for a 10% bandwidth around the center frequency. We note that the envelope correlation for pair 2 & 3 is zero at 2.7 GHz, which corresponds to the very low mutual coupling S_{23} shown in Figure 57 at the same frequency. We also note that the correlation for pair 1 & 3 peak at 2.7 GHz which corresponds to the mutual coupling peaking at 2.7 GHz. These results confirm that the mutual coupling is indeed very important for low envelope correlation over the entire far-field sphere.

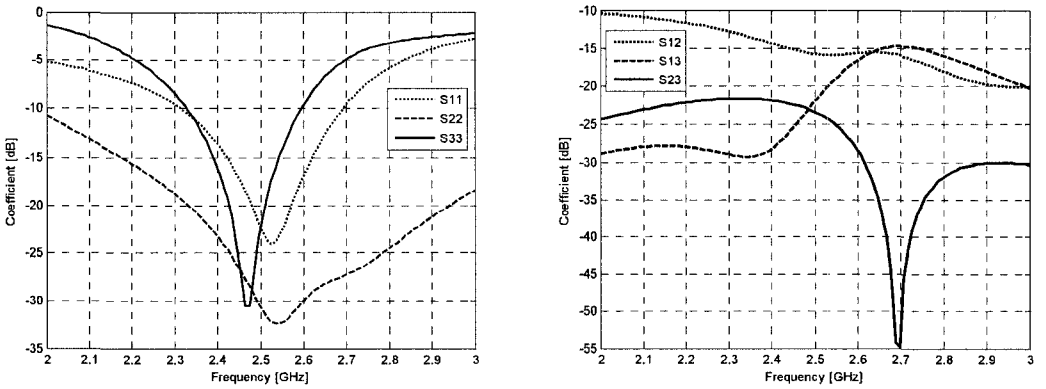

(a) (b)

Figure 57 – S-parameters of Alternative Three Antenna Design

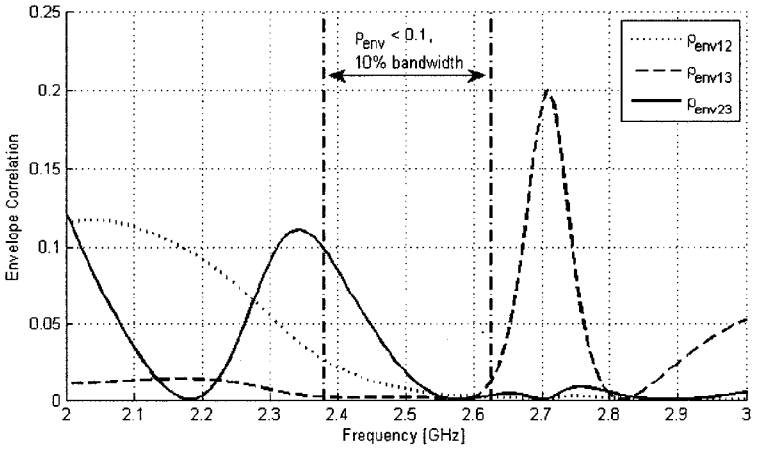

Figure 58 – Envelope Correlation of Alternative Three Antenna Design

5.8.3 – Four Antenna Design Exploiting Antenna Symmetry

We now consider a design that exploits the connection between the physical symmetry of a PEC plate with the characteristic modes of said plate. The physical layout of the antenna is seen in Figure 59 and modal excitations in Figure 61 (a)-(d). The arguments as to why we obtain low envelope correlation despite exciting similar characteristic modes is the same as those discussed in section 5.7, only we extend the concept to four antennas. We also include the simulated S-parameters as seen in Figure 60 (a),(b) where we see excellent matching characteristics, with identical behaviour for all four ports due to the symmetry of the antennas. Additionally, we see low mutual coupling as well as the expected pairing of the parameters due to the symmetry of the antenna structure.

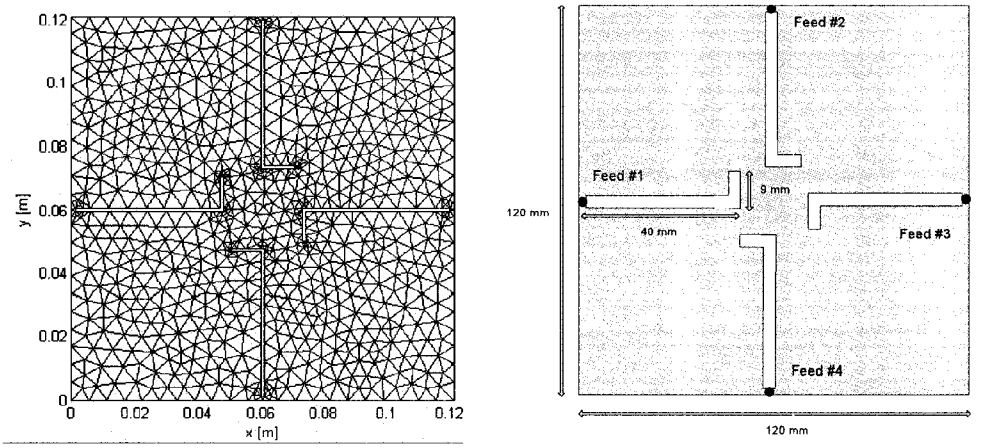

Figure 59 – Four Antenna Design Taking Advantages of Structural Symmetry

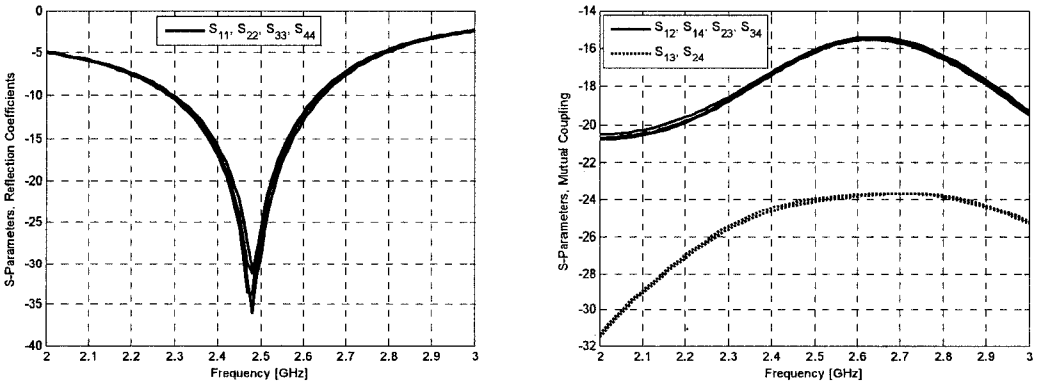

(a) (b)

Figure 60 – S-Parameters of Four Antenna Design

We also see very low envelope correlation at the design frequency of 2.5 GHz as shown in Figure 62 along with low envelope correlation over the entire frequency range.

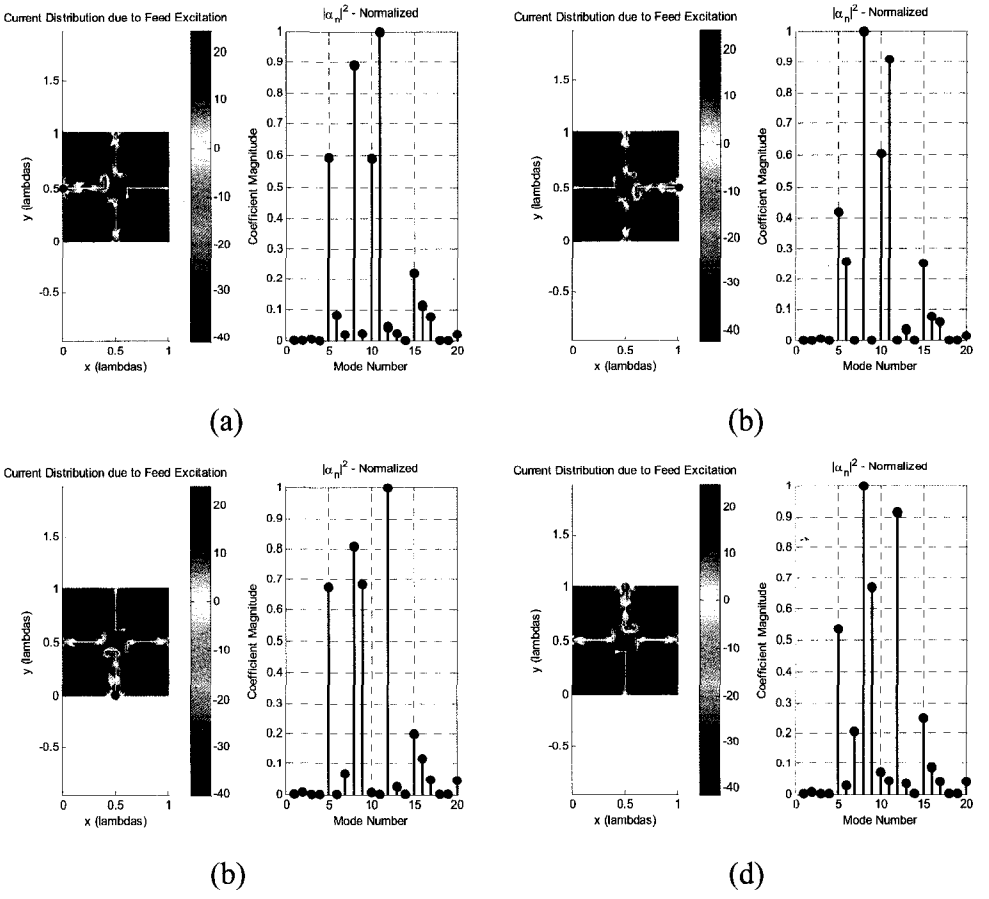

Figure 61 –Mode Spectrum of (a) Antenna 1, (b) Antenna 2, (c) Antenna 3, (d) Antenna 4

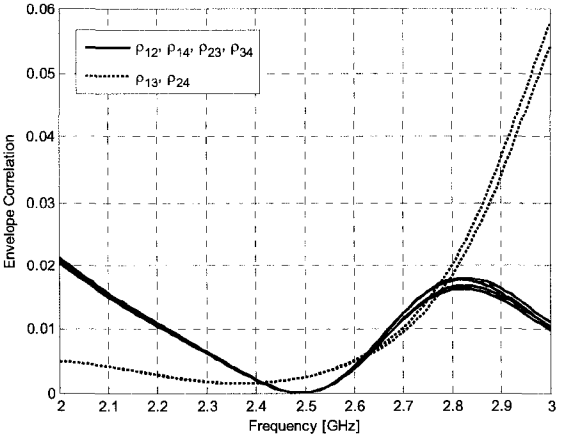

Figure 62 – Envelope Correlation of Four Antenna Design

5.8.4 – MIMO Antennas Designed onto Arbitrarily Shaped Plate

In this section we attempt to show the flexibility of the design process by considering an arbitrarily shaped plate, analyzing the modes and designing a set of low envelope correlation antennas onto the plate. We begin by computing the characteristic modes of a 1 wavelength squared plate, arbitrarily deformed as shown in Figure 63. If we consider the current distributions, we note the possibilities for ideal feeding locations in Figure 64.

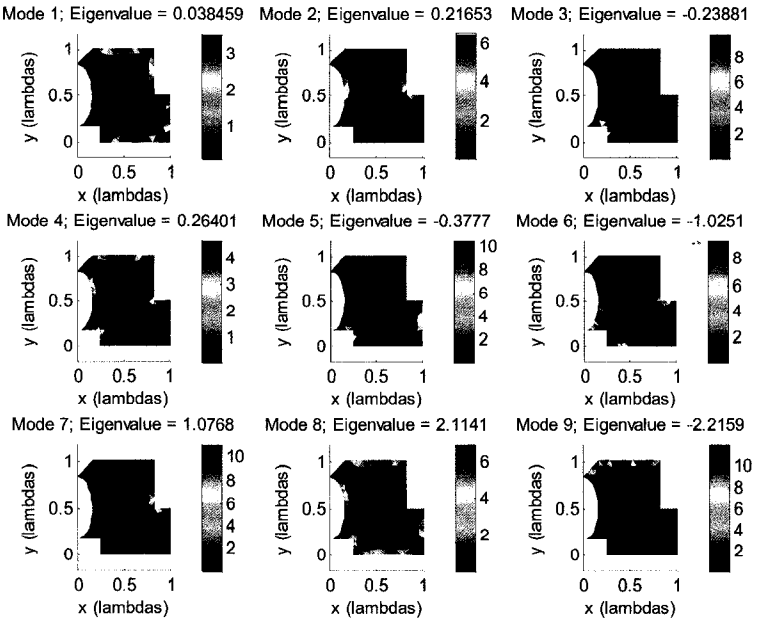

Figure 63 – Characteristic Modal Currents of Arbitrarily Shaped PEC Plate

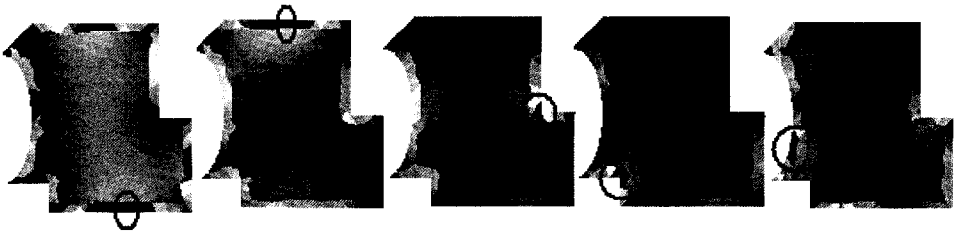

Figure 64 – Characteristic Modes of Interest of Arbitrarily Shaped PEC Plate

The current distributions imply that the feeding scheme shown in Figure 65 should yield low envelope correlation antennas. Note that we have chosen a set of three antennas that is not unique to this structure. Only three of the possible five feeding locations were chosen, implying other combinations of three antennas would be possible. The choices would be made based on other considerations such as structural stability, bandwidth and the like.

One might consider this design as representing a structurally constrained ground plane, as part of a laptop or other similar structure. What is of greatest importance is the fact that given an arbitrary structure, one can analyze the characteristic modes and determine the suitable locations for excitation. One can imagine applying these concepts to models of any conceivable radiating structure and deriving a set of antennas appropriate for MIMO communications (or any other form of communication relying on antenna with low envelope correlation).

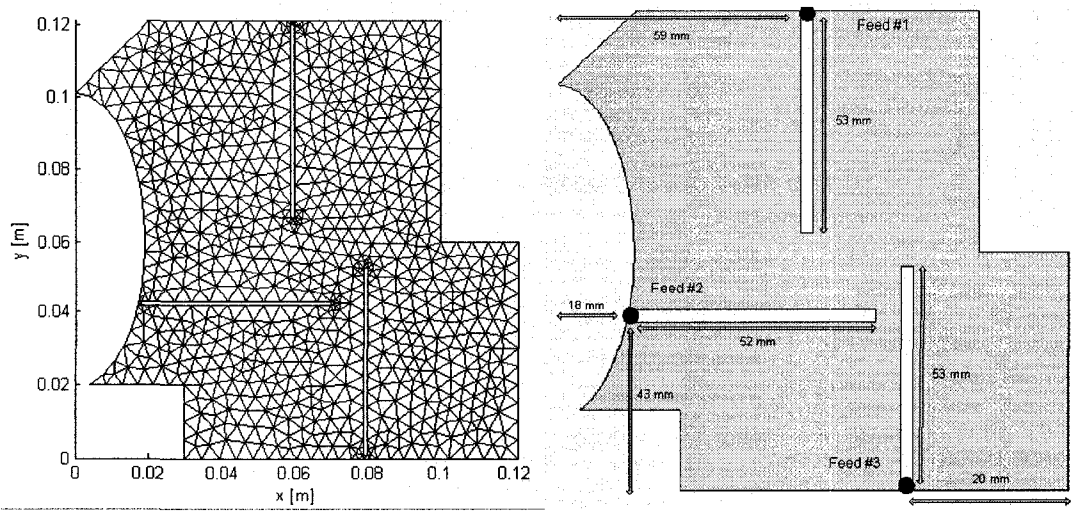

Figure 65 - Arbitrary Plate Design with Mesh and Physical Dimensions

The chosen characteristic impedances for the three ports are 80 Ohms, 80 Ohms and 60 Ohms for ports 1, 2 and 3 respectively. The simulated S-parameters are computed as shown in Figure 66. We see excellent matching characteristics for all three antennas, with greater than 20% 10dB RL bandwidth for all three antennas. Additionally, we find very low mutual coupling between the antennas. From these S-parameters, we can compute the envelope correlation as shown in Figure 67.

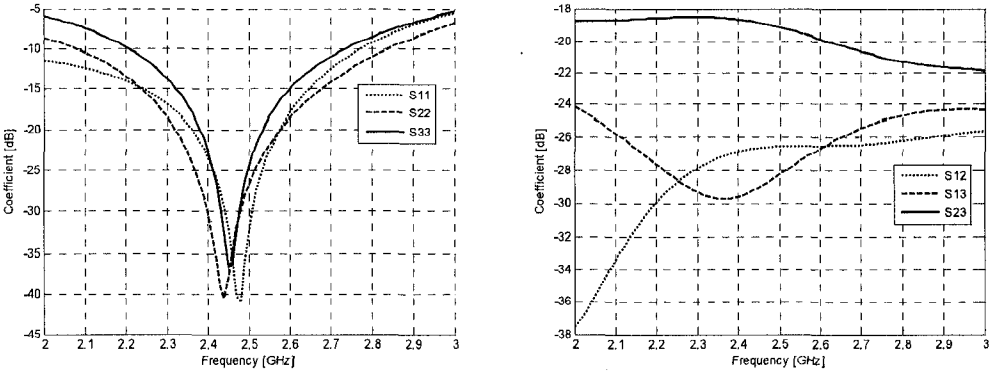

Figure 66 – S-parameters for Arbitrarily Shaped Plate

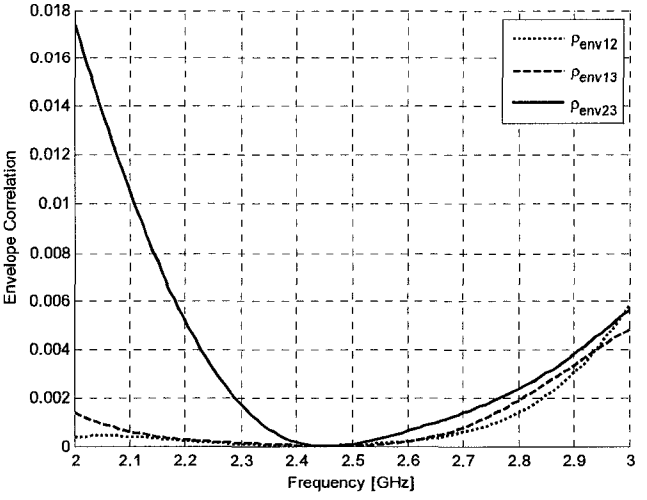

Figure 67– S-parameters for Arbitrarily Shaped Plate

We find the envelope correlation drops quite low around the center frequency, and increases gradually at both extremities of the frequency span. We find the envelope correlation is well below 0.1 over the entire measured frequency span, implying excellent performance for MIMO communications.

In the preceding discussion we have shown the strength of the method since we were able to consider an arbitrarily shaped perfectly conducting plate and design three very low envelope correlation antennas into the existing structure.

What is important to note is that an optimization scheme using the same plate and given the freedom to place arbitrary slot antennas would possibly return a similar design, with similar performance for MIMO communications. However, there is no ambiguity in our approach as we have shown the reasoning behind the low envelope correlation, i.e. unique excitation of characteristic modes – not just a simple matter of running an optimizer until a viable design is handed to the user.

5.9 – Concluding Remarks

In this chapter we discussed various methods one can use to control the excitation of unique sets of characteristic modes. In section 5.2 we discussed the modal theory applicable to MIMO antenna design, and showed that antennas exciting unique sets of CMs are ideal for MIMO communications.

In the simplest case, as shown in section 5.3 and 5.4 one can analyze a generic structure such as a perfectly conducting plate (or any other geometry) and compute the characteristic modes and modal currents. By analyzing these surface currents, and locating their maxima, we showed that one can predominantly excite individual characteristic modes with excitation schemes coinciding with the current maxima. In this initial foray we considered feeding via a voltage gap. Since the plate was not altered in any way, very low input resistance and high input reactance resulted (due to current shorts around the feed). We also considered an electrically small plate, showing that the electrical size is not the limiting factor but rather, the practicality of dealing with the undesirable input impedances and narrow bandwidths typically associated with electrically small antennas.

A solution to the input impedance problem was proposed in the form of slot antennas as discussed in section 5.5. This allowed the unique excitation of modes using the same principles as mentioned before, while simultaneously yielding good impedance matching. By re-computing the modes every time a new slot was added, as outlined in section 5.6, the location of the next antenna could be determined. This design methodology has been published in [14]. Another theoretical approach to MIMO antenna design involving physical symmetry arguments was discussed in section 5.7, which we will elaborate further on in Chapter 7.

Example designs were shown in section 5.8, with simulated S-parameters, far-field patterns and computed envelope correlations. In all examples the antennas have good impedance bandwidths, with very low envelope correlation between antenna pairs in the vicinity of the design frequency. Additionally, the low envelope correlation was maintained over very wide bandwidths. The first two designs involved models of cell phone chassis and elaborated on the various advantages of using CM theory in designing MIMO antennas. These advantages include: low envelope correlation due to unique set of modal excitation, freedom to choose reference impedances without changing envelope correlation, and the flexibility in the choice of feeding mechanisms.

Furthermore, the first example design was constructed and tested, with the measured S-parameters agreeing well with simulation. From the measured S-parameters, we were also able to compute the envelope correlation, which also agreed well with simulation results.

The preceding chapter focused on designing MIMO antennas by exciting unique groups of characteristic modes, which yielded far-field orthogonality of antenna patterns. This approach assumed a perfect scattering environment, where the region of interest for orthogonality is the entire far-field sphere. In the next chapter we will consider the practical case of non-uniform spread of incident electromagnetic power and use the theory of generalized characteristic modes to design low envelope correlation antenna for these practical distributions of interest.

CHAPTER 5 REFERENCES

[1] R. Garbacz, H. Newman, "Characteristic Modes of Symmetric Wire Cross", *IEEE Transactions on Antennas and Propagation*, Vol. AP-28, No. 5, Sept 1980.

[2] R. F. Harrington, J. Mautz, "Control of Radar Scattering by Reactive Loading", *IEEE Transactions. on Antennas and Propagation*, Vol. AP-20, No. 4, pp 446 – 454, July 1972.

[3] R. Garbacz, D. Pozar, "Antenna Shape Synthesis using Characteristic Modes", *IEEE Transactions on Antennas and Propagation*, Vol. AP-30, No. 3, May 1982.

[4] G. Amendola, G. Angiulli, G. Di Massa, "Numerical and Analytical Characteristic Modes for Conducting Elliptic Cylinders", *Microwave and Optical Technology Letters*, vol. 16, No. 4, November 1997.

[5] N. Inagaki, R. Garbacz, "Eigenfunctions of Composite Hermitian Operators with Application to Discrete and Continuous Radiating Systems", *IEEE Transactions on Antennas and Propagation*, Vol. AP-30, No. 4, pp 571 – 575, July 1982.

[6] N. Inagaki, R. Garbacz, "Antenna Synthesis and Optimization Using Weighted Inagaki Modes", *IEEE Transactions on Antennas and Propagation*, Vol.32, No.2, pp 159-165, July 1984.

[7] N. Inagaki, R. Garbacz, "Antenna Synthesis and Optimization Using Generalized Characteristic Modes", *IEEE Transactions on Antennas and Propagation*, Vol. AP-38, No. 6, pp 862 – 868, June 1990.

[8] W. Schroeder, C. Famdie, K. Solbach, "Utilization and Tuning of the Chassis Modes of a Handheld Terminal for the Design of Multiband Radiation Characteristics," *Wideband and Multi-band Antennas and Arrays*, IEE, September 2005, pp. 117-121.

[9] C. Famdie, W. Schroeder, K. Solbach, "Numerical Analysis of Characteristic Modes on the Chassis of Mobile Phones," *European Microwave Conference,* Oct. 2007, pp. 987 – 990.

[10] S. Chadhury, W. Schroeder, H. Chaloupka, "MIMO Antenna System based on Orthogonality of the Characteristic Modes of a Mobile Device," *2nd International ITG Conference on Antennas*, March 2007, pp. 58 – 62.

[11] P. Hallbjorner, "The Significance of Radiation Efficiencies when using S-parameters to calculate the received signal correlation from two antennas," *IEEE Antennas and Wireless Letters,* Vol. 4, 1995, pp 97 – 99.

[12] J. Thaysen, K. Jakobsen, "Envelope Correlation in (N, N) MIMO Antenna Array from Scattering Parameters," *Microwave and Optical Technology Letters*, Vol.48, No.5, pp. 832-834, May 2006.

[13] R.G. Vaughan, J.B. Andersen, "Antenna Diversity in Mobile Communications," *IEEE Trans on Vehicular Technology*, Vol. VT-36, No. 4, pp. 149 – 172, Nov. 1987.

[14] **Jonathan Ethier**, Eric Lanoue and Derek McNamara, "MIMO Handheld Antenna Design Approach Using Characteristic Mode Concepts", *Microwave and Optical Technology Letters*, Volume 50, No. 7, July 2008.

Chapter 6

Generalized Characteristic Mode Theory and MIMO Antenna Design

6.1 – Introduction

In Chapter 5 we considered the use of Characteristic Modes (CM) [1] to design MIMO antennas. We used the far-field orthogonality of the modes to design antennas with low envelope correlation over the entire sphere. In section 6.2 we will consider an alternative modal formulation, Generalized Characteristic Modes (GCM) [2] which determines a set of modal currents that have far-field patterns orthogonal relative to a specific weight. This weight can simply be a constrained region of the far-field, such as the MCS case [3], a sectored window, or it can be more complicated and take the form of a function such as a Laplacian [4], Gaussian [5] or Double Exponential [6]. We will extend this concept in section 6.3 to include polarization effects, yielding a polarization sensitive generalized characteristic mode formulation, the first time such a formulation has been proposed.

We will show that the design methodology developed in Chapter 5 where we were able to control the excitation of regular CMs can also be applied to the control and excitation of GCMs, specifically the newly defined polarization sensitive GCMs. We will explore two such designs in section 6.4, for two uniquely defined PAS distributions. These distributions include the urban macrocell, ideally suited for mobile phones and the indoor picocell, ideally suited for laptop antennas. We will also consider an oft-omitted

MIMO antenna performance metric, the total array reflection coefficient (TARC) which accounts for the effect of all MIMO antennas in a system operating simultaneously, and predicting the reduced impedance matching caused by destructive interference.

We will conclude in section 6.5 with an investigation of various MIMO antenna designs and how well they perform in scattering environments they were not specifically designed for. The results will show the necessity of not simply designing for full-sphere orthogonality, but rather for the particular PAS distribution a MIMO system is bound to reside within.

6.2 – Generalized Characteristic Modes and MIMO

The use of Generalized Characteristic Modes (GCM) in MIMO antenna design is of greatest benefit when the communications scenario does not assume an equally likely spread of incident electromagnetic energy. For these cases, we require the envelope correlation between antennas to be measured with respect to the given power angular spread (PAS). The classical characteristic modes yield patterns that are orthogonal over the entire sphere, but have no particular bias for any given constrained region defined by an arbitrary PAS. This is where the GCMs show their usefulness, since these modes are defined to be orthogonal relative to some arbitrarily chosen weighting function. In fact, in the limit of the weight function becoming the entire far-field sphere, the GCMs become equivalent to the CMs, showing CMs are a special case of the GCMs (hence the 'generalized' moniker). The generalized modes can be computed by solving the eigenvalue problem:

$$[X][J_n] = \lambda_n'[H][J_n] \tag{6.2-1}$$

where $[H_{ij}] = \langle W(\theta,\phi)F_i(\theta,\phi), W(\theta,\phi)F_j(\theta,\phi)\rangle / \eta_o$, the functions $F_{i/j}(\theta,\phi)$ are the far-fields of the moment method expansion functions and $W(\theta,\phi)$ is the chosen

weighting function. The far-field patterns produced by the surface currents J_n are orthogonal relative the weight function in the following manner:

$$\langle WE_n, WE_m \rangle = \oiint_{S_\infty} (WE_n) \cdot (WE_m)\, dS = A\delta_{mn} \tag{6.2-2}$$

where A is a constant, and is dependent on how one normalizes the surface currents. We shall normalize the surface currents to radiate 1 watt over the entire sphere, making the constant A always less than unity. The angular dependence of the functions W and E is assumed throughout. What is important is the integral is zero when *m* does not equal *n*, and we therefore have far-field orthogonality relative to the weight $W(\theta,\phi)$. Thus, following precisely the same arguments from Chapter 5, a collection of antenna ports that each excites a unique set of GCMs will have low envelope correlation relative to the chosen weight function $W(\theta,\phi)$. The GCMs are thus useful for constrained regions of orthogonality where the incident electromagnetic power is equally likely in both polarizations and constant over the prescribed region. Two examples of regions such as these include the MCS and Sectored regions, described below:

$$\text{MCS: } W(\theta,\phi) = \text{constant},\ 60^o \le \theta \le 90^o, 0^o \le \phi \le 360^o \tag{6.2-3a}$$

$$\text{Sector: } W(\theta,\phi) = \text{constant},\ 60^o \le \theta \le 90^o, 30^o \le \phi \le 150^o \tag{6.2-3b}$$

The generalized characteristic modes determine a set of surface currents that reside on the structure being analyzed which produce far-field patterns that are mutually orthogonal over the region $W(\theta,\phi)$ defined either as MCS or Sectored (or any other arbitrary distribution). While the MCS PAS is a good approximation to the incident electromagnetic power a mobile would expect to see in practice, it still falls short of capturing the true functional distribution as well as the polarization sensitivity of typical mobile scattering environments. Kalliola et al. [6] performed extensive measurements of these distributions, and found results something akin to MCS (as discussed in Chapter 2, section 2.2.3) although the polarization discrimination was quite significant. In order to properly measure the various MIMO related quantities, namely envelope correlation and mean effective gain, the polarization bias must be taken into account.

A special case of note occurs when $W(\theta,\phi) = 1$ for all angles, which triggers the GCMs to be equivalent to the CMs.

6.3 –Polarization Sensitive Generalized Characteristic Modes

In order to deal with the polarization bias (namely the strong theta polarization) found in measured PAS distributions, we need to include polarization sensitivity in the GCM formulation. This is the first time such a derivation has been developed. Moreover, this is the first time the GCM formulation has been applied to MIMO antenna design.

We begin with the derivation of the [H] operator:

$$[X][J_n] = \lambda_n'[H][J_n] \tag{6.3-1}$$

where $[H_{ij}] = \langle W(\theta,\phi)F_i(\theta,\phi), W(\theta,\phi)F_j(\theta,\phi)\rangle / \eta_o$. Recall that the operator $\langle A,B\rangle$ represents the inner product taken over the sphere at infinity. We begin by expanding the $W(\theta,\phi)$ function into theta and phi polarized components as follows:

$$W(\theta,\phi) = W_\theta(\theta,\phi)\hat{\theta} + W_\phi(\theta,\phi)\hat{\phi} \tag{6.3-2}$$

Recall that previously the function $W(\theta,\phi)$ was a scalar quantity but we have now defined it as a vector quantity. The expansion functions $F_i(\theta,\phi)$ and $F_j(\theta,\phi)$ can be expanded similarly:

$$F_i(\theta,\phi) = F_{i\theta}(\theta,\phi)\hat{\theta} + F_{i\phi}(\theta,\phi)\hat{\phi} \tag{6.3-3}$$

and

$$F_j(\theta,\phi) = F_{j\theta}(\theta,\phi)\hat{\theta} + F_{j\phi}(\theta,\phi)\hat{\phi} \tag{6.3-4}$$

Applying these expanded weighting functions to the original expression for the [H] operator, we find:

$$\begin{aligned}[H_{ij}] = \Big\langle &\left(W_\theta(\theta,\phi)\hat{\theta} + W_\phi(\theta,\phi)\hat{\phi}\right)\left(F_{i\theta}(\theta,\phi)\hat{\theta} + F_{i\phi}(\theta,\phi)\hat{\phi}\right), \\ &\left(W_\theta(\theta,\phi)\hat{\theta} + W_\phi(\theta,\phi)\hat{\phi}\right)\left(F_{j\theta}(\theta,\phi)\hat{\theta} + F_{j\phi}(\theta,\phi)\hat{\phi}\right)\Big\rangle / \eta_o\end{aligned} \tag{6.3-5}$$

In simplifying expression 6.3-5 we find the result:

$$[H_{ij}]=\left[H_{\theta ij}\right]+\left[H_{\phi ij}\right] \tag{6.3-6}$$

where:

$$\left[H_{\theta ij}\right]=\left\langle W_{\theta}(\theta,\phi)F_{i\theta}(\theta,\phi),W_{\theta}(\theta,\phi)F_{j\theta}(\theta,\phi)\right\rangle/\eta_{o} \tag{6.3-7a}$$

$$\left[H_{\phi ij}\right]=\left\langle W_{\phi}(\theta,\phi)F_{i\phi}(\theta,\phi),W_{\phi}(\theta,\phi)F_{j\phi}(\theta,\phi)\right\rangle/\eta_{o} \tag{6.3-7b}$$

Casting this back into the original eigenvalue problem: $[X][J_n]=\lambda_n'[H][J_n]$ we find the newly defined far-field orthogonality is given by:

$$\begin{aligned}\left\langle W_{\theta}(\theta,\phi)E_{m\theta}(\theta,\phi),W_{\theta}(\theta,\phi)E_{n\theta}(\theta,\phi)\right\rangle+\ldots\\ \left\langle W_{\phi}(\theta,\phi)E_{m\phi}(\theta,\phi),W_{\phi}(\theta,\phi)E_{n\phi}(\theta,\phi)\right\rangle=A\delta_{mn}\end{aligned} \tag{6.3-8}$$

where $E_{m\theta}(\theta,\phi)$ and $E_{n\theta}(\theta,\phi)$ are the m^{th} and n^{th} far-field patterns produced by the modal surface currents J_m and J_n, A is a constant depending on how one normalizing these currents (A < unity) and δ_{mn} is the Kronecker delta.

We therefore have the orthogonality of the modes in the precise manner we desire provided we define the function $W(\theta,\phi)=W_{\theta}(\theta,\phi)\hat{\theta}+W_{\phi}(\theta,\phi)\hat{\phi}$ appropriately. Since we have orthogonality of the form: $\langle W_{\theta}E_{m\theta},W_{\theta}E_{n\theta}\rangle+\langle W_{\phi}E_{m\phi},W_{\phi}E_{n\phi}\rangle=A\delta_{mn}$ and we require $\left\langle E_{m\theta},(XPR)P_{\theta}E_{n\theta}\right\rangle+\left\langle E_{m\phi},P_{\phi}E_{n\phi}\right\rangle=A\delta_{mn}$ given a power angular spread defined by the functions $(XPR)P_{\theta}$ and P_{ϕ}, we can then equate the weighting functions to the PAS functions as follows:

$$W_{\theta}(\theta,\phi)=\sqrt{XPR}\sqrt{P_{\theta}(\theta,\phi)} \tag{6.3-9a}$$

$$W_{\phi}(\theta,\phi)=\sqrt{P_{\phi}(\theta,\phi)} \tag{6.3-9b}$$

thus giving us the necessary orthogonality for an arbitrarily defined PAS function, with theta and phi polarization discrimination. We shall denote these modes polarization-sensitive Generalized Characteristic Modes.

6.4 – MIMO Antenna Design for Practical Scattering Environments

6.4.1 – Description of PAS Regions of Interest

As described in Section 2.2's coverage of MIMO, an excellent approximation to experimentally measured PAS is the double exponential. As measured by Kalliola [6], each environment exhibits a unique set of values describing the center, spread and relative strengths of each polarization. The two PAS distributions of greatest interest are the Urban Macrocell Environment and Indoor Picocell Environment. These two distributions are shown in Figure 68.

The Urban Environment best represents the PAS a mobile user would find themselves in as they go about their day. The Indoor Picocell Environment best represents the static environment found in an office or workspace, which has direct application to laptop based antennas for MIMO communications. We will consider designing MIMO antennas for these two environments, namely a mobile MIMO antenna design for an *urban macrocell* environment and a laptop antenna design for an *indoor picocell* environment.

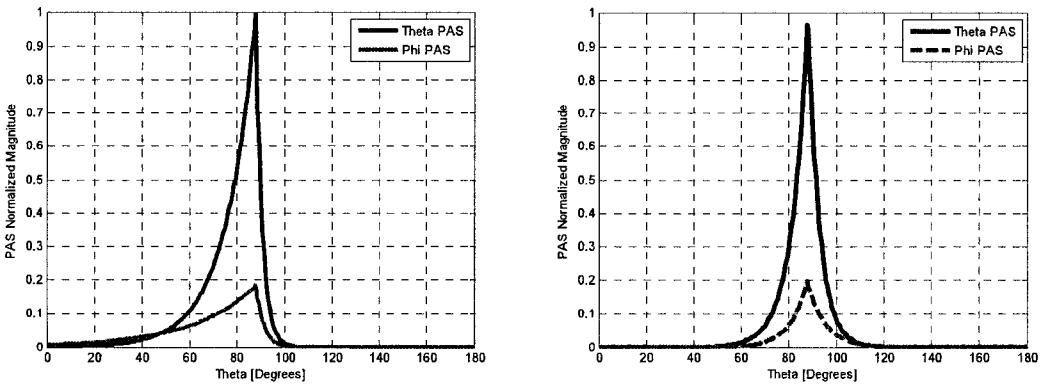

Figure 68 – Double Exponential PAS Functions Based on Experimental Measurements in [6], (a) Urban Macrocell, (b) Indoor Picocell

6.4.2 – Polarization Sensitive GCM Design for Urban Macrocell

We consider a typical bar-type mobile phone chassis, 1 lambda by 0.5 lambdas at 2.5 GHz or 120mm by 60mm. We consider the *polarization sensitive* generalized characteristic modal currents, with orthogonality properties matching the Urban Macrocell PAS described by Kalliola et al [6 – Table IV, pg. 831]. The four dominant polarization sensitive GCM modes are shown in Figure 70 (a) – (d). The physical mesh used in the GCM computations is shown in Figure 69. The mesh density was 80 triangles by 40 triangles, for a total of 3,200 triangles. The average edge length in the simulation was (1/80) x 120mm = 1.5mm or 1.25% of a wavelength, definitely implying a dense enough mesh for accurate simulation results. Rule of thumb for moment method meshing typically requires triangle edge length between 5 – 10% of a wavelength as discussed in Chapter 3.

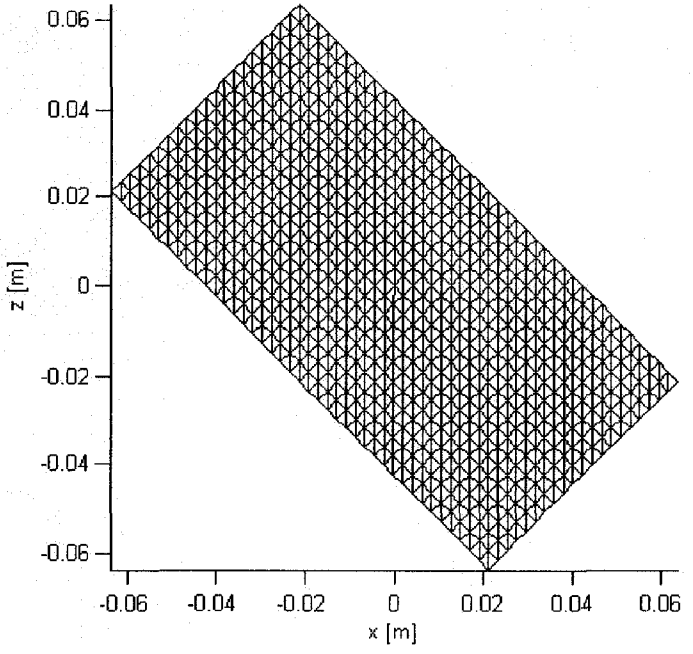

Figure 69 – Physical Mesh Used to Compute Polarization Sensitive Generalized Characteristic Modes

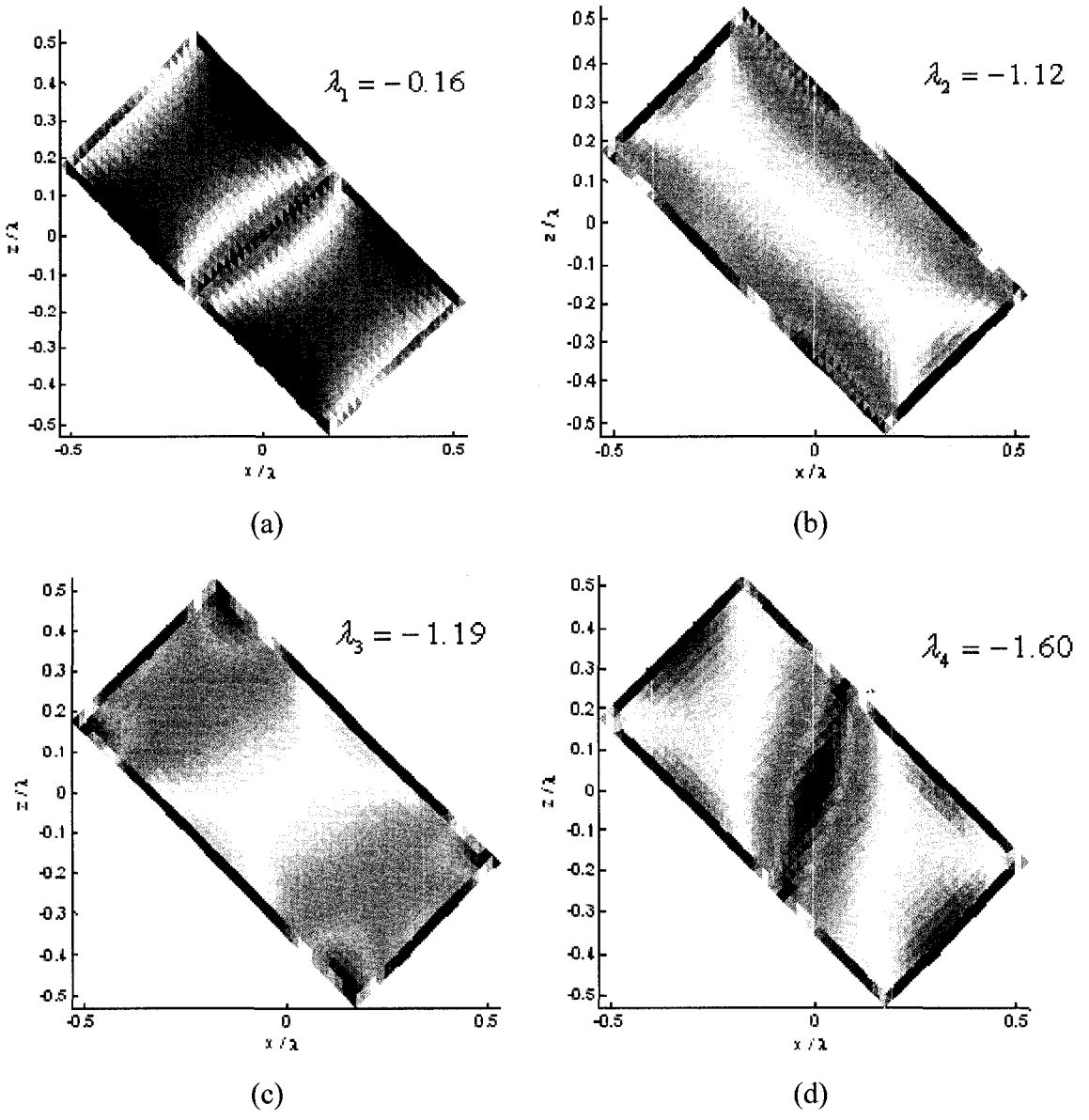

Figure 70 – First Four Polarization Sensitive Generalized Characteristic Modes, Current in [dB]

We follow precisely the same design methodology as developed in Chapter 5, following the step by step procedure discussed at the end of Chapter 5, Section 5.6. We will also show another property of this method: multiple design paths leading to similar final designs. Our first design path involves utilizing the dominant polarization sensitive GCM, as shown in Figure 70 (a). We begin by placing the first antenna at the center of the location marked in Figure 71. In doing so we excite the modes associated with current maxima at said location. We then re-compute the GCM's in the presence of the first slot

antenna and notice a newly formed low-eigenvalue mode that has surface current maxima separate from the first antenna. This mode is shown in Figure 72, with the second feeding location clearly marked.

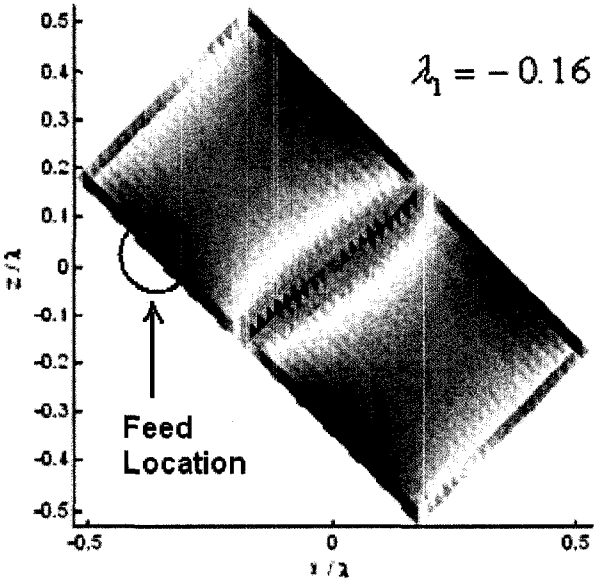

Figure 71 – Dominant Polarization Sensitive GCM, with Optimize Feeding Location Marked

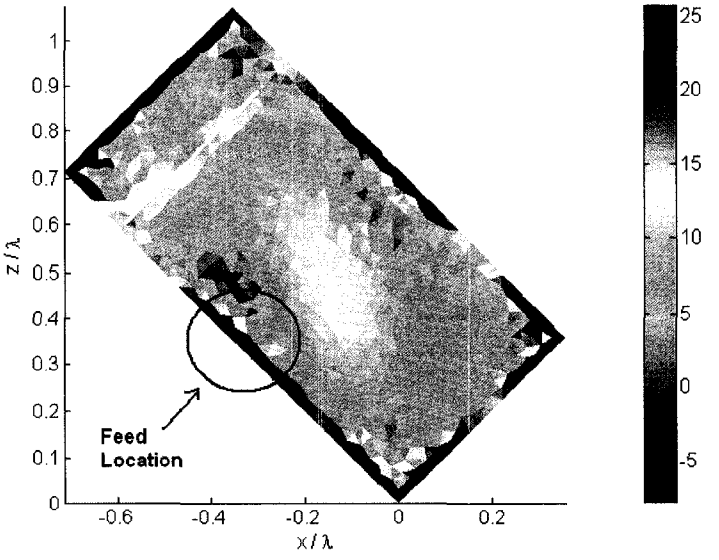

Figure 72 – Newly Formed Dominant Polarization Sensitive GCM including First Antenna, with Optimize Feeding Location Marked

Adding the second antenna, we re-compute the GCMs again and note yet another newly formed GCM with a current distribution that has clearly distinct feeding locations forms. This mode is shown in Figure 73, with the feeding location noted. The final three-antenna design is shown in Figure 74 (a) and (b), showing both the meshed structure as well as the physical dimensions of the slot antennas.

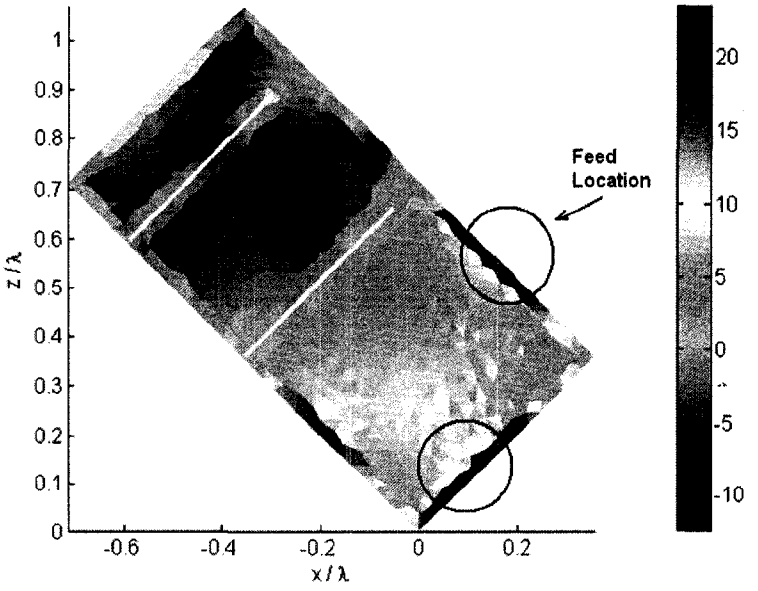

Figure 73– Newly Formed Dominant Polarization Sensitive GCM including Two Antennas, with Optimal Feeding Locations Marked

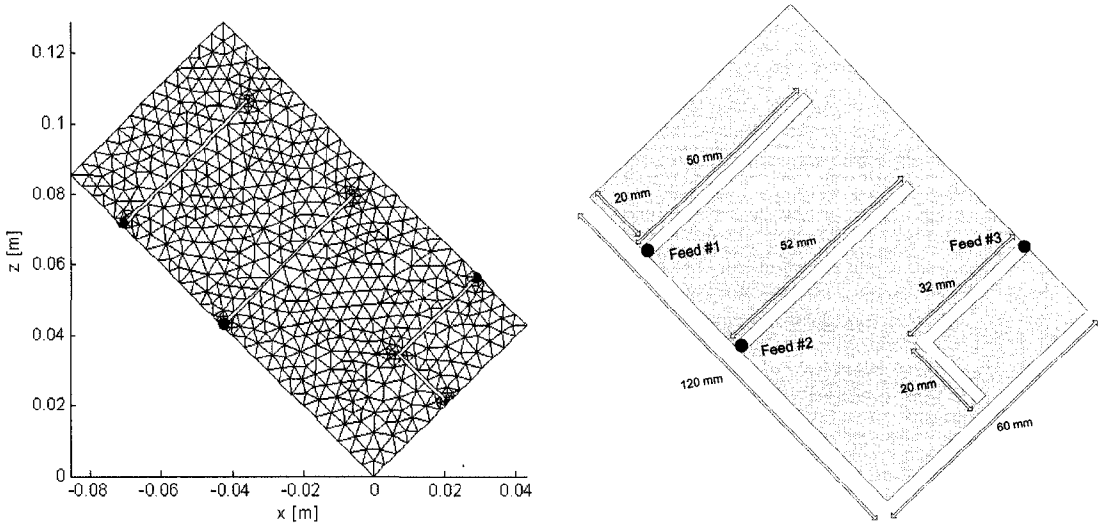

Figure 74 – Physical Dimensions and Mesh for Three Antenna Urban Macrocell Design

A secondary design route is possible, but one finds the final design is the same in the end. Rather than starting with the lowest eigenvalue mode Figure 70 (a), we begin with the third mode, shown in Figure 70 (c). The resulting meshed structure, as well as the new mode of interest found by re-computing the GCMs is shown in Figure 75. By placing the first slot antenna in this manner, we find the second antenna is precisely the same as the first antenna placed in the initial design route. The third antenna would be precisely the same as well, since both methods lead to the same initial first two antennas.

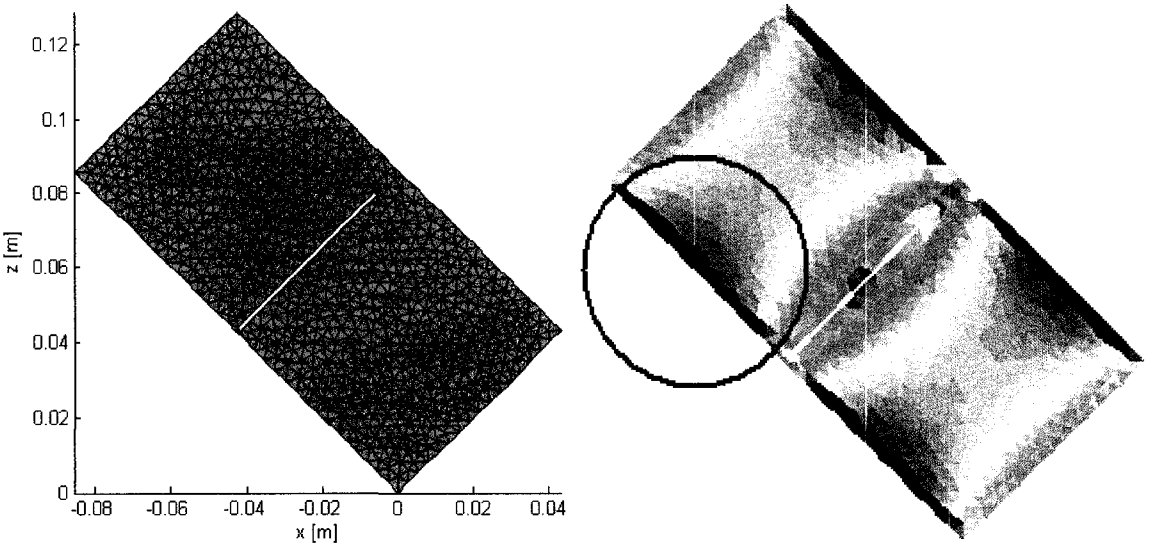

Figure 75 – Alternative Design Route for Urban Macrocell Design

Let us now consider the S-parameters of the urban mobile design, as shown in Figure 76 (a) and (b). We observe an excellent 17% 10dB RL bandwidth, with the antennas resonant at slightly different frequencies. Surprisingly, we find the mutual coupling for this design is larger than the mutual coupling computed in the many designs in chapter 5. Furthermore, we find the mutual coupling peaks at center frequency, which is the opposite of what we expect from previous full-sphere designs. We then compute the envelope correlation, as shown in Figure 77. We see an excellent 16% bandwidth where the envelope correlation is less than 0.1. The envelope correlations do not necessarily overlap with minima at the desired frequency, nor are they necessarily zero at the center frequency either. However, there is a very distinct operating band where the correlation is indeed low. It is important to point out that the method of computation for the envelope

correlation uses the field integration method, as opposed to the S-parameter method, since no known relationship exists between S-parameters and arbitrarily defined PAS function – only between S-parameters and the full sphere.

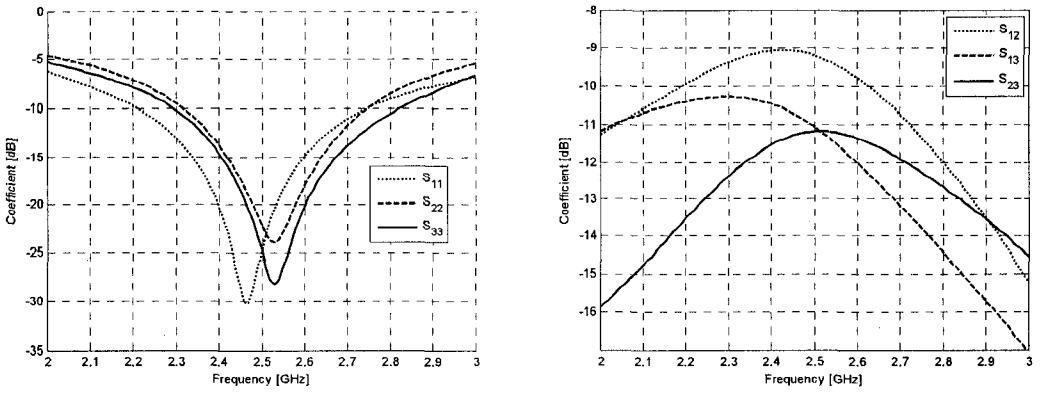

(a) (b)

Figure 76 – Simulated S-parameters of Mobile Urban Macrocell Three Antenna Design

We now consider the mean effective gain of the antennas relative to the chosen double exponential power distribution, including the effects of finite conductivity, as shown in Figure 78. The values for MEG are reasonable when compared to the measured results quoted by Kalliola [6] which range from -5.1 dB to -9.8 dB. Our values for MEG (at center frequency) are between -4 dB and -8 dB. It should be noted that the results quoted by Kalliola are for a single antenna on a mobile device, whereas our values for MEG are for the set of three antennas on a single mobile chassis. The presence of multiple antennas will obviously constrain the achievable values for MEG since with a single antenna one has the luxury of orienting it any way one desires – a luxury that does not exist when dealing with multiple antennas since we are trying to minimize the envelope correlation between all antenna pairs.

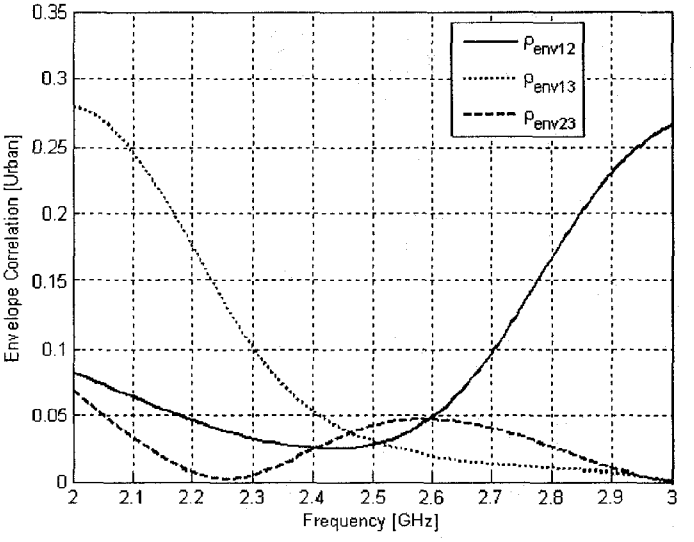

Figure 77 – Simulated Envelope Correlation of Mobile Urban Macrocell Three Antenna Design

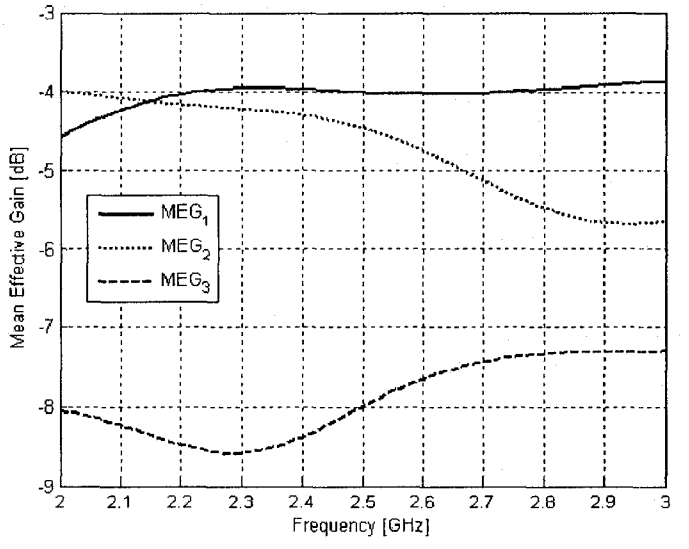

Figure 78 – Simulated Mean Effective Gain of Mobile Urban Macrocell Three Antenna Design

Notice also in Figure 78 that the MEG values for antenna 1 and 2 are quite reasonable, but antenna 3 is less than ideal. The third antenna, in the form of a bent slot antenna, is the cause of the low MEG. Should we extend the slot outwards rather than bending it as shown in Figure 79 (c) one maintains similar impedance bandwidth, vastly improved MEG (Figure 79 (b)) but the envelope correlation suffers greatly (Figure 79 (a)). There is a tradeoff between low envelope correlations, large values of MEG, equal values of

MEG, and wide impedance bandwidth. Fortunately, the design procedure developed in this thesis is able to ensure low envelope correlation and reasonable impedance bandwidth, but it does not explicitly consider MEG in the computation and is therefore not guaranteed in the final design. Mean effective gain and envelope correlation can be at odds with each other: the tighter the constraint on the orthogonality, the less room one has to have directive patterns in the directions of desired orthogonality.

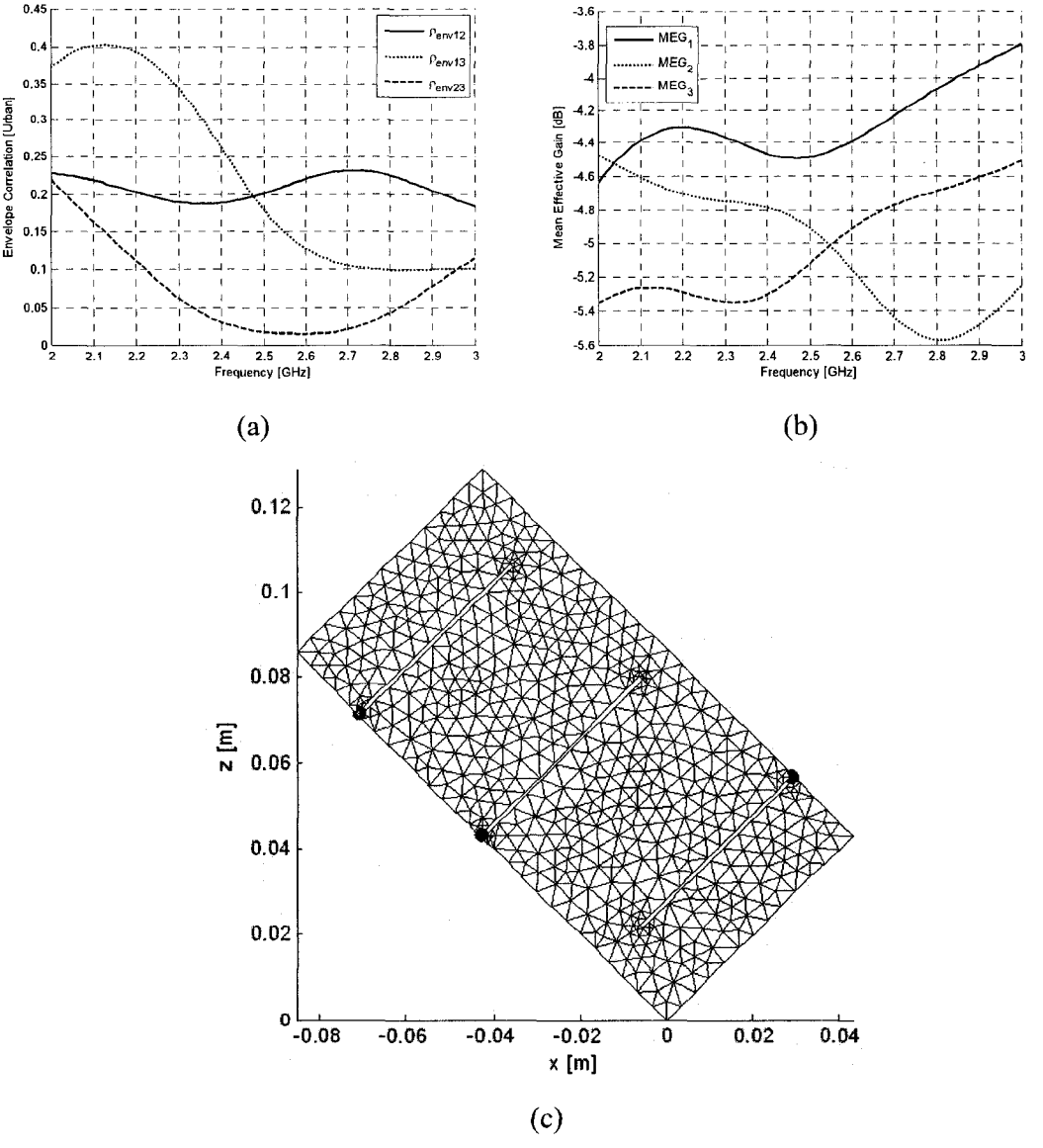

Figure 79 – Plots of (a) Envelope Correlation and (b) Mean Effective Gain of Alternative Urban Macrocell Design, as well as the (c) Physical Mesh

Purely for illustrative purposes, we show normalized 3D polar plots of the electric field far-field embedded patterns in figure 80 (a) – (c). Once again, we emphasize that these plots are for qualitative purposes; they are not included to give technical details regarding the fields.

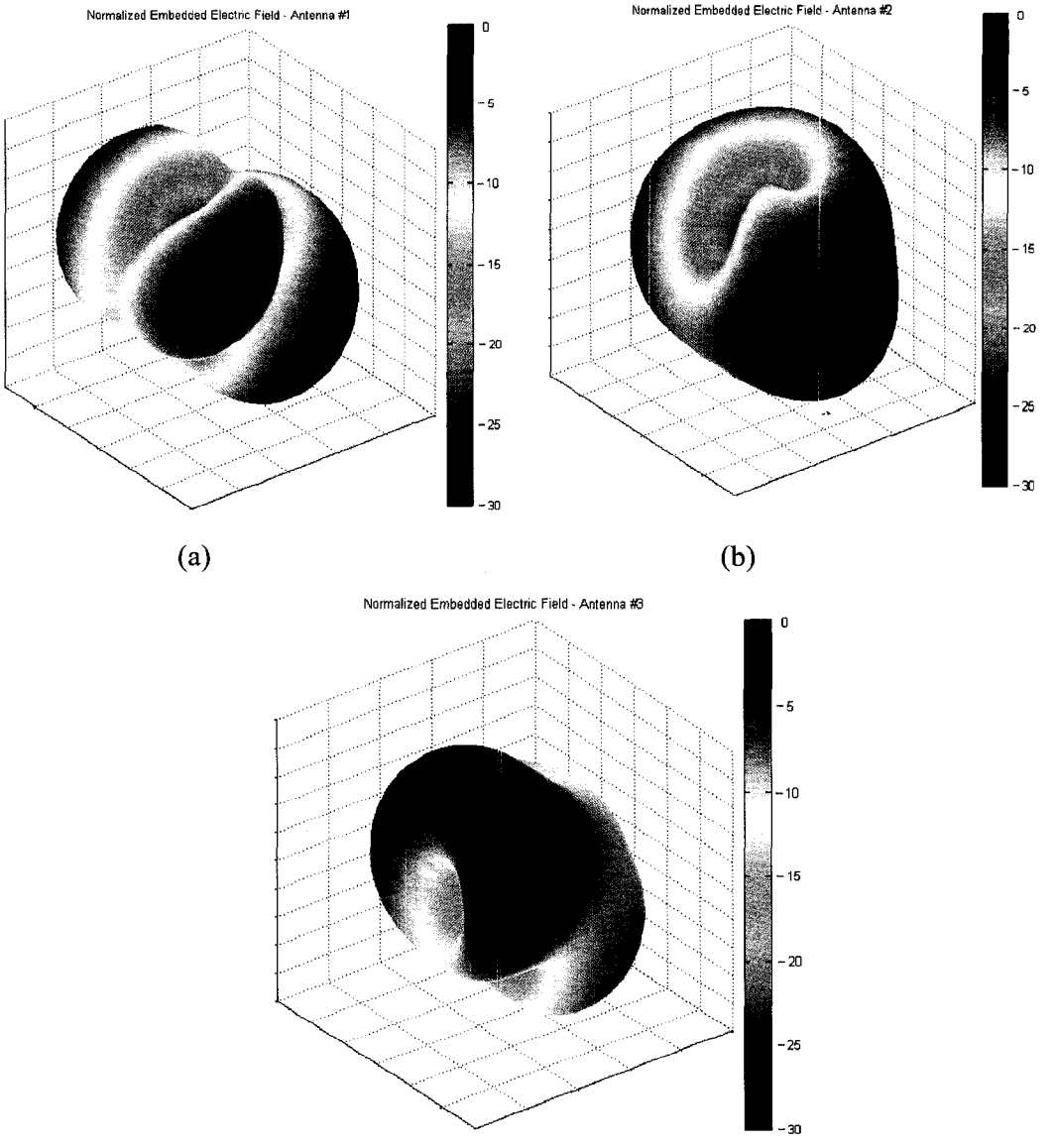

Figure 80 – 3D Polar Plots of Normalized Electric Field (a) Antenna 1, (b) Antenna 2, (c) Antenna 3

In order to further justify the methodology we developed in this thesis, we compute the modal excitation coefficients of the design, in a similar manner as we did in chapter 5. This allows us to judge which modes are being excited and with what strength. We compute these coefficients and normalize such that the summation of these terms yields unity for each antenna. We can therefore conclude, given these values, about the percentage of power each mode is responsible for relative to the region of orthogonality. The modal excitation coefficients are shown in Figure 81, and summarized in Table 9.

The percentage of power associated with unique GCMs are lower than what we computed in Chapter 5, but this is to be expected since our envelope correlation is not as low as the full-sphere CM designs in chapter 5. Since our envelope correlations are between 0.025 and 0.05 at our center frequency, we expect some cross-excitation of modes between the antennas.

In particular, we notice that Antenna 1 excites mode 6 with strength of 5.8%, which is one of antenna 3's strongest excited modes. This leads to an increase in the envelope correlation between antenna 1 and 3, denoted $\rho_{env(1,3)}$. Additionally, antenna 3 excites mode 5 with strength of 6%, which is one of Antenna 1's strongest excited modes. This further increases in the envelope correlation between antenna 1 and 3. The same argument applies to the remaining two antennas pairs, only with different modes considered. At times is appears that cross-excitation is unavoidable, but one tries to minimize it as much as possible. Under these percentage power results, we find that all envelope correlations are below 0.05 at center frequency, and additionally maintain a bandwidth of 16% over which all envelope correlations are below 0.1 (see Figure 77).

The design methodology, newly developed modal formulation and experimental results have been published in [10].

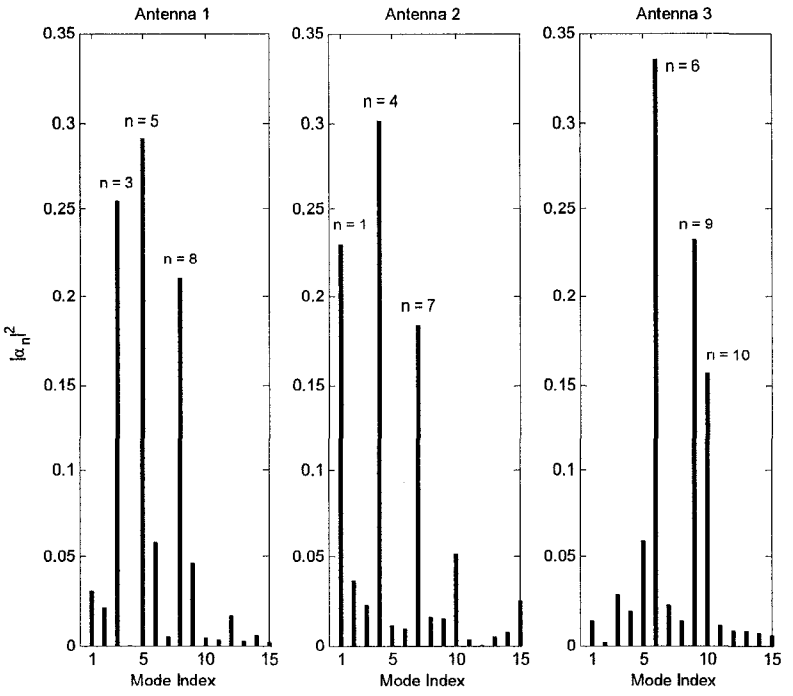

Figure 81 – GCM Mode Spectrum of Urban Macrocell Mobile Design

Table 9 – Details of the Mode Spectrum, Including Radiation Efficiency

Antenna #	Dominant Modes	Percentage of Power	Radiation Efficiency
1	3, 5 & 8	75.7%	99.2%
2	1, 4 & 7	71.5%	99.4%
3	6, 9 & 10	72.4%	91.5%

In order to validate a majority of the simulated design parameters we construct and experimentally measure the S-parameters of the three antenna urban mobile design. Similar in construction as the experimental design in Chapter 5, we once again scale the model, this time using a scale factor of 1:3.8, resulting in a shifted center frequency of 660 MHz. The resulting design is 460mm by 307mm, with all slot dimensions scaled up by a factor 3.8 as well. The physically constructed design is shown in Figure 82, and once again, we find a balun is not required since the feed is many orders smaller than the operating wavelength.

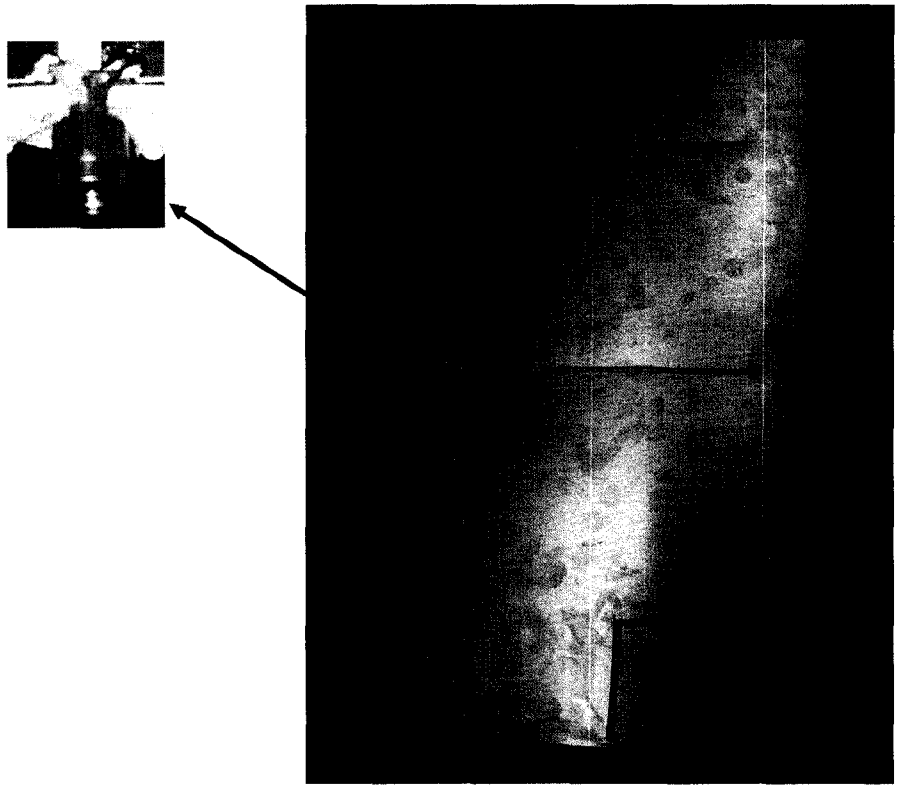

Figure 82 – Photo of Experimental Urban Macrocell Mobile Design

We conclude by comparing the measured and simulated S-parameters in Figure 83 of the constructed design shown in Figure 82. The measured input reflection coefficients all match well with simulated data, with all measurements showing the same or better bandwidth performance. We see all S-parameters match well, with the possible exception of S23, whose general trend is similar, but is off at some frequencies by around 1.5 dB.

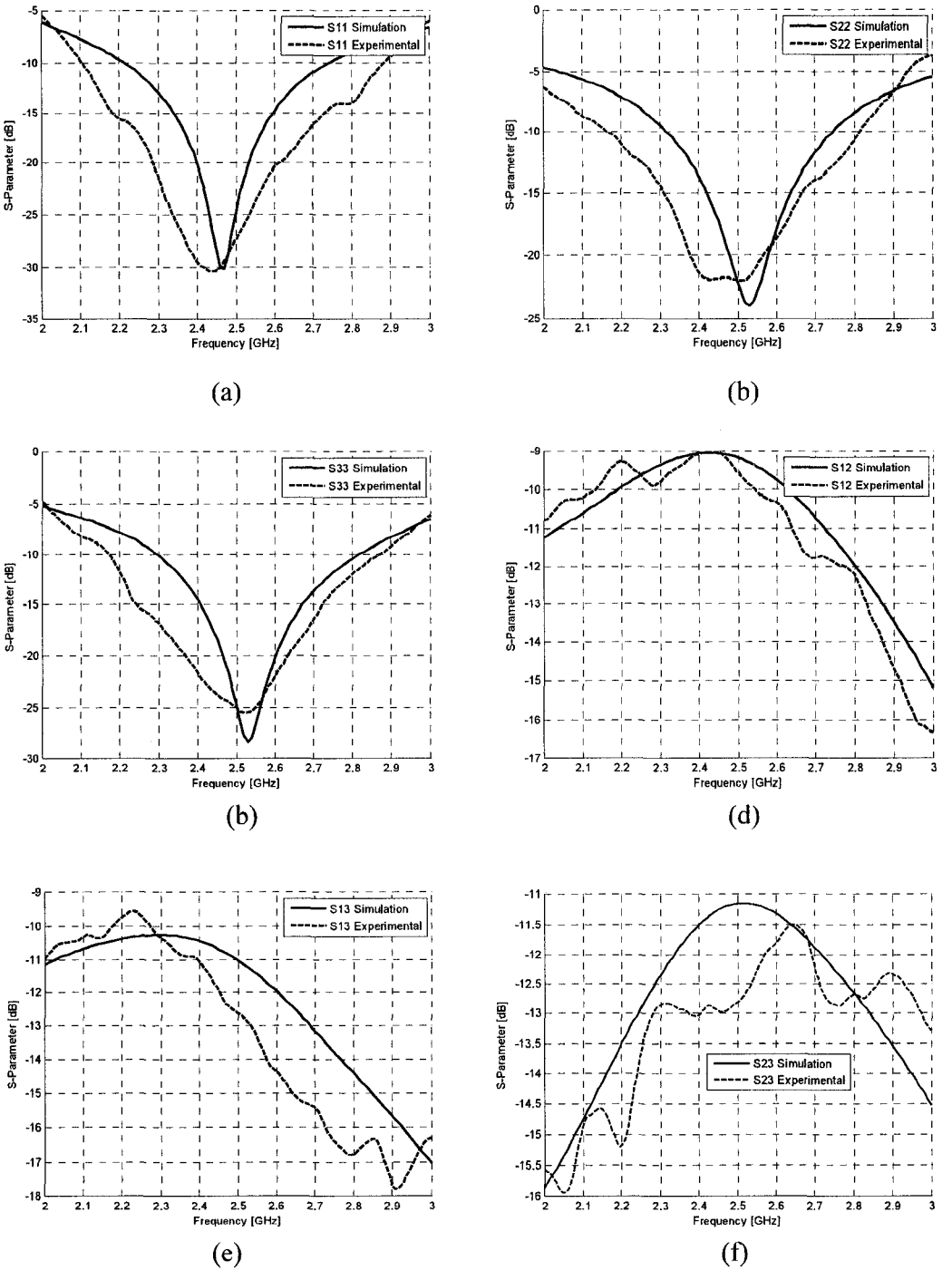

Figure 83 – Comparison of Measured and Simulated S-parameters of Urban Macrocell Mobile Three Antenna Design

We have outlined three important measures for MIMO antenna performance, including low envelope correlation between antenna pairs relative to the scattering environment, large values for mean effective gain, and to a lesser extent, approximately equal magnitude mean effective gain for all antennas. The usual parameter of impedance matching, as required in most antenna applications is present in MIMO communications as well. However, the true measure of input reflection coefficient is not as straightforward at first glance. Since all antennas in a MIMO system are operating simultaneously, the true input reflection coefficient of an antenna port must take into account the incident waves at said port due to the operation of the remaining ports in the system. This is synonymous with the active input reflection coefficient in array design. Since the information being transmitted by each MIMO antenna is in some ways distinct, there is no definitive method of computing the actual active input reflection coefficient in general, whereas in the array approach, the information at each element is identical.

However, one can measure what is known as the total array reflection coefficient, or TARC for short, which is discussed in [7] and [8]. It is a straightforward computation where one assumes unit amplitude incident waves at every antenna port of the MIMO system, where the waves have uniformly random phase. One then computes the resulting reflected waves at all ports, which of course takes into account the effect of all ports excited simultaneously. One then computes an averaging function of the reflected power over the incident power forming the quantity TARC and this is performed over the frequency range we are considering (keeping the randomly chosen phase constant over these frequencies). A new set of random phases are chosen, and then the process is repeated. Repeating this process many times develops an upper and lower bound to the values of TARC, with the upper bound serving at the 'worst case scenario' for the system performance, as measured by TARC. Since our mobile design for the urban macrocell environment has noticeably larger mutual coupling than previous designs, we wish to characterize the design using the additional performance metric TARC.

One begins by randomly choosing the phase for the excitation vector $[a]$, maintaining unit magnitude incident waves. The reflected waves are then computed using the

expression $[b]=[S][a]$ where $[S]$ are the scattering parameters of the antenna system and $[b]$ are the resulting reflected waves. At each frequency of interest, the quantity TARC is computed using the expression:

$$TARC = \frac{\sqrt{\sum_{i=1}^{N}|b_i|^2}}{\sqrt{\sum_{i=1}^{N}|a_i|^2}}$$

TARC is bound between 0 and 1, with 0 indicating all incident power at the ports is radiated, and a value of 1 indicating all incident power is reflected and / or enters into the ports. By randomly selecting the phase of the incident waves, we compute TARC over frequency and plot the resulting curve. This is repeated numerous times, forming the upper and lower bounds as previously discussed. We show in Figure 84 (a) an example run through 10 iterations, whereas Figure 84 (b) distinctly shows the upper and lower bounds on the value of TARC.

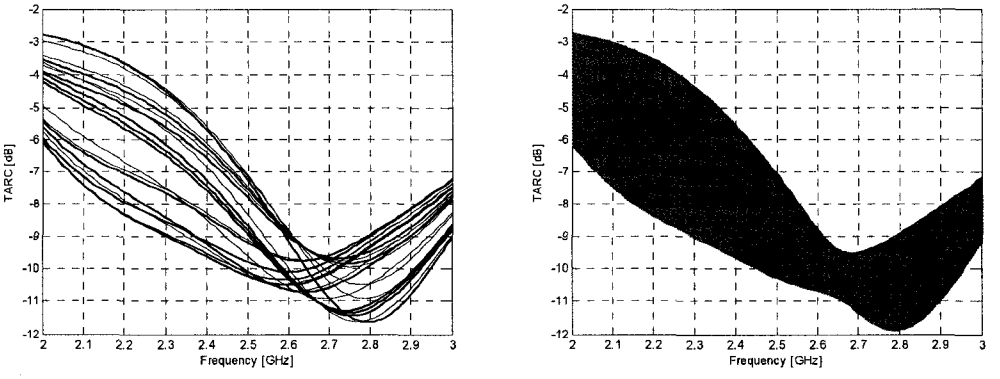

(a) (b)

Figure 84 – Simulated TARC for Mobile Design after (a) 10 Iterations, (b) 1000 Iterations

In order to evaluate our computed TARC, we consider reference [7] where two examples are shown including TARC performance: one involving two antennas, another with four antennas. The worst case TARC for the two antenna case is -9dB, and -4 dB for the four antenna case. Our worst case TARC is around -9dB, which is on par with the simpler two antenna case shown in [7] showing our design is performing reasonably well, despite the relatively large mutual coupling.

6.4.3 – Polarization Sensitive GCM Design for Indoor Picocell

Lastly we consider the design of MIMO antennas for indoor operations, with an appropriate application being laptop antenna design. We are utilizing the measurement data provided by Kalliola et al. [6], specifically the Indoor Picocell parameters that subsequently define an appropriate double exponential PAS distribution, as shown in Figure 68 (b).

Laptop antennas are typically placed on the back of or around the monitor of the laptop, and are often of the inverted-F type [9]. We shall consider a ground plane 350mm by 250mm, corresponding to the actual screen dimensions of the laptop currently used to type this thesis. The first 16 generalized characteristic modes are shown in Figure 85.

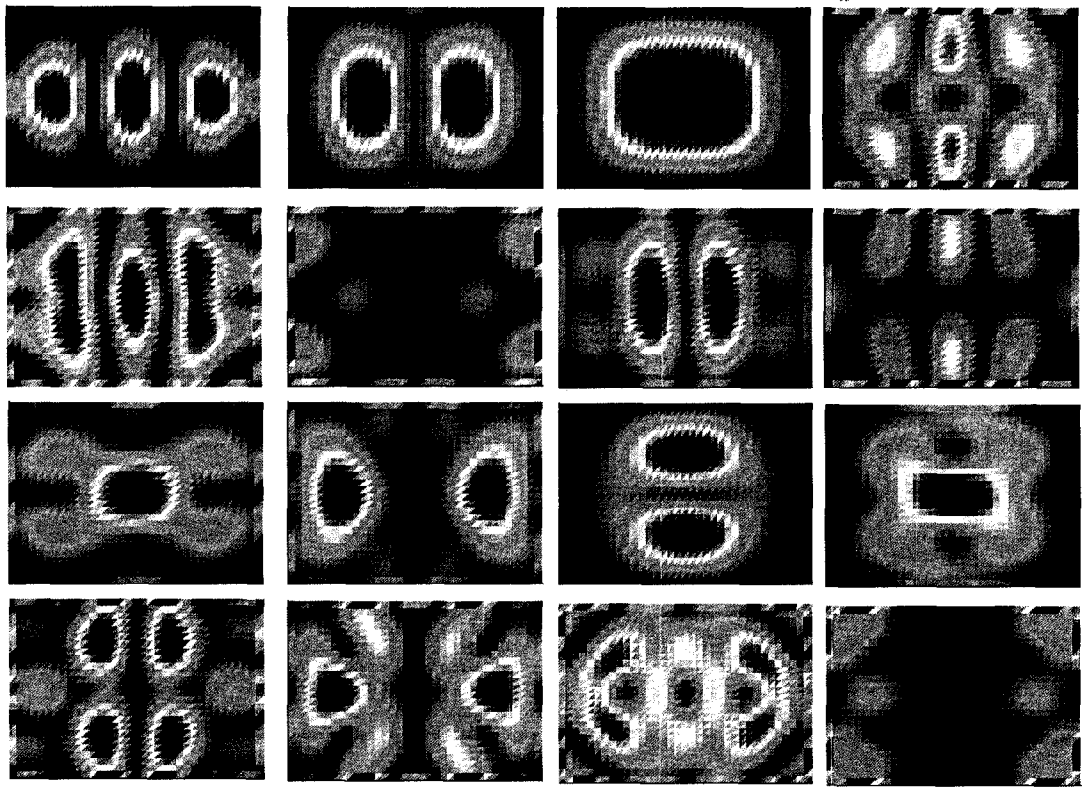

Figure 85 – Indoor Picocell Polarization Sensitive GCMs for PEC Plate

Due to the electrically large size of the plate, we are presented with many options for excitation. These options present themselves, as usual, in the locations of the current maxima. We make the following observations:

- We could use center fed slots to excite many of the modes, namely 1, 2, 3, 5, 7, and 9 through 12. While this is feasible, it is wiser to keep the antennas near the outer edges of the plate to ensure we interact as little as possible with the other material that in inevitably be located on the ground plane in practice.

- Since we have discrimination between theta and phi polarizations in the far-field, we ideally want excitations that predominantly produce theta-polarized far-fields. With slot antennas, the far-field polarization is opposite to that of their monopole and dipole counterparts and we therefore want *horizontally* oriented slot antennas to maximize the theta polarization.

Considering phi polarization dominance, the modes of interest would include those shown in Figure 86. From that figure it is immediately apparent the possibilities for excitation of up to four different modes using slot antennas. Let us consider the more important theta polarization, and the modes of interest shown in Figure 87. We immediately see a problem arise: the majority of the current maxima overlap, namely the 1^{st}, 2^{nd} and 4^{th} modes shown in Figure 85, making it very difficult to excite individual modes and maintain low envelope correlation relative to the indoor picocell PAS distribution. This phenomenon was further confirmed using the step-by-step procedure developed in Chapter 5, and applied in the previous section, which showed that at most three low envelope correlation antennas were possible using our procedure. In order to get around this limitation, we shall consider using a center fed slot antenna inside the structure itself, thereby exciting modes separate from those found at the edges. We therefore consider the three feeding locations as shown in Figure 88.

Our options are to either design for theta or phi polarization (or perhaps a mix between the two). We can design for phi polarization but given that the XPR (strength of theta

polarization to the phi polarization) for the indoor picocell suggests designing (and perhaps solely) for theta polarization. Nevertheless, we wish to show that low envelope correlation designs are possible for either polarization, but the important design requirement of large mean effective gain will be affected.

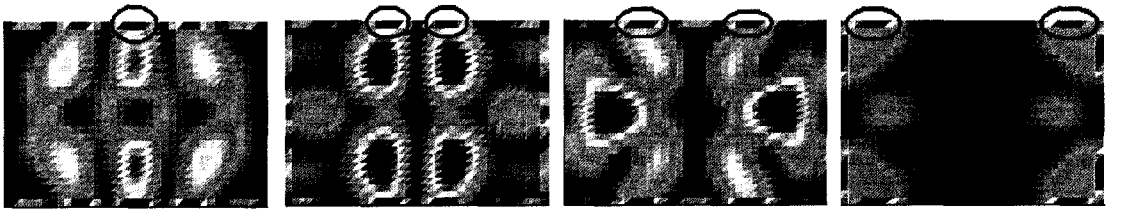

Figure 86 – GCMs of Interest for Phi-polarized Slots

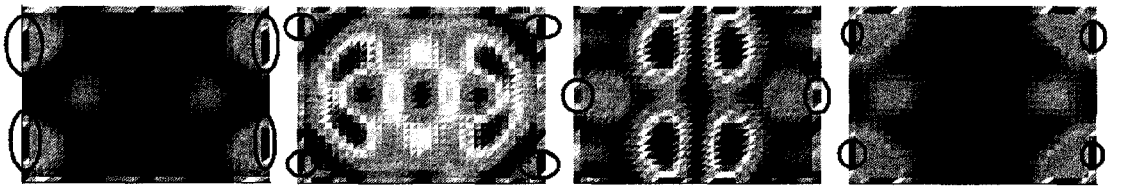

Figure 87– GCMs of Interest for Theta-polarized Slots

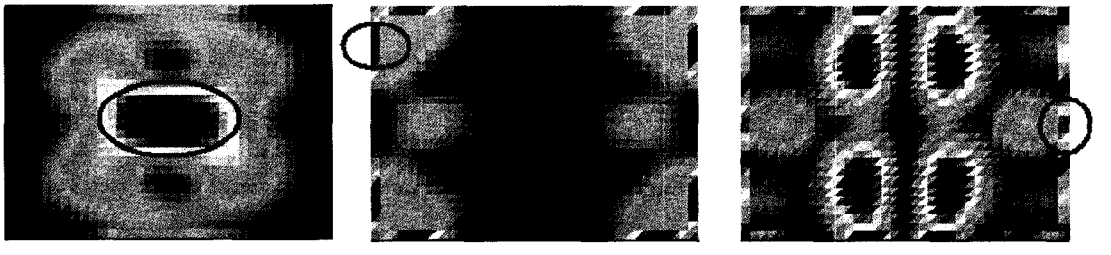

Figure 88– Alternative GCMs of Interest for Theta-polarized Slots

It is also important to realize that we are now constrained to design for many criteria: impedance bandwidth, low envelope correlation and high mean effective gain. In the event that it is difficult to match the antennas properly to 50 ohms, let alone have all four antennas resonant at the same center frequency, it will be necessary to sacrifice envelope correlation or MEG in order to match the antennas (the converse is true as well).

Two such designs are shown in Figures 89 and 90 with Figure 89 representing the theta polarized design and Figure 90 the design for phi polarization. In practice, we would never want to use the phi-polarized design since it is not aligned with the polarization of the expected incident power, but we show it for illustrative purposes.

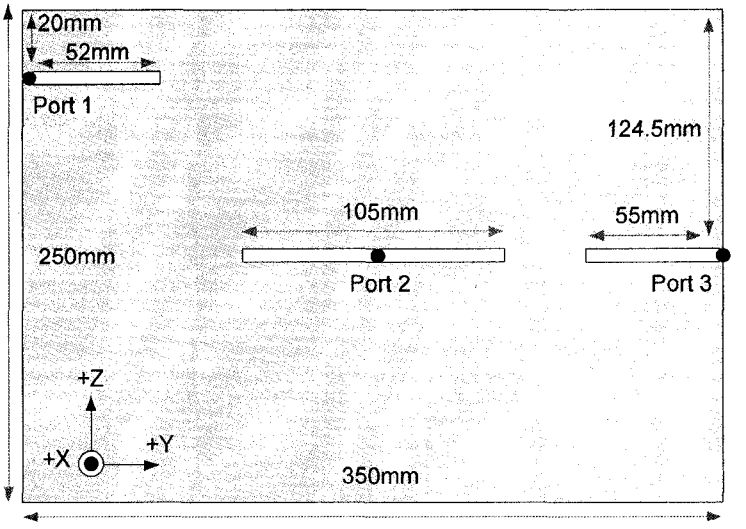

Figure 89 – Theta-Polarized Design for Indoor Picocell

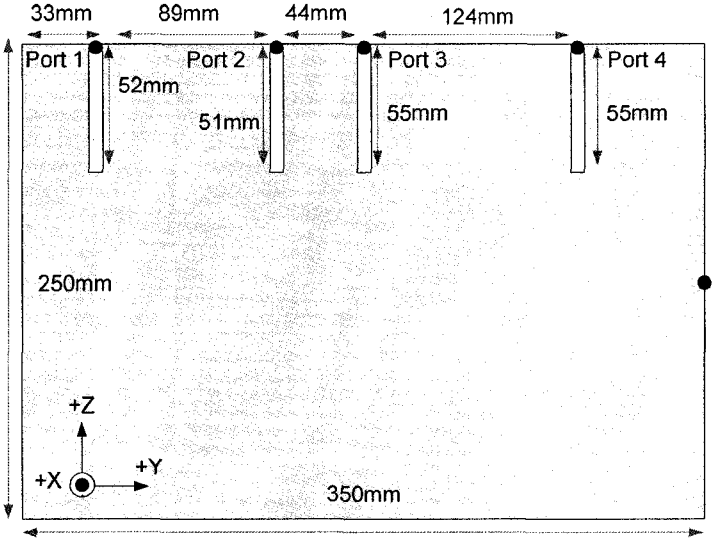

Figure 90 – Phi-Polarized Design for Indoor Picocell

Firstly, let us consider the phi-polarization design where the slots are oriented vertically. Recall that this design is less than ideal since the slots are oriented in the incorrect fashion to receive power from the urban macrocell environment. The S-parameters of the design are shown in Figure 91 and the envelope correlation and mean effective gain in Figure 92. We see an excellent 15 % 10 dB return loss bandwidth. We see excellent envelope correlation, with the correlation less than 0.1 starting at 2.375 GHz and onwards, resulting in a 10% bandwidth at a minimum. Finally, as expected, the MEGs for the four antennas vertically oriented are quite low, at or below -7 dB at center frequency. This makes them undesirable for MIMO antenna use, but certainly doesn't prevent their use.

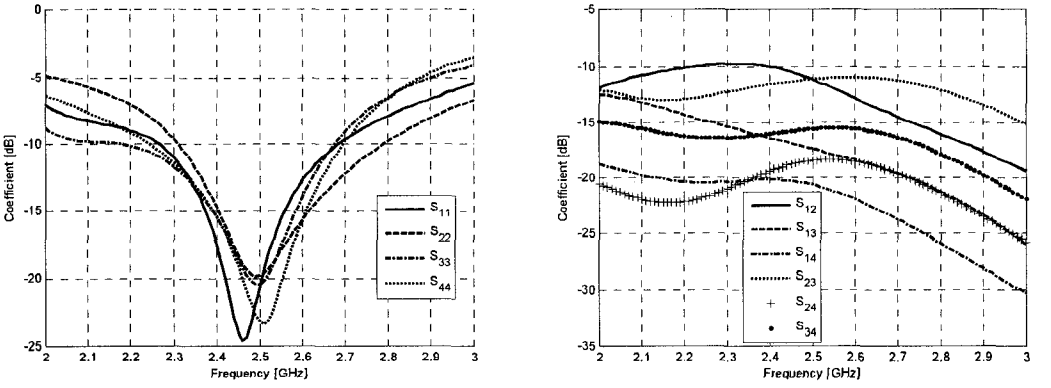

(a) (b)

Figure 91 – Simulated S-parameters of Phi-Polarized Design

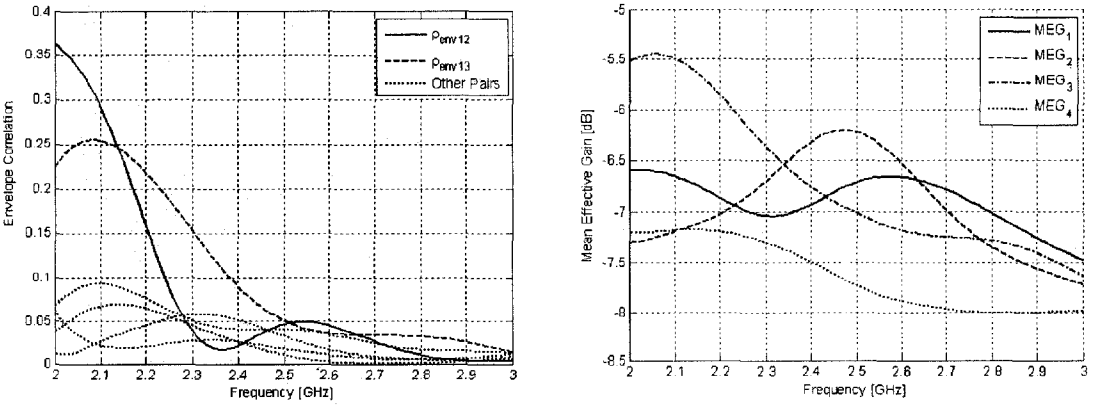

(a) (b)

Figure 92 – Simulated Envelope Correlation and Mean Effective Gain of Phi-Polarized Design

The question remains: are the locations of these four antennas unique, or can a set of four well spaced antennas on a laptop yield low envelope correlation? The generalized characteristic modes clearly show the positions of the antennas are indeed unique and simply placed aesthetically located antennas would likely not function well, so we shall consider an alternative design and consider their performance relative to the indoor picocell distribution. We consider *equally spacing the four antennas* across the top edge of the perfectly conducting plate, and tuning each antenna to match as best as possible to 50 ohms. We are able to tune all lengths such that the input reflection coefficient at each port is less than -20 dB, indicating an excellent match. We compute the envelope correlations and plot their frequency behaviors in Figure 93. We see significantly higher envelope correlation by equally spacing the antennas over the perfectly conducting laptop plate. This is **not** to say anyone would design such a set of antennas for indoor MIMO, it is only included to show that the placement of the antennas is important, and is found *efficiently* using the generalized characteristic modes.

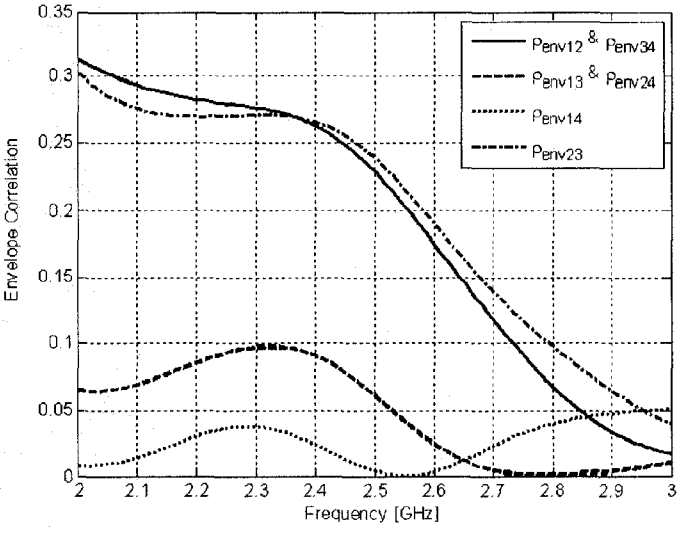

Figure 93 – Simulated Envelope Correlation of Equi-spaced Top Edge Slot Design

This brings up a very important point regarding the work put forth in this thesis. An appropriately designed optimization routine would likely find the ideal antenna placement shown in Figure 90 but the reasoning behind the location of the antennas would be unknown to the designer. It is for this reason that using the generalized modes is advantageous since it gives justification for a resulting MIMO antenna design.

We conclude with the analysis of the *theta-polarization design* as shown in Figure 89, which is the more appropriate design to consider in practice since it will likely meet the three design requirements: large MEG, decent impedance bandwidth and low envelope correlation. The S-parameters of this design is shown in Figure 94 where we note a wide 16% 10dB RL bandwidth. Furthermore, the mutual coupling is quite low. Using the field integration method, we can compute the envelope correlation between the antenna pairs as shown in Figure 95 where we the correlations are extremely low.

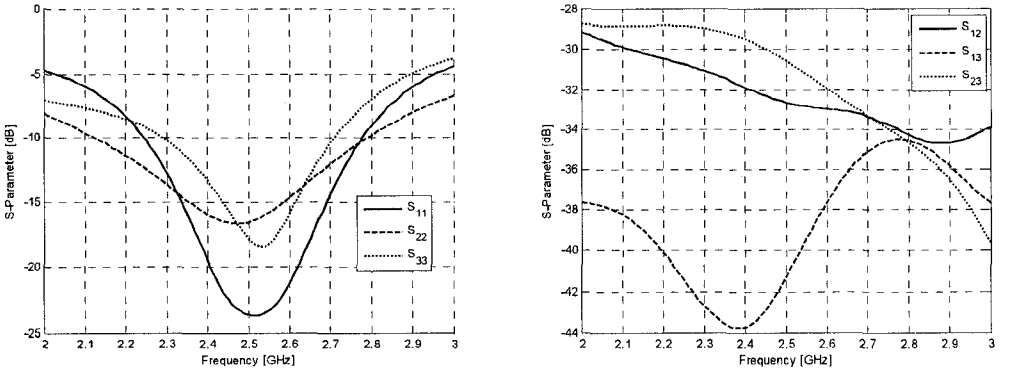

(a) (b)

Figure 94 – Simulated S-Parameters of Theta Polarized Design for Indoor Picocell PAS

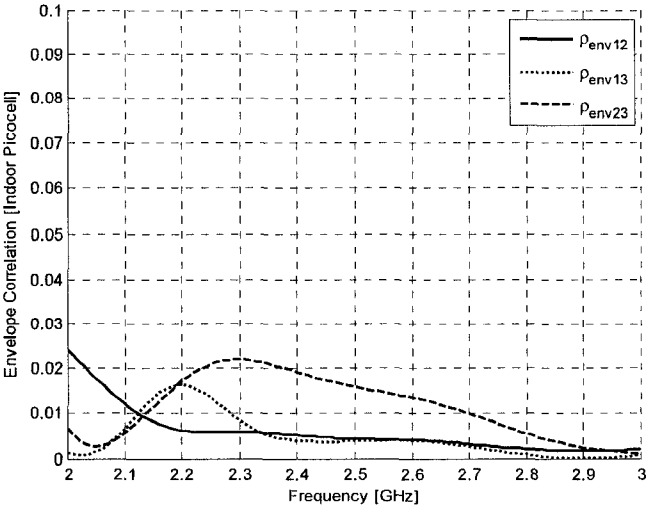

Figure 95– Simulated Envelope Correlation of Theta Polarized Design for Indoor Picocell PAS

We compute the mean effective gain as shown in Figure 96. We see good MEG performance, with all three antennas better than -4.5dB, which is on par with the best performance of the antennas measured by Kalliola in [6]. The reasons for the acceptable values for MEG are two fold:

- With horizontally oriented slots, we have ensured surface currents that yield predominantly theta-polarized far-field patterns. Since the PAS is predominantly theta polarized, we maintain high mean effective gain.

- Slot antennas are mostly omni-directional, and the indoor PAS has a similar omni-directional form. The far-field patterns of the slot antennas naturally overlap the indoor picocell PAS distribution, maximizing the MEG relative to this region.

Notice also that the mean effective gains are roughly the same value at the center frequency, which is another desirable condition for MIMO antenna design.

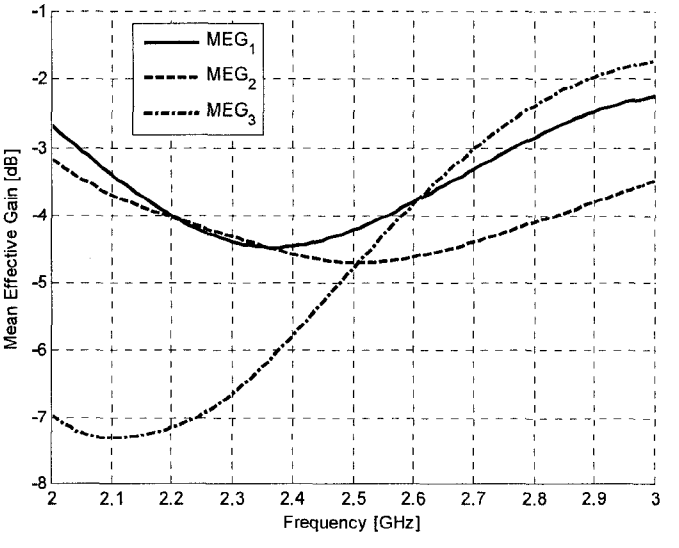

Figure 96 – Simulated Mean Effective Gain of Theta Polarized Design for Indoor Picocell PAS

We conclude the performance measurements of the theta-polarized design by computing the TARC of the three antenna system. We expect decent results for TARC given the very low values for mutual coupling which are all less than -30 dB at center frequency. The resulting plots of TARC are shown in Figure 97 (a) and (b), where (a) shows 10 iterations and (b) shows the upper and lower limits of the simulated TARC values. As expected, the TARC is indeed quite low, as low as –17 dB at center frequency. In fact, the TARC -10dB bandwidth of 18% rivals systems where the antennas operate independently. However, we owe the bulk of the excellent TARC performance to how physically separated the three antennas are, which is mainly due to the electrically large size of the laptop plate, and not to any results derived from modal arguments.

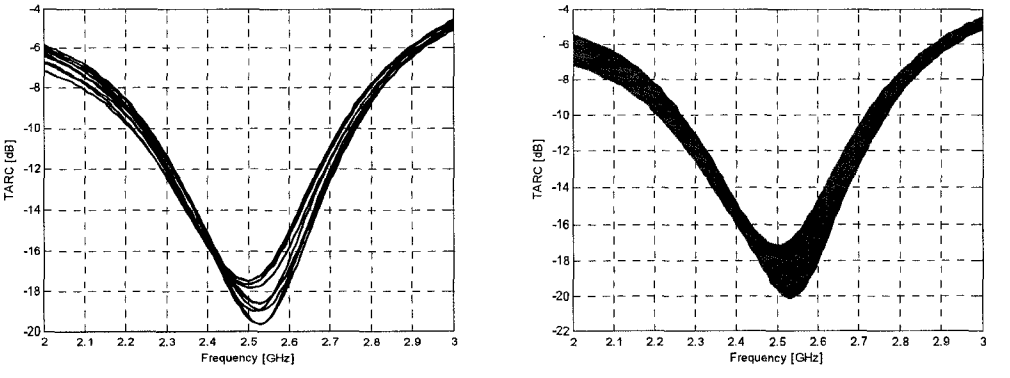

(a) (b)

Figure 97 – Simulated TARC for Indoor Picocell Design after (a) 10 Iterations, (b) 1000 Iterations

We shall also consider whether the placement of the antennas is unique, and whether sufficiently large separation of antennas is enough to ensure low envelope correlation relative to the urban PAS distribution. Here we consider two edge fed slot antennas separated by 80mm or 0.67 lambdas. The physical dimensions are shown in Figure 98. At center frequency, the envelope correlation relative to the entire sphere is extremely low at 0.0014, since the mutual coupling parameter S12 is -10 dB and the input reflection coefficients are -25 dB. Here the S-parameters alone show the system has low envelope correlation over the entire far-field sphere.

However, one finds that the envelope correlation between antennas relative to the indoor PAS distribution is an enormous 0.8791. This result very clearly shows that a set of antennas that have low envelope correlation in one scattering environment does not guarantee similar low envelope correlation in alternative environments. Of further interest is changing the reference impedance. By halving the reference impedance to 25 ohms, the envelope correlation increases further to 0.9120. By doubling the reference to 100 ohms, we find the opposite effect, where the envelope correlation decreases to 0.8366. While not sufficient in bringing the envelope correlation down to acceptable levels, it might be useful in other situations where sacrificing some impedance bandwidth to reduce correlation is acceptable.

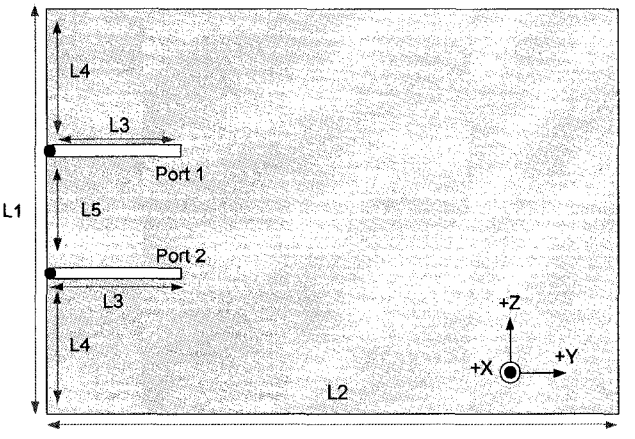

Figure 98 – Example Design Showing Placement of slot antennas is absolutely not arbitrary, with L1 = 250mm, L2 = 350mm, L3 = 55mm, L4 = 83mm, and L5 = 41mm.

6.5 – Performance of MIMO Antennas in Alternative Regions

6.5.1 – GCM Design Performance over Full-Sphere

We shall consider the envelope correlation of the various designs over regions of the far-field they were not expressly designed for. We note that the implications of an antenna system with reflection and coupling coefficients that are quite low are that they are suitable for full-sphere MIMO operation.

First, we consider the performance of the mobile urban design in section 6.4.2 relative to the full-sphere and plot the envelope correlation in Figure 99. Notice that the correlation behaviour is low enough around the center frequency for full-sphere MIMO operation. However, notice also that the correlation is not quite zero at center frequency and that outside the center frequency the correlation becomes quite large. This is mainly due to the relatively large mutual coupling when compared to the previous designs in this section. Once the frequency moves outside of the well matched region, the mutual coupling cannot compensate and keep the envelope correlation low.

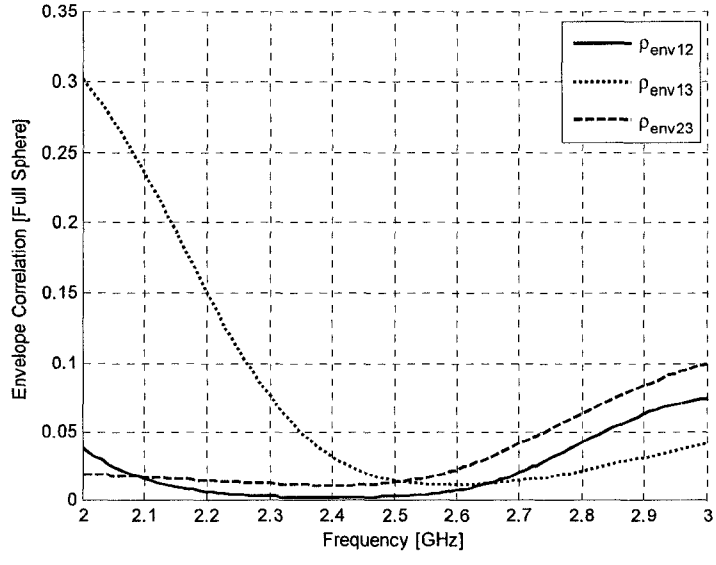

Figure 99 – Envelope Correlation of Urban Macrocell Design in a Perfect Scattering Environment (i.e. Full-Sphere Orthogonality)

Lastly, we consider the laptop design (Section 6.4.3) and its envelope correlation behaviour relative to the full sphere as shown in Figure 100. To no surprise, the envelope correlation is indeed very low, thanks to the low mutual coupling and excellent impedance performance.

As predicted, the two example GCM designs have low envelope correlation over the full sphere despite each having been individually designed to have low envelope correlation relative to their respective (and unique) PAS distributions. This is to be expected since **any** set of antennas that are well matched with reasonably low mutual coupling can be used for full-sphere MIMO operation.

What is critical to point out is that the reverse is not true. A set of well-matched antennas with low mutual coupling **does not** ensure low envelope correlation over arbitrarily defined regions or weighting over the far-field.

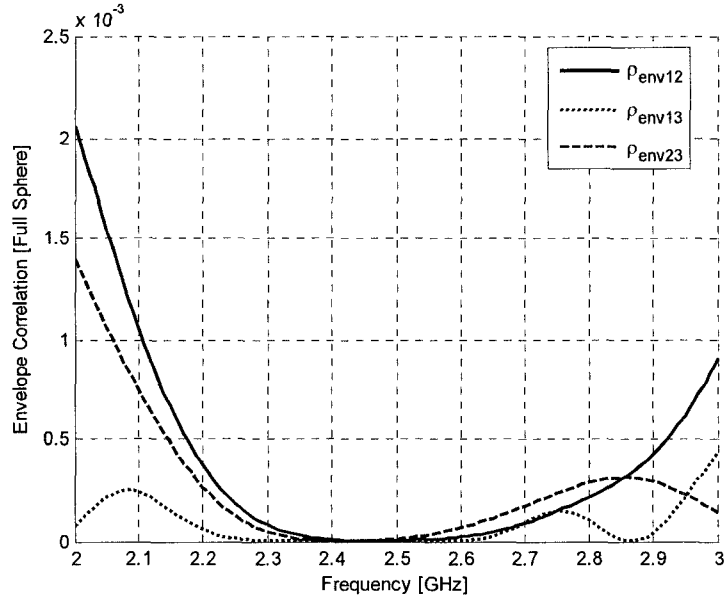

Figure 100 - Envelope Correlation of Indoor Picocell Design in a Perfect Scattering Environment (i.e. Full-Sphere Orthogonality)

6.5.2 – CM Full-sphere Designs and their Performance in Constrained Regions of Orthogonality

We shall consider the full-sphere three antenna design in *Chapter 5, Section 5.8.1* (which was validated experimentally) and simulate the antennas' envelope correlation relative to the MCS and sectored regions defined in section 6.2, and plot these results in Figures 101 (a) and (b) respectively. Note that the handheld is oriented vertically along the z-axis, and then rotated 45° into talk position in order to accurately compare these results to the newly designed mobile in Chapter 6. We immediately notice the significantly large envelope correlation, with values greater than 0.3 for the MCS case and 0.4 for the sectored case, both quoted around the center frequency.

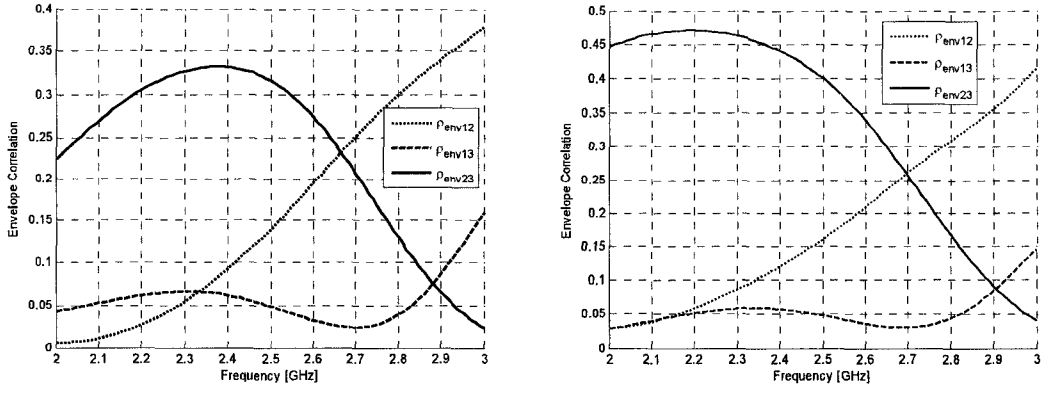

Figure 101 – Envelope Correlations of Full-sphere Designs measured against (a) MCS and (b) Sector

As a final test, we consider the three-antenna design from Chapter 5 and compute its performance relative to the urban environment (which is an excellent measure of real-world performance, since the urban environment is based on measured data). We consider its envelope correlation and mean effective gain in Figures 102 (a) and (b). We see very large values of envelope correlation for urban macrocell environment, with upward values nearing 0.5. This makes MIMO communications undesirable with this design, since we are reaching the limits of envelope correlation that allow for an appreciable benefit in channel capacity. We also see lower values for MEG as expected

since the mobile antennas based on the CMs was not explicitly designed with the urban PAS in mind. However, the values of MEG are not low enough to prevent device operation. This is simply a consequence of having nearly omni-directional antennas, which is typically the case for mobile antennas. That being said, the reasonable values for MEG do not suffice for MIMO communications, with the highly correlated antennas preventing one from maximizing MIMO channel capacity.

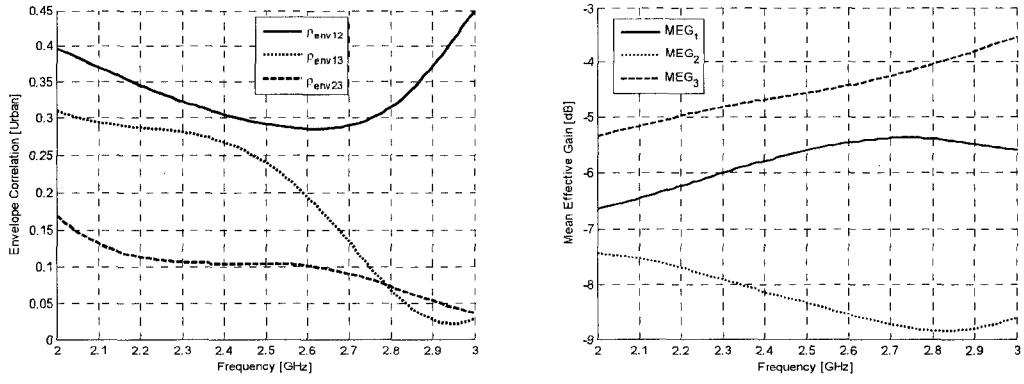

(a) (b)

Figure 102 – Envelope Correlation of Full-sphere Design Measured against (a) Urban Macrocell and (b) Simulated Mean Effective Gain

In general, we see significantly larger envelope correlation over the constrained regions of the far-field. Clearly, designing for full-sphere orthogonality does not ensure low envelope correlation over other constrained regions.

Conversely, the simple requirements for full-sphere (well-matched and low mutual coupling) are typically achieved whether explicitly designing for full-sphere or not. For this reason, a set of MIMO antennas designed for constrained regions of the sphere will most likely operate well relative to the entire sphere.

Additionally, we see that the modal theory used to excite modes that are orthogonal for a given region works for both the full-sphere and constrained regions. The fact that the two are not interchangeable implies the modes determined for the constrained regions (GCM) are indeed unique, and thus the feeding scheme remains unique as well.

6.6 – Concluding Remarks

In this chapter we considered the use of Generalized Characteristic Modes for the design of MIMO antennas in arbitrary scattering environments. In section 6.2 we showed that the GCMs, as defined by Inagaki, can be implemented for MIMO antenna design for scattering environments such as the MCS region or possibly sectored regions of interest. In section 6.3, we extended Inagaki's GCM theory to include polarization discrimination, the first of its kind in the literature. This theory allows one to generate GCMs that have orthogonality relative to arbitrary PAS functions, namely those with parameters matching measured data described by Kalliola et al.

Using the design methodology developed in Chapter 5, we considered two distinct designs in section 6.4. The first was a mobile chassis design, with low envelope correlation performance relative to the urban macrocell scattering environment. The second involves a laptop chassis, where the design emphasis was for the indoor picocell environment. Both aforementioned environments are based on measured results, and best represent the actual PAS distributions these types of communications devices would be exposed to in practice. We also discussed and computed an often omitted performance index known as TARC. Both example designs yielded reasonable performance, with the second design performing best since it had very low mutual coupling.

Lastly, in section 6.5 we investigated the performance of full-sphere designs from Chapter 5 and computed their envelope correlation relative to MCS, sectored and urban macrocell scattering environments. We found that the full-sphere designs did not yield low inter-antenna envelope correlations despite having excellent matching and low mutual coupling. These results concretely showed that the conditions necessary for low envelope correlation in realistic regions are far more complex than simply optimizing for S-parameters. Conversely, it was shown that the two GCM based designs, namely the urban macrocell and indoor picocell performed well in a full-sphere scattering environment, since their S-parameters allowed for such performance.

CHAPTER 6 REFERENCES

[1] R.F. Harrington, J Mautz, "Theory of Characteristic Modes for Conducting Bodies", *IEEE Transactions on Antennas and Propagation*, Vol. AP-19, No. 5, Sept 1971.

[2] N. Inagaki, R. Garbacz, "Eigenfunctions of Composite Hermitian Operators with Application to Discrete and Continuous Radiating Systems", *IEEE Transactions on Antennas and Propagation*, Vol. AP-30, No. 4, pp 571 – 575, July 1982.

[3] R.G. Vaughan, J.B. Andersen, "Antenna Diversity in Mobile Communications," *IEEE Transactions on Vehicular Technology*, Vol. VT-36, No. 4, pp. 149 – 172, November 1987.

[4] T. Svantesson, "Correlation and Channel Capacity of MIMO Systems Employing Multimode Antennas," *IEEE Transactions on Vehicular Technology*, Vol. 51, No. 6, pp. 1304 – 1312, November 2002.

[5] T. Taga, "Analysis for Mean Effective Gain of Mobile Antennas in Land Mobile Radio," *IEEE Transactions on Vehicular Technology*, Vol. 39, No. 2, pp 117 – 131, May 1990.

[6] Kalliola et al., "Angular Power distributions and Mean Effective Gain of Mobile Antenna in Different Propagation Environments", *IEEE Transactions on Vehicular Technology,* Vol. 51, No. 5, pp. 823 – 838, September 2002.

[7] D. Browne, M. Manteghi, M. Fitz, Y. Rahmat-Samii, "Experiments with Compact Antenna Arrays for MIMO Radio Communications," *IEEE Transactions on Antennas and Propagation*, Vol. 54, No. 11, November 2006.

[8] M. Manteghi, Y. Rahmat-Samii, "Multiport Characteristics of a Wide-Band Cavity Backed Annular Patch Antenna for Multipolarization Operations," *IEEE Transactions on Antennas and Propagation*, Vol. 53, No. 1, January 2005.

[9] D. Liu, E. Flint, B. Gaucher, "Integrated Laptop Antennas – Design and Evaluation", *IEEE Antennas and Propagation Society International Symposium*, Vol. 4, pp. 56 – 59, June 2002.

[10] **Jonathan Ethier** and Derek McNamara, "The Use of Generalized Modes in the Design of MIMO Antennas", *13th Biennial IEEE Conference on Electromagnetic Field Computation (CEFC 2008) Digest.*

Chapter 7

Characteristic Port Mode Theory Applied to MIMO Antenna Design

7.1 – Introduction

In Chapters 5 and 6 we considered the use of Characteristic Modes (CM) and Generalized Characteristic Modes (GCM) in the design of MIMO antennas for both full angular spread and constrained regions of orthogonality. In both cases the modes exist as surface currents that subsist over the entire surface of the conducting object. We were able to develop a design methodology using these currents in the deployment of MIMO antennas.

Alternatively, one can define port voltages that exist only at the defined ports of an antenna system. This modal formulation is denoted Characteristic Port Modes (CPM), defined by Mautz and Harrington [1] in 1973. These modes are derived from the admittance (Y) parameters and maintain the same tantalizing far-field orthogonality as the classical CMs and are therefore applicable to MIMO antenna design.

These modes are determined from antenna port properties, yielding a set of port modes where the number of port modes is equal to the number of defined antenna ports. Other modal formulations exist that are mathematically equivalent to the port mode theory [4], but they appear after the work of Mautz and Harrington [1]. Alternative formulations exist distinct from the CPM theory involving the S-parameters as discussed by Stein [2].

In Section 7.2 we shall discuss the properties of the CPM theory, how it relates to MIMO antenna design and how one can implement them practically. We will also consider other distinct port modal formulations that exist and how they compare to the CPM theory.

We begin by considering symmetry in radiating structures and the implications this has for CPM theory in section 7.3. The nature of the admittance matrices for symmetric layouts of antenna ports makes for very interesting properties, allowing us to generalize the eigen-voltages independent of the types of radiating structure and the operating frequency and depending only on the number of physically symmetric ports.

Continuing with our CPM discussion in Section 7.4, we consider cases where the ports and radiating structure are asymmetric, which leads to frequency-dependent weights. This frequency dependence rears its ugly head in the form of narrow low envelope correlation bandwidth if one fixes the eigen-voltage weights for a given center frequency. This leads to limitations on closely spaced asymmetric antenna configurations, a concept not considered in the literature. Moreover, we point out that there is a lack of consideration in the literature for the frequency performance of envelope correlation and omitting such critical data offers an incomplete study of a MIMO antenna design.

In section 7.5 we consider another popular port mode formulation involving Stein's formulation [2] and consider the use of either formulation for MIMO antenna design. We conclude the section by showing that under port symmetry conditions the CPM and Stein Modes are identical.

Concluding in section 7.6 we show the relationship between CPM theory and CM theory, which is only possible from a moment method perspective. We also show some interesting results that tie the symmetry in CM design with the symmetry in the CPM approach.

7.2 – Characteristic Port Modes and MIMO

The computation of Characteristic Port Modes is similar to the computation of Classical Characteristic Modes, but the results are vastly different. Both methods involve eigenanalysis, with the former having a much smaller matrix to solve compared to the latter. While Characteristic Modes consider eigenvalues associated with the impedance operator (computed discretely using a moment method formulation), the Characteristic Port Modes (CPM) are computed from the impedance / admittance parameters, also known as the Z/Y-parameters. These parameters can be computed using many different tools including computational electromagnetics (MOM, FEM, FDM) and measurement data using a network analyzer. As discussed in chapter 2, the Port modes are computed by solving the eigenvalue problem:

$$[B][V_n] = \mu_n [G][V_n] \tag{7.2-1}$$

where the [Vn]'s are the eigen-voltages, and *[G]* and *[B]* are the real and imaginary parts of the admittance (*Y*) parameters and μ_n is the eigenvalue associated with the problem. An antenna system with *N* ports has a collection of *N* eigenvectors that excites each of the *N* ports. The resulting far-fields due to these *N* excitations are mutually orthogonal, thereby making them ideal candidates for MIMO antenna design. This is made possible not only by their orthogonality in the far-field, but also by the orthogonality at the ports: the linear superposition of each mode excitation can appear at each port, and maintain the orthogonality in the overall antenna pattern.

This concept has been explored by Chaloupka [4] and Eber [5] using the theory proposed by Rasmussen [3]. However, the work outlined by Rasmussen was published at a later date than Mautz [1], so we shall properly consider Mautz and Harrington as the first proponents of Characteristic Mode Port Theory. A similar, although distinct port mode theory was developed by Stein [3] and applied to MIMO antenna design by Weber [6] and Volmer [7].

As discussed in [4] and [5], one can weight a collection of N signals destined for MIMO communication using a matrix *[U]*, which consists of the eigenvectors of the eigenvalue problem shown in Equation 7.2-1. The "orthogonalizing" of the N signals is achieved using this matrix *[U]* in the following manner:

$$[K]=[U][S] \tag{7.2-2}$$

where *[K]* is the total voltage appearing at the terminals of the device ports, *[U]* is the collection of eigenvectors (or eigen-voltages) which act as signal weights and *[S]* are the signals we wish to transmit. Expanding in terms of the individual weights and signals, we see the following relationship:

$$\begin{bmatrix} K_1 \\ K_2 \\ \vdots \\ K_N \end{bmatrix} = \begin{bmatrix} V_1^{Mode1} & V_1^{Mode2} & \cdots & V_1^{ModeN} \\ V_2^{Mode1} & V_2^{Mode2} & \cdots & V_2^{ModeN} \\ \vdots & \vdots & \vdots & \vdots \\ V_N^{Mode1} & V_N^{Mode2} & \cdots & V_N^{ModeN} \end{bmatrix} \begin{bmatrix} S_1 \\ S_2 \\ \vdots \\ S_N \end{bmatrix} \tag{7.2-3}$$

Thus, we can think of *[U]* as a transformation that embeds the N signals onto the N ports, ensuring the information remains orthogonal in the far-field pattern of the antenna system. There is no longer a collection of antennas radiating independently – we have a single radiating device that radiates a *single* far-field pattern, but the information of each of N signals remains orthogonal over the far-field of the radiating system. We can also represent the matrix [*U*] as a black-box (for the case of three ports) that appropriately weights the MIMO signals 1, 2, 3 to the port voltages *A*, *B*, *C* as shown in Figure 103.

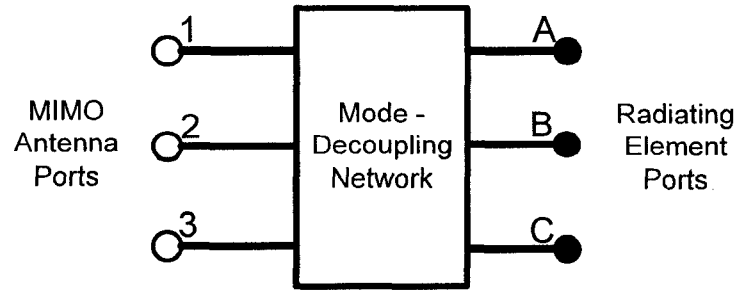

Figure 103 – Example Mode Decoupling Network

To contemplate the implications of CPM theory farther, consider an N-element antenna array. One typically feeds each array element the same information content, and uses amplitude and phase weighting in order to steer the main beam, reduce sidelobe levels and the like. Consider now that we have multiple streams of data to transmit in parallel. Our goal is to maintain orthogonality in the far-field between these streams of information. The CPM theory shows that one can achieve this using a simple weighting scheme, derived from the Z/Y-parameters of the antenna ports. By applying the appropriate weighting schemes, one can ensure the information remains orthogonal in the far-field in an array. The CPM theory takes any set of N ports and determines the necessary weights to ensure orthogonality of N embedded patterns.

Symmetries in the analyzed structure offer some interesting properties. In [4 – 7] one finds the weighting schemes do not require any active components. An entirely passive solution, involving hybrid couplers performs the necessary adjustments to the incoming signals, and effectively acts as the matrix [U] defined previously. Additionally, we see in [5] that symmetry yields reasonably attainable weights that can be implemented passively as well. The advantage to using symmetry in the radiating structure is seen in the weights, but this clearly constrains the physical layout of the antenna since symmetry cannot always be maintained. Surface mounted components, RF shields and user interactions all break the symmetry of a radiating mobile device.

When space is tightly constrained as it certainly is for mobile devices, it is often difficult to maintain symmetry in feeding schemes. The CPM theory allows a user to design MIMO antennas within tight design constraints such as high feed proximity (as pointed out by [6], [7]) but additionally allowing one to design with asymmetry, around obstacles (RF shields, battery packs) and other physical constraints one would struggle to deal with in conventional excitation schemes. The beauty of the CPM approach is one can seemingly be unconcerned with mutual coupling since the procedure immediately computes the necessary weights *in the presence* of mutual coupling. In terms of network parameters, all we are concerned with is getting power into the terminals and hence work towards low and wideband input S-parameters.

One can take two approaches in terms of implementation:

(1) Compute the eigen-voltages (weights) at the center frequency, and hold them constant over the entire operating band. This will ensure zero envelope correlation (orthogonality) at the center frequency, but not necessarily at frequencies off center. As one moves above and below the center frequency, the weights are no longer the appropriate weights for the system. The rate at which the envelope correlation degrades is directly related to how quickly the weights change as operation moves away from the center frequency.

(2) Compute the eigen-voltages at a fixed number of frequencies within the operating band and apply the weights as an interpolated weighted frequency response. This complicates the procedure considerably by requiring amplifiers (or possibly DSP) that has frequency dependent weighting. The advantage is having envelope correlations over frequency as low as one desires that is dependent only on the accuracy with which one can compute the eigen-voltages and then implement them in practice.

Let us consider some simple cases of characteristic port modes, to better understand the implications of the theory. We begin with considering one of the simplest two antenna combinations: dipoles. Taking two dipoles oriented identically (co-polarized) separated by a very small distance (much less than a half-wavelength) one would imagine their fields would have very high correlation. This is indeed the case for the scenario of two 0.5m dipoles separated by 62.5mm, the envelope correlation behaviour between the antennas (for $f = 300$ MHz) is shown in Figure 104. We find that the envelope correlation has a minimum around the center frequency of the dipoles but is still quite high with a minimum value of 0.4.

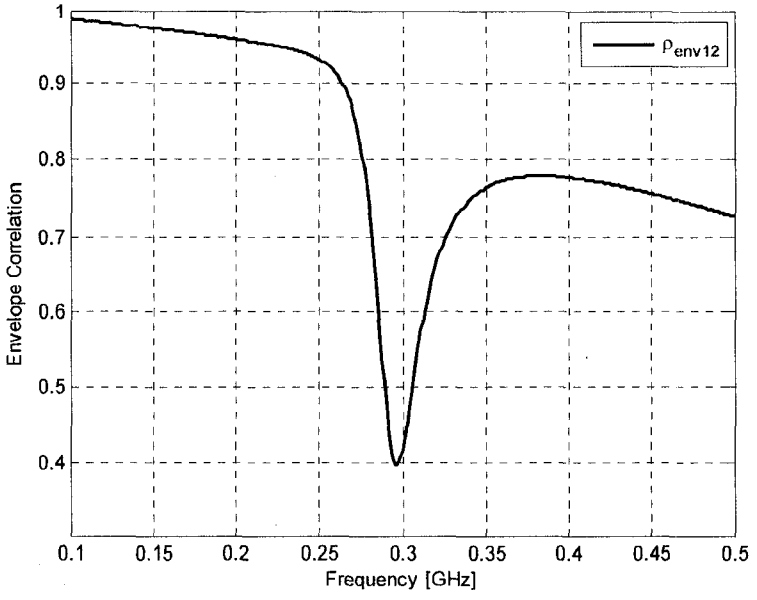

Figure 104 – Envelope Correlation of Two Closely Spaced Dipoles

Consider the admittance matrix for the dipoles at center frequency:

$$Yparams = \begin{bmatrix} Y_{self} & Y_{mutual} \\ Y_{mutual} & Y_{self} \end{bmatrix} = \begin{bmatrix} 0.9997 - 0.018i & 0.0220 - 0.013i \\ 0.0220 - 0.013i & 0.9997 - 0.018i \end{bmatrix} \quad (7.2\text{-}4)$$

The Y-matrix in Expression 7.2-4 is split into its real and imaginary parts, and the eigenvalue problem $BV_n = \mu_n GV_n$ is solved. The eigenvectors of this eigenvalue problem are:

$$V_1 = \begin{bmatrix} 1 \\ 1 \end{bmatrix} \text{ and } V_2 = \begin{bmatrix} 1 \\ -1 \end{bmatrix} \quad (7.2\text{-}5)$$

The two corresponding far-fields patterns produced by these excitations are shown in Figure 105. Notice that the second weight yields the typical dipole torus pattern, whereas the first weight produces a directive pattern. Both weights yield theta-polarized fields, and share similar directivity of maximum directivity. How do these patterns maintain orthogonality? The phase of the electric field vectors in one lobe is 180 degrees out of phase with the field in the remaining lobe. When taking the inner product between the

electric fields of the directive double-lobed pattern and the torus, one finds the phase anti-symmetry causes the contributions from one half-space cancel with the other half-space.

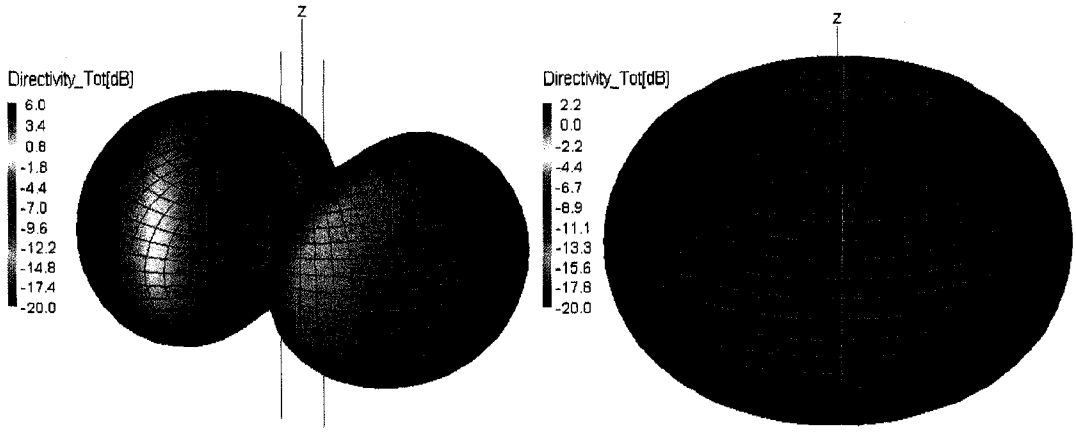

Figure 105 – CPM Far-fields for Two Dipole Antennas

From a signals perspective, let $x_1(t)$ be the first MIMO signal we wish to transmit and $x_2(t)$ be the second. At the port of the first dipole, we transmit $x_1(t)+x_2(t)$ and at the port of the second dipole we transmit: $x_1(t)-x_2(t)$. In doing so, the signals $x_1(t)$ and $x_2(t)$ remain uncorrelated in the far-field, for the case of a perfect scattering environment. If we do excite the dipoles in this manner, we find very low envelope correlation over a very wide bandwidth well below 10-6 over a wide 100% bandwidth.

That being said, **any** two identical antennas constructed from reciprocal material will yield a Y matrix of the form shown previously, and thus the same eigen-voltages regardless of the frequency or the antennas.

7.3 – Physical Symmetry and Characteristic Port Modes

Let us consider three *30mm* monopole antennas, equi-spaced on a circular ground plane, with radius *50mm*. The starting positions of the monopoles are shown in Figure 106 with the resulting envelope correlation shown in Figure 107. The resulting envelope correlation between antennas is quite reasonable, namely due to the physical separation of the antennas. The monopoles are in fact resonant around 2.35 GHz, allowing the ideal region of MIMO operation to coincide with the best impedance matching.

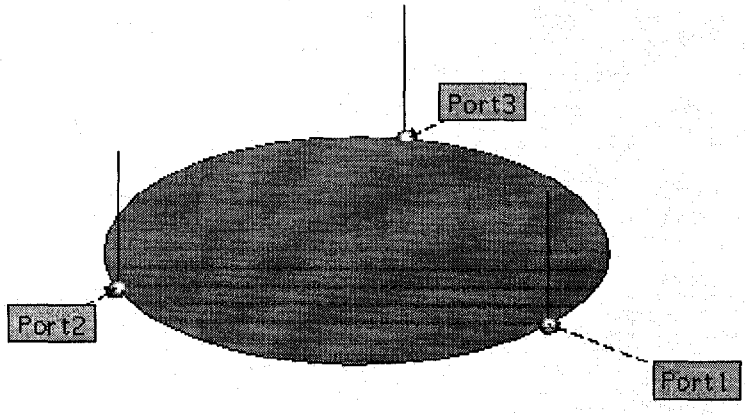

Figure 106 – Three Monopoles and Ground Plane, Monopoles on Outer Edge

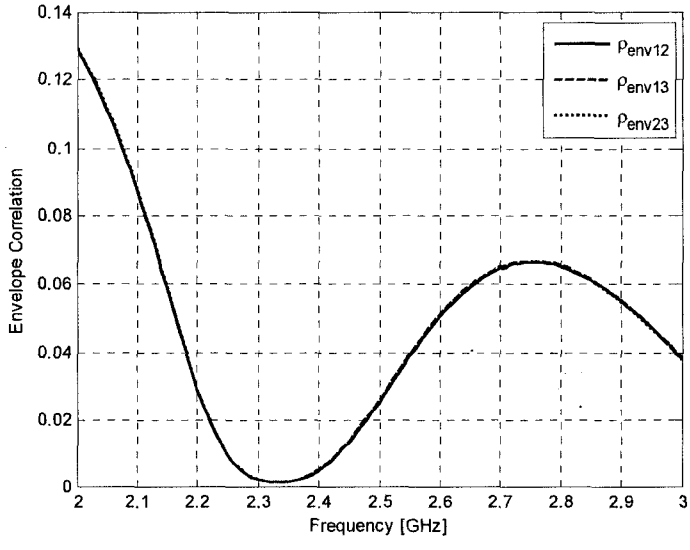

Figure 107 – Envelope Correlation of Three Monopoles and Ground Plane, Outer Edge

Despite having low envelope correlation at the center frequency, we compute the CPM voltages. At 2.35 GHz, we find the following eigen-voltages:

$$[V_1 \quad V_2 \quad V_3] = \left[\begin{bmatrix} 0.5765 \\ 0.5767 \\ 0.5789 \end{bmatrix} \quad \begin{bmatrix} 0.0045 \\ 0.7051 \\ -0.7048 \end{bmatrix} \quad \begin{bmatrix} 0.8134 \\ -0.4071 \\ -0.4075 \end{bmatrix}\right] \tag{7.3-1}$$

These eigen-voltages are approximately equal to:

$$[V_1 \quad V_2 \quad V_3] = \frac{1}{\sqrt{6}}\left[\begin{bmatrix} \sqrt{2} \\ \sqrt{2} \\ \sqrt{2} \end{bmatrix} \quad \begin{bmatrix} 0 \\ \sqrt{3} \\ -\sqrt{3} \end{bmatrix} \quad \begin{bmatrix} 2 \\ -1 \\ -1 \end{bmatrix}\right] \tag{7.3-2}$$

The approximation matches precisely with the weights computed by Eber and Chaloupka in [5] noting the similarities and difference between both antennas sets in Figure 108. Notice, however, that the two designs differ *significantly* in implementation – one involves wire antennas and the other a multiple-probe fed patch antenna. Yet analyzing both designs yield precisely the same CPM weightings. The only similarity that *does* exist is the symmetry, which is the reason for the identical weightings. We therefore propose that under the conditions of symmetry, the antennas do not determine the weights, but rather, the symmetry relative to the chosen ports.

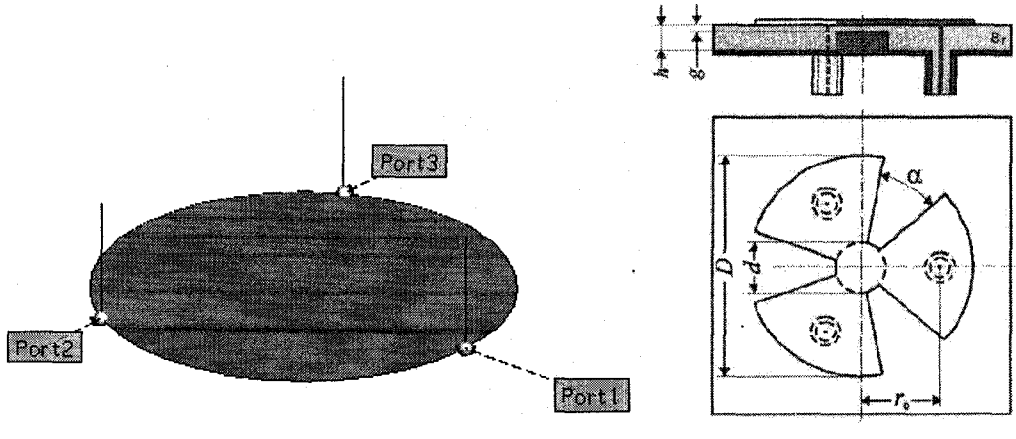

Figure 108 - Comparison of Symmetric Three Antenna Designs, Image to the right after Eber and Chaloupka [5]

We shall further show this property by bringing the three monopole antennas physically closer to the mid-points of the ground plane radius, maintaining the perfect symmetry, as shown in Figure 109. The envelope correlation remains low, as evident in Figure 110 while the resonant frequencies of the antennas increase to around 2.45 GHz.

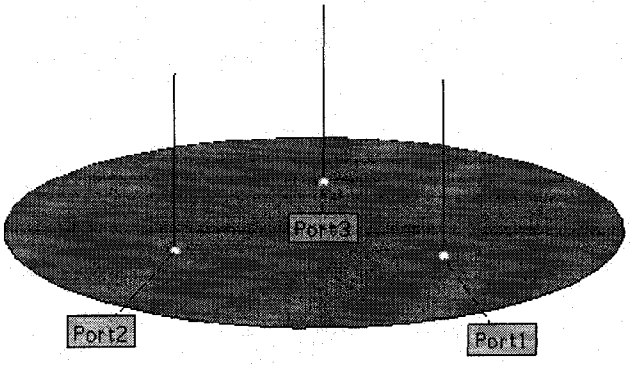

Figure 109 - Three Monopoles and Ground Plane, Monopoles in Middle of Plate

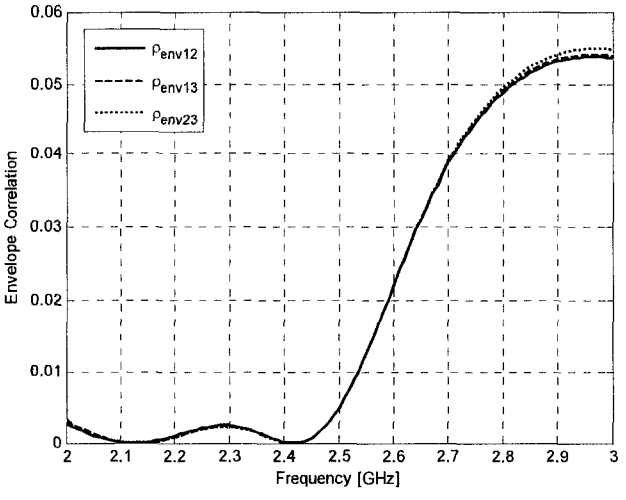

Figure 110 – Envelope Correlation of Three Monopoles and Ground Plane, Middle of Plate

To no surprise, the new eigen-voltages are virtually unchanged:

$$\begin{bmatrix} V_1 & V_2 & V_3 \end{bmatrix} = \begin{bmatrix} \begin{bmatrix} 0.5764 \\ 0.5767 \\ 0.5774 \end{bmatrix} & \begin{bmatrix} 0.0033 \\ 0.7041 \\ -0.7036 \end{bmatrix} & \begin{bmatrix} 0.8124 \\ -0.4069 \\ -0.4071 \end{bmatrix} \end{bmatrix} \tag{7.3-3}$$

In fact, the weightings (eigenvectors) do not change based on the frequency in which the Y-parameters are computed. This is simply because the symmetry of the structure is not a function of the frequency. To ensure these weights are indeed accurate and that the computation takes advantage of the symmetry, the meshing must also be symmetrical and dense in order to ensure the currents around each antenna will be identical. For final consideration of the monopoles, we shall bring the monopoles very close, to ensure the monopoles have large envelope correlation between each other as shown in Figure 111. We see very high envelope correlation in Figure 112 since the antennas are now very closely spaced (6mm separation). Nevertheless, we find the weightings to be precisely the same as the two previous cases, despite having vastly different spacing.

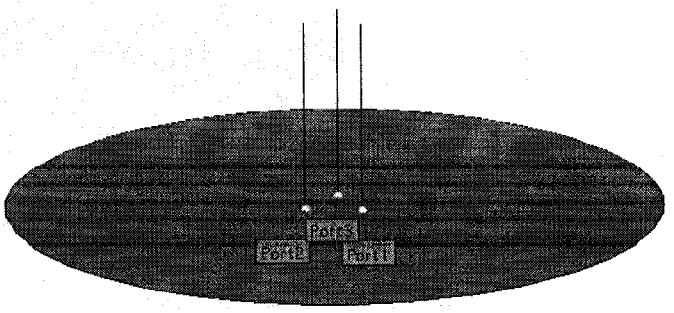

Figure 111 - Three Monopoles and Ground Plane, Monopoles Closely Spaced

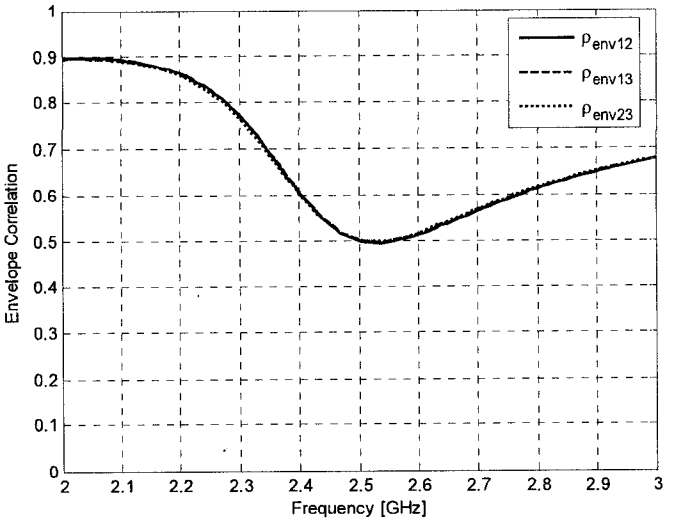

Figure 112 – Envelope Correlation of Three Monopoles and Ground Plane, Closely Spaced

Of further interest is to point out that Eber and Chaloupka's paper [5] considers CPM's from the port current perspective, whereas our method considers port voltages. Despite the difference in formulations, one finds the same weights for the given choice of port symmetry regardless of the modal formulation. We will conclude by considering three dipoles having symmetry in the same manner as the previous examples, and show the corresponding envelope correlation in Figure 113. We find that the envelope correlation is better for the case of three dipoles when compared with the three monopoles, but it is still generally significantly larger than previous designs seen in chapter 5 and 6. We subsequently compute the eigen-voltages associated with the Y-parameters and find, yet again, the same weights:

$$[V_1 \quad V_2 \quad V_3] = \left[\begin{bmatrix} 0.5774 \\ 0.5773 \\ 0.5774 \end{bmatrix} \begin{bmatrix} -0.0033 \\ 0.7073 \\ -0.7078 \end{bmatrix} \begin{bmatrix} 0.8160 \\ -0.4080 \\ -0.4085 \end{bmatrix}\right] \tag{7.3-4}$$

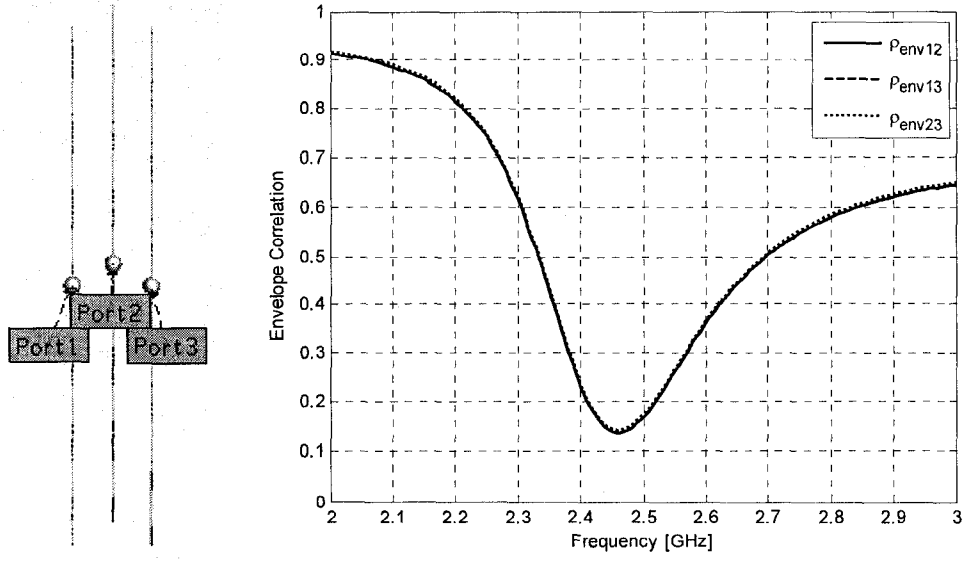

Figure 113 – Envelope Correlation of Closely Spaced Dipole Antennas

The source of the eigen-voltage (eigenvector) invariance can also be shown from mathematical arguments. These matrices are of the type Circulant, the properties of which are discussed at length in [8] and [9]. An important property of circulant matrices is that their eigenvectors diagonalize any other circulant matrix of the same N x N dimension. Since all of the antennas considered thus far are made of reciprocal materials, the parameter matrices are also symmetric, and hence the Y, Z and S parameters are circulant symmetric. The general form of a symmetric circulant matrix is shown below:

$$[A]=\begin{bmatrix} a_o & a_1 & \cdots & a_N \\ a_1 & a_o & \ddots & \vdots \\ \vdots & \ddots & \ddots & a_1 \\ a_N & \cdots & a_1 & a_o \end{bmatrix} \tag{7.3-5}$$

It is clear from expression 7.3-5 that all one needs is the first column vector in [A] to know the details of the entire matrix [A]. If we consider the first column written in terms of the Y-parameters of an N-port system, we find the following:

$$\begin{bmatrix} Y_{11} \\ Y_{21} \\ \vdots \\ Y_{N1} \end{bmatrix} \tag{7.3-6}$$

This column vector represents all of the self and mutual admittance interactions of the first port with itself and all remaining ports. Due to symmetry, the column vectors of the remaining N – 1 ports are identical up to a cyclical shift of the entries.

Hence, for symmetric structures like the three monopole and dipole sets discussed in this section and the Chaloupka and Eber [5] antenna it is the fact that the matrices are circulant that the same eigenvectors arise. We conclude that for any two sets of structures sharing the same port symmetry, the CPM weights will be the same, and are thus universal for N-point symmetries.

7.4 – Asymmetric Design of MIMO Systems using CPM Theory

We consider a small bar-type chassis with dimension 80mm by 40mm at 2.5 GHz, significantly smaller than previously considered designs. As such, we expect that the envelope correlations of the individual antenna pairs will be larger than acceptable. To add further complications, we include a mock-up of RF shields, surface mount components, as well as an approximation to a battery pack as shown in Figure 114. The three antennas are resonant at 2.5 GHz. We shall not consider the S-parameters, and assume that a matching network will be included to match the RF circuitry to the antennas. Furthermore, one can consider the onboard components as shown as mimicking the matching networks, in addition to the other components they represent. The envelope correlation of the individual antennas is shown in Figure 115. Notice that all three envelope correlations are well above 0.1 over the entire measured frequency span. Moreover, the values are significantly larger (as high as 0.9) than previously encountered in earlier chapters. By applying CPM theory, we should have zero envelope correlation at the desired center frequency.

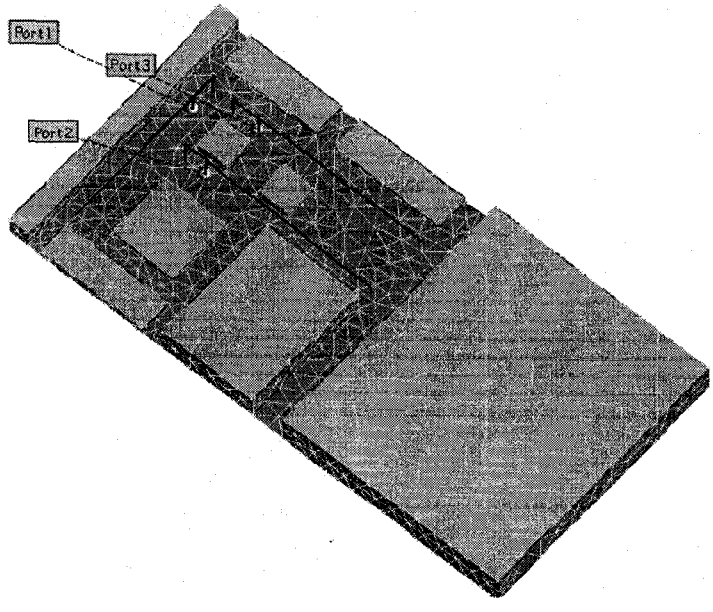

Figure 114 – Example Mobile Device Including Three Antennas

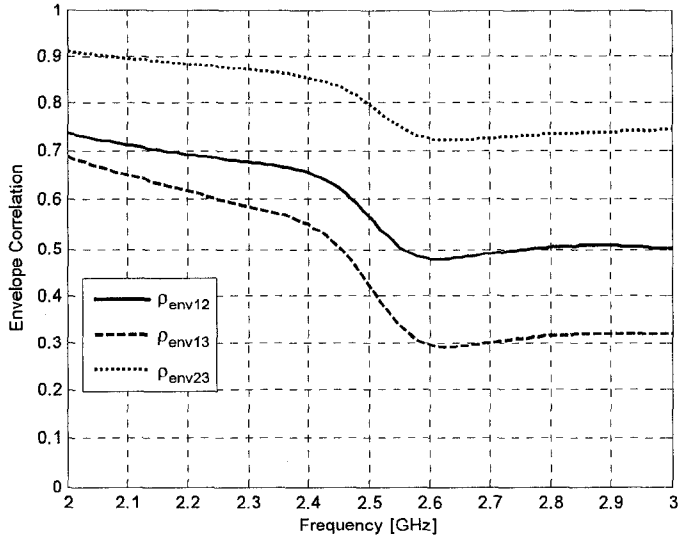

Figure 115 – Envelope Correlation of Three Antenna Mobile Device, Individual Antennas

At the center frequency, the CPM eigen-voltages are computed:

$$[V_1 \quad V_2 \quad V_3]_{@2.5GHz} = \left[\begin{bmatrix} 0.42 \\ -0.57 \\ 1.00 \end{bmatrix} \begin{bmatrix} -1.00 \\ -0.02 \\ 0.62 \end{bmatrix} \begin{bmatrix} -0.52 \\ -0.63 \\ -1.00 \end{bmatrix}\right] \tag{7.4-1a}$$

Additionally, at the higher end (3 GHz) the weights are as follows:

$$[V_1 \quad V_2 \quad V_3]_{@3GHz} = \left[\begin{bmatrix} 0.29 \\ -1.00 \\ 0.41 \end{bmatrix} \begin{bmatrix} -1.00 \\ 0.05 \\ 0.54 \end{bmatrix} \begin{bmatrix} -0.52 \\ -0.59 \\ -1.00 \end{bmatrix}\right] \tag{7.4-1b}$$

Finally, at the lower end (2 GHz) the weights are as follows:

$$[V_1 \quad V_2 \quad V_3]_{@2GHz} = \left[\begin{bmatrix} -0.20 \\ 1.00 \\ -0.62 \end{bmatrix} \begin{bmatrix} -1 \\ 0.12 \\ 0.53 \end{bmatrix} \begin{bmatrix} -0.63 \\ -0.60 \\ -1 \end{bmatrix}\right] \tag{7.4-1c}$$

We note that because of the complete lack of symmetry in the three antenna system, the weights are no longer insensitive to frequency changes. Hence, in order to truly maintain zero envelope correlation over a wide bandwidth we must apply different

weights at every frequency. However, we can compute the weights at the center frequency, and hold them constant over the operating bandwidth. If the weights are not *too* sensitive to frequency, orthogonality of the far-field patterns will be ensured at the center frequency and the envelope correlation will gradually increase as one moves away from the center frequency.

Notice however that the weights for mode 1 change drastically from 2 to 3 GHz. The lack of symmetry presents itself in the form of frequency-sensitive CPM weights. We nevertheless apply the weights as computed for the center frequency, holding them constant over frequency and measuring the envelope correlation between the individual modal excitations, as shown in Figure 116.

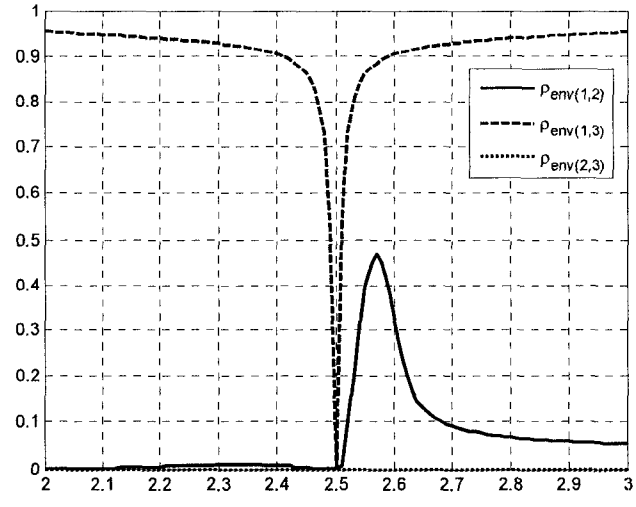

Figure 116 – Envelope Correlation of Mobile Device using CPM Weights

We notice four important results:

(1) One finds that all three envelope correlations are precisely zero at the chosen center frequency, as required by the CPM theory.

(2) One of the envelope correlation pairs (2, 3) is well below 0.1 for the entire measurable bandwidth. This is a significant improvement over the results for operating each antenna individually.

(3) The envelope correlation (1,2) is very low below center frequency but increases to larger values above center. Nonetheless, the envelope correlation is indeed zero at the center frequency.

(4) We notice an extremely narrow low envelope correlation for pair (1,3). The theory performs precisely as expected yielding zero envelope correlation at the desired frequency. However, there is no guarantee that the envelope correlation will remain low over any length of bandwidth. Because of the asymmetry, and thus frequency dependence of the eigen-voltages, the low envelope correlation is only assured at the center frequency.

What can be very misleading from these results is quoting a single value for envelope correlation. Various authors [4 – 7] have used CPM theory or similar modal decomposition theories and assumed the envelope correlation is very low (effectively zero) at the chosen design frequency for the correctly chosen weights, and fail to compute envelope correlation to confirm this result. It is not necessarily wrong to assume the envelope correlation is indeed low or zero at the center frequency, as this is guaranteed by the modal decomposition theories. What is ill-advised is to assume that since the envelope correlation is zero at the design frequency, an acceptable low-envelope correlation bandwidth would naturally follow. We have shown that this is clearly not the case when there is asymmetry in the radiating structures' ports.

A valid method to correct this situation would be to apply frequency-dependent weights. These weights can be applied in a continuous manner thereby ensuring low envelope correlation over a wide bandwidth. This approach would theoretically yield zero envelope correlation at any frequency, but one would no longer be capable of achieving the signal weighting uses passive microwave circuits. Furthermore, the weightings change quite drastically with frequency making the application of these rapidly changing weights very difficult in practice. This could be implemented using microwave amplifiers with frequency responses matching the necessary weights. Again, this would be very difficult in practice. The last possibility we shall consider involves

applying the weights via DSP. With the exponential rise in computing power, it is only a matter of time before digital signal processing will occur at carrier frequencies [10].

Let us now consider a more reasonable design where the envelope correlations of the individual antennas are not so drastically high and apply CPM theory to the asymmetric design. An example of such a design is shown in Figure 117. The physical dimensions of the represented handheld are identical to the previous example, but we have separated the IFAs and re-organized the surface mounted components in order to reduce the antenna's individual envelope correlations. The individual antenna envelope correlations are shown in Figure 118 and are significantly lower than the previous examples, although not comparable to Chapter 5 results where CM theory was used in the design process.

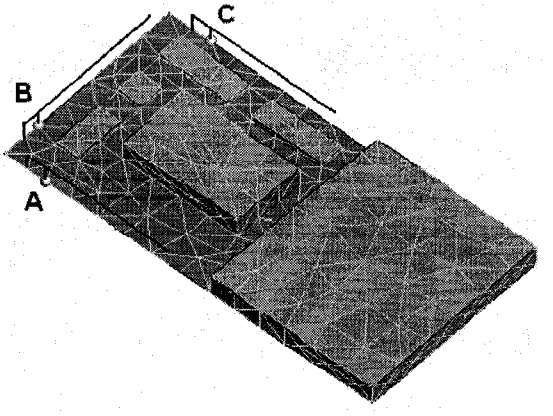

Figure 117 – Alternative Mobile Device with Greater Spacing Between Antenna Elements

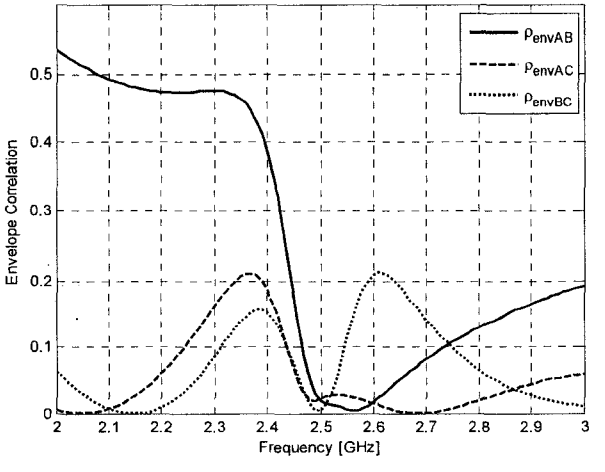

Figure 118 - Envelope Correlation of Alternative Mobile Device, Individual Antennas.

Assume now that a user moves from one area of coverage to another, where the operating frequency changes from 2.5 GHz to 2.4 GHz, and requires low envelope correlation far-field patterns at this new center frequency. Considering Figure 118, we find the envelope correlations of the individual antennas are large at 2.4 GHz with values ranging from 0.15 to 0.5. Using CPM theory, one could apply the appropriate weights (eigen-voltages), computed at 2.4 GHz and effectively shift the region of low envelope correlation to the desired frequency. The eigen-voltages at 2.4 GHz are as follows:

$$[V_1 \quad V_2 \quad V_3]_{@2.4GHz} = \left[\begin{bmatrix}-1.00\\-0.66\\0.81\end{bmatrix} \begin{bmatrix}0.92\\-1.00\\-0.54\end{bmatrix} \begin{bmatrix}0.73\\0.61\\1.00\end{bmatrix}\right] \qquad (7.4\text{-}2)$$

Applying these voltages, we find the envelope correlations between modes (no longer between antennas) as shown in Figure 119. Notice that the envelope correlation between the modes is precisely zero at the center frequency of 2.4 GHz, and maintain an appreciable bandwidth around this frequency. Notice also that as one moves away from center frequency the low envelope correlation does break down, since the radiating structure and the selected ports are asymmetric, making the required eigen-voltages (or weights) a function of frequency.

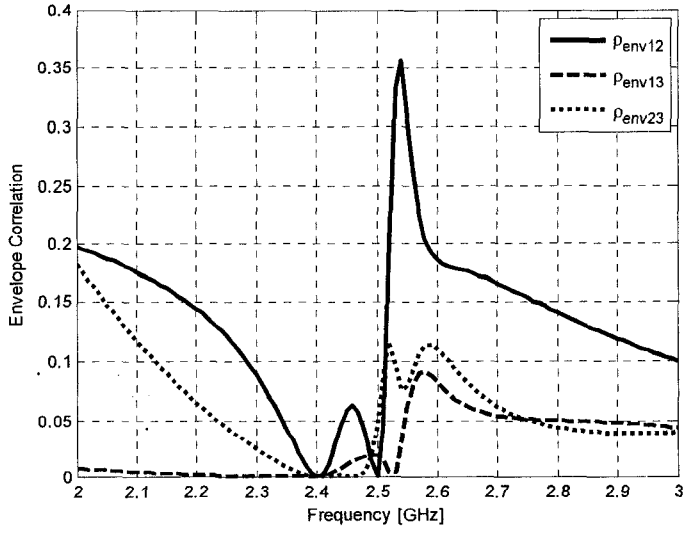

Figure 119 – Envelope Correlation between CPM Modes at 2.4 GHz

As a last investigation into the effect of asymmetry on characteristic port modes, we consider the cartwheel shaped antenna proposed by Wang and Lee [11 – 12]. Using clever arguments regarding fundamental sources of radiation, the antenna has four ports excited using what they labeled a 'modal decomposition network' or MDN for short. Each signal then excites one of the four fundamental sources of radiation: two orthogonal dipoles modes, a magnetic dipole and an electric quadrupole. The MDN consists of multiple four-port hybrid couplers, which allowed appropriate weightings of input signals at each of the antenna's four ports. The weights are as follows:

$$\begin{bmatrix} V_1 & V_2 & V_3 & V_4 \end{bmatrix} = \begin{bmatrix} \begin{bmatrix} 1 \\ 1 \\ 1 \\ 1 \end{bmatrix} & \begin{bmatrix} 1 \\ 1 \\ -1 \\ -1 \end{bmatrix} & \begin{bmatrix} 1 \\ -1 \\ 1 \\ -1 \end{bmatrix} & \begin{bmatrix} 1 \\ -1 \\ -1 \\ 1 \end{bmatrix} \end{bmatrix} \tag{7.4-3}$$

Performing a CPM analysis on said structure reveals identical weightings as stated by Wang and Lee. Applying these weights one finds the envelope correlation is always zero between excitations and is independent of frequency. Furthermore, the cartwheel shape in and of itself is not responsible for the excitation of orthogonal far-field patterns. Any structure with four-axis symmetry as is the case in Wang and Lee's antenna will yield the very same weights. Some examples of this structural symmetry include:

- Four monopoles positioned symmetrically on a square or circular ground plane.
- Four individually fed patch antennas, maintaining four-axis symmetry.

Provided the symmetry is maintained, the eigen-voltages as stated by Wang and Lee [12] apply and thus yield far-field pattern orthogonality that is insensitive to frequency. *The question remains:* what behaviour can one expect if the symmetry is lost? From simulation results of the symmetrical structure, it is clear that asymmetry can change CPM results drastically as diligence was needed to ensure the physical meshing was also symmetrical, thereby ensuring the symmetry of the structure would appear in the computed parameters.

As a simple case, we consider the cartwheel proposed by Lee and Wang, and break the symmetry slightly by shifting one of the arms of the cartwheel as shown in Figure 120. In particular, port D is shifted from the edge to the middle of central plate. We then compute the CPM weights at the center frequency and measure the envelope correlation of the modes over frequency. The weights of the asymmetric structure are as follows:

$$[V_A \quad V_B \quad V_C \quad V_D] = \left[\begin{bmatrix} 0.90 \\ 0.96 \\ 0.81 \\ 1.00 \end{bmatrix} \begin{bmatrix} 0.71 \\ 0.33 \\ -1.00 \\ -0.44 \end{bmatrix} \begin{bmatrix} 0.81 \\ -0.66 \\ 0.75 \\ -1.00 \end{bmatrix} \begin{bmatrix} 0.82 \\ -1.00 \\ -0.83 \\ 0.78 \end{bmatrix}\right] \qquad (7.4\text{-}4)$$

It is interesting to note that the orientation of the voltages (+ or -) remains the same as the symmetric structure, but the weight magnitudes are no longer all unity, due to the asymmetry of the physical ports. The envelope correlations between the modes of the newly asymmetric four port device is shown in Figure 121.

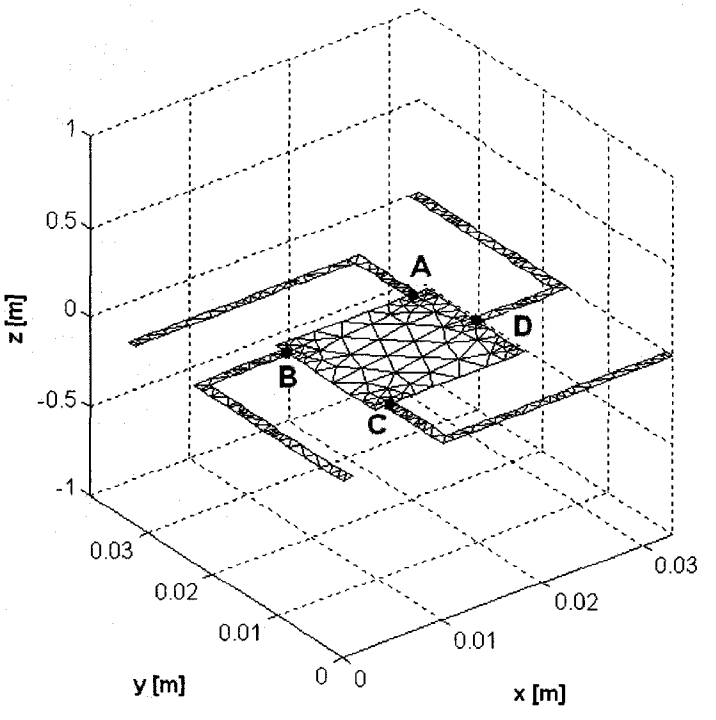

Figure 120 – Example Asymmetric Design, Altered Design after Wang & Lee [12]

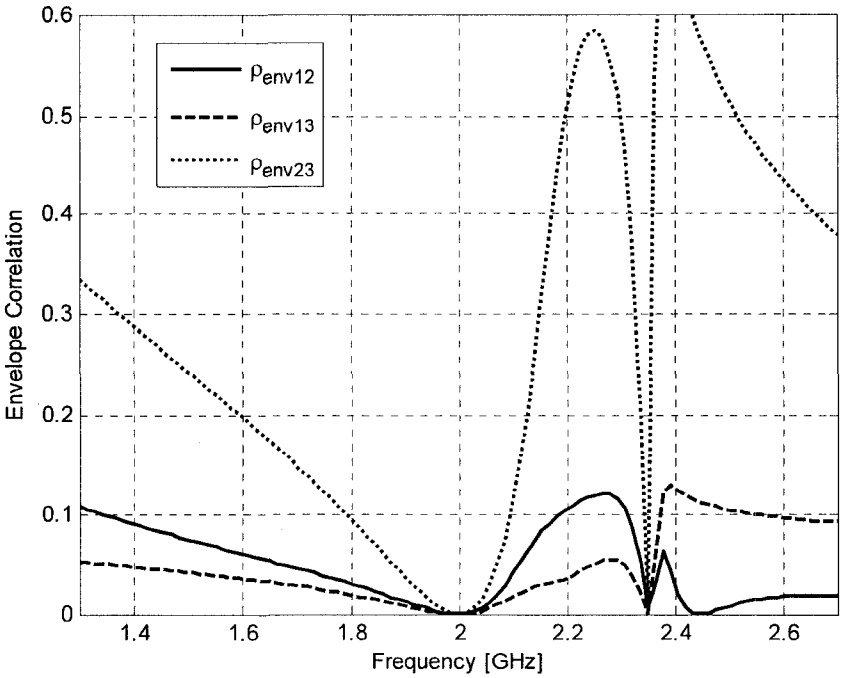

Figure 121 – Resulting Envelope Correlation Due to Asymmetry in the Physical Layout

The envelope correlation is indeed zero at the center frequency for which the CPM weights were computed. However, by breaking the symmetry in the design we have significantly reduced the usable bandwidth for which the envelope correlation is low. Moreover, the breaking of symmetry is not severe and yet the resulting envelope correlation bandwidth is severely limited. A mobile communications device is rarely able to ensure physical symmetry due to the natural asymmetry introduced by the RF shields, amplifiers and the like. Even if symmetry could be maintained in the handheld, the user introduces an inevitable symmetry breaking.

There is a distinct lack of reporting in the literature about the frequency behaviour of envelope correlation, be it for the CPM theory material or even the general optimization for MIMO antennas approach. As evident in this section, a low envelope correlation at one frequency is not enough of a measure to state that one has a system of antennas ideal for MIMO communications. The frequency performance of envelope correlation must be ascertained in order to make any conclusions about MIMO antenna design.

7.5 – Relation of CPM Theory to Recent Mode-Decoupled Antennas

The theory used by Eber and Chaloupka [4, 5], who reference Rasmussen's work from 1976 [3] is equivalent to the theory proposed by Mautz and Harrington in 1973 [1]. Another set of publications by Weber and Volmer [6, 7] utilize the mode decoupling theory proposed by Stein [2]. The CPM approach uses the Y (or Z) parameters to compute the eigen-voltages, and is independent of port terminations. The theory proposed by Stein and implemented by Weber and Volmer includes the effect of the port terminations since it is derived from the S-parameters.

It is clear that both the CPM and S-parameter approach leads to modes having zero envelope correlation over the entire far-field, but questions remain as to which theory is the ideal one to use, and considerations as to what conditions are necessary for both approaches to be equivalent.

We consider the 3-port slot design shown in Figure 122 consisting of a PEC plate with three slots designed into the 100mm by 50mm plate. The ports are chosen in a manner that one might consider works around design constraints of physical area. We subsequently compute the CPM voltages and the eigenvectors of the "radiation" matrix $H = U - S^H S$ defined by Stein and implemented by Weber & Volmer for the structure as shown in Figure 122.

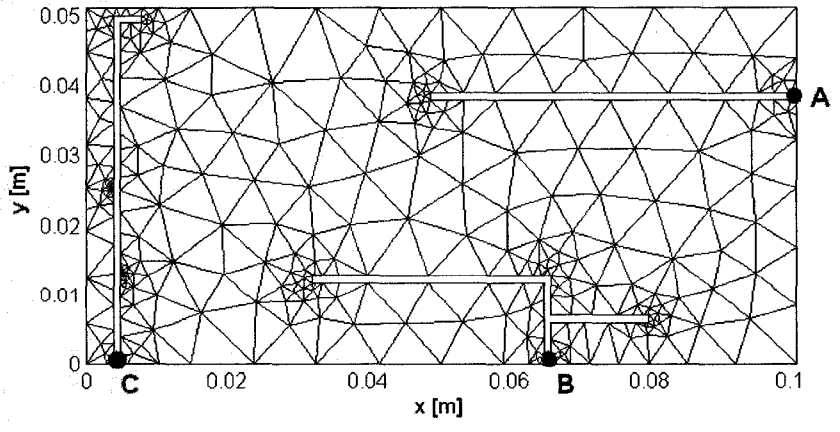

Figure 122 – Example Three Slot-Antenna Design, with Significant Asymmetry

We can compute the generator voltages from the CPM approach using:

$$[V_g^{port}] = Z_o[I^{port}] + [V^{port}] \tag{7.5-1}$$

Whereas with the "radiation" matrix modes the generator voltages are determined by:

$$[V_g^{port}] = Z_o[I^{port}] + \sqrt{Z_o}\left\{[U] + [S^{port}]\right\}[a^{port}] \tag{7.5-2}$$

where $[U]$ is the identity matrix and $[a^{port}]$ are the incident voltage waves as determined by Stein's method.

The resulting envelope correlations of the CPM modes and what we will colloquially call STEIN modes are shown in Figure 123 (a) and (b) respectively. It is clear from the two plots that the two methods yield low envelope correlation modes, and indeed zero at center frequency, but their behaviours are different and thus the far-fields are unique

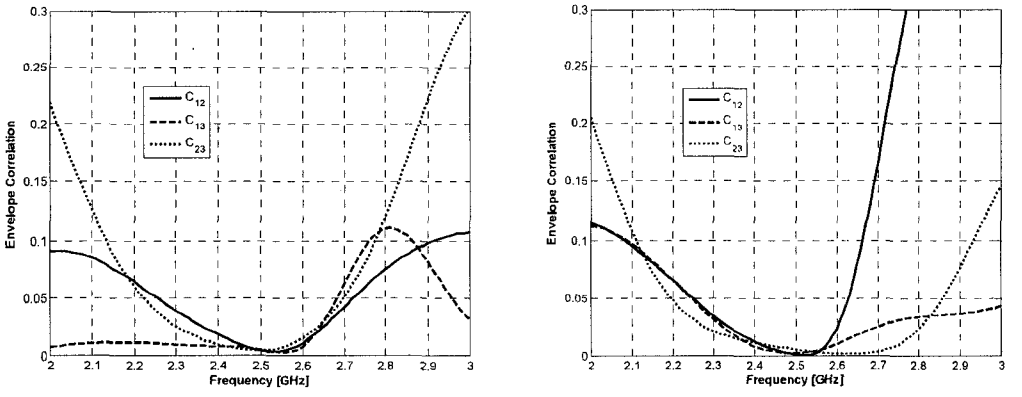

Figure 123 – Resulting Envelope Correlation by Applying (a) CPM Weightings, (b) Stein Weightings

It is difficult to quantify whether the STEIN modes or the CPM theory are superior. The applicability likely depends on the situation, where one method might present itself as more attractive than the other. For the current discussion, as shown in Figure 123, the CPM theory provides larger low envelope correlation bandwidth when compared to the STEIN modes, but this is a situational dependence and not a general conclusion.

What is of greater interest is whether there are conditions in which the Characteristic Port Modes are equivalent to the Stein (or Radiation) modes. Consider the situation where we have perfect symmetry in the N-port system, leading to the circulant matrix property for the Y and Z parameters. Under these conditions, the S-matrix is also circulant. From the matrix properties of circulant matrices outlined in [8] and [9], the conjugate transpose of a circulant matrix is a circulant matrix, the multiplication of two circulant matrices is circulant, and finally, the addition of two circulant matrices is circulant. With these three properties applied to the matrix $[H]=[U]-[S]^{H}[S]$, it is clear that if $[S]$ is circulant, then $[H]$ must be as well. A further property of circulant matrices is that their eigenvectors diagonalize any other circulant matrix of the same N x N dimension. Hence, for symmetric structures like the three monopole and dipole sets discussed in section 7.3, the Chaloupka and Eber [5] antenna or the cartwheel antenna by Wang and Lee [12], the CPM and STEIN modes are identical.

7.6 – Connection between CMs and CPMs

It is always satisfying to find connections between theories, as it helps to clarify uncertainties in understanding. As such, we showed a connection between CMs and GCMs, where the CMs are shown to be a special case of the GCMs when the weight operator $W(\theta,\phi)$ is chosen to be unity over the entire sphere.

Additionally, we can find a connection between the CMs and CPMs. In the rigorous mathematical formulation of characteristic modes, the number of modes is infinite. In practice, the number of modes one can compute is limited by (and in fact equal to) the number of moment method expansion functions used in the formulation. If one were to define each moment method expansion function as a port (effectively every adjoining triangle edge) the Characteristic Port Modes are equivalent to the Characteristic Modes for the same equivalently meshed structure. Stated alternatively, in the limit of the number of defined ports N equaling the number expansion functions M, the CPMs converges to the CMs. This of course requires one to use a moment method formulation to compute the CPMs, such that the ports defined in both formulations are identical. The connection exists as follows: The CPMs based on the Z-parameters (port currents) are related to the CMs defined by the impedance operator. Alternatively, the CPMs based on the Y-parameters (port voltages) are related to the CMs defined by the admittance operator. Regardless, the concepts apply whether one considers admittance or impedance as the starting point for analysis.

That being said, it is straightforward to then show it is quite difficult to excite a single characteristic mode of a structure. In doing so one would effectively require M ports where M = N expansion functions and apply port voltages equal to the corresponding computed CPM weights. That is to say, to excite a single CM, one would need a multitude of ports over the entire surface and apply the very specific excitation voltages at every port. To illustrate this point further, we consider an arbitrary PEC plate meshed as shown in Figure 124.

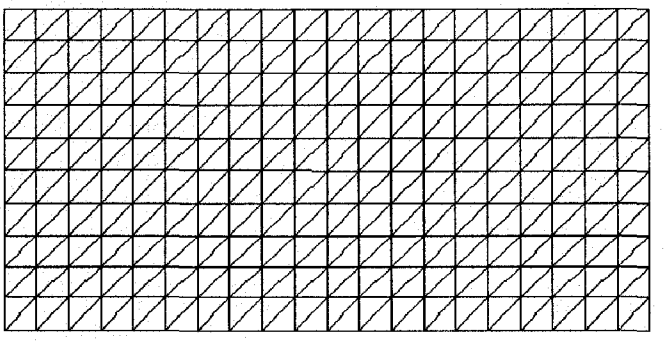

Figure 124 – Example Meshed Structure for CM and CPM Similarity Considerations

In order to perfectly excite a single characteristic mode of the aforementioned plate, one would need a voltage gap feed at every single adjoining triangle edge. While theoretically possible, this would be a daunting, if not impossible task for an antenna designer.

It is likely that for this reason the design proposed by Chaudhury & Schroeder [13] has difficulty in achieving the desired results for MIMO antenna design, and perhaps why the necessary envelope correlation simulations are absent from the paper. To excite a single characteristic mode is indeed difficult.

However, there is a solution to this problem as discussed in Chapters 5 and 6, as one can increase the degrees of freedom by extending the requirement to exciting unique groups of characteristic modes, not just a single characteristic mode. Whether one devises excitation schemes that excite single characteristic modes or sets of unique CMs, the result is the same: each antenna produces a far-field pattern that is orthogonal relative to other antennas in the system. That being said, we have shown that it is much easier to excite sets of CMs, rather than a single CM, as evident in the theoretical and experimental results discussed in Chapters 5 and 6.

Let us conclude our discussion by considering the two slot antenna CM design from Chapter 5, Section 5.7, shown in Figure 125 (a). Recall that the top most port excited the difference of modes 2 and 4, whereas the bottom port excited the addition of modes 2 and

4. Computing the CPM eigen-voltages finds the expected two vectors, since the structure has symmetry that yields a circulant symmetric Y parameter matrix.

$$V_1 = \begin{bmatrix} 1 \\ 1 \end{bmatrix} \text{ and } V_2 = \begin{bmatrix} 1 \\ -1 \end{bmatrix} \tag{7.6-1}$$

Notice that the analysis leads to eigen-voltage V_1 predominantly exciting mode 2, and eigen-voltage V_2 exciting mode 4. From the symmetry of the structure, this modal excitation approach holds over all frequencies but absolutely requires that the antennas operate simultaneously using a modal decomposition network (MDN), which complicates the implementation aspect of the design. Under special circumstances, which come about with symmetry arguments and modal excitation tuning as shown in Chapter 5, Section 5.7, one can operate the antennas independently of each other, forgoing the need for a modal decomposition network, and thus a simplifying the practical implementation.

Lastly, we consider the four antenna design discussed in Chapter 5, Section 5.8.3 shown in Figure 125 (b). Computing the CPM eigenvectors we find the following modal voltages:

$$[V_1 \quad V_2 \quad V_3 \quad V_4] = \begin{bmatrix} \begin{bmatrix} 1 \\ 1 \\ 1 \\ 1 \end{bmatrix} & \begin{bmatrix} 1 \\ 1 \\ -1 \\ -1 \end{bmatrix} & \begin{bmatrix} 1 \\ -1 \\ 1 \\ -1 \end{bmatrix} & \begin{bmatrix} 1 \\ -1 \\ -1 \\ 1 \end{bmatrix} \end{bmatrix} \tag{7.6-2}$$

which are precisely the same eigen-voltages computed for Wang and Lee's cartwheel antenna. The equivalence is due to the circulant matrix properties as discussed at the end of Section 7.3. Again, under special circumstances (symmetry and modal tuning) one can forgo the MDN and move immediately to exciting the antennas individually, since each port has a modal properties necessary for single antenna operation (as discussed in Section 5.7).

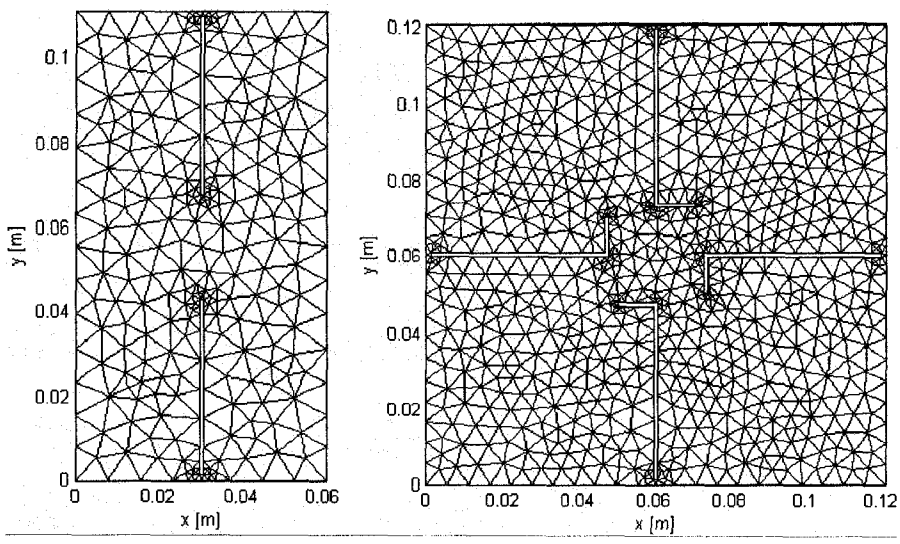

(a) (b)

Figure 125 – Example Designs using CM theory that have Connection with CPM theory, (a) Two Antenna Symmetry, (b) Four Antenna Symmetry

Our discussions are not intended to downplay the CPM method, as it can be very useful (if not necessary) when dealing with electrically small antennas, since they typically exhibit large envelope correlation between closely spaced antenna pairs. But regardless of the approach, it is advisable to not rely on structural symmetry, as we showed the consequences of minor symmetry-breaking is a drastic reduction in usable envelope correlation bandwidth. The majority of the research findings and simulation results have been published in [14].

7.7 – Concluding Remarks

In Section 7.2 we discussed the properties of CPM theory and how it relates to MIMO antenna design. We showed how one can implement the theory in practice. We also considered other distinct port modal formulations, namely the Stein modes.

We then considered symmetry in radiating structures and the implications this has for CPM theory in section 7.3. For the case of physically symmetric ports, the eigen-voltages are independent of the types of radiating structures and operating frequency and are therefore dependent only on the number of physically symmetric ports.

We continued our CPM discussion and extended it to include asymmetric structures in Section 7.4 where we showed such structures lead to frequency-dependent CPM weights. This frequency dependence showed itself in the form of narrow low envelope correlation bandwidth when one fixes the eigen-voltage weights for a given center frequency. This led to limitations for closely spaced asymmetric antenna configurations, a fact not considered in the literature. Moreover, we pointed out that there is a lack of consideration in the literature for the frequency performance of envelope correlation and omitting such critical data offers an incomplete study of a MIMO antenna design.

In section 7.5 we considered another popular port mode formulation involving Stein's formulation [2], and considered the use of either formulation for MIMO antenna design. We concluded the section by showing that under port symmetry conditions the CPM and Stein modes are identical, allowing the approaches to be interchangeable.

We concluded our discussion in section 7.6 by showing the relationship between CPM theory and CM theory, which was shown to only be possible from a moment method perspective. This led us to show some interesting results that tie the symmetry arguments in CM design developed in Chapter 5 with the symmetry arguments in the CPM approach.

CHAPTER 7 REFERENCES

[1] J. Mautz, R.F. Harrington, "Modal Analysis of Loaded N-Port Scatterers", *IEEE Transactions on Antennas and Propagation*, Vol. AP-21, No. 2, March 1973.

[2] S. Stein, "On Cross Coupling in Multiple-Beam Antennas", *IEEE Transactions on Antennas and Propagation*, Vol. 10, Issue 5, pp 548 – 557, September 1962.

[3] J.B. Anderson, H.H. Rasmussen, "Decoupling and descattering networks for antennas", *IEEE Transactions on Antennas and Propagation*, vol. 24, pp. 841 – 846, Nov. 1976.

[4] H. Chaloupka, X. Wang, "Novel Approach for Diversity and MIMO antennas at small Mobile Platforms," *IEEE PIMRC-Symposium Digest*, Vol. 1, pp. 1229 – 1232, 2004.

[5] D. Eber, H. Chaloupka, "Design Approach for a Class of Compact Multiport Antennas," *Microwave, Antennas, Propagation and EMC Technologies for Wireless Communications*, Vol. 1, pp 144 – 147, Aug 2005.

[6] J. Weber, C. Volmer, K Blau, R. Stephan, M. Hein, "Miniaturized Antenna Arrays Using Decoupling Networks With Realistic Elements," *IEEE Transactions on Microwave Theory and Techniques*, Vol. 54, No. 6, pp. 2733 – 2740, June 2006.

[7] J. Weber, C. Volmer, K Blau, R. Stephan, M. Hein, "Miniaturized Antenna Arrays Using Decoupling Networks With Realistic Elements," *IEEE Transactions on Microwave Theory and Techniques*, Vol. 54, No. 6, pp. 2733 – 2740, June 2006.

[8] R. Horn, C. Johnson, *Matrix Analysis,* Cambridge University Press, New York 1985.

[9] R. Horn, C. Johnson, *Topics in Matrix Analysis,* Cambridge University Press, New York 1991.

[10] J. Mitola, Software Radio Architecture: A Mathematical Perspective, IEEE Journal on Selected Areas in Communications, vol. 17, issue 4, pp. 514 – 538, April 1999.

[11] T. Lee., Y. Wang, "Maximized Capacity of Coupled Antennas Based on Multipolar Radiations", *Radio and Wireless Symposium 2007,* pp. 99 – 101, January 2007.

[12] T. Lee., Y. Wang, "A Planar Multipolar Antenna for MIMO Applications", *IEEE Antennas and Propagation International Symposium* 2007, pp. 2429 – 2432, June 2007.

[13] S. Chadhury, W. Schroeder, H. Chaloupka, "MIMO Antenna System based on Orthogonality of the Characteristic Modes of a Mobile Device," *2nd International ITG Conference on Antennas,* March 2007, pp. 58 – 62.

[14] **Jonathan Ethier** and Derek McNamara, "An Interpretation of Mode-Decoupled MIMO Antennas in Terms of Characteristic Port Modes", *13th Biennial IEEE Conference on Electromagnetic Field Computation (CEFC 2008) Digest.*

Chapter 8

General Conclusions

The principal contributions of this thesis are as follows:

- A complete design procedure for MIMO antennas using the Theory of Characteristic Modes for the first time. This procedure is general enough to handle arbitrarily shaped conducting plates and chassis and is not only limited to mobile phones. An example design was experimentally validated.

- An extension of the aforementioned design procedure for MIMO antenna design to arbitrarily defined scattering environments using polarization sensitive Generalized Characteristic Modes. This is the first time a design procedure is proposed for arbitrary scattering environments, let alone using the GCMs in the design process. An example design was experimentally validated.

- A literature review on port mode approaches to MIMO antenna design and conclusions on the limitations of the theory, showing the requirement of more reporting of data in the literature, equivalences between a number of theories and similarities between port mode and characteristic mode approaches.

Some of the lesser contributions, although still significant, are as follows:

- Two *newly* defined modal formulations including the finite conductivity or "lossy" Characteristic Modes and the polarization sensitive Generalized Characteristic modes, the first of their kind.

- Fundamental conclusions regarding the significance of characteristic modes with a newly defined figure of merit denoted "modal significance" that betters serves the analysis procedure when ranking characteristic modes.

There are a number of issues whose investigation in the future would prove useful in the design of MIMO antennas. Firstly, there exist volumetric modal formulations as discussed previously where one can include lossy dielectrics. These can be used to model users' head and hands, and be included in the design procedure for full sphere orthogonality. It is expected that the same principles and design methodology outlined in this thesis would also be applicable for the lossy dielectric formulation.

Furthermore, a new modal theory that incorporates the polarization sensitive generalized characteristic modes and a lossy dielectric volumetric approach would allow a complete qualitative and quantitative description of the radiating system, and allow for a well defined MIMO antenna design methodology in the presence of the user.

List of Figures

List of Tables